Universidade Federal do Rio de Janeiro

HYDROGEN–MICROSTRUCTURE–MECHANICAL PROPERTIES INTERACTIONS IN SUPER DUPLEX STAINLESS STEEL COMPONENTS

Pedro da Silva Craidy

2018

HYDROGEN–MICROSTRUCTURE–MECHANICAL PROPERTIES INTERACTIONS IN SUPER DUPLEX STAINLESS STEEL COMPONENTS

Pedro da Silva Craidy

Tese de Doutorado apresentada ao Programa de Pós-graduação em Engenharia Metalúrgica e de Materiais, COPPE, da Universidade Federal do Rio de Janeiro, como parte dos requisitos necessários à obtenção do título de Doutor em Engenharia Metalúrgica e de Materiais.

Orientadores: Dilson Silva dos Santos
Laurent Briottet

Rio de Janeiro
Junho de 2018

HYDROGEN–MICROSTRUCTURE–MECHANICAL PROPERTIES INTERACTIONS IN SUPER DUPLEX STAINLESS STEEL COMPONENTS

Pedro da Silva Craidy

TESE SUBMETIDA AO CORPO DOCENTE DO INSTITUTO ALBERTO LUIZ COIMBRA DE PÓS-GRADUAÇÃO E PESQUISA DE ENGENHARIA (COPPE) DA UNIVERSIDADE FEDERAL DO RIO DE JANEIRO COMO PARTE DOS REQUISITOS NECESSÁRIOS PARA A OBTENÇÃO DO GRAU DE DOUTOR EM CIÊNCIAS EM ENGENHARIA METALÚRGICA E DE MATERIAIS.

Examinada por:

_____

Prof. Dilson Silva dos Santos, D.Sc.

_____

Laurent Briottet, D.Sc.

_____

Prof. Sergio Souto Maior Tavares, D.Sc.

_____

Prof. Xavier Feaugas, D.Sc.

_____

Prof. Luiz Henrique de Almeida, D.Sc.

RIO DE JANEIRO, RJ - BRASIL

JUNHO DE 2018

Craidy, Pedro da Silva

Hydrogen – Microstructure – Mechanical Properties Interactions in Super Duplex Stainless Steel Components/Pedro da Silva Craidy. – Rio de Janeiro: UFRJ/COPPE, 2018.

XVI, 226 p.: il.; 29,7 cm.

Orientadores: Dilson Silva dos Santos

Laurent Briottet

Tese (doutorado) – UFRJ/COPPE/Programa de Engenharia Metalúrgica e de Materiais, 2018.

Referências Bibliográficas: p. 195-204.

1. Aços inoxidáveis super duplex. 2. Fragilização por hidrogênio. 3. Difusão de hidrogênio. 4. Proteção catódica. I. Santos, Dilson Silva dos *et al*. II. Universidade Federal do Rio de Janeiro, COPPE, Programa de Engenharia Metalúrgica e de Materiais. III. Título.

Acknowledgments

I would like to express my sincere gratitude to the advisors dr. Laurent Briottet and prof. Dilson dos Santos, to Propmec/UFRJ, CEA (Grenoble and Saclay) and to the Université Grenoble Alpes. I thank Petrobras for its inestimable support during the doctorate, especially the stay time in France.

I am deeply grateful for all the assistance provided by the colleagues from Propmec - Leandro Martins de Oliveira, Angela Cardenas, Carla Woyames, Renata da Silva and Robson Araujo - and by Bruno Ricetti, Eric de Vito, Florence Porcher and Jean-Marie Gentzbittel from CEA.

I thank for the material and recommendations provided by Thiago Chehuan, Vanessa Dreilich and Fatima Cunha from TechnipFMC. The project would not be possible without the invaluable help of Daniel Fruchart, John Quintero (UEPG), Leonardo Wu (LNNano), Marcelo Piza, Agildo Badaró Moreira, Diego Garcia, Ricardo Marinho, Gustavo Leitão Vaz, Jefferson Rodrigues de Oliveira, Eduardo Latge, Washington da Silva, Rose Mencarelli and Ailton de Souza (Petrobras) and Bruno Rente (UFRJ).

I finally must thank my parents, Bruno Stelet, Verônica Fernandez, Ana Lucia Pontes and Cristiano Godinho for all the support.

Resumo da Tese apresentada à COPPE/UFRJ como parte dos requisitos necessários para a obtenção do grau de Doutor em Ciências (D.Sc.)

INTERAÇÕES HIDROGÊNIO-MICROESTRUTURA-PROPRIEDADES MECÂNICAS EM COMPONENTES DE AÇO INOXIDÁVEL SUPER DUPLEX

Pedro da Silva Craidy

Junho/2018

Orientadores: Dilson Silva dos Santos

Laurent Briottet

Programa: Engenharia Metalúrgica e de Materiais

A demanda crescente por energia tem demandado a exploração de petróleo e gás em colunas d'água mais profundas e em condições mais severas. Esses sistemas de produção exigem o uso de equipamentos forjados de aços de maior resistência, como aços inoxidáveis austeno-ferríticos (duplex). Estes componentes possuem maior tendência a exibir perda de ductilidade e desempenho mecânico geral causado pelo hidrogênio gerado p.ex. por sistemas de proteção catódica. Os componentes de aços inoxidáveis duplex apresentam um vasto histórico de danos causados pelo hidrogênio a baixas temperaturas derivado de várias fontes. Mesmo sendo este tipo de dano bastante recorrente, várias informações relacionadas ainda precisam ser elucidadas, devido à complexa interação do hidrogênio com a microestrutura e o caráter localizado da geração e transporte de hidrogênio no material. O presente trabalho visa melhorar a compreensão da interação entre o hidrogênio e a microestrutura, bem como os efeitos de diferentes procedimentos de hidrogenação nas propriedades mecânicas de componentes forjados fabricados com o aço inoxidável super duplex UNS S32750.

O desenvolvimento desta compreensão envolve a avaliação dos efeitos do hidrogênio nas propriedades mecânicas do material através de ensaios de tração em diferentes ambientes ricos em hidrogênio. Com base nos resultados de ensaios de tração sob baixa taxa de deformação, uma relação quantitativa entre a fragilização causada por hidrogênio gasoso e caregamento catódico é proposta, e possíveis efeitos do transporte de hidrogênio e fragilização por hidrogênio assistido por discordâncias são discutidos. Descrições quantitativas e qualitativas do transporte de hidrogênio, incluindo a análise dos efeitos de diferentes microestruturas e caminhos de difusão, e da posição do hidrogênio na rede cristalina e na microestrutura (segregação para aprisionadores) são propostas. Estas descrições são alcançadas considerando resultados obtidos através de diferentes técnicas experimentais: ensaios de permeação, espectroscopia de dessorção térmica, espectroscopia de massa de íons secundários por tempo de vôo e espalhamento de nêutrons.

Abstract of Thesis presented to COPPE/UFRJ as a partial fulfillment of the requirements for the degree of Doctor of Science (D.Sc.)

HYDROGEN–MICROSTRUCTURE–MECHANICAL PROPERTIES INTERACTIONS IN SUPER DUPLEX STAINLESS STEEL COMPONENTS

Pedro da Silva Craidy

June/2018

Advisors: Dilson Silva dos Santos

Laurent Briottet

Department: Metallurgical and Materials Engineering

The increasing demand for energy requires the exploration of oil and gas at deeper water locations and on more severe conditions. These production systems have demanded the use of forged equipments made of higher strength steel grades, such as austenitic-ferritic (duplex) stainless steels. These components are more prone to exhibit loss of ductility and general mechanical performance caused by hydrogen generated e.g. by cathodic protection. Duplex stainless stainless steels components present a vast history of hydrogen damage at low temperatures, due to hydrogen derived from various sources. Even being this kind of damage fairly recurring, various related information remains to be elucidated, due to the complex interaction of hydrogen with the microstructure and localized character of hydrogen generation and transportation in the material. The present work aims to improve the physical understanding of the interaction between hydrogen and the microstructure as well as the effects of different hydrogen charging procedures on the mechanical properties of forged components made of the super duplex stainless steel grade UNS S32750.

The development of such understanding involves the evaluation of the effects of hydrogen on the mechanical properties of the material through tensile tests in different hydrogen-rich environments. Based on results of slow-strain rate tensile tests, a quantitative relationship between embrittlement caused by gas hydrogen and cathodic charging is proposed, and possible effects of dislocation-assisted hydrogen transportation and embrittlement are discussed. Quantitative and qualitative descriptions of the hydrogen transportation, including analysis of the effects of different microstructures and diffusion paths, and of its position in the lattice and in the microstructure (hydrogen segregation to traps) are proposed. These descriptions are achieved considering results of different testing techniques: permeation tests, thermal desorption spectroscopy, time-of-flight secondary ion mass spectroscopy and neutron scattering.

Contents

List of Figures

List of Tables

1. Introduction

Hydrogen damage comprises different phenomena that reduce the capacity of metals and alloys to withstand mechanical loading. Hydrogen embrittlement (HE) is responsible for important economic losses in several industries. It occurs on a large scale because atomic hydrogen can be introduced into the material during manufacturing (casting, welding, machining, electrochemical coating, heat treatments etc.) and/or exposure to the service environment. A wide variety of environments can generate atomic hydrogen, from gases such as H_2, H_2S and hydrocarbons to aqueous solutions at pH's of 0 to 14 and potentials above and below the corrosion potential. Hydrogen atomic fractions as low as 10^{-5} can severely embrittle metals and cause loss of ductility [1].

Hydrogen embrittlement of steels has been reported since William Johnson's pioneering work [2]. There is a long history of hydrogen damage in the exploration and production of oil and gas. In particular, failure due to hydrogen-assisted cracking is an important phenomenon in subsea stainless steel pipelines, components and structures used on this industry. Hydrogen on these cases is produced in service by corrosive processes and cathodic protection systems. Hydrogen assisted cracking is a problem of great concern also in the welding of high strength steels. Restriction of maximum diffusible hydrogen contents are usually established in the welding of steels with high mechanical strength [3].

Nowadays, duplex stainless steels (DSS) are widely used in the energy, petrochemical and naval industries in pressure vessels, heat exchangers, reactors, linepipes, umbilical lines, pumps, etc. These steels present excellent corrosion resistance combined to high mechanical strength and impact toughness. These characteristics are attributed to a fine two-phase microstructure composed of ferrite and austenite in similar proportions. The presence of the ferritic phase confers a considerable increase in the mechanical resistance and the stress corrosion in these steels when compared to the austenitic stainless steels. The so-called super duplex stainless steels (SDSS) differ from DSS by the higher pitting corrosion resistance index determined by their alloying elements.

Even though the phenomenon of hydrogen embrittlement is reasonably usual and there is much published data on the mechanical properties of hydrogen-charged (S)DSS, the failure mechanisms are not completely elucidated, and a number of information has not yet been established. These issues arise mainly due to the complexity of the phenomenon and the localized character of the generation, absorption and transportation of hydrogen and its interaction with the cracks and the microstructure of the metal.

In this work, it is aimed to improve the physical understanding of the interaction between hydrogen and the microstructure as well as the effects of different hydrogen charging procedures on the mechanical properties of forged components made of the super duplex stainless steel grade UNS S32750.

The development of such understanding involves:

1) The evaluation of the effects of hydrogen on the mechanical properties of the material through tensile tests in different hydrogen-rich environments.

2) Quantitative and qualitative description of the hydrogen transportation, of its position in the microstructure (trapping, segregation) and interactions with microstructural features. This description is achieved by different techniques: permeation tests, thermal desorption spectroscopy, time-of-flight secondary ion mass spectroscopy and neutron scattering.

3) The establishment of relationships between the mechanical/fracture behavior and the diffusion and trapping of hydrogen.

2. Literature Review

2.1. Duplex Stainless Steel Grades

Duplex stainless steels are ferrous alloys composed by a two-phase microstructure of austenite and ferrite, each of the phases containing at least 12% Cr. In general, they present compositions in the range of 18-26% Cr, 4-8% Ni and in many cases 2-3% Mo, usually with some nitrogen content. Super duplex stainless steels show levels of alloying elements in the upper or slightly above the mentioned ranges [4].

Table 1 gives the chemical composition of usual duplex stainless steels. Duplex stainless steels are classified in relation to the pitting resistance equivalent number (PRE) according to [5]:

Lean duplex ≤ 35 < Duplex < 40 ≤ Super duplex < 45-49 ≤ Hyper duplex

PRE numbers are derived from empirical relationships and can take several forms. The most widely ones employed for DSS are shown in **Equations 1** and **2**.

$$PRE = \%Cr + 3{,}3(\%Mo) + 16(\%N) \quad \textbf{(Equation 1)}$$

$$PRE_W = \%Cr + 3{,}3(\%Mo) + 0{,}5(\%W) + 16(\%N) \quad \textbf{(Equation 2)}$$

Table 1. Chemical composition of DSS (wt%) [6].

UNS	EN	C*	Cr*	Ni*	Mo*	N*	Mn*	Cu*	W*
20Cr - Lean alloy (PRE: 24-30)									
S32001	1.4482	0,03	19,5-21,5	1,0-3,0	0,60	0,05-0,17	4,0-6,0	1,0	-
S32101	1.4162	0,04	21,0-22,0	1,35-1,7	0,10-0,80	0,20-0,25	4,0-6,0	0,10-0,80	
22Cr - Duplex (PRE: 30-40)									
S31803	1.4462	0,03	21,0-23,0	4,5-6,5	2,5-3,5	0,08-0,2	2	-	-
S32205	1.4462	0,03	22,0-23,0	4,5-6,5	3,0-3,5	0,14-0,2	2	-	-
25Cr - Super duplex (PRE: 40-48)									
S32750	1,4410	0,03	24,0-26,0	6,0-8,0	3,0-5,0	0,24-0,32	1,2	0,50	-
S32760	1,4501	0,03	24,0-26,0	6,0-8,0	3,0-4,0	0,20-0,30	1,0	0,50-1,0	0,5-1,0
27Cr – Hyper duplex (PRE: 48-55)									
S33207	1.4485	0,03	29,0-33,0	6,0-9,0	3,0-5,0	0,40-0,60	1,5	1,0	-
S32707	1,4658	0,03	26,0-29,0	5,5-9,5	4,0-5,0	0,30-0,50	1,5	1,0	-

***** Single values denote maximum allowable.

The first reference to duplex stainless steel appeared in 1927, when Bain and Griffith published about the existence of a two-phase ferrite/austenite field in the Fe-Cr-Ni system. The first commercial DSS products – 453E, 453S, URANUS 50 and 3RE60 grades - date from the period between 1929 and 1937. The first duplex stainless steels were susceptible to pitting corrosion due to the preferential enrichment of ferrite in elements that confer pitting corrosion resistance such as chromium and molybdenum. Even with the increase of the Cr and Mo contents of the steel, the pitting corrosion resistance of austenite remained low. This problem was only solved later with the adoption of higher level contents of nitrogen. Other detrimental properties of this first generation of duplex stainless steels were, due to the excess of ferrite, worse weldability (low toughness in the heat affected zone) and lower corrosion resistance [4].

The Korean War (1950-51) caused a nickel shortage, which lead to further research into lower Ni-content duplex alloys. The developments in this period did not lead to products with good toughness due to lack of solubilization treatment followed by rapid cooling to avoid precipitation reactions. Improvements were made by the introduction of a quench-annealing treatment. During the late 1960s and early 1970s, there was another nickel shortage that pushed up the price of austenitic alloys, combined with increased activity in the offshore oil industry which demanded stainless steels to handle aggressive environments. Also, steel production process techniques improved dramatically with the introduction of the vacuum and argon oxygen decarburization (VOD and AOD) practices. These techniques led to steels with simultaneously low C, S and O contents, while allowing for greater control of composition, especially nitrogen. One example of such a steel was UNS S31500 which had a maximum carbon content of 0,03%.

The addition of nitrogen improved corrosion resistance and high temperature stability of the duplex structure by stabilizing austenite. The hot workability and rolling experience was greatly improved, making possible the production of wide sheets and coils. Another approach taken in the Soviet Union was to add Ti to the steel (about 0,4%Ti). Preferential formation of titanium carbides (rather than chromium carbides) reduced the occurrence of intergranular corrosion. The titanium carbides also helped to pin the grain boundaries and restricted excessive ferrite grain growth in the HAZ.

In the early 1970s, the 22%Cr duplex grade (DIN 1.4462, UNS S31803) was developed in Germany and Sweden in the context of the North Sea oil exploration and production. SAF 2205 became popular due to its balanced chemistry (Cr/Ni equivalent ratio) and the addition of nitrogen. 25%Cr grades were also developed, such as the S32550 (Ferralium 255), which contain up to 2% Cu. These alloys were originally developed as castings, such as pumps and valves, and have been extensively used in the offshore industry and for sulfuric acid service [4].

The emphasis on higher N contents characterizes the third generation of DSS. During the 1980s and 1990s, more highly alloyed DSS grades were developed to withstand more aggressive environments. The super duplex grades have pitting resistance equivalent numbers (PRE) typically greater than 40.

Sandvik recently launched on the market the so-called hyper duplex stainless steels, which have a PRE number higher than 45-49. The steels of this family, such as UNS S32707 and UNS 33207, are used in the form of seamless pipes mainly in heat exchangers and umbilicals.

The development of specifications and standards to cover duplex stainless steels is an on-going process. For instance, the standard ISO17781 (Test methods for quality control of microstructure of ferritic/austenitic (duplex) stainless steels) was published in 2017 with the aim to establish quality control criteria of duplex stainless steels in components for the oil and gas industry. Evaluation of microstructure and ferrite content, Charpy V-notch impact tests and corrosion tests are specified, and acceptance criteria are indicated.

2.2. Microstructure

Duplex stainless steels are characterized by a mixture of fcc austenite in a bcc ferrite matrix, in a proportion of about 50-50%. **Table 2** presents some features of phases and precipitates commonly observed in duplex stainless steels. The character and morphology of these phases vary markedly, as do the kinetic and mechanisms of formation and their effect on properties.

Table 2. Phases observed in duplex stainless steels [7,8]. .

Phase	Chemical formula	Formation range (ºC)	Lattice type	Space group	Lattice parameter (Å)	Preferred location
Main Phases						
Ferrite (δ)	-	-	bcc	Im3m	a = 2,86-2,88	Matrix
Primary austenite (γ)	-	<1250	fcc	Fm3m	a = 3,58-3,62	Intra-δ
Secondary austenite (γ_2)	-	<650-900	fcc	Fm3m	a = 3,58-3,63	Intra-δ, δ/γ, δ with σ
Alpha prime (α')	-	300-525	bcc	Im3m	a = 2,86-2,88	Intra-δ
Martensite ε	-		hcp	$P6_3/mmc$	a = 2,50-2,55, c = 4,10-4,20	

Intermetallic Phases						
G	$(Ni, Fe, Cr)_{16}(Nb, Ti)_6Si_7$	300-400	fcc	Fd3m	a = 11,15-11,20	Inter α/α'
R	$Fe_{22}Mo_{18}Cr_{13}$, $(Fe,Ni)_{10}Cr_5Mo_3Si_2$		Hexagonal	R3	a = 10,8-11,0, c = 19,2-19,4	
Sigma (σ)	Fe-Cr-Mo	600-1000	Tetragonal	$P4_2/mnm$	a = 8,79, c = 4,54	Inter δ/γ
Chi (χ)	$Fe_{36}Cr_{12}Mo_{10}$	700-900	bcc	I43m	a = 8,92	Inter δ/γ
Laves	Fe_2Mo	550-650	Trigonal	R3	a = 10,903, c = 19,34	δ/γ, δ
Chromium nitrides	Cr_2N	700-950	Trigonal	P31m	a = 4,795, c = 4,469	Intra δ
	CrN	700-950	Cubic	Fm3m	a = 4,13-4,47	Intra δ
Pi (π)	$Fe_7Mo_{13}N_4$	550-600	Cubic	$P4_132$	a = 6,47	Intra δ
Epsilon (ε)	Cu-rich	Not defined				Intra δ
Tau (τ)	Not determined	550-650	Orthorhombic	Fmmm	a = 4,05, b = 4,85, c = 2,86	
Nitrides	MN	700-900	Ordered fcc	Fm3m	a = 4,097-4,577	
	M_2N		Hexagonal	P31m	a = 4,75-4,80, c = 4,43-4,47	
	Z phase		Tetragonal	P4/nmm	a = 3,03-3,06, c = 7,38-7,40	
Carbides	M_7C_3	960-1050	fcc	Pnma	a = 4,52, b = 6,99, c = 12,11	Inter δ/γ
	MC		Ordered fcc	Fm3m	a = 4,131-4,698	
	M_6C		fcc	Fd3m	a = 10,85-11,28	
	$M_{23}C_6$	650-950	fcc	Fm3m	a = 10,56-10,65	Inter δ/γ

When exposed to temperatures lower than 1000ºC, duplex stainless steels are subject to various phase transformations. **Figure 1** presents characteristic time-temperature-transformation curves of 2507 super duplex stainless steel. In the 970 to 650ºC temperature range, intermetallic phases precipitation may occur, mainly sigma phase, as well as carbides and nitrides. In the 300 to 500ºC temperature range, alpha prime (α') may be formed. Below 300ºC, austenite of lower alloyed DSS, if plastically deformed, transforms partially into martensite. Annealing of the worked material leads to the martensite reversion into austenite and to recrystallization [8].

The addition of Cr, Mo, W and Si tends to accelerate the formation of the precipitates, particularly the σ and χ phases. The stainless steel duplex UNS S32304, with a lower content of Mo, is less prone to the formation of intermetallic compounds, requiring many hours for the beginning of the precipitation of these compounds at temperatures lower than 900ºC. On the other hand, alloys such as UNS S32205 and S31803 are more prone to the precipitation of intermetallic compounds due to the addition of Mo. In super duplex stainless steels containing 25% Cr, the incubation time for formation of the intermetallic phases is lower and the temperature ranges of formation thereof are higher. These characteristics derive from their high levels of Cr, Mo and Cu.

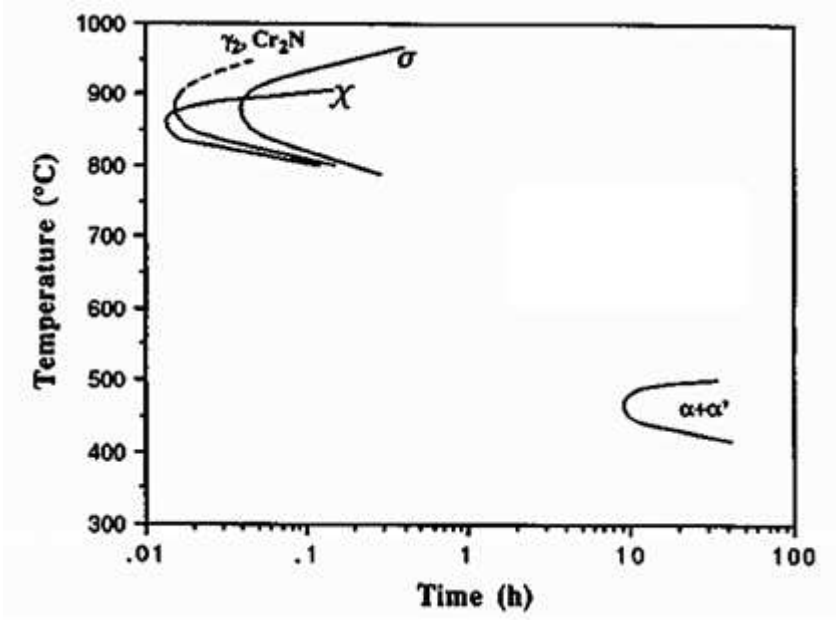

Figure 1. Time-temperature-precipitation curves for various precipitates observed in SAF 2507. Adapted from [9].

The most important phases are briefly discussed in the following subsections.

2.2.1. Austenite and Ferrite

Figure 2 presents the typical partition coefficients $K = C_\alpha/C_\gamma$ of chemical elements in equilibrium conditions for materials solution annealed and water quenched. Ferrite is enriched in P, W, Mo, Si and Cr and austenite in N, Ni, Cu and Mn. The partition coefficient for nitrogen is seen to vary markedly between alloys. Chromium and manganese increase nitrogen solubility, which explains why super duplex grades can contain higher nitrogen content than the lower Cr variants.

The nitrogen partition coefficient is also governed by temperature. During a solution annealing, even though the solubility of N in ferrite may increase a little, the volume fraction of austenite decreases markedly. This leads to enrichment of nitrogen in the

remaining austenite, and so nitrogen partitioning is increased, i.e. K tends away from unity. On cooling, austenite formation occurs, and ferrite becomes rapidly saturated with nitrogen, with the excess nitrogen diffusing into austenite. The equilibrium solubility limit in ferrite is 0,03-0,05%N. Further addition of nitrogen to the bulk alloy composition leads to nitrogen enrichment in austenite [4].

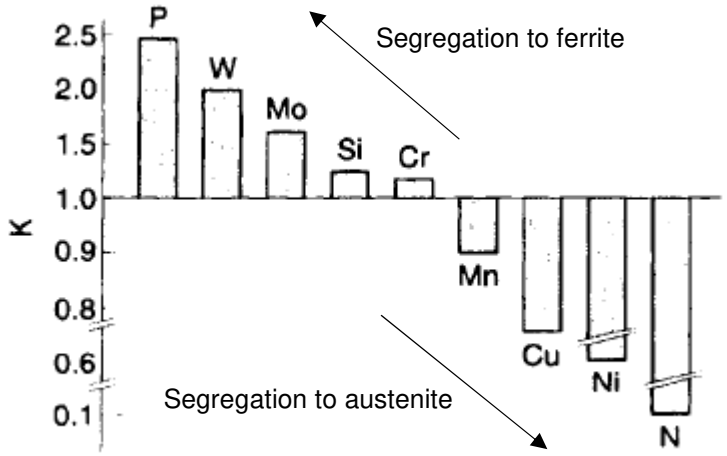

Figure 2. Partition coefficients indicating the segregation trend in duplex stainless steels. Adapted from [4].

The austenite occurring in duplex stainless steels can be classified in accordance to the formation mechanism [8]:

- Primary: during solidification ($L \rightarrow \delta + \gamma_1$).
- Secondary: precipitation from ferrite ($\delta \rightarrow \delta + \gamma_2$).
- Tertiary: eutectoid reaction ($\delta \rightarrow \sigma + \gamma_3$).

Secondary austenite (γ_2) can form relatively quickly and by different mechanisms depending on the temperature. Between 550 and 650°C, γ_2 has a similar composition to the surrounding ferrite, suggesting a diffusionless transformation. REDJAÏMIA *et al.* [10] have discovered that the orientation relationships between the early stage austenite formed below 650°C and the ferrite matrix are as follows: $(111)_{\gamma_s}//(011)_{\delta}$; $[\bar{1}01]_{\gamma_s}//[\overline{11}1]_{\delta}$; $[\bar{1}2\bar{1}]_{\gamma_s}//[\bar{2}1\bar{1}]_{\delta}$. At temperatures between 650 and 800°C, where diffusion is more rapid, Widmanstätten austenite can precipitate. In this range, γ_2 obeys the K-S relationship, its formation involves diffusion as it is enriched in Ni compared to the ferrite matrix. Even though there is some enrichment of nitrogen in γ_2 compared to the ferrite matrix, both Cr and N contents of γ_2 are substantially below that of primary austenite.

In the 700-900°C range, an eutectoid of γ_3 + σ can also form, as γ_3 absorbs Ni and rejects Cr and Mo, encouraging Cr, Mo-rich precipitates, such as sigma phase. Similarly, one form of γ_3 which forms at δ/γ boundaries is found to be depleted in Cr, especially if it has co-precipitated with Cr_2N. These reactions can create areas susceptible to pitting corrosion.

The deviations from the K-S relations have been investigated in detail by SHEK *et al.* [11]. These authors have studied the growth of Widmanstätten austenite and the change in its crystallographic orientation with the ferrite matrix. It has been revealed that austenite allotriomorphs form initially at ferrite/ferrite boundaries, which then grow preferentially into one of the ferrite grains. The growing tip of austenite is faceted and its orientation relationships with the ferrite matrix deviate from the K-S relation (deviation angle $\theta_{[100]\alpha} \approx 2{,}4°$). The growing austenite tips then grow along the invariant line direction $[0\bar{1}1]_\gamma // [1\bar{1}1]_\alpha$ and eventually develop into Widmanstätten austenite needles. The deviation from the K-S relation varies from the root to the tip for a Widmanstätten needle, with the tip showing minimum deviation (deviation angle $\theta_{[100]\alpha} \approx 1°$).

Sympathetic nucleation is defined as the nucleation of a precipitate crystal at an interphase boundary of a crystal of the same phase when these crystals differ in composition from their matrix phase throughout the transformation process. The typical morphology of sympathetically nucleated austenite has been investigated by TEM by CHEN *et al.* [12]. It is apparent that, after the initial intragranular nucleation of austenite, the subsequent small particle of austenite forms at the broad face of the prior large austenite grain. The electron diffraction patterns for sympathetically nucleated austenite grains demonstrated that the adjacent grains have a very similar orientation in space.

2.2.2. Chi (χ) Phase

Both chi and sigma are intermetallic phases that form frequently in stainless steels upon thermal ageing between 700 and 900°C. While sigma phase is present in the binary Fe-Cr system, chi phase appears only on the Fe-Cr-Mo ternary and in the Fe-Cr-Ni-Mo and Fe-Cr-Ni-Ti quaternary systems. In comparison with the sigma phase, chi phase is richer in Mo and poorer in Cr. It is generally agreed that the precipitation of intermetallics is associated with degradation of mechanical properties.

Chi phase nucleates mainly at the ferrite/austenite interface but also at the ferrite/ferrite grain boundaries. Several studies have concluded that although the chi phase forms earlier than the sigma phase, it is not thermodynamically stable, and transforms to the sigma phase upon prolonged ageing. Carbon is believed to be soluble in the chi phase and so it is also called $M_{18}C$ carbide by some authors. The chi phase is more enriched with Mo than is the sigma phase, and so the addition of Mo tends to

encourage the precipitation of the former. The occurrence of the chi phase in stainless steels is conditioned to a minimum of Mo content, about 2 wt%. Mo is sometimes replaced by W to improve resistance to stress corrosion cracking. Tungsten enhances the formation of the chi phase, having an opposite effect on the sigma phase [7,8].

2.2.3. Sigma (σ) Phase.

The deleterious Cr-, Mo-rich σ phase is a hard embrittling precipitate which forms between 650 and 1000°C. At the peak temperature of around 900°C, ferrite decomposition to sigma may take as little as two minutes in super duplex stainless steels. Because of its significant influence, the sigma phase has been investigated for a long time by different researchers.

The tetragonal sigma phase is non-magnetic, and has as elemental cell of 32 atoms and 5 crystallographically different atom sites. These are occupied by different atoms, whereas the lattice occupation of atoms depends on the concentration. Concerning the ternary Fe-Cr-Ni system, the sigma phase is a thermodynamically stable phase that forms on the Cr-rich site of the pseudo-binary phase diagram Fe-Cr-Ni (**Figure 3**) [7].

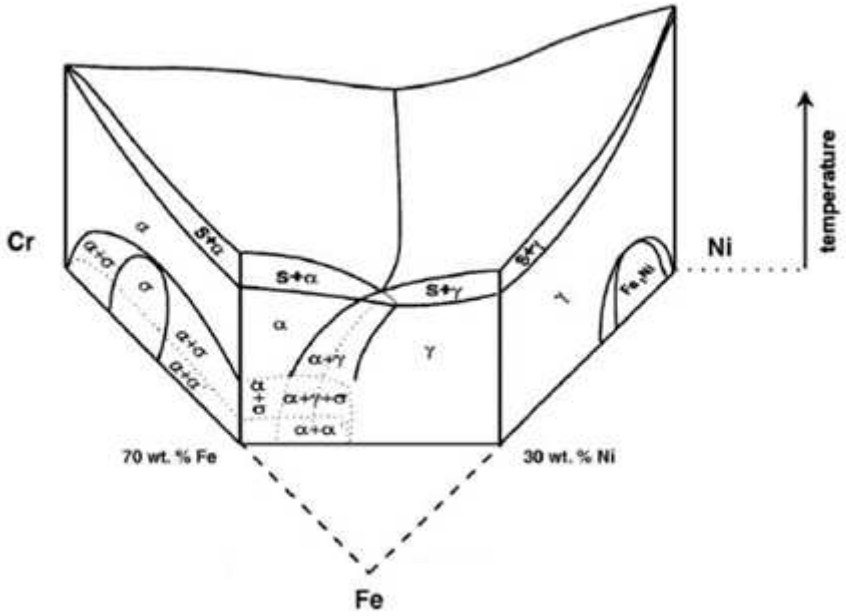

Figure 3. Ternary Fe-Cr-Ni phase diagram. Adapted from [13].

The condition for the formation of the sigma phase has been suggested in several studies. Since the sigma phase is enriched with Cr, diffusion of Cr is usually regarded as one of the controlling factors for its precipitation. The kinetics of sigma phase precipitation is faster for the austenitic stainless steels, and slower for the duplex stainless steels. The elements Cr, Mo, Si and Mn have been noted to encourage sigma formation. Nickel has been found also to enhance σ formation, but it reduces its

equilibrium volume fraction. This occurs as nickel induces γ formation and so concentrates the σ-promoting elements in the remaining ferrite.

As the sigma phase forms, Cr and Mo are enriched in these particles and simultaneously Ni diffuses into the ferrite. The enrichment of γ stabilizing elements in ferrite and the loss of α stabilizing elements lead to an unstable ferrite, transforming into an austenitic phase γ_3. This austenite is depleted in Cr and Mo. As the Cr content of the tertiary austenite falls below 11%, the phase becomes prone to corrosion.

The formation of the sigma phase depends heavily on grain size, as it affects the density of sigma nucleation sites. A decrease in grain size provides more grain boundaries for the sigma phase to form. In duplex stainless steels, it has been shown that a higher crystallographic misorientation between the austenite phase and the ferrite phase favors σ precipitation. Around 10% plastic strain decreases the time required to form sigma by one order of magnitude, while higher solution annealing temperatures increase δ content, reduce the concentration of σ-promoting elements and so retard its formation.

The sigma phase grows into ferrite instead of growing into austenite because sigma is rich in ferritizing elements (such as Cr, Mo, Si) and is poor in austenitizing elements (such as Ni, C and N). Furthermore, diffusion in ferrite is faster than in austenite. The process of sigma formation comprises two stages. The first stage is attributed to the precipitation of carbides and the second one to the formation of the sigma phase. The first stage of carbide formation involves grain boundary diffusion of Cr. Once carbides have fully formed, the original, nearly continuous ferrite network is broken up. The second stage of sigma precipitation involves lattice diffusion of Mo. It seems $M_{23}C_6$ and the sigma phase are intimately related. They tend to be in contact, but it is not a consensus that $M_{23}C_6$ acts as the precursor to the sigma phase [8].

According to the precipitation temperature, the morphology of the sigma phase changes. At lower precipitation temperatures (up to 800ºC), a coral-like eutectoid $\sigma + \gamma_3$ or $\sigma + \delta$ lamellar aggregates are formed. The amount of single sigma nuclei at the beginning of the precipitation is rather high due to the shorter diffusion distances at lower temperatures. Hence, lower diffusion velocity causes higher local supersaturation and leads to a higher density of precipitations. At temperatures higher than around 900ºC, the sigma phase is bigger and more compact and the linking between single sigma crystals is marginal, resulting from a lower nucleation formation force but a high diffusion rate [13].

Several research projects have studied the influence of the sigma phase on mechanical properties. The formation of intermetallic phases between 750 and 950ºC leads to a severe loss of toughness. One percentage of precipitated intermetallic phases

leads to a loss of the notch bar impact value down to one third of the solution annealed state [8].

There are distinctions among the several precipitation temperatures. The lower the precipitation temperature, the more brittle is the behavior. The embrittlement degree depends primarily on the morphology of the sigma phase. Even small deformations of the material cause transgranular, finely structured brittle fracture of sigma phase particles, due to the TCP structure. In the more net-like morphology precipitated at lower temperatures, cracks are enabled to run through sigma phase particles over long distances. The narrow fields of surrounding ferrite are forced to cleave, as the small austenitic phases show ductile failure. Whereas the bigger and more bulk sigma phase at higher precipitation temperatures has a bigger surrounding matrix of ferrite and austenite. This enhances the surrounding ferrite to a more ductile failure mode.

Sigma phase may improve the hot ductility. It is believed that a fine and homogeneous dispersion of σ+γ improves the tensile elongation, because large cavities may easily form at the boundaries of large austenite grains. Sigma phase may also enhance the superplasticity of duplex stainless steels by retarding grain growth at high temperatures [7].

2.2.4. Laves and R Phases

The R and Laves phases are intimately related because they are related crystallographically. Laves phase (Fe_2Mo) precipitates in small quantities between 550 and 650ºC after several hours of exposure. They form at both intra- and intergranular sites, are Mo-rich and reduce pitting corrosion resistance. Those that precipitate at intergranular sites introduce higher effect on pitting resistance, as they contain slightly more Mo (40% compared to 35% at intragranular sites).

The R phase ($Fe_{22}Mo_{18}Cr_{13}$) was studied very early on by some workers using X-ray diffraction and neutron diffraction and it was concluded to have a trigonal crystal structure. Between 550 and 700°C, the formation of the Mo-rich intermetallic R phase in the ferrite phase of duplex stainless steels may lead to rapid and serious loss of toughness. In duplex stainless steels, this R phase may form both intergranularly and intragranularly in the ferrite phase and obey the following orientation relationships with the ferrite matrix: $\langle 111\rangle_\alpha // \langle 0001\rangle_R$; $\{110\}_\alpha // \{30\bar{3}0\}_R$ or $[1\bar{3}2]_\alpha // [2\bar{1}\bar{1}0]_R$ [7].

2.2.5. Nitrides

Nitrogen is added to duplex alloys to stabilize austenite and to improve strength and pitting resistance. Because high-nitrogen stainless steels are in increasing use, many recent studies have been dedicated to the precipitation of nitride in this class of steels. The solubility of nitrogen is considerably higher in austenite than in ferrite, and has been shown to partition to the former phase. Above the solution annealing temperature (about 1040ºC), the volume fraction of ferrite increases; until just below the solidus a completely ferritic microstructure can be present, though in the higher alloy grades some austenite may remain. At these temperatures, the nitrogen solubility in ferrite is high, but on cooling the solubility drops and ferrite becomes supersaturated in nitrogen, leading to intragranular precipitation of needle-like Cr_2N particles with the crystallographic relation $\langle 0001 \rangle_{Cr_2N} // \langle 011 \rangle_{\delta}$ [4].

When Cr-Mn-N stainless steels are isothermally aged between 700 and 1000°C, the austenite will transform in a cellular/discontinuous manner:

$$\gamma \rightarrow \gamma' + Cr_2N$$

where γ is the N-supersaturated austenite matrix; γ' is the lamellar austenite inside the cell and Cr_2N is the lamellar nitride inside the cell.

Precipitation of cellular Cr_2N is, in most cases, detrimental. For instance, ductility is compromised. The sites of precipitation of Cr_2N have been investigated by several publications. It was observed in an undeformed Cr-Mn-N stainless steel containing 0,9 wt%N that the precipitation of Cr_2N only occurs at grain boundaries, never at twin boundaries. However, when the content of N is low (< 0,4 wt%N), intragranular precipitation of Cr_2N may precede cellular Cr_2N precipitation. The explanation is that when %N is high, large lattice distortions will exist in the grain interiors, causing N to segregate to grain boundaries and thereby aiding cellular precipitation at grain boundaries. Prestraining encourages intragranular precipitation of Cr_2N. This suggests that deformation retards cellular Cr_2N as it encourages intergranular and intragranular precipitation of chromium nitrides [7].

It has been suggested that the formation of cellular nitride is preceded by clustering and ordering involving N, Fe, Cr and Ni. The sigma phase is usually associated with Cr_2N. During cell growth of Cr_2N, Cr becomes sufficiently enriched at the cell front and so the sigma phase forms at the cell boundary. Alternatively, the depletion of N near the cell front can promote sigma formation at the cell boundary, since N is known to suppress the formation of sigma.

Whereas hexagonal Cr_2N appears to be the predominating type of nitride, cubic CrN has been observed in the heat affected zone of welds of duplex stainless steels. However, little or no adverse effect on toughness and corrosion properties were observed [7].

2.2.6. Carbides

In stainless steels, different types of carbides may form. M_7C_3 forms between 950 and 1050ºC at ferrite/austenite grain boundaries. However, as its formation takes 10 minutes, it can be avoided by normal quenching techniques. Further, as modern duplex grades contain less than 0,02%C, carbides of either form are rare. In duplex grades with moderately high carbon levels of about 0,03%, the carbide $M_{23}C_6$ rapidly precipitates between 650 and 950ºC, requiring less than one minute to form at 800ºC. $M_{23}C_6$ has a fcc lattice.

Arguably the most widely used method to retard the formation of $M_{23}C_6$ is the addition of strong carbide-forming alloying elements like V, Nb, Ti, Zr, Hf and Ta. When these elements are added, MC carbides form in preference to $M_{23}C_6$, lessening sensitization and improving mechanical properties. While fine MC carbides are desirable, coarse MC carbides degrade properties, such as creep-fatigue resistance and fracture resistance. Because of the importance of keeping MC precipitates fine, ways to retard the growth of them have been proposed. For instance, to impede the growth of TiC, addition of nitrogen and suitable amounts of plastic deformation may be employed [7].

2.2.7. Deformation-induced Martensite

Austenite can transform into ε (hcp) or α' (bcc) martensites in different ways. The formation of α' is related closely to shear bands, which are planar defects associated with the overlapping of stacking faults on $\{111\}_\gamma$. Depending on the nature of the overlapping, twins, ε martensite or stacking fault bundles may form. Twins form when stacking faults overlap on successive {111} planes, whereas ε martensite is generated if the overlapping of stacking faults occurs on alternate {111} planes. Stacking fault bundles arise from the irregular overlapping of stacking faults.

It is generally accepted that the intersections of the ε martensite may act as the sites of nucleation of α'. Alpha prime martensite is also capable of nucleating in a single ε martensite plate at high strain rates. As regards transformation routes, both $\gamma \rightarrow \varepsilon \rightarrow \alpha'$ and $\gamma \rightarrow \alpha'$ have been suggested to be feasible. In the transformation $\gamma \rightarrow \varepsilon \rightarrow \alpha'$, ε martensite acts as the precursor phase of α'.

The presence of the ε martensite, like α', can lead to strengthening. It was verified in austenitic stainless steels that the appearance of ε leads to a rapid decrease in strain hardening, but as soon as α' forms, the rate of strain hardening increases. An uniform distribution of ε produced in high-strain-rate deformation is believed to enhance ductility in super austenitic stainless steels. Damage brought about by cavitation erosion is also mitigated by ε because part of the impact energy is absorbed by its formation [7].

Several factors may influence the martensitic transformation in metastable austenitic steels, such as directionality of external loads, external fields, grain size etc. Coarser grains lead to higher amounts of α'. Increasing strain rate lowers the amount of α'. In the presence of an external magnetic field, the ε → α' transformation is facilitated [7].

The formation of α' relates intimately to the intersection of planar deformation structures like mechanical twins and ε martensite. The deformation structures and dislocation evolution of austenitic stainless steels depend critically on stacking fault energy (SFE). Therefore, the stability of austenite correlates strongly with its SFE. High SFE values (narrow stacking faults) may impede the formation of shearing bands having sufficient thickness for acting as the embryos for martensitic transformation. Decreasing of SFE (i.e. widening the stacking faults) favors planar deformation structures like twins, ε-martensite etc., thereby enhancing the formation of α'.

Several empirical relations have been proposed for calculation of SFE, for instance [14]:

$$SFE\ (mJ/m^2) = -25{,}7 + 2(\%Ni) + 410(\%C) - 0{,}9(\%Cr) - 77(\%N) - 13(\%Si) - 1{,}2(\%Mn)$$

(Equation 3)

The effects of elements that are not present in the empirical expression above have also been investigated in several studies. Hydrogen has been found to reduce SFE because of the formation of H-H pairs in faulted zones [15]. The reduction of SFE leads to earlier formation of ε martensite. In studying the microstructural changes in a hydrogen-charged duplex stainless steel, it was found that the stacking fault density of the austenite phase increased after H-charging, which is in agreement with the view that hydrogen can reduce SFE [16].

Niobium also reduces significantly SFE. Copper, on the other hand, is twice as effective in increasing SFE of austenitic stainless steels as is Ni.

2.2.8. Other phases: π, η, τ and ε_{Cu}

The phase π is a nitride that has been found to precipitate intergranularly in the ferrite phase of duplex stainless steels and Mn-alloyed austenitic stainless steels after isothermal heat treatment at 600°C for several hours. The orientation relationships between the π phase and the ferrite are as follows: $\langle 100\rangle_\alpha // \langle 100\rangle_\pi, \{110\}_\alpha // \{130\}_\pi$. It is Cr and Mo rich and so has been previously confused with σ phase.

The phase eta (η), discovered in nitrogen-alloyed stainless steels upon ageing at 850°C, is rich in Si and possesses fcc lattice and Fd3m structure. This last characteristic distinguishes it from the G phase, as the latter has Fm3m structure.

The intermetallic τ phase may form after ageing between 550 and 650°C and it possesses a needle-like morphology and an orthorhombic structure. It forms in δ/δ boundaries and contains a lot of stacking faults. The orientation relationships between the τ phase and the ferrite matrix are as follows: $(\bar{1}10)_\delta // (100)_\tau, \langle 001\rangle_\delta // \langle 001\rangle_\tau, \langle 110\rangle_\delta // \langle 010\rangle_\tau$.

In alloys containing copper, the supersaturation of ferrite due to the decrease in solubility at lower temperatures leads to the precipitation of extremely fine Cu-rich ε_{Cu} phase particles after 100h at 500ºC [7].

2.3. Mechanical Properties

Duplex and super duplex stainless steels present a combination of the properties of each phase. They have higher mechanical strength than austenitic and ferritic stainless steels and higher toughness than ferritic steels. In the range of 25-300ºC, the yield strength of duplex and super duplex stainless steels decreases with temperature rises but remains higher than AISI 316L austenitic stainless steel.

The high values of yield stress (σ_y) and mechanical strength (σ_R) of duplex and super duplex stainless steels are due to the action of several simultaneous mechanisms [4]:

- Interstitial solid solution hardening (C, N).
- Substitutional solid solution hardening (Cr, Mo, Ni etc).
- Strengthening by grain refinement by the formation of biphasic austenite + ferrite structure.
- Hardening caused by the formation of secondary austenite (γ_2).
- Strengthening due to the ferritic phase, provided that it has chemical composition similar to the austenitic phase.
- Strain induced by the differential contraction of the two phases on cooling from the annealing temperature.

Equations 4 and **5**, derived from regression analysis, relate the values of yield strength (YS) and ultimate tensile strength (UTS) with the mass percentages of the alloying elements and microstructural characteristics of these steels [4]:

$$\mathrm{YS(MPa)} = 120 + 210\sqrt{\%\mathrm{N} + 0{,}02} + 2(\%\mathrm{Mn} + \%\mathrm{Cr}) + 14(\%\mathrm{Mo}) + 10(\%\mathrm{Cu}) + \\ + (6{,}15 + 0{,}054\delta)\delta + [7 + 35(\%\mathrm{N} + 0{,}02)]\mathrm{d}^{-1/2} \quad \textbf{(Equation 4)}$$

$$\mathrm{UTS(MPa)} = 470 + 600(\%\mathrm{N} + 0{,}02) + 14(\%\mathrm{Mo}) + 1{,}5\delta + 8\mathrm{d}^{-1/2} \quad \textbf{(Equation 5)}$$

where:

- δ: percentage of ferrite.
- d: spacing between the austenite islands (mm).

As shown on these equations, nitrogen has a preponderant role. In duplex steels with contents less than 0,1%N, austenite has lower UTS than ferrite, so that plastic deformation occurs more easily in austenite, resulting in the initiation and preferential growth of cracks in austenite. In duplex steels with contents greater than 0,1-0,2%N, the mechanical strength of austenite is higher, so that ferrite cracking, for example in solutions containing chlorides, may occur.

Nitrogen also influences the stacking fault energy (SFE). As shown in **Equation 3**, the increase of N content in the alloy decreases the SFE value. Because of this decrease, the separation between two partial dislocations will be wide, causing the dislocations to be piled-up in their shear plane. This phenomenon confers high hardening coefficient and strength, without substantial variations in elongation.

Another element that introduces a hardening effect, though not as noticeable as N, is copper. With the addition of this element, it is possible to obtain an increase in mechanical strength without excessive loss of toughness. For this to occur, an aging heat treatment must be performed.

The mechanical properties of duplex and super duplex stainless steels are highly anisotropic. This anisotropy is caused by the grains with elongated morphology and the crystallographic texture, which results from the hot or cold rolling processes. The mechanical strength is greater in the direction perpendicular to the rolling direction. Toughness is also greater when the crack propagates perpendicular to the rolling direction.

Despite the high mechanical strength, duplex stainless steels exhibit reasonably good ductility and impact toughness compared to ferritic carbon or stainless steels as well as a more gradual ductile-brittle transition. The absorbed energy of duplex stainless steels falls around -50°C, due to the ductile-brittle transition of ferrite.

The precipitation of secondary phases influences significantly the mechanical properties of duplex and super duplex stainless steels. For instance, duplex stainless steels submitted to isothermal treatments between 300ºC and 1000ºC present typically two peaks of hardness: the first around 400ºC related to the phase α' and the second around 800ºC to the phases χ and σ [4].

The precipitation of secondary phases influences the impact toughness. In the temperature range between 600ºC and 1050ºC, carbides ($M_{23}C_6$, M_7C_3), nitrides (Cr_2N, CrN) and several intermetallic phases (such as χ, σ, R and π) can precipitate. At temperatures between approximately 350°C and 600°C, a spinel decomposition of the ferrite occurs and the precipitation of different intermetallic phases (e.g. the G phase) occurs inside ferrite grains or at α/γ interfaces.

Since austenite and ferrite have different physical and mechanical properties, duplex stainless steels present a heterogeneous micro-mechanical behavior, i.e. the stresses and strains do not distribute uniformly in microstructural scale. **Figure 5** shows schematically the typical mechanical response of each phase of a duplex stainless steel. Applying an external load, initially the stress in ferrite increases faster than in austenite. Below the overall yield stress, austenite has lower strength than ferrite, resulting in higher plastic strain in austenite than in ferrite. In order to preserve continuity, ferrite must be deformed plastically. This leads to the so-called cold creep i.e. increasing straining under constant loads below proof stress. At this stress level, tensile residual stresses develop in austenite and compressive residual stresses in ferrite [17].

With increasing strain - and overall material yielding – more important work hardening of austenite occurs. This behavior is expected, considering the higher N content in austenite. At this point, tensile micro-strain localization tends to occur in ferrite, with compressive micro-strains formed in austenite. As mentioned, the lower initial mechanical properties of austenite (and higher of ferrite) are strongly dependent on the N content in the material. In duplex steels with contents greater than 0,2%N, for instance hyper duplex stainless steels, the initial strength of austenite tends to be higher than that of ferrite [18].

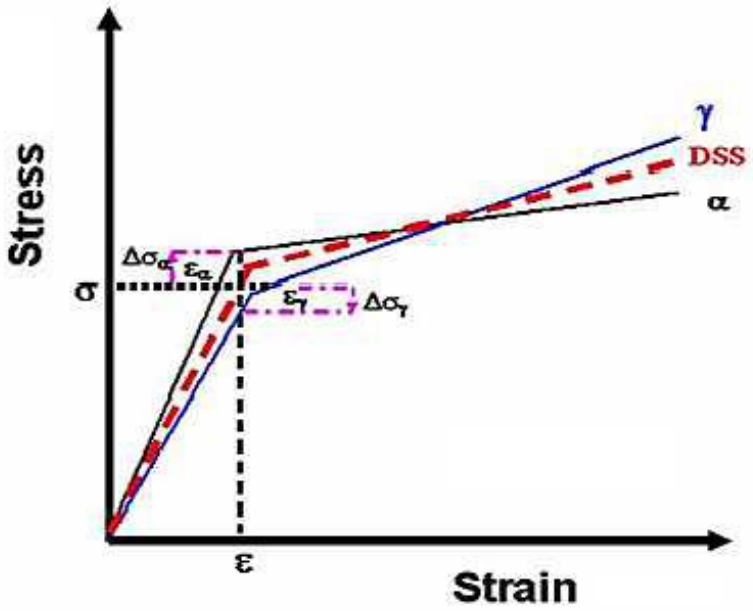

Figure 4. Schematic stress-strain curves for austenite and ferrite in a DSS [18].

2.4. Forming Process

Duplex and super duplex stainless steels have higher yield strength and lower ductility than austenitic steels. Consequently, higher forces/loads are required to perform the cold plastic forming of the former. At room temperature, a duplex stainless steel responds to forming approximately similarly to a 300 series austenitic steel with twice the thickness. Due to their high mechanical strength, duplex and super duplex steels also have a greater springback during forming operations. Due to the high hardness and work hardening coefficient, duplex and super duplex stainless steels reduce tool life more severely than austenitic steels, especially considering machining operations that require long times. Solubilization cycles may be required in forming or machining operations due to the rapid loss of ductility.

Due to their two-phase microstructure, duplex steels can be easily formed above 950°C. Typical hot forming temperatures lie between 1050°C and 1280°C for super duplex stainless steels. An upper limit of 1100-1150°C is suggested by many manufacturers due to the effect of high temperatures on the dimensional stability of the parts and the increase in the tendency of scale formation with increasing temperature. If hot forming is performed at a very low temperature, the deformation accumulates in the ferrite, which may result in ferrite cracking. Cooling in the range of 1000°C to 700°C must be carried out in less than 2 minutes in order to avoid precipitation of undesirable phases. Care should also be taken to avoid creep during heat treatments. This problem can be avoided by the induction heating technique. Superplastic behavior, i.e. very high elongations (600-800%) to fracture, are possible in duplex steels with very refined microstructure (grain size around 1µm) and deformed very slowly above 900°C [4,19].

The ability of a material to be hot worked in a safe way depends on both the intrinsic material ductility and the process itself. The risk of cracking of duplex stainless steels during hot working processes increases with N content. The negative effect of this element is double because it increases the volume fraction of austenite and significantly increases its strength. The crack sensitivity index (CSI) for 2205 steel is given by [20]:

$$CSI = 45,2(\%C) + 18,3(\%N) + \%Mo + \%Cu + 0,65(\%Ni) - 297(\%B) - 0,14(\%Cr) - 0,7(\%Mn) \quad \textbf{(Equation 6)}$$

When the value of CSI is higher than 5,5, the stainless steel is susceptible to edge crack.

The hot ductility index (HDI) can be expressed by:

$$HDI = \%Cr + 0,6(\%Mo) - 0,9[\%Ni + \%Cu + 1,9\%Mn + 35(1,5\%C + \%N)] + 270(2,5\%B - \%S) \quad \textbf{(Equation 7)}$$

The higher the HDI, the better the hot ductility of the duplex stainless steel.

Impurities and trace elements can seriously deteriorate hot workability as segregation can produce “hot shortness”. Among these elements, the most harmful are S and P, but trace elements like Pb, Bi and Sn can also have a detrimental effect. To avoid this problem, the concentration of S should be reduced below 30 ppm or the steel should be alloyed with cerium while the content of S is kept low.

After hot forming, a complete solubilization annealing, followed by rapid quenching, is required to fully recover the mechanical properties and corrosion resistance. The temperature of the part must be kept above the minimum solubilization annealing temperature for a sufficient time to dissolve any intermetallic precipitates. At the solubilization annealing temperatures, duplex stainless steels are considerably ductile, allowing the potential for deformations and distortions if the part is not adequately supported. Straightening DSS parts is more difficult than austenitic stainless steels ones because of the high mechanical strength at room temperature of the former. Attempts to minimize distortions through short annealing times, slow heating to the annealing range or the use of lower annealing temperature may hinder the dissolution of intermetallic phases, reducing corrosion resistance and toughness. The use of stress relief treatment is not recommended since there is no satisfactory temperature below the solubilization annealing temperature at which stress relief can be performed without the danger of intermetallic phase formation.

Different mechanisms act on microstructural modifications during hot forming of duplex stainless steels, such as plastic deformation, rotation, phase boundary sliding, shear banding, fragmentation etc [20].

The microstructural evolution taking place during hot working within austenite and ferrite in a duplex microstructure can differ significantly from that observed in single-phase materials. This is because, in addition to their respective high (ferrite) and low (austenite) stacking fault energies (SFE), other factors, such as relative strength, morphology and strain partitioning also play an important role.

Dynamic recovery is the primary softening mechanism activated in ferrite. The high stacking fault energy of ferrite makes easy the dislocations climb or cross slip at high temperature. The degree of recovery during hot working tends always to be higher in ferrite than in austenite. The remaining dislocations are stored in low-angle dislocation walls, resulting in polygonized sub-grains which become larger and more perfect at increasing temperature and decreasing strain rate and stress. As a consequence, the ferritic phase is characterized by high ductility during hot working.

The low SFE of austenite makes dislocations less mobile and so dynamic recovery is limited. Austenite undergoes significant work hardening before the onset of dynamic

recrystallization at hot working temperatures. After recrystallization, most of the dislocations are eliminated through the development of new grains containing few dislocations [21].

The interphase boundary imposes restrictions and, as the strain increases, ferrite becomes partially entrapped between γ stringers. This is a heterogeneous process that leads to the formation of narrow bands of ferrite, limited laterally by the interphase boundaries. When deforming at 1000ºC or lower temperatures, the interphase boundary remains flat. However, as the deformation temperature increases, the interphases become mobile and bulges develop. The interference of the interphase take place on a small scale (fractions of μm) and lead to interpenetration of both ferrite in austenite and vice-versa.

Interphase boundary sliding involves the translation of a grain with respect to another by a shear movement parallel to their common boundary. Damage at austenite-ferrite phase boundaries by sliding is an important source of defects under hot working conditions in DSSs. The ease of sliding depends on the character of the boundary: coherent and semi-coherent interfaces are less apt for sliding than incoherent boundaries.

Laboratory testing, modelling and observation of industrially deformed austeno-ferritic stainless steels have shown that these materials have a tendency towards strain localization and shear band formation. The presence of two phases with significantly different mechanical strengths is considered as the primary cause for shear band formation [20].

At around 1000ºC and below, shear bands crossing the interphase boundary can produce fragmentation of austenite. At deformation temperatures above 1100ºC, interphase mobility is high enough to produce bulging and local scale rearrangements in the microstructure, leading to fragmentation of austenite.

Duplex stainless steels have good weldability, and can be welded through conventional processes. In general, pre- and post-heating are not required. However, careful control of the heat input and interpass temperatures is required to maintain a suitable ferrite/austenite balance. Low heat input, with a consequent high cooling rate, impairs the transformation of the primary ferrite into austenite in the weld. Low austenite fraction in the weld metal imply low impact toughness. In addition, high ferrite fractions favor the precipitation of nitrites and chromium carbides in the ferrite, especially close to α/γ phase boundaries. Cr depletion near precipitates reduces the corrosion resistance of the weld metal and heat affected zone. High heat input favors the austenite formation kinetics; however excessive heat inputs and interpass temperatures deteriorate the

mechanical properties and the corrosion resistance due to the formation of intermetallic phases [20].

2.5. Hydrogen Damage

The deleterious effects of hydrogen on steels can be classified as: hydrogen embrittlement, hydrogen attack, martensitic transformation, and formation of vacancies. The schematic diagram of **Figure 6** orders these phenomena according to the usual temperature ranges of occurrence.

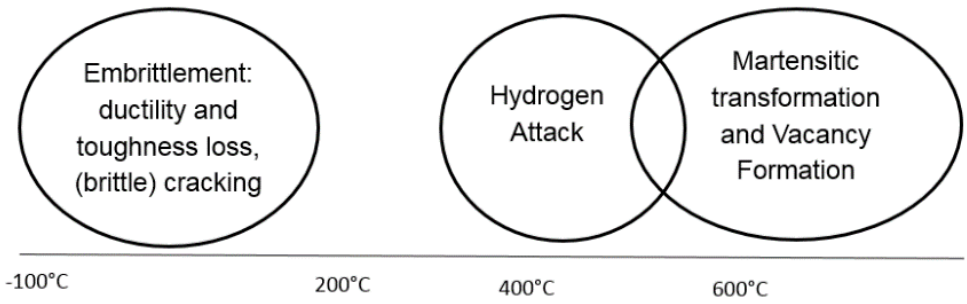

Figure 5. Classification of hydrogen degradation in steels according the occurrence temperature.

Hydrogen attack occurs at high temperatures, usually between 300-500°C. On this mechanism, absorbed hydrogen reacts with carbides and/or the carbon present in the lattice, forming methane inside cavities at grain boundaries. The increase in internal pressure, together with diffusion along grain boundaries in creep regime, lead to cavity coalescence and subsequently to intergranular cracking.

The presence of hydrogen at high pressures and temperatures increases the equilibrium concentration of vacancies in metals, generating so-called superabundant vacancies (SAVs). This effect is explained by the decrease in the activation energy for interdiffusion in the matrix, induced by the weakening of the atomic bonds due to the presence of hydrogen. The generation of SAVs is also related to an increase in the amount of trapped hydrogen, mainly promoted by the formation of stable phases consisting of complexes of vacancies and hydrogen atoms. In the case of iron, the formation of the complex $VacH_6$, consisted of six hydrogen atoms, has been proven. The generation of SAVs was initially discovered in palladium and nickel, and was subsequently observed in other metals such as Fe, Cr, Mn and Co. SAVs remain stable at ambient temperature and pressure, suggesting that high temperatures and pressures only accelerate their formation kinetics [22,23].

Hydrogen embrittlement is the degradation of the mechanical properties caused by the presence of hydrogen at temperatures typically from -100 up to 200°C. The standard BS EN ISO 15156/NACE MT0175 (Materials for use in H_2S-containing environments in

oil and gas production, 2015) distinguishes the mechanisms of hydrogen-induced cracking (HIC) and hydrogen-induced stress cracking (HISC), usually called hydrogen embrittlement. The former term is assigned to planar cracks occurring in low-alloy steels when atomic hydrogen diffuses in the lattice and combines to form molecular hydrogen at trapping sites. No external stress is required for the crack formation. Hydrogen-induced stress cracks on the other hand result from the presence of hydrogen in a metal subjected to tensile stresses.

According to GANGLOFF [24], for high strength steels it is also possible to distinguish between internal and external hydrogen-assisted cracking. The first case refers to previously hydrogen-charged material subsequently loaded mechanically; while in the second, mechanical loading occurs concomitantly with the generation of hydrogen directly at the crack tip. In both mechanisms, the cracking may be intergranular or follow crystallographically defined planes through the grains (quasi-cleavage). These two mechanisms differ on hydrogen activity and crack growth kinetics. One can also distinguish the embrittlement by reversible and irreversible hydrogen. In the first mechanism, embrittlement results from hydrogen in solution, which can be removed through heat treatments at moderate temperatures. In the second case, the hydrogen is present in solution typically in higher concentrations, being able to segregate as hydrogen gas in voids or internal interfaces, forming cracks or blisters.

According to several authors, the term "hydrogen-assisted cracks or fractures" is more appropriate than "hydrogen embrittlement" because it includes not only fractures at lower stresses and deformations due to hydrogen, but also considers the possibility that the fracture is not necessarily brittle. The terms "hydrogen embrittlement" and "stress corrosion cracking" have sometimes been applied indistinctly in the literature. In general, anodic dissolution is responsible for SCC, while HE is caused solely by hydrogen absorption. Cathodic protection reduces or eliminates SCC, but can favor hydrogen embrittlement [24].

Hydrogen may come from a corrosive process, electroplating, from residual water during welding, through water reduction by means of a cathodic potential imposed or from a medium where there is a partial pressure of hydrogen gas. Coming from different sources, it can diffuse through the lattice and/or be transported by dislocations. It tends to accumulate at grain boundaries, inclusions, voids, dislocation arrays and solute atoms. The cracking process can involve cleavage, intergranular or ductile (microvoid coalescence) fracture micromechanisms.

2.5.1. Hydrogen Embrittlement in Duplex Stainless Steels

The performance of duplex and super duplex stainless steels in hydrogen-rich environments is a combination of the behavior of the phases that constitute their microstructure. Ferrite is more susceptible to hydrogen embrittlement than austenite. Consequently, HE resistance increases with the austenite fraction. Ferrite has high hydrogen diffusivity and low solubility, whereas the opposite occurs with austenite. Thus, hydrogen-embrittled fully ferritic steel recovers most of its ductility and toughness a few days after being withdrawn from the hydrogenating medium. Depending on the hydrogen charging, this recovery can be more rapid. By contrast, under a high hydrogen charging degree, cracks will develop inside the material and damage will remain after hydrogen desorption. Presence of min. 15% austenite results in a much lower recovery after removal of the material from this environment. No ductility recovery was noticeable in a thermally pre-charged 2205 steel containing about 35% austenite after exposure to air at room temperature for periods between 55 days and 3 years. However, nearly complete recovery of ductility was achieved after heating at 300°C for 4 hours. In general, duplex and super duplex stainless steels with dissolved hydrogen exhibit substantial loss in ductility under tensile and bending tests with notched and smooth specimens. The effects of hydrogen also manifest under fatigue. Work-hardened materials present higher susceptibility [25].

The fracture surface morphology of metals and alloys under hydrogen-rich environments can be unaffected or changed from ductile microvoid coalescence to quasi-cleavage, cleavage and intergranular failure. The microvoids may be shallower and fewer in the presence of hydrogen but, in general, the fundamental mechanisms controlling the nucleation, growth and coalescence remain unchanged, albeit with nucleation enhanced due to hydrogen accumulation at precipitates and growth accentuated by hydrogen-induced shear localization processes. Cleavage involves fracture on well-defined planes and intergranular failure involves crack formation and propagation along grain boundaries. The latter may be caused by a combined and synergistic effect of hydrogen and other grain boundary segregants, or just by the segregated hydrogen. Quasi-cleavage fracture is used to describe failure on non-cleavage planes that are frequently decorated with fine lines called river markings that run approximately parallel to the crack propagation direction. These river markings originate in the grain interior rather than at the grain boundary and the river markings on opposing fracture surfaces match ridge-to-ridge as opposed to mating step-to-step as in cleavage [26].

In the following sections, the hydrogen embrittlement phenomenon is analyzed in two general media: aqueous solutions under a cathodic potential and gaseous environments containing hydrogen.

2.5.1.1. Hydrogen Embrittlement in Aqueous Solutions under Cathodic Potentials

Hydrogen embrittlement in aqueous solutions with applied cathodic potentials depends on several variables related to the metal or alloy (chemical composition, microstructure, surface conditions), to the environment (temperature, pH, hydrostatic pressure, presence of promoters or inhibitors for hydrogen entry, cathodic current density and electrode potential) and to the stress and strain features. The environment variables control predominantly the hydrogen entry into the metal, being responsible for the concentration of dissolved hydrogen in the lattice subsurface and for the total amount of absorbed hydrogen [27].

In a subsea steel structure subjected to a cathodic protection system, in order to have a protective current in the anodic areas of the structure, it is necessary that reduction reactions occur in the cathodic areas. In these reactions, water dissociates into H^+ and OH^- ions, which can be reduced with the release of H_2, or oxidized with the release of O_2. The most frequent reduction reactions at the cathode surface are:

a) Neutral and aerated solution: $H_2 + ½O_2 + 2e \rightarrow 2OH^-$ **(Equation 8)**

b) Neutral and deaerated solution: $H_2O + 2e \rightarrow H_2 + 2OH^-$ **(Equation 9)**

c) Acid and aerated solution: $2H^+ + ½O_2 + 2e \rightarrow H_2O$ **(Equation 10)**

d) Acid and deaerated solution: $2H^+ + 2e \rightarrow H_2$. **(Equation 11)**

Figure 7 shows the potential-pH diagram of the Fe-H_2O system. In this diagram, the region delimited by dashed lines (a) and (b) represents the thermodynamic stability domain of water at 25°C and 1atm. Below line (a), water will tend to decompose by reduction. In other words, if cathodic protection is applied to sufficiently negative potentials, the production of hydrogen on the metal surface becomes thermodynamically feasible.

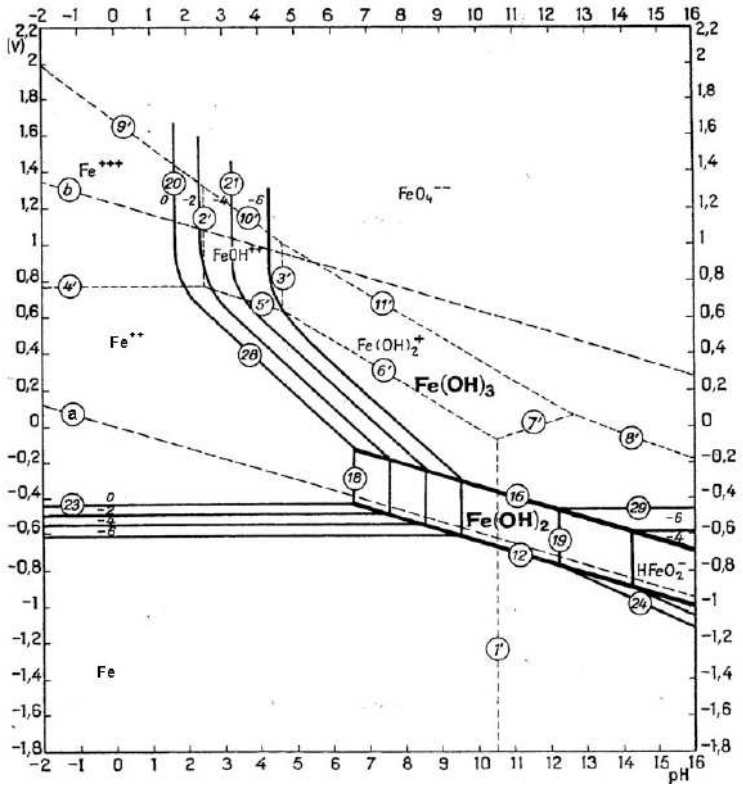

Figure 6. E-pH equilibrium diagram for the iron-water system at 25 ° C, showing the region of water stability between dashed lines (a) and (b) [28].

The recommended practice DNV-RP-B401 (Cathodic Protection Design, 2011) mentions that duplex stainless steels subjected to cathodic protection systems are potentially susceptible to HISC, regardless of the levels of material yield strength and hardness. According to BS ISO 15589 (Cathodic protection of pipeline transportation systems, 2014) submerged components of duplex and super duplex stainless steels are well protected against corrosion at potentials more negative than about -500mV$_{Ag/AgCl}$. Sacrificial anodes made of aluminum and zinc, commonly used for the protection of carbon steel structures, have a potential in the range of -1030 to -1050mV$_{Ag/AgCl}$. To keep components of duplex and super duplex stainless steels at a potential close to -500mV$_{Ag/AgCl}$, complete electrical isolation from other structural elements protected to more negative potentials is required, incurring in additional costs. For this reason, duplex and super duplex steel structures submerged in seawater are often under cathodic protection at considerably more negative potentials than required. BS ISO 15589 recommends that, having a risk of hydrogen embrittlement, more negative potentials than -800mV$_{Ag/AgCl}$ should be avoided.

Tensile tests performed with UNS S32760 specimens at low strain rates (10^{-6} s^{-1}) in synthetic seawater under different cathodic potentials indicated that relevant

embrittlement, i.e. ductility loss above 25% in comparison to the air properties, occurs at potentials equal and more cathodic than -900mV$_{SCE}$ [29].

Tensile tests at low strain rate (2,6.10^{-7}s^{-1}) were performed with samples of UNS S31308 in air and in acid and basic aqueous solutions, with and without the addition of the hydrogen adsorption promoter As_2O_3. The samples tested in aqueous solution were subjected to previous and in-situ cathodic charging at a current density of 20mA/cm². There was a severe reduction in the fracture strain for the samples tested in aqueous solution, especially with the addition of As_2O_3. After the tests, the hydrogen concentrations of the samples were measured by the electrochemical desorption technique. The relationships between hydrogen concentrations and the ratios of time to failure and reduction of area in relation to the values measured in air were obtained. Abrupt embrittlement occurred at still low levels of hydrogen, around 0,2.10^{-3} mol/cm³ (26 ppmw). Extrapolating the curves to values of embrittlement index equal to 1, hydrogen concentrations of 5 ppm (time to failure ratio) and 0.7 ppm (reduction of area ratio) are obtained. These hydrogen levels can be considered the limit values below which embrittlement would not be measurable [30].

The analyzed failure cases caused by hydrogen-assisted stress cracking in subsea components made of duplex and super duplex stainless steels from the oil and gas industry indicate that [31,32]:

- The fractures initiated mostly in the weld metal or heat affected zone, were related to large forgings with coarse microstructures, with unfavorable grain orientation (in the thickness direction) and/or high ferrite fractions. There were also some failures in seamless tubes severely work hardened.
- In many cases, poor manufacturing, inadequate weld sizing or high local deformations acted decisively for the failure occurrence.
- Most failures occurred near galvanic anodes (1m or less).
- The failures were usually related to uncoated components or with severe flaws in the coating.
- In most cases, cracking was associated to thickness transitions, e.g. transitions from pipe to flange, hub or connector.
- Localized yielding and total stress higher than the design value were verified in many failures.

On a platform of BP in the North Sea, several failures in cathodically protected UNS S32550 duplex stainless steel bolts were reported. Ferrite fraction was found to be around 70%. Associated with this imbalance of phases, it was verified that the material

had been aged around 500ºC. The α' phase precipitated in this treatment contributed to the increased susceptibility to hydrogen embrittlement [29].

HISC was reported on small diameter stainless steel couplings of UNS S32760 and UNS S31803. These parts presented subsea service and failed after 1,5 to 5 years. The interaustenitic spacing measured in the materials was less than 20 μm, and no nitrites and other deleterious precipitates were identified. Mean values of hydrogen between 40 and 60 ppm were measured, which are the expected values under cathodic protection for a period of 5 years. The method of installation involved cold stamping, which caused severe hardening along the thickness and introduction of high residual stresses. Hydrogen cracks propagated from the outer diameter, where hardness values around 500HV (about 49HRC or 470HB) were measured. ISO 21457 (Materials selection and corrosion control for oil and gas production systems, 2010) and ISO 13628-1 (Design and operation of subsea production systems, 2010) standards specify maximum hardness of 35HRC or 328HB for any steel component under cathodic protection, while BS EN ISO 15156-3 requires values below 36HRC for duplex stainless steels. EEMUA nº 194 (Guidelines for materiais selection and corrosion control for subsea oil and gas production equipment, 2012) limits in max. 28HRC (280HB) the hardness of duplex stainless steel fasteners [17,33].

2.5.1.2. Hydrogen Embrittlement in Gaseous Environments

Hydrogen entry into the metal in gaseous atmospheres involves the adsorption of the H_2 molecule, its dissociation into hydrogen atoms and subsequent diffusion of the atoms adsorbed into the crystalline lattice. For perfectly clean, film-free surfaces, the rate controlling step is the H_2 dissociation, which is proportional to the hydrogen partial pressure. Usually, surface films and the presence of other gases that competitively adsorb to hydrogen play an important role in the process [34].

High rates of subcritical cracking growth are reported for tensile steels in gas mixtures containing H_2 and H, as well as mixtures containing HBr, HCl and H_2S. It has been verified that small additions of O_2 cause the arrest of hydrogen-assisted cracks in steels exposed to water vapor or H_2. Hydrocarbons such as ethylene and acetylene added to a medium containing H_2 are able to react with the metal surface, consuming the adsorbed hydrogen and inhibiting hydrogen embrittlement. When present at high concentrations, hydrocarbon molecules can catalytically dissociate, producing hydrogen and promoting embrittlement. Cracking rates according to this latter mechanism, however, are substantially lower than those occurring in H_2-rich media [35].

Hydrogen embrittlement is generally more pronounced by reducing the strain rate and increasing the H_2 pressure. In the work of ZHENG *et al.* [36], slow strain rate tensile tests

($\dot{\varepsilon}$ = 1,7.10^{-2} to 1,2.10^{-5} s^{-1}) were performed using 2205 duplex stainless steel samples. **Figure 7** presents the ductilities measured for the uncharged specimens tested in atmosphere of hydrogen gas at pressures up to 2 bar. The loss in ductility increased with gas pressure until a saturation value. The embrittlement was strain-rate dependent and increased with increasing hydrogen pressure. At sub-atmospheric pressure, the ductility passed through a minimum value at a strain rate in the region of 3.10^{-4} s^{-1} and there was much less embrittlement at lower strain rates. Testing in 1 bar H_2 gave results closer to the values at the higher hydrogen pressure but again with a minimum ductility at an intermediate strain rate (ca. 6.10^{-4} s^{-1}) [36].

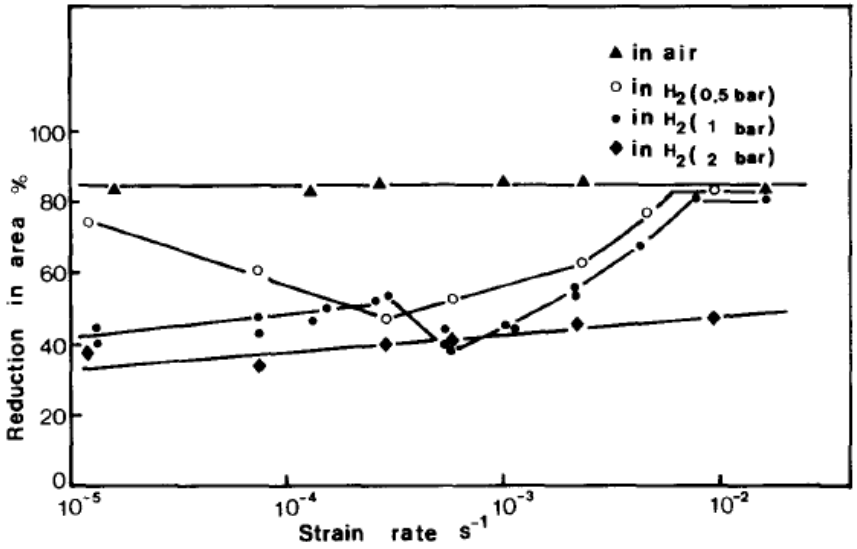

Figure 7. Effect of strain rate and hydrogen pressure on the reduction in area at fracture compared with results for the material tested in air [36].

Additional embrittlement under the appropriate combination of hydrogen environment and strain rate was associated to formation of ε-martensite from the unstable austenite. The appearance of ε-martensite was confirmed by the occurrence of $(101)_\varepsilon$ reflection and diminishing of $(111)_\gamma$ reflection. The greater abundance of hydrogen in the tests at higher pressure (2 bar) reduces the necessity for the contribution of ε-phase to the embrittling process. Where hydrogen supply is more restricted, at lower pressures, formation of ε-martensite also plays a significant role in embrittlement [36].

2.5.2. Factors Affecting Hydrogen Embrittlement

It is generally required for hydrogen embrittlement to occur:

- The presence of a hydrogen source and transport of hydrogen to the regions in the material where embrittlement occurs.
- Application of mechanical loading (even in the elastic regime).
- Susceptible material or microstructure.

Crack propagation and the performance of hydrogen-embrittled steels are affected by several variables, such as: mechanical loading or stress intensity level, loading rate, chemical composition (average and at grain boundaries), mechanical properties, microstructure, surface conditions, environmental parameters (temperature and pressure), hydrogen concentration and diffusivity.

A schematic relationship for tempered steels obtained between the applied stress intensity factor, hydrogen content at the crack tip and fracture mode is shown in **Figure 8**. Under constant loading, steel containing a certain amount of hydrogen will initially fracture intergranularly (IG) when the factor of stress (K) is low. By increasing the applied K, with crack growth, propagation occurs by quasi-cleavage (QC) and, finally, by microcavity coalescence (MVC). Increase of the hydrogen concentration reduces the stress level at which these processes occur (as well as the total time to failure). At high concentrations of hydrogen, intergranular fracture occurs at any K level for many steels.

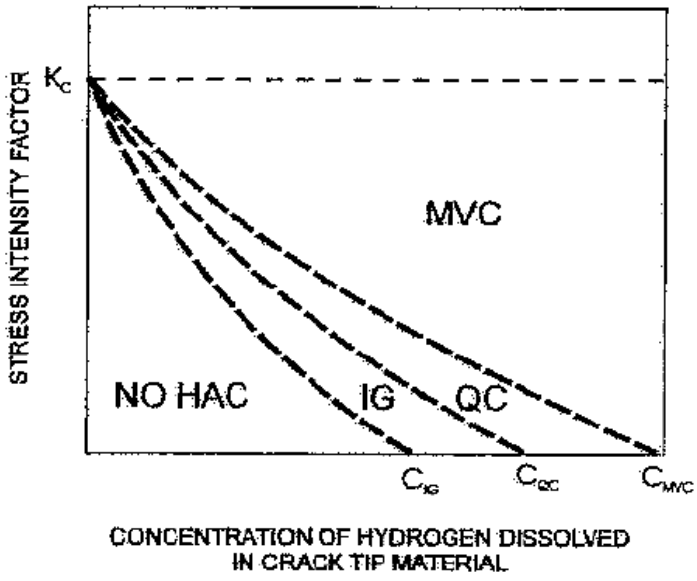

Figure 8. Interrelationship between stress intensity factor, dissolved hydrogen content, and HISC deformation mode at constant load [37].

Hydrogen embrittlement is minimized by temperature increase. CASSAGNE *et al.* [38] verified through slow strain rate tensile tests under cathodic potential that duplex

stainless steels were more brittle at 20°C than at 70-80°C. It is proposed that the temperature increase reduces the hydrogen content close to the region of crack propagation or the fracture process zone. There are results indicating that embrittlement is more severe close to room temperature, becoming less intense at lower or higher temperatures. At temperatures much lower than the room temperature, due to the lower hydrogen diffusivity, hydrogen cannot diffuse through the lattice [35].

The hydrogen concentration in the alloy is a function of the fugacity or concentration of hydrogen on the surface exposed to the environment. Therefore, hydrogen embrittlement is controlled by the pressure of gaseous H_2 or pH of the medium, as well as elements in the environment that accelerate or inhibit the hydrogen entry into the material. Elements such as S, P, Sb, Sn and As (and compounds containing these elements) inhibit the reaction of recombination of the atomic hydrogen in aqueous solutions, facilitating the entry of atomic hydrogen. As mentioned, oxygen has the opposite effect, reducing the growth rate of hydrogen-assisted cracks.

Regarding the effect of hydrostatic pressure (i.e. the water column or the pressure of the aqueous environment) on the susceptibility to hydrogen assisted cracking in subsea components, there are few published results. OLSEN *et al.* [39] charged electrochemically samples of supermartensitic and super duplex stainless steels under hydrostatic pressures of 1 bar and 25 bar. After 80-90 days, hydrogen levels considerably higher were observed in the samples tested under the higher hydrostatic pressure level [39]. FESTY [40] reported no effect of water pressure (in the range between 1 and 300 bar) on hydrogen embrittlement risk of several steel grades tested in natural seawater at -1050 mV_{SCE}. MIKKELSEN *et al.* [41] performed hydrogen charging and CTOD testing of 22% and 25%Cr samples at 1 and 100 bar. Only a marginal effect on the hydrogen concentration after 324 days of charging was verified. The samples tested at 100 bar showed more subcritical crack growth as compared to the samples tested at 1 bar, so that the hydrogen-assisted cracking seemed lower at 100 bar than at 1 bar. A conclusive study on the effects of the hydrostatic pressure on the mechanical performance is still lacking.

The threshold stress intensity for hydrogen cracks initiation in general decreases with increasing yield strength limit. High strength steels with martensitic microstructure and yield stresses between 1200 and 2200 MPa are particularly embrittled by hydrogen. Microstructurally, the susceptibility to hydrogen damage increases in the following order: lower bainite, tempered martensite, pearlite, spheroidized microstructures and untempered martensite. Fine grains and carbides of smaller sizes are beneficial, as are more pure compositions. Impurities such as sulfur and phosphorus are deleterious. The

increase in carbon content tends to increase susceptibility to hydrogen-assisted cracking. Manganese and silicon are harmful when segregated to grain boundaries [35].

The increase in the austenite fraction generally improves the resistance to hydrogen embrittlement in duplex and super duplex stainless steels, due to the ability of this more ductile phase to arrest the cracks. Aspects such as austenitic grain size, structural orientation and spacing between the austenitic grains (interaustenitic spacing) influence the hydrogen diffusion free path, the hydrogen trapping tendency and the ability to restrict the cracks propagation in the material. In microstructures with ferrite and austenite bands oriented perpendicular to the crack opening stress, the hydrogen-assisted cracks tend to propagate along the ferrite bands. If the opening stress is applied in the longitudinal direction, the cracks can be interrupted in the first austenitic band. Finely dispersed austenite grains promote long paths for diffusion, compared to a structure with coarse austenitic grains. In general, greater fracture stresses are obtained with smaller grains and interaustenitic spacings. Because of this effect, materials made through powder metallurgy are less susceptible to hydrogen embrittlement than forged materials of similar dimensions [38].

2.5.3. Hydrogen Embrittlement Mechanisms

The mechanisms of hydrogen embrittlement are not fully elucidated by the scientific community. Several theories have been postulated, none accepted as general for all cases. Exceptions are austenitic stainless steels and metals with a strong tendency to form hydrides, for which there is already reasonable explanation for the embrittlement [42].

The most important mechanisms proposed to describe HE in metals are next described.

a) Hydride formation

Certain metals such as Pd, Nb, Zr and Ti are strongly prone to form hydrides. Stresses favor the hydride formation, so that the crack tip is a preferred site for their nucleation. These hydrides favor cleavage fracture, enhancing crack growth. The hydride mechanism only occurs in temperatures and strain rate regimes where hydrogen has time to diffuse to regions ahead of the crack tips, and only at temperatures where the hydride phase is stable and brittle. Only at very high pressures (of the order of 5 GPa) the formation of iron hydrides occurs [43].

b) Hydrogen-enhanced decohesion (HEDE)

This model was proposed in 1958 by Troiano, receiving, after, important contributions from Oriani and Gerberich. The HEDE mechanism is based on the hypothesis that interstitial hydrogen decreases the material cohesive strength due to crystalline lattice dilation. The decrease in atom bonding cohesion is due to the hydrogen electron donation to the metal electronic cloud, causing an increase in the repulsive force. As a result, microscale plasticity is prevented, and the fracture energy is reduced, promoting brittle cracking. According to this mechanism, the fracture begins in the fracture process zone (FPZ) a short distance ahead of the crack tip, where the local crack opening stress exceeds the atomic bonding cohesion strength, decreased locally by the presence of hydrogen. The fracture propagation proceeds by nucleation of microcracks within the plastic zone, these microcracks then joining with the main crack.

This model has validity restricted to brittle, intergranular fractures, failing to explain the presence of plasticity in brittle fractures. Despite confirmation by ab-initio simulations, this mechanism has relatively scarce experimental support, i.e. it has not yet been demonstrated directly through experimental measures that hydrogen decreases interatomic bonding cohesion or alters elastic properties or surface energy [44].

c) Hydrogen enhanced local plasticity (HELP)

The two following models (HELP and AIDE) are based on experimental observations showing hydrogen-dislocations interactions.

The HELP mechanism, introduced by Birnbaum and Sofronis in 1994, considers that hydrogen causes an increase in dislocation mobility near the crack tip in preferential crystallographic planes. The mechanism can be described as an enhanced local plasticity that makes the material macroscopically brittle. A crack by HELP will tend to start from sliding planes near the crack tip.

According to the HELP mechanism, hydrogen atoms shield dislocations from interacting with each other and with other obstacles, which enhances the dislocation density and mobility along preferential crystallographic planes. Also, hydrogen reduces the SFE, increasing the separation distance between partials, decreasing the tendency for cross-slip and increasing slip planarity. Both effects tend to enhance pile-up of dislocations at grain boundaries. Hydrogen-assisted transgranular cracking may be explained directly by the enhancement of the local stress level due to improved dislocation pile-up. Intergranular cracking is related to accommodation of dislocations in the grain boundaries. As hydrogen is carried with the mobile dislocations, the hydrogen content is increased in the grain boundaries. The dynamic hydrogen content of the grain

boundary is controlled by the slip transfer process and by the binding energy of hydrogen to the grain boundary, which is greater than at a dislocation [45].

Experimental observations have shown that the presence of hydrogen in the core of dislocations can increase their mobility. This behavior was observed in fcc, bcc and hcp metals and alloys, in tests performed at relatively low temperatures and under low strain rates, when the hydrogen atmospheres are stable and mobile. The increase of local mobility of the dislocations results in reduction of the yield stress and transgranular cracking with microvoid coalescence along these preferential planes. A decrease in the start stress for the dislocation slip ('microscopic' yield stress) caused by hydrogen in austenitic steels was shown by in situ transmission electron microscopy observations, which is a very convincing experimental proof of the HELP mechanism. Also, increases in dislocation mobility enhance the slip localization, so that the introduction of hydrogen can generate a macroscopical ductility loss (43-45).

Unlike the HEDE mechanism, the HELP mechanism has not yet been sufficiently developed to generate quantitative prediction models of K_{th} and da/dt and cannot yet be used for the analysis of equipment integrity [44].

d) Adsorption-induced dislocation emission (AIDE)

The AIDE mechanism was first proposed by Lynch in 1976. Weakening of interatomic bonds by adsorbed hydrogen facilitates the dislocation emission, which encompasses both nucleation and subsequent movement of dislocations. The AIDE model also involves nucleation and growth of microvoids (or nano-voids) ahead of crack tips. When hydrogen adsorption weakens interatomic bonds and thereby promotes dislocation emission from crack tips, a greater proportion of dislocation activity results in crack growth. Coalescence of cracks with voids occurs at lower strains and shallower dimples are produced on fracture surfaces when AIDE occurs. Crack paths produced as a result of AIDE mechanism can be intergranular or transgranular depending on where dislocation emission and void formation occur more easily.

The AIDE mechanism is supported by the presence of high concentrations of hydrogen adsorbed on surfaces (and within a few atomic distances of surfaces), surface science observations, atomistic modelling, observations of hydrogen embrittlement at high crack velocities relative to hydrogen diffusivities and metallographic and fractographic observations [43].

e) Theory of internal pressure

Under the original name of "molecular pressure theory," this theory was proposed by Zapffe and Sims in 1940 to explain the decrease in plasticity of steels containing much higher hydrogen concentrations than the equilibrium hydrogen solubility at room temperature [46].

According to this mechanism, hydrogen in excess (in concentration greater than the equilibrium solubility in the material) precipitates in the molecular form in internal defects, such as micropores, developing sufficient internal pressure for the growth of the pores and consequent microcrack formation. This theory does not explain the embrittlement at reduced hydrogen pressures

f) Martensitic transformation of austenite

In austenitic steels, the introduction of hydrogen into austenite produces expansion of the lattice and sufficient stresses so that part of austenite transforms to martensite. This transformation can generate cracks on the surface without external mechanical stresses being applied. The phenomenon is restricted to superficial zones, due to the low hydrogen diffusivity in austenite. Partial transformation of austenite may generate two martensitic phases: martensite ε (hcp), nucleated during the hydrogen charging, and α'-martensite (bcc), nucleated during the degassing process from ε martensite. The formation of ε is considered the dominant mechanism on hydrogen embrittlement of austenitic steels, since the habit plan of this phase, (111), is the plane of hydrogen-assisted cracks in these materials [47].

Through scanning electron microscopy (SEM) and electron backscattered diffraction (EBSD), α'-martensite plates were observed in the austenitic phase of a previously hydrogenated duplex stainless steel [48].

g) Other theories

KIRCHHEIM [49] proposed that the interaction of hydrogen with microstructural defects (phase and grain boundaries, vacancies, dislocations, stacking faults etc.) could be better explained if the hydrogen segregated to these defects was considered a "defect-acting agent" or "defactant". A defactant would have the effect on microstructural defects analogous to the effect surfactants (surface-acting agents) have on the surface tension of liquids. Surfactants reduce the energy formation for new surfaces, which is reflected as an increase in liquid wettability (detergent effect). In this view, hydrogen acts as an agent that induces a reduction in the energy of formation of new defects enhancing deformation and crack growth [22,49].

Nagumo presented in 2004 the hydrogen-enhanced strain-induced vacancy model (HESIV). The model proposes that the primary function of hydrogen in degradation is to enhance the strain-induced creation and agglomeration of vacancies, thus promoting the fracture process [50].

Petch (1956) suggested that hydrogen adsorption decreases the energy of the surface created during crack propagation, thus reducing fracture work and promoting crack growth. There are arguments against this model: it underestimates the fracture work; it does not fit with discontinuous propagation verified through acoustic emissions and, mainly, the fact that oxygen, with a greater adsorption energy on iron, does not promote crack growth. In fact, oxygen promotes crack arrest, probably by competitive adsorption, preventing the entry of hydrogen [51,46].

2.5.3.1. Mechanisms for Hydrogen Embrittlement in Duplex Stainless Steels

Due to the heterogeneous microstructures and different elastic and plastic deformation behavior in the individual phases, the mechanisms of HISC in duplex stainless steels are still not quite understood. It is generally accepted that HELP, HEDE and AIDE are the principal mechanisms for hydrogen embrittlement in DSS [43,52]. For failure occurrence, they act concurrently or competitively for the decrease of stress or strain to failure. It is believed that HEDE mechanisms are dominant in ferrite, whereas HELP is controlling in austenite [52].

Based on microscopy and fractographic results, a physical model was postulated for hydrogen-assisted fracture in super duplex stainless steels [53]. A schematic representation of this model is provided in **Figure 9**. As stress increases on the crack tip, the first fracture event is the formation of cleavage microcracks in the ferrite phase. As cleavage microcracks form in ferrite, stress is concentrated in austenite, causing fracture through the austenite grains. Fracture of austenite or along phase boundaries links the cleavage cracks. The fracture segments connecting cleavage facets are steeply oblique relative to the nominal fracture plane.

Considering fracture through austenite grains, studies on austenitic stainless steels concluded that hydrogen-assisted fracture is governed by plastic deformation, where hydrogen can promote localized deformation in discrete bands [54]. Deformation localizes along planes of high shear stress, which are inclined relative to the nominal fracture plane. Oblique fracture planes through austenite grains reflect the predominance of localized deformation. Furthermore, these oblique planes exhibit dimples, indicating that these fracture events involved microvoid formation. The stages of microvoid fracture (nucleation, growth and coalescence) can be accelerated by localized deformation as well as mechanism involving high concentration of hydrogen.

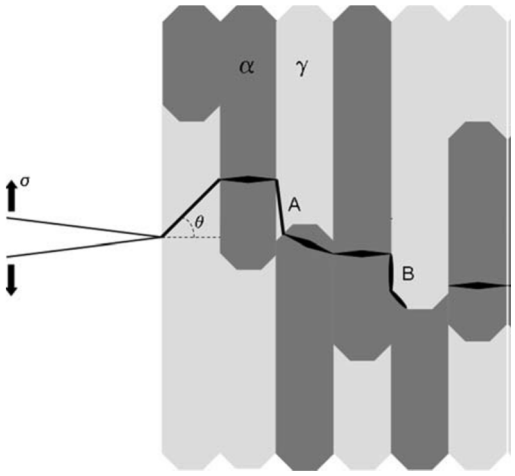

Figure 9. Schematic of H-assisted crack propagation in 2507 steel [53].

It is suggested that crack propagation in hydrogen-exposed SDSS is governed by strain-controlled, hydrogen-assisted fracture in the austenite phase. The fracture toughness could therefore be improved by enhancing resistance to hydrogen-assisted ductile fracture in the austenite phase. Improved H-assisted fracture resistance in austenitic stainless steels has been correlated with higher stacking fault energy (SFE) – SFE governs slip mode. The available trends for austenitic stainless steels are that N decreases SFE, while Ni and Cr increase SFE. Because N and Ni partition to austenite in duplex steels, SFE and associated hydrogen-assisted fracture resistance could be increased by lowering N and enriching Ni.

It was demonstrated that the supply of hydrogen to austenitic grains is controlled by localized damages occurring at the α/γ boundary. These damages result from the formation of a crack embryo, the length of which is of the order of few microns. They are due to the penetration of cleavage cracking from the hydrogen embrittled ferrite. This induced short crack allows the localized hydrogen supply to the austenitic grain. This will lead to the zig-zag microcracking which corresponds to the situation described by the corrosion-enhanced plasticity model for the transgranular stress corrosion cracking of fcc materials [55].

From this model (**Figure 10**), the following steps can be proposed:

i) Creation of the microcrack in austenite from the cleavage of ferrite (step 1).

ii) Localised entry of hydrogen at the crack tip and particularly along the slip planes (step 2).

iii) Hydrogen enhances the mobility of dislocations, which will induce the formation of pile-ups ahead of the diffusion zone (step 3). The “virtual” obstacle corresponds to the interface between the enhanced plasticity zone and the previously hardened zone related to the applied mechanical deformation.

iv) The fracture process results from a competition between the kinetics of dislocation emission and motion and kinetics of diffusion. When a critical stress is reached at the virtual obstacles (corresponding to a critical number of dislocation in the pile-up and a related hydrogen concentration which decreases the decohesion energy of the {111} facets), a crack's embryo can form.
v) The normal stress to the {111} microfacets can be sufficient to open the crack (step 4). Dislocation are then emitted on a symmetrical plane relative to the average crack plane, shielding the new crack.
vi) A new sequence from (i) to (v) is then possible. This is expected to lead to regular chances of crack planes, resulting in a zig-zag microcracking along slip plane.

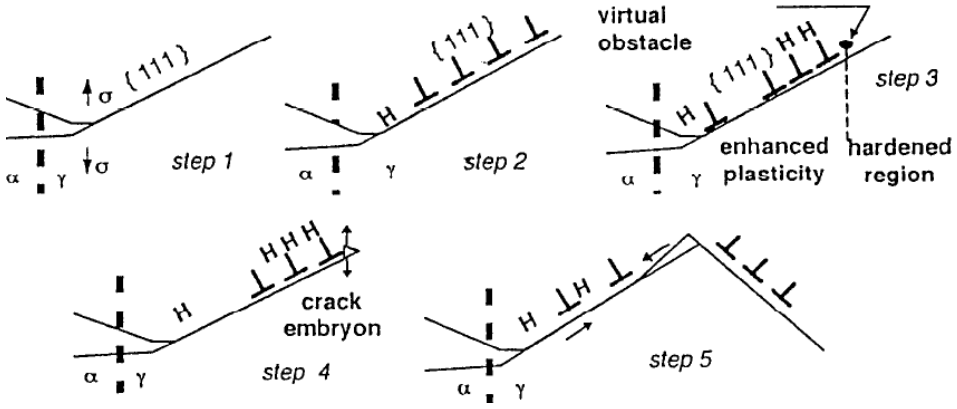

Figure 10. Schematization of the steps involved in the hydrogen cracking of an austenitic grain [55].

It has also been reported that strain-induced martensite contributes to hydrogen-assisted fracture in single-phase austenitic stainless steels as well as in duplex stainless steels. Higher N and Ni contents stabilize austenite with respect to martensitic transformations, which may further improve resistance to hydrogen-assisted fracture. Chromium would be necessary to balance changes in Ni and N contents in duplex alloys, which will also impact hydrogen compatibility – high Cr contents appear also to improve hydrogen compatibility [25].

2.6. Hydrogen-Steel Interactions

The processes of hydrogen entry and dissolution in the metal involve in general the steps of adsorption, penetration through the subsurface (absorption) and diffusion.

Adsorption is the adhesion of atoms to a surface. The adsorption process involves in general two steps: physisorption and chemisorption. During physisorption, lower energy bonds (< 0,5 eV) are established due to Van der Waals forces between the atoms of the metallic surface and the adsorbent. No electronic exchange is developed between the species in contact. It is a reversible process, accompanied by an enthalpy change approximately equal to the heat of condensation of the gaseous adsorbent (≤20 kJ/mol). In the chemisorption step, on the other hand, electronic exchanges are developed between these atoms, and more energetic bonds are created (> 0,5 eV). Since short-range chemical forces are involved, chemisorption is limited to a monolayer. Chemisorption is usually slow, activated and either slowly reversible or irreversible. For gaseous hydrogen, an intermediate step is necessary: the dissociation of the H_2 molecule. This reaction is usually fast on transition metals as iron, but it can be considerably affected by the presence of surface oxides [56].

The magnitude of adsorption depends on several factors as pressure, temperature and surface crystallographic orientation. The preferable adsorption sites are those with high coordination level, i.e., to which the adsorbent atoms can establish higher number of bonds.

The global hydrogen adsorption reaction can be written as:

$$2M + H_2 \rightarrow 2MH_{ads} \qquad \textbf{(Equation 12)}$$

where M stands for the metal.

The final step in the gas-solid interaction set, absorption, involves the incorporation of the products of chemisorption into the metal bulk lattice. The hydrogen absorption equation can be expressed as:

$$MH_{ads} \rightarrow MH_{abs} \rightarrow H_{lattice} + M \qquad \textbf{(Equation 13)}$$

In equilibrium the chemical potential of the gas must be equal to the chemical potential of the hydrogen dissolved in the material, i.e.:

$$\frac{1}{2}\mu^0_{H_2} = \mu^0_H \qquad \textbf{(Equation 14)}$$

Assuming H_2 as a real gas and that the atomic hydrogen dissolved in the material behaves as a diluted solution, then:

$$\frac{1}{2}\left(\mu^0_{H_2} + RTln(f)\right) = \mu^0_H + RTln(C_i) \qquad \textbf{(Equation 15)}$$

where:

- $\mu^0_{H_2}$, μ^0_H : standard state chemical potentials.
- C_i: equilibrium subsurface hydrogen concentration.
- f: equilibrium fugacity of H_2.

The subsurface hydrogen concentration C_i depends on both the adsorption kinetics and the equilibrium fugacity of H_2 (f).

The chemical potential difference between the molecular and atomic hydrogen states relates to the enthalpy and entropy of formation or dissolution of hydrogen in the metal, respectively ΔH and ΔS, by the following expression:

$$\mu^0_H - \frac{1}{2}\mu^0_{H_2} = \Delta H - T\Delta S \qquad \textbf{(Equation 16)}$$

Combining **Equations 15** and **16**, the following relationship can be obtained between the concentration of subsurface hydrogen and the fugacity of H_2:

$$C_i = C = kf^{1/2} \qquad \textbf{(Equation 17)}$$

being K the equilibrium coefficient given by:

$$K = \exp\left(-\frac{\Delta G}{RT}\right) = \exp\left(\frac{\Delta S}{R}\right).\exp\left(-\frac{\Delta H}{RT}\right) \qquad \textbf{(Equation 18)}$$

where ΔG, ΔH and ΔS are the Gibbs free energy, enthalpy and entropy, respectively, in the reaction of **Equation 13**.

By definition, the solubility S is the concentration C of hydrogen dissolved in the metal. Therefore, the solubility can be expressed by:

$$S = \exp\left(\frac{\Delta S}{R}\right)\exp\left(-\frac{\Delta H}{RT}\right).f^{1/2} \qquad \textbf{(Equation 19)}$$

For a gaseous hydrogen-metal system in thermal equilibrium at high temperatures (typically above 400ºC) and lower pressures (up to 200 bar), ideal gas behavior can be considered. In this case, f → P, and the relationship between the molecular hydrogen pressure (p_{H2}) and the dissolved hydrogen concentration (C) is described by the empirical relation known as Sievert's law, as follows:

$$C_i = C = s.p^{1/2}_{H_2} \qquad \textbf{(Equation 20)}$$

The proportionality constant, “s” the Sievert’s parameter, has the Arrhenius standard form:

$$s = s_o\exp\left(\frac{-\Delta H}{RT}\right) \qquad \textbf{(Equation 21)}$$

Hydrogen concentration can be affected by the stress-strain states at microstructural scales. Internal and/or applied stresses can modify the solubility of hydrogen. The relationship between the hydrogen concentration in the lattice with and without hydrostatic stresses is given by [57]:

$$\frac{C_{Ls}}{C_{Lo}} = \exp\left(\frac{V_H.\bar{\sigma}}{RT}\right) \quad \textbf{(Equation 22)}$$

where:

- C_{Ls}: hydrogen concentration in the lattice subjected to a hydrostatic stress state.
- C_{Lo}: hydrogen concentration in the unstressed lattice.
- $\bar{\sigma}$: mean hydrostatic stress.
- V_H: parcial molar volume of hydrogen.

The effect of stress on the hydrogen concentration in the lattice is higher at lower temperatures. For steels at room temperature, due to the lattice expansion, there is an increase on the hydrogen concentration of approximately 50% for hydrostatic tensile stresses of about 500MPa. For hydrostatic compression of 500MPa, a reduction in the hydrogen concentration of about 30% is expected [53].

2.6.1. Hydrogen Charging Methods

Electrochemical and gaseous charging are two common methods employed for hydrogen charging. Molten salt baths at high temperatures can also be mentioned. The electrochemical process implies the deposition on the metal surface of hydrogen in the atomic form, while in the gaseous or thermal process the dissociation step of the H_2 molecule is necessary. The dissociation reaction is highly dependent on the hydrogen temperature and pressure. In the cathodic charging the kinetically-controlling dissociation step is eliminated. On the other hand, the reducing atmosphere present in the gaseous charging minimizes the formation of surface oxides.

The charging mode influences the hydrogen concentration profile in the material. Due to the usually higher temperature, the gaseous hydrogen charging is expected to give a more uniform hydrogen concentration, whilst the lower temperature aqueous charging is expected to generate a steeper gradient. These different distributions were experimentally verified using samples of the super duplex stainless steel UNS S39274 [58].

Figure 11 presents the evolution of the hydrogen concentrations (normalized by the surface concentration) along the thickness in membranes of 316L charged cathodically and thermally. The total hydrogen content introduced cathodically (approx. 240ppm at 0,5M H_2SO_4, 50h, 50mA/cm², 95°C) was considerably higher than using gas hydrogen

(ca. 51ppm at 180bar, 48h, 600°C). However, the cathodic charging generated a strongly heterogeneous hydrogen distribution, while in the gaseous charging the material became uniformly saturated with hydrogen [59].

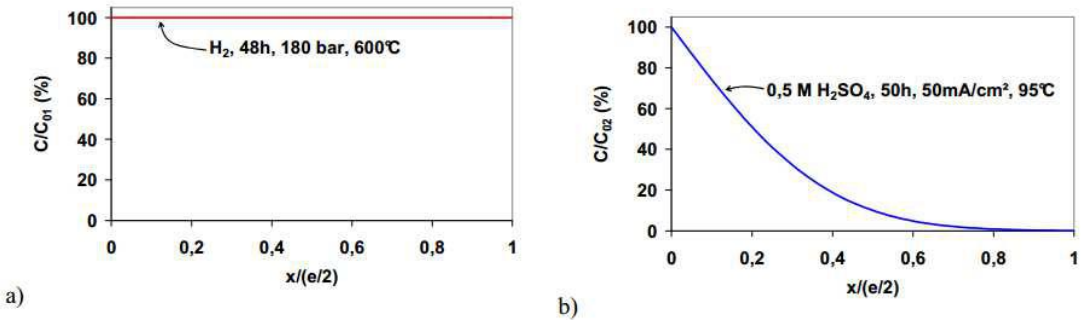

Figure 11. Hydrogen profiles as function of the charging procedure measured in 316L: (a) cathodic and (b) gaseous or thermal charging [59].

2.6.2. Diffusion

Hydrogen diffusion in a crystalline lattice occurs by a Brownian migration of protons or ionic hydrogen from an interstitial site to the closest one. [56]. The trajectory of the atoms during diffusion is constituted by random successive, elementary jumps. For this to be accomplished, an energy input E_L is necessary to overcome the energy barrier between the interstitial sites. E_L depends mainly on the crystallographic structure, if mechanical loading and electromagnetic fields are not present; and it affects the diffusion coefficient D according to following Arrhenius-type relationship:

$$D = D_o \exp\left(-\frac{E_L}{RT}\right) \qquad \textbf{(Equation 23)}$$

Being:

- D_o: pre-exponential or frequency factor.
- E_L: activation energy.
- R: ideal gas constant (8,314 J/mol.K).
- T: temperature (K).

Fick's first law (**Equation 24**) describes the diffusion process in steady state conditions. The transient regime can be described by Fick's second law (**Equation 25**):

$$J = -D\frac{dC}{dx} \qquad \textbf{(Equation 24)}$$

$$\frac{dC}{dt} = -\overrightarrow{\nabla J} \qquad \textbf{(Equation 25)}$$

Fick's second law for diffusion transient regime can be solved by different methods, e.g. Laplace transformation or separation of variables.

The presence of grain boundaries can bring about the phenomenon of diffusion "short circuits" or preferential diffusion along grain boundaries, which is only observed in metals with low diffusivities. In metals with elevated hydrogen diffusion rate, the presence of grain boundaries does not promote considerable diffusion acceleration [60].

The grain boundaries can be modeled as slices with defined thickness equal to "δ" and diffusion coefficient D_j, while the matrix has grain sizes equal to "d" and diffusion coefficient D_v, being $D_j > D_v$. Considering these parameters, three regimes can be distinguished:

a) If $\sqrt{D_v t} >> d$, the material behaves homogeneously. Diffusion can be described in this case by an effective coefficient equal to:

$$D_{eff} = (1 - f_{gb})D_v + f_{gb}.D_j \qquad \textbf{(Equation 26)}$$

Being "f_{gb}" the volumetric fraction of grain boundaries.

b) If $\frac{\delta}{2} << \sqrt{D_v t} << d$, three processes contribute to the diffusion: bulk (intragranular) diffusion, grain boundary (intergranular) diffusion and lateral diffusion from the grain boundaries to the grain bulk.

c) If $\frac{\delta}{2\sqrt{D_v t}} >> 1$, the polycrystal behaves homogeneously as composed solely by grain boundaries.

Coatings and oxide layers can modify the hydrogen permeability. In general, coatings placed in between the metal and the hydrogen-bearing environment can act as barriers, by strongly reducing the hydrogen diffusion and permeability, or can be used to favor hydrogen absorption in steels by increasing the hydrogen activity on the surface and/or avoiding the corrosion of the base metal. Palladium is the most common element used for the latter purpose [61].

The presence of oxides on the permeation membrane surfaces can reduce the kinetics of hydrogen dissociation and recombination as well as the global kinetics of the permeation process due to a lower hydrogen diffusion velocity within the oxide. The oxide layer is usually about 3-5 nm thick in steels. Its hydrogen diffusion coefficient lies between 10^{-14} m²/s (wustite) and 10^{-21} m²/s (hematite) [62]. Chromium oxide has a hydrogen diffusivity of approx. 10^{-20} m²/s. [63] When the surface phenomena are much slower than the hydrogen bulk diffusion, the value of D obtained in the permeation tests does not correspond to the lattice diffusion of the metal. One can define the times τ_m and τ_{ox} necessary for hydrogen to cross respectively the metallic membrane and the oxide layer as:

$$\tau_i = \frac{e_i^2}{D_i} \qquad \textbf{(Equation 27)}$$

Disregarding initially the effects of oxides in the reactions of H_2 dissociation and recombination, two general cases can be established:

- If $\tau_{ox} << \tau_m$, the hydrogen diffusion time through the oxide layer is negligible, i.e. the influence of the oxide is not relevant.
- If $\tau_{ox} >> \tau_m$, the diffusion over the oxide is the kinetically limiting process.

2.6.2.1. Influence of Trapping

Trapping is a phenomenon induced by the possibility of the hydrogen atoms to reduce their chemical potential by segregating at the trapping sites. Hydrogen trapping was first suggested in 1949 by DARKEN and SMITH [65], based on the results of permeation tests.

The main consequences of hydrogen trapping in metals and alloys are: increased apparent hydrogen solubility, decreased apparent hydrogen diffusivity (increasing diffusion time), local increase of the hydrogen concentration (segregation), enhancing or minimizing hydrogen embrittlement [22]. Hydrogen trapping in favorable traps is a way of minimizing the embrittlement of steels by reducing the accumulation of hydrogen atoms at potential sites for crack initiation and propagation, such as inclusions, second phase particles and the crack tip [64].

Typical regions of hydrogen trapping are dislocations, cavities, vacancies, grain boundaries, phase boundaries, precipitates, precipitate-matrix interfaces, and inclusions. **Figure 12** shows schematics of different hydrogen microstructural trapping sites.

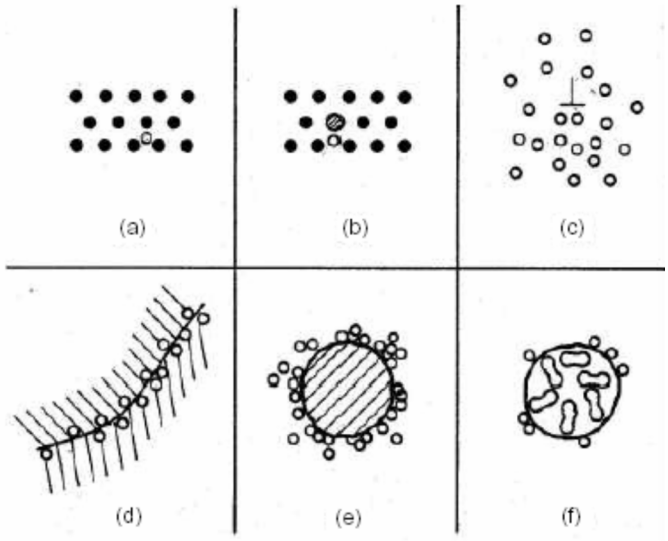

Figure 12. Hydrogen-microstructure interaction possibilities: (a) solid solution, (b) hydrogen-solute pair, (c) dislocation core atmosphere, (d) accumulation in grain boundary, (e) accumulation in matrix-particle interface, (f) hydrogen recombined in cavities [65].

The energy relations between hydrogen in the gas phase, in the lattice and in a trap are shown schematically in **Figure 13**. The activation energy for permeation is given by E_S, the hydrogen migration energy is represented by E_m, and E_b is the binding energy of hydrogen with the trap. If $E_b > E_s$, the trapping site is the lowest energy state in the system. For iron, E_s = 27,2 kJ/mol. Iron is an endothermic hydrogen absorber. Thus, hydrogen solubility in iron increases with temperature, and at low temperatures hydrogen tends to move to the lowest energy state.

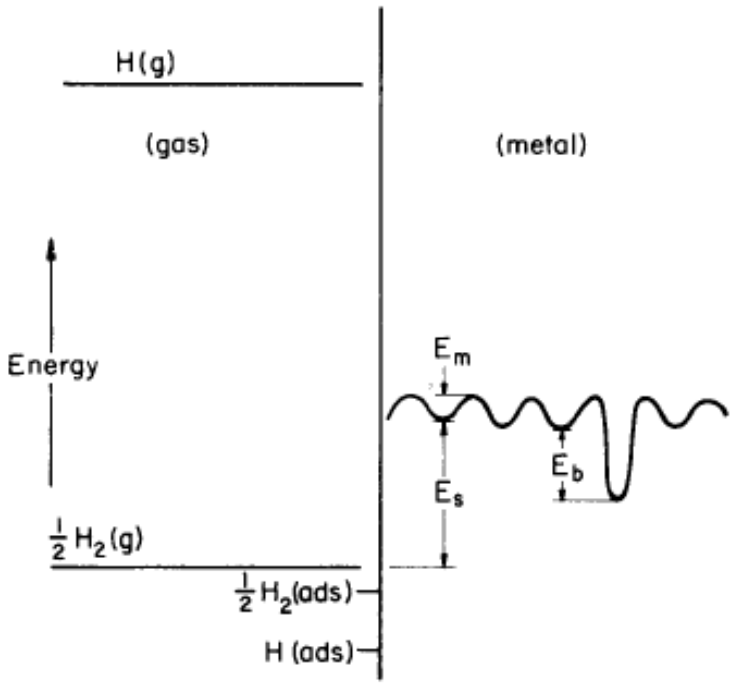

Figure 13. Schematic of energy relations between hydrogen in the gas phase, in the lattice and in a trap site [66].

There are at least two ways to classify trapping sites: according to saturability and reversibility. The concept of saturable and non-saturable traps is based on the trap capacity. Saturable trapping sites are those whose capacity to trap hydrogen atoms is finite. Dislocations, impurities, vacancies and internal interfaces are saturable traps. Non-saturable traps can accommodate an infinite number of hydrogen atoms. Micro-cavities are classic examples of non-saturable traps.

According to reversibility, traps can be divided in two categories: reversible and irreversible. In reversible traps, hydrogen can be released with the reduction of the lattice hydrogen concentration or by means of a low temperature heat treatment (100-300ºC). The release of trapped hydrogen produces a local increase of the H concentration in the metal, which may accelerate the damage process under certain conditions. In irreversible traps, hydrogen has a residence time in the trap that greatly exceeds the diffusion time.

Typical irreversible traps for hydrogen are vacancies, precipitates and non-metallic inclusions interfaces (MnS, Al_2O_3 and TiC). Austenite, due to its low diffusion coefficient, is considered an irreversible trap. Reversibility can also be defined according to the binding energies (E_b). Values of binding energies for various hydrogen traps in ferrous alloys are listed in **Table 3**. These values were either calculated or measured using permeation tests or internal friction techniques. The traps possessing a binding energy less than 60 kJ/mol are usually called reversible traps. Completely reversible or weak traps, such as dislocations and Cr and Mo solutes, possess binding energies smaller than approximately 16-20 kcal/mol. Those with E_b higher than 60-100 kJ/mol are termed irreversible or strong traps, e.g. spherical precipitates, nonmetallic inclusions, interfaces between retained austenite and martensite laths. Intermediate traps present E_b around 50 kJ/mol, e.g. austenite grain boundaries, microcavities and martensite laths interfaces. [67,68].

Table 3. Hydrogen trapping energies E_b in iron. Reference state: atomic H in a perfect lattice [3,69,70].

Trapping site	**Binding energy (kJ/mol)**
Dislocation elastic stress field	0-20,2
Screw dislocation core	20-30
Dislocation – Ferrite	26
Dislocation - Austenite	13,5
Mixed dislocation core	59
Grain boundary	18-59
Free surface	70-95
Fe-oxide interface	47
AlN interface	65
Y_2O_3 interface	70
MnS interface	72
Austenite grain boundary	75
Al_2O_3 interface	79
Fe_3C interface	84
TiC interface	87-95

In general, the interaction of hydrogen with traps is determined by the crystallographic coherence that they conserve with respect to the matrix lattice. Hydrogen is weakly trapped by defects that introduce low degree of distortion in the lattice. Studies to analyze

the effect of grain size in iron and steels on hydrogen trapping showed that the trapped hydrogen content decreased with increasing grain size [3].

There is a considerable body of evidence to show that hydrogen accumulates at dislocations, both in the core and in the stress field. Hydrogen trapping in dislocations acts in different ways, depending on the type of dislocation, its distribution, as well as the level of stresses, temperature and hydrogen concentration. Effects of the interactions between hydrogen and dislocations include reduction of the cohesive strength of the lattice, effects on the electronic structure of the dislocation core and the hydrogen shielding mechanism [71]. Dislocations are the major hydrogen trapping sites in bainitic and martensitic steels, due to the high density of these line defects in these phases. Under plastic deformation, the amount of dislocations increases, thus, there are more sites for hydrogen trapping.

The permeation of hydrogen in steel is strongly affected by the presence of precipitates and inclusions. The efficiency of the hydrogen trapping by the action of the second phase particles depends on their size, distribution, morphology and coherence, being proportional to the distortion they cause. In low alloy steels, the presence of fine cementite in ferrite alters the permeation kinetics, increasing solubility and reducing diffusivity. The diffusivity decreases with Fe_3C dispersion.

One can distinguish two situations, depending on the values of the migration enthalpy (E_m) and the trapping energy (E_b). If $E_m << E_b$, as in ferritic or martensitic steels, trapping has a strong influence on the hydrogen diffusion kinetics. If $E_m \geq E_b$, as in austenitic steels, trapping does not influence significantly the diffusion kinetics, and it does not tend to modify the permeation results in a high degree.

Trapping is responsible for deviations from Fickian diffusion behavior because this behavior is consistent with the theory of a dilute diffuser jumping among identical interstitial positions that straightforwardly leads to classical Fick's laws with Arrhenius-type diffusion coefficient. Trapping provokes an extension of the transient regime in permeation tests, eventually leading to a lower apparent diffusion coefficient. However trapping does not modify the steady state flux value.

In order to evaluate trapping effects, different experimental methods can be employed:

a) Execution of successive permeation tests at room temperature.

A first permeation run is performed, followed by a rapid degassing step and a second permeation run. When the second run initiates, the permeation happens as if the material presented no trapping sites, because they are saturated with hydrogen. If the material possesses a considerable trapping capacity, a reduction on the duration of the transient

regime in the second run will be clearly observed. The diffusion coefficient obtained from the second permeation run tend to approach the so-called lattice diffusivity.

The duration Δt of the degassing step should be brief to avoid hydrogen de-trapping, but sufficiently long to allow the desorption of the lattice (interstitial) hydrogen. If Δt is too long, the hydrogen in the lower energy traps will be released; and these non-saturated traps will affect the second run, reducing the diffusivity. On the other hand, if Δt is too short, there will not be enough time for the desorption of the lattice hydrogen. In this case, the hydrogen flux in the second run comes initially from this residual lattice hydrogen. Because of this, it is recommended to perform these sequential runs several times, varying Δt and checking its influence on the results, in order to obtain an optimal value [60].

b) Study of the diffusion coefficient evolution with the temperature.

Trapping is thermally activated. In ferritic and martensitic steels, one verifies experimentally that when T > 200-250°C, trapping does not affect diffusion, while at lower temperatures, typically T < 200°C, it leads to a longer transient regime. According to **Equation 23**, the evolution of the diffusion coefficient logarithm is linear as a function of 1/T:

$$\ln(D) = \ln(D_o) - \frac{E_L}{R}\frac{1}{T} \qquad \textbf{(Equation 28)}$$

2.6.3. Hydrogen Diffusion in Duplex Stainless Steels.

The preference of hydrogen for a given interstitial site depends on the ease offered by the lattice for the positioning of the hydrogen atom in that place. In ferrite hydrogen diffuses along tetrahedral sites, whereas in austenite hydrogen diffusion occurs preferably along octahedral sites. The radius of the largest interstitial of the bcc structure, which is tetrahedral, is approximately equal to the smallest interstice of the fcc structure. Therefore, hydrogen solubility in austenite is higher than in ferrite. On the other hand, the distance between the interstitial sites in the bcc structure is smaller than in the fcc structure, resulting in a lower energy barrier for the hydrogen diffusion in the bcc lattice than in the fcc structure. The calculated dissolution energy of hydrogen in tetrahedral sites in ferrite is smaller than in octahedral interstices, while for austenite, the dissolution energy is smaller at octahedral sites [72]. According to **Table 4**, the hydrogen solubility at room temperature in austenite is 2500 times greater than in ferrite, but the diffusion coefficient is about 10^6 times smaller. It is expected, therefore, that ferrite transports hydrogen and that it is trapped in austenite.

Table 4. Hydrogen solubility and diffusivity in ferrite and austenite at 293K [73].

	Solubility (atoms H/Fe)	**Diffusivity (m^2/s)**
Ferrite	$2{,}8.10^{-8}$	approx. 10^{-10}
Austenite	$7{,}0.10^{-5}$	approx. 10^{-16}

In austenitic-ferritic steels, diffusion in the austenitic phase can be considered as having an insignificant influence on the effective or apparent diffusion coefficient if the austenite volumetric fraction is in the range of 15% to 44%. However, diffusion in these steels is slower than in ferritic steels: the hydrogen diffusivity in a fully ferritic steel is about 400 times greater than in a microstructure containing 44% austenite. This behavior is caused by the increase in the distance to be covered by the hydrogen in the ferrite due to the presence of austenite grains (tortuosity) and the occurrence of trapping in the austenitic phase and in α/γ phase boundaries [25,73]

The effective or apparent diffusivity D_{eff} of a duplex steel can be given in a simplistic way by the inverse rule of mixtures, according to **Equation 29** [25]:

$$\frac{1}{D_{eff}} = \frac{1-f_\gamma}{D_\alpha} + \frac{f_\gamma}{D_\gamma} \qquad \textbf{(Equation 29)}$$

being:

- D_α, D_γ: hydrogen diffusivity in ferrite and austenite respectively.
- f_γ: austenite volumetric fraction.

The following equation relates, considering only reversible and saturable traps, the interstitial diffusion coefficient D_L with the effective or apparent coefficient D_{eff}, the value usually measured in permeation tests [66]:

$$D_{eff} = \frac{\omega D_L}{1+\sum_{r=1}^{n}\left(\frac{N_r k_r}{p_r}\right)} \qquad \textbf{(Equation 30)}$$

where

- ω: tortuosity factor.
- N_r: density of traps “r”.
- k_r: rate of hydrogen capture by traps “r” (or the probability of a trap to capture a hydrogen atom).
- p_r: rate of hydrogen release from the traps “r” (or probability of a trap to release a hydrogen atom).

The value of ω depends on the shape, orientation and volume fraction of the embedded phase (austenite). Considering austenitic phase (volume fraction of 44%) as

rods oriented parallel to direction of hydrogen flux, the value of ω was estimated between 0,47 and 0,56. For rods oriented perpendicular to the hydrogen flux direction, values between 0,25 and 0,27 were calculated [73].

Table 5 shows the hydrogen diffusivity values for super duplex stainless steels under different conditions.

Table 5. Hydrogen diffusion coefficients of super duplex stainless steels [74-76]

Steel	H diffusion coefficient (m^2/s)	H-charging conditions	Temperature (ºC)	Austenite percentage
SAF2507 (lattice diffusion)	$1,1.10^{-15}$	1mA/cm² in 0,1M NaOH	22	49
SAF2507	$6,5.10^{-15}$	1mA/cm² in 0,1M NaOH	25	44,4
SAF2507 (lattice diffusion)	$4,5\text{-}5,2.10^{-15}$	1mA/cm² in 0,1M NaOH	50	49
SAF2507 (lattice diffusion)	$1,8\text{-}2,5.10^{-14}$	1mA/cm² in 0,1M NaOH	80	49
SAF2507 (with trapping effects)	$4,6.10^{-16}$	1mA/cm² in 0,1M NaOH	22	49
SAF2507	$9,5.10^{-11}$	20 bar H_2	350	52
SAF2507	$2,4.10^{-10}$	20 bar H_2	400	52
SAF2507	$6,1.10^{-10}$	20 bar H_2	450	52
SAF2507	$2,6.10^{-9}$	20 bar H_2	500	52
UNS S32760	$1,6\text{-}4,9.10^{-12}$ (desorption)	$-1V_{Ag/AgCl}$	150	40-49
UNS S32760	$0,1\text{-}1,0.10^{-14}$	$-1V_{Ag/AgCl}$	4	40-49
H25N5M (thickness 0,148mm)	$1,8.10^{-12}$	10mA/cm² in 0,1M NaOH	25	40
H25N5M (1,0mm)	$1,0.10^{-13}$	10mA/cm² in 0,1M NaOH	25	40

Apparent hydrogen diffusivity values in different duplex stainless steels as function of temperature are shown in **Figure 14**. Decrease of the austenite fraction promotes the increase of the diffusion coefficient by approximately three orders of magnitude. Usually

one observes experimentally the line presents a discontinuity around 200°C. This discontinuity evidences more important trapping when T<200-250°C, and that the diffusion coefficients obtained at lower temperatures are lower than predicted by extrapolation of the higher temperature results. As temperature increases, the effect of trapping on apparent diffusivity decreases [25].

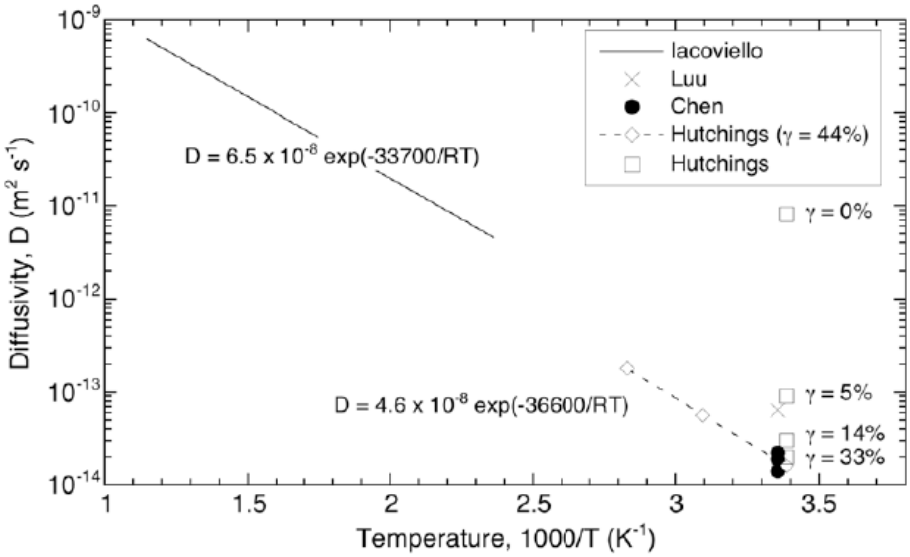

Figure 14. Hydrogen diffusion coefficients in duplex stainless steels at different temperatures. Iacoviello, Luu and Chen: 2205 grade. Hutchins: Uranus 50 grade [25].

2.6.4. Hydrogen Diffusion Modelling

Hydrogen diffusion in steels cannot be described correctly in terms of a Fourier's-type equation (**Equation 25**) due to effects of traps, diffusion obstacles, stresses, non-uniform (position-dependent) solubilities and transport by dislocations. Models which have been proposed to replace this equation can be divided into different classes [77]:

a) Models for diffusion with trapping, as those developed by McNabb-Foster and Oriani.

b) Non-uniform solubility model, in which Fourier's equation is replaced by [78]:

$$\partial C/\partial t = \nabla \cdot (DS\nabla(C/S)) \qquad \textbf{(Equation 31)}$$

being "S" the hydrogen solubility.

c) Models that consider hydrogen transport by dislocations.

A robust model for the description of hydrogen permeation in a steel membrane should take into account different aspects:

- If important, superficial features must be considered, as adsorption kinetics and the effects of metal coating and surface oxides. Surface phenomena may also occur in inner (bulk) interfaces. Additionally, if relevant, diffusion along grain/phase boundaries should

be included. Surface oxides and grain boundary diffusion tend to be more relevant in the austenitic phase.

- Regarding the effects of trapping, McNabb and Foster, Oriani, Caskey, Iino and Leblond models were introduced [54,68,77,79]. Irreversible traps are considered in detail by the models of Iino and Leblond. Saturable traps are in general assumed by equilibrium models, as McNabb-Foster and Oriani. The model of Leblond on the other hand considers non-saturable traps as the general case, being saturable sites non-linearities. Only Leblond considers obstacles effects quantitatively.
For the quantification of effects of traps, the trapping sites must be characterized. One should define if each site is saturable or non-saturable; reversible or irreversible; an obstacle or not. Diffusion obstacles are sites surrounded by very high potential barriers, through which diffusion does not occur or is very improbable. Concerning duplex stainless steels, ferrite is saturable and reversible, austenite is saturable and, at low temperature (<200°C) and shorter time periods, it is an irreversible trap. The α-γ boundaries can be assumed as non-saturable and reversible. Boundaries between other phases may behave differently in terms of saturability. Austenite is not a diffusion obstacle, but some inclusions and/or intermetallic precipitates (like carbonitrides) may behave as (quasi-)obstacles.

- Parameters as diffusivity, equilibrium hydrogen concentration in the sites (and saturation concentration), density of interstitial sites and traps should be known. In the case of heterogeneous systems, besides the microstructure, these parameters may depend on profiles of temperature, chemical composition and stresses, i.e. they depend on the position along the metal.
Because of the multiplicity of diffusion and trapping characteristics involved in models, the simultaneous derivation of the parameters from fittings of experiments is difficult. In addition, this approach can produce inconsistent or inconclusive results because of lack of solution uniqueness proofs. Consequently, such procedures require validation processes combining a sensitivity assessment, complementary tests and their simulations using an obtained set of candidate parameter values [80,81].
A further aspect that introduces much more complexity occurs in systems submitted to temporal variations, for instance, during a non-monotonic mechanical loading or under raising plastic deformation. In these cases, hydrogen transportation by dislocations may be also included.

3. Material and Experimental Methods

3.1. Material

All material used was obtained from ANSI/API 6A, $2^{1}/_{6}$ in. inner diameter weld-neck flanges (work pressure 5000 psi) made of grade UNS S32750. **Figure 15** presents aspect of two flanges welded together. The welding joints are not evaluated in the present project. **Figure 16** indicates the flange design dimensions in inches. The flanges were donated by FMC Technologies in 2014. H. Van Triel GmbH Co (from IPP group) performed the forging manufacturing process.

The flanges should follow the specifications of standard ASTM A182 (Standard Specification for Forged or Rolled Alloy and Stainless Steel Pipe Flanges, Forged Fittings, and Valves and Parts for High-Temperature Service, 2014) grade F53. Specified minimum tensile properties according to this standard, considering maximum section thickness > 2 inches, are UTS 730 MPa, YS 515 MPa and 15% elongation.

According to the supplier, the flanges were manufactured by hot forging. The forging start temperature was kept at 1230ºC and the end temperature above 1000ºC. The material was then solution annealed at 1100ºC and water quenched.

Figure 15. Aspect of a flange used in the project.

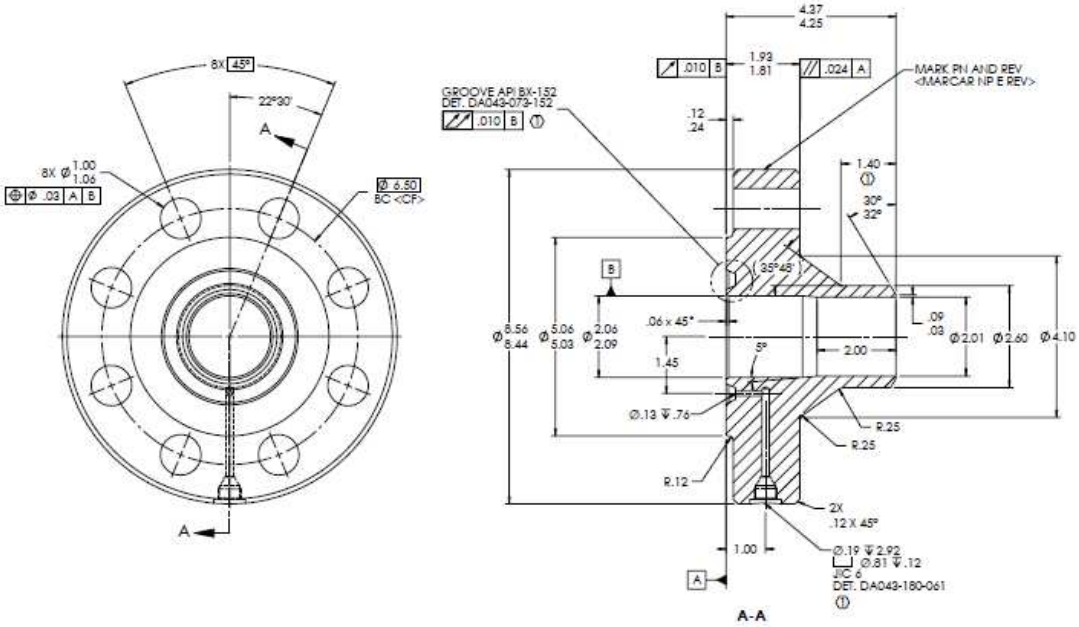

Figure 16. Drawing of the flanges used. Dimensions in inches.

The chemical compositions obtained by atomic absorption (elements C, Cr, Mo, Ni, V, Ti, W and N) and optical emission spectroscopy (the other elements) in the flange body of three flanges and in a neck flange are indicated in **Table 6**. The specimens were obtained from these two flange regions, indicated schematically in **Figure 17**. Because these flange regions go through different reduction ratios during the forging process, they tend to possess slightly different properties. PRE values were calculated following **Equation 2** (PRE= %Cr + 3,3(%Mo + 0,5%W) + 16(%N)). Body and neck presented mostly similar chemical compositions. The neck presented a slightly higher Si content. Si is tends to enhance sigma formation [4].

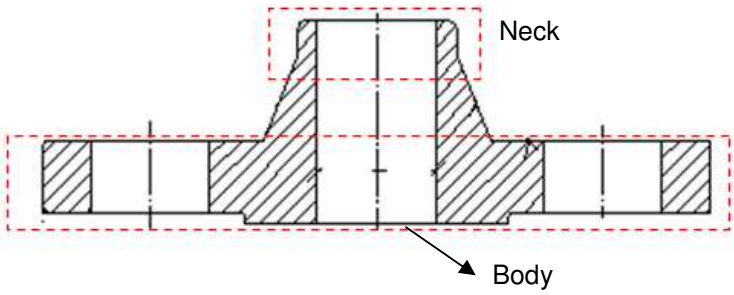

Figure 17. Flange regions.

Table 6. Chemical composition of the tested material (%wt).

	Body 1	**Body 2**	**Body 3**	**Neck 3**	**Specification ASTM A182-14 grade F53**
C	0,027	0,027	0,027	0,027	max. 0,030
Si	0,477	0,4865	0,478	0,531	max. 0,80
Mn	1,0095	1,0215	1,011	1,03	max. 1,20
P	0,01	0,012	0,01	0,01	max. 0,035
S	0	0	0	0	max. 0,020
Cu	0,21	0,2125	0,215	0,22	max. 0,50
Al	0,001	0,002	0,018	0,009	-
Cr	25,7	25,8	25,9	25,9	24,0-26,0
Mo	4,36	3,80	3,94	4,02	3,0-5,0
Ni	7,7	7,8	7,8	7,8	6,0-8,0
V	0,079	0,082	0,082	0,08	-
Ti	0,008	0,0085	0,009	0,009	-
Nb	0,0695	0,0735	0,071	0,076	-
Co	0,0705	0,073	0,073	0,075	-
W	0,07	0,06	0,07	0,07	-
N	0,2	0,2	0,2	0,2	0,24-0,32
Fe	Balance	Balance	Balance	Balance	-
PRE(w)	43,40	41,64	42,22	42,48	

3.1.1. Thermodynamic Simulations

Thermodynamic calculations were performed using the software Thermocalc and the database TCFE6 to estimate the thermodynamically expected phases from 25 to 2000ºC. The adopted chemical composition used in the simulations was of the “body 1” from **Table 6**: Fe + 0,027 wt%C, 0,477%Si, 1,010%Mn, 25,7%Cr, 4,36%Mo and 7,70%Ni.

The principle of equilibrium calculations is to find the minimum of the Gibbs energy at different values of temperature, pressure, and amounts of components (chemical elements) in the considered system. For these calculations, an analytical expression of the molar Gibbs energy for each phase as a function of temperature, pressure and the mole fractions of the components in each phase are necessary. The procedures for minimizing the expressions of Gibbs free energy and the routines to obtain the parameters of the models from experimental data are described elsewhere [82].

3.1.2. Microstructural Evaluation

3.1.2.1. Optical and Scanning Electron Microscopy

The microstructure of the flanges was analyzed by optical and scanning electron microscopy in three positions or orientations: normal to the longitudinal direction, to the circumferential direction and to the radial direction. These positions are defined schematically in **Figure 18**. Energy dispersive spectroscopy (EDS) analyses were also performed.

Sections close to the flange surface were mounted and prepared according to standard ASTM E3 (Standard Guide for Preparation of Metallographic Specimens, 2017), including proper mechanical polishing. The samples were electrochemically etched following two procedures:

- Aqueous solution of 10 wt % oxalic acid under a potential of 5V, for around 10 seconds. This etching procedure is used to reveal clearly austenite/ferrite boundaries and detect nitride precipitates.
- Aqueous solution of 10 wt % KOH under a potential of 3V for 10-20 seconds. This procedure allows a better contrast between ferrite and austenite and the detection of intermetallic phases.

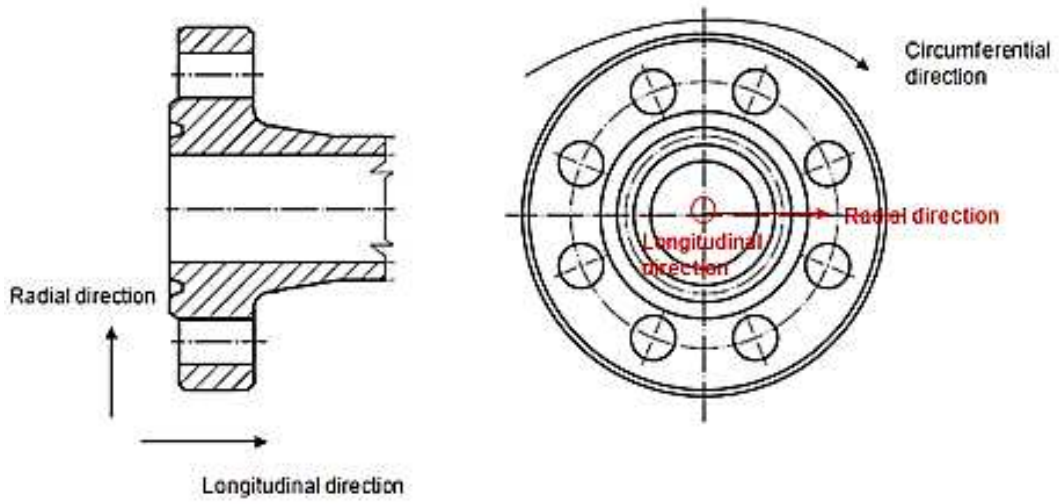

Figure 18. Positions of microstructural evaluation of the flanges.

The austenite grain sizes and the interaustenitic spacings were measured from the micrographs using the line intercept method, as described on DNV-RP-F112. For the inter-austenitic spacing measurements, clusters composed by small austenite grains between larger austenite islands were disregarded, as recommended by DNV-RP-F112.

3.1.2.2. Transmission Electron Microscopy

TEM and electron diffraction are used to characterize the phases. The TEM studies were performed using the FEI Titan G2 80-200 microscope at an acceleration potential of 200 kV. Cylinders with 3 mm diameter were machined in the longitudinal direction of the flange body and neck. Specimens were cut in slices of around 0,2-0,5 mm thickness, then mechanically thinned and polished. Final thinning to thickness values between 70-90 µm and polishing were performed in the jet electropolishing equipment TENUPOL-3 (Struers). Sample preparation conditions involved solution of 90 v% acetic acid + 10% perchloric acid, potential of 20,5V and current of 53-58 mA for 96-127 s at 4,5-17,5ºC. Chemical micro-analysis of selected areas was performed by X-ray diffraction using the EDS mapping system Bruker ChemSTEM coupled to the TEM.

3.1.3. X-Ray Diffraction

X-ray diffraction (XRD) measurements were performed in order to identify and quantify the phases present in the material. The specimens were submitted to synchrotron x-ray at the XRD1 beamline of the Brazilian Synchrotron Light Laboratory (LNLS, Campinas, Brazil). A specimen positioned for measurement is shown in **Figure 19**.

All tests were done at room temperature under vacuum (10^{-1} Pa), using beam energy of 12 keV (λ = 1,033 Å). This beam energy implies a penetration depth of the synchrotron radiation less than 20 µm. Only information on the sample surface was therefore obtained. The diffraction data were recorded at 2θ = 20°-120º. The continuous scan was performed using a step of $\Delta 2\theta = 0{,}0078°$.

Five specimens were prepared from the flange body. **Figure 20** indicates the geometry of the specimens. The measurement region was the center of the 3-mm wide of the specimen gauge area. The surface of the specimens was polished up to 1 µm diamond suspension.

One of the five specimens tested was previously hydrogen-charged electrochemically for 7 days at room temperature in a 0,1M H_2SO_4 solution, under a cathodic current density of 20 mA/cm². After charging, the specimen was stored cryogenically until the test.

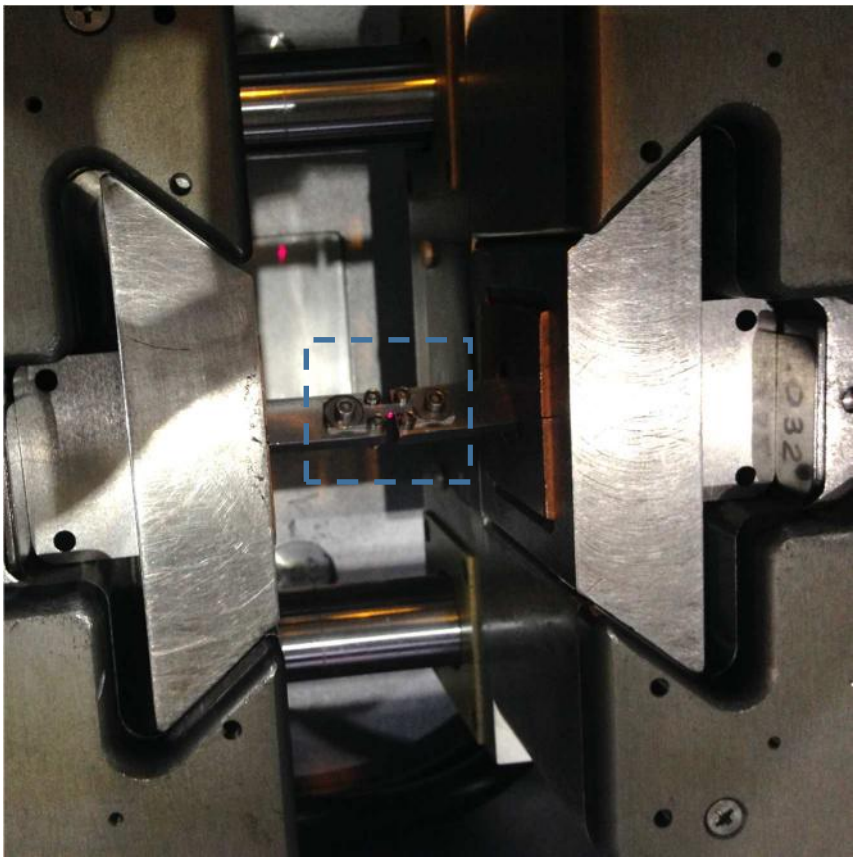

Figure 19 Aspect of specimen placed in the holder.

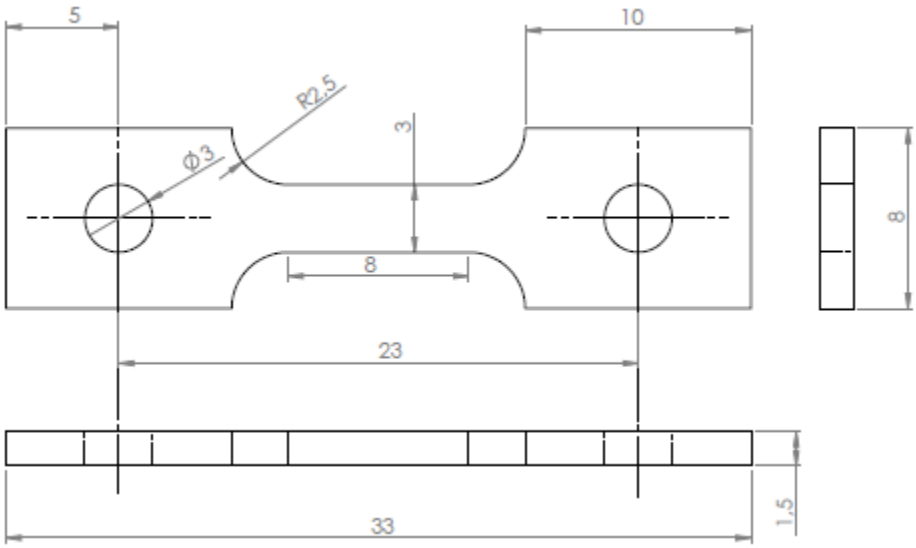

Figure 20. Dimensions of the specimens used on the XRD measurements.

The quantitative estimation of phases is based on the principle that the total integrated intensity of all diffraction peaks for each phase in an alloy is proportional to the volume fraction of that phase. If the grains of each phase are randomly oriented, considering the presence of only austenite and ferrite, i.e. $x_\gamma + x_\alpha = 1$, the volume fractions (x_i) of each

phase i = α, γ are estimated from the integrated intensities (I_i) for numerous peaks "j" and the theoretical intensities R_i, according to the direct comparison method, by [83]:

$$x_i = \frac{\left(\frac{1}{n}\right)\sum_{j=1}^{n}\left(I_i^j/R_i^j\right)}{\left(\frac{1}{n}\right)\sum_{j=1}^{n}\left(I_\gamma^j/R_\gamma^j\right)+\left(\frac{1}{n}\right)\sum_{j=1}^{n}\left(I_\alpha^j/R_\alpha^j\right)} \quad \textbf{(Equation 32)}$$

where "n" is the number of peaks examined.

The theoretical intensities are calculated by:

$$R_i = \left(\frac{1}{v^2}\right)F^2 p(LP)\exp(-2M) \quad \textbf{(Equation 33)}$$

where

- F: structure factor for reflecting plane (hkl)
- p: plane multiplicity factor.
- v: unit cell volume.

The Lorentz polarization factor is equal to:

$$LP = 1/[4(\sin^2\theta.\cos\theta)] \quad \textbf{(Equation 34)}$$

The temperature factor "exp(-2M)" is not considered because all tests were performed at room temperature. A pseudo-Voigt function was used for X-ray diffraction profile fitting.

3.2. Experimental Methods

Several experimental methodologies can be used to characterize the solubility, location, state, and diffusion of hydrogen in metals and alloys, as well as the interaction with their microstructure and effects on mechanical properties. General information about the techniques applied and the procedures adopted on the present project is given below.

3.2.1. Permeation Tests

Hydrogen permeation tests aim to obtain parameters that describe hydrogen solubility, diffusion, and trapping in metallic membranes. In the gas-volumetric method, gaseous hydrogen is used, while in the electrochemical procedure, hydrogen charging and extraction occurs through electrochemical reactions.

The electrochemical permeation method was developed by Devanathan and Stachurski [84]. Standards such as BS EN ISO 17081 (Method of measurement of hydrogen permeation and determination of hydrogen uptake and transport in metals by an electrochemical technique, 2008) and ASTM G148 (Standard Practice for Evaluation of Hydrogen Uptake, Permeation, and Transport in Metals by an Electrochemical Technique, 2011) describe this method. The electrochemical method comprises a simpler procedure and presents higher flexibility with regard to experimental conditions.

Their main disadvantages are the poor reproducibility, related usually to surface effects, and the temperature limitation (typically below 90ºC) [85]. The metal membrane subjected to hydrogen permeation acts as a bipolar electrode, separating the electrolytes from two compartments isolated of a double electrochemical cell. In the cathodic (charging) semi-cell, hydrogen is generated and absorbed which, after permeating the membrane, is extracted on the anodic (or detection) semi-cell. In the detection semi-cell, a mildly anodic potential is applied, so that all hydrogen arriving on this surface is oxidized.

The electrochemical permeation cell is shown schematically in **Figure 21**.

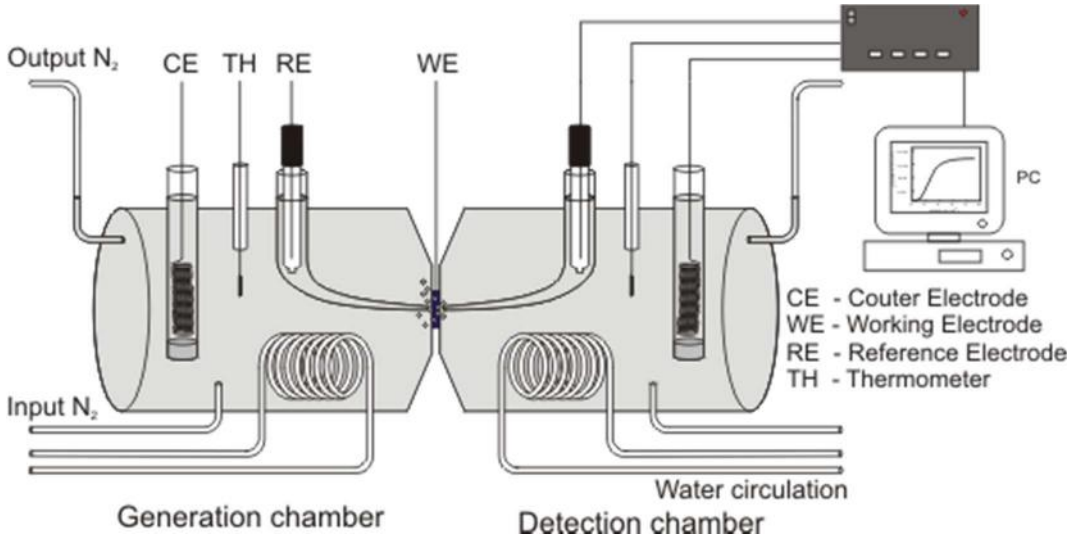

Figure 21. Schematic of the Devanathan and Stachurski electrochemical permeation cell [86].

Figure 22 shows a schematic of the electrochemical permeation cell with the hydrogen reactions involved.

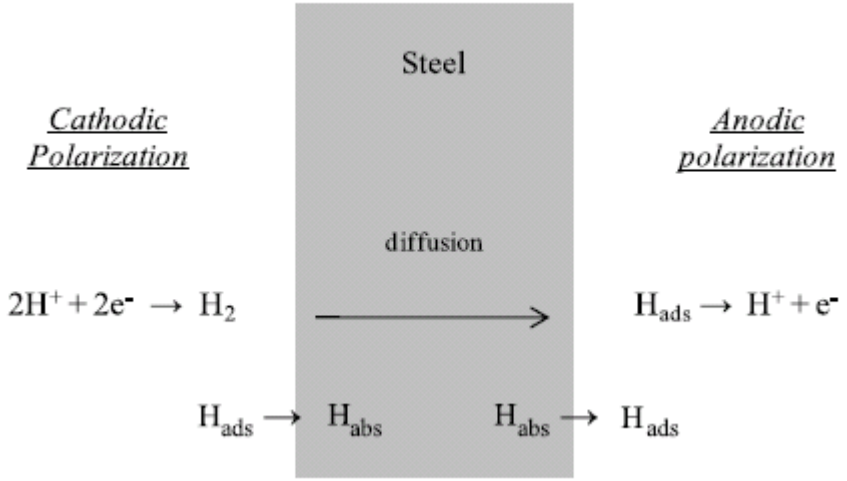

Figure 22. Schematic of the electrochemical permeation cell [87].

The subsurface hydrogen concentration is defined by many factors, such as the pH of the electrolyte, the presence of hydrogen recombination poisons, surface conditions, current, potential, temperature, etc. Surface impedance can be reduced by the deposition a thin layer of palladium on each surface of the permeation membrane. The palladium layer is an efficient catalyst for the decomposition of the hydrogen molecule. The specimen thickness is selected usually to ensure that the measured flux reflects volume (bulk) controlled hydrogen atom transport. Thin specimens may be used for evaluation of the effect of surface processes on hydrogen entry or exit (absorption kinetics or transport in oxide films) [66].

The permeation method is based on the instantaneous measurement of hydrogen flux leaving the surface of the membrane in the detection semi-cell, which is proportional to the oxidation current read by the potentiostat. The measured anodic current density (i) provides a direct measure of the hydrogen flux by the following expression:

$$i = F.J_L \qquad \textbf{(Equation 35)}$$

where:

- J_L: hydrogen mass flux (mol/m²s).
- F: Faraday constant (96485 As/mol).

Figure 23 presents schematically the hydrogen concentration profiles during permeation (a) and the transient permeation flux or rate (b). The concentration of hydrogen in the membrane increases over time, producing a corresponding increase in the permeation current density measured at the exit or outer surface.

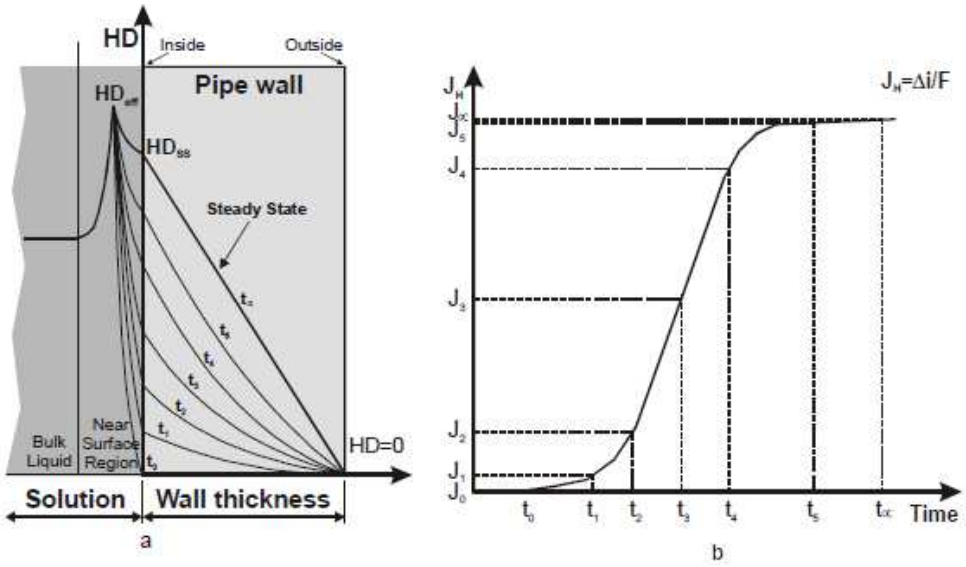

Figure 23. Schematic of the hydrogen permeation profile in a membrane. HD: hydrogen concentration, JH: hydrogen flux through the membrane [88].

The information obtained in the transient and steady states of the permeation tests, shown in **Figure 24**, describes the hydrogen transport and solubility in the metal. At steady state, the hydrogen flux measurements allow to obtain the diffusivity and solubility. The permeation time in the transient regime provides, in addition to the diffusivity in the network, also parameters of hydrogen trapping.

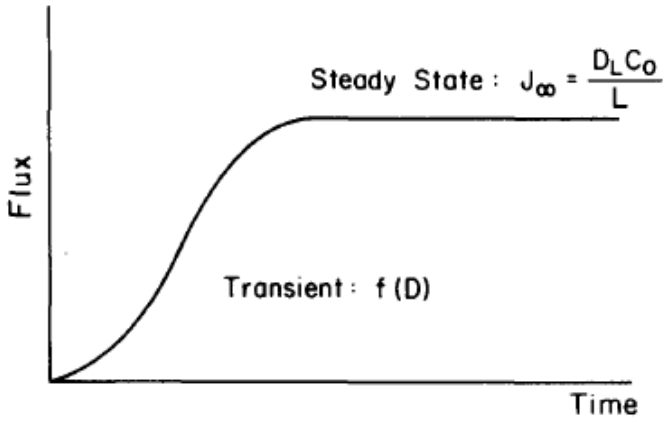

Figure 24. Schematic representation of the permeation curve [66].

The versatility of electrochemical techniques is based on the numerous possibilities of varying experimentally the boundary conditions at both the entrance and the detection sides of the sample [85]. Depending on the way polarization is performed, i.e. the initial and boundary conditions, the electrochemical permeation test results in different responses. The most commonly used modes are galvanostatic-potentiostatic and double-potentiostatic procedures. In both modes, an anodic potential is applied in the detection semi-cell.

The galvanostatic-potentiostatic mode consists in applying a constant cathodic current in the generation semi-cell, maintaining a constant hydrogen flux on the cathode surface during the test. The initial and boundary conditions are $C(x,0) = 0$; $J(0,t) = J_o$; $C(L,t)\big|_{t>0}$ = constant. The solution of the Fick's second law for these conditions is given by **Equation 36**:

$$\frac{J_L}{J_o} = 1 + \frac{4}{\pi}\sum_{n=1}^{\infty}\frac{(-1)^n}{2n-1}\exp\left(\frac{-(2n-1)^2.\pi^2.D_{ap}t}{4L^2}\right) \qquad \textbf{(Equation 36)}$$

being:

- J_L: permeation rate or hydrogen mass flux measured at the exit surface (thickness L) on time t (mol/m²s)
- L: membrane thickness (m).
- D_{app}: hydrogen apparent diffusivity (m²/s).

In the double potentiostatic configuration, a constant cathodic potential is applied in the generation semi-cell. The boundary and initial conditions are: $C(x,0) = 0$, $C(0,t) = C_o$, $C(L,t)\big|_{t>0}$ = constant. The solution of the Fick's second law is described by **Equation 37**:

$$\frac{J_L}{J_o} = 1 + 2\sum_{n=1}^{\infty}(-1)^n.\exp\left(\frac{-n^2.\pi^2.D_{app}t}{4L}\right) \qquad \textbf{(Equation 37)}$$

In the steady state, the current density is given by:

$$i_\infty = \frac{F.D_{app}.C_o}{L} \qquad \textbf{(Equation 38)}$$

where:

- D_{app}: hydrogen apparent or effective diffusivity (m^2/s).
- C_o: steady-state subsurface hydrogen concentration (mol/m^3).
- L: membrane thickness (m).
- F: Faraday constant (96485 As/mol).

Through **Equations 35** and **38**, the following expression can be obtained for the effective or apparent diffusion coefficient:

$$D_{ap} = \frac{J_\infty.L}{C_o} \qquad \textbf{(Equation 39)}$$

with J_∞ being the steady-state hydrogen flux.

The diffusivity can also be obtained through permeation transient data. The time-lag method makes use of the integration of the permeation or desorption (decay) curves on time. The integration of the flux values over time provides the total amount of hydrogen that passes through the sample at each instant. The tangent at the steady state to the curve of cumulated flux (or total amount of hydrogen) vs time crosses the time axis in the so-called time-lag "t_L" (**Figure 25**). The time at $J/J_\infty = 0{,}629$ corresponds to the time-lag.

Under constant concentration on the entry side (double potentiostatic procedure), the apparent diffusion coefficient can be then calculated using **Equation 40**.

$$D = \frac{L^2}{6.t_{lag}} \qquad \textbf{(Equation 40)}$$

At t_{lag}, the diffusivity in the galvanostatic mode, is calculated by:

$$D = \frac{L^2}{2.t_{lag}} \qquad \textbf{(Equation 41)}$$

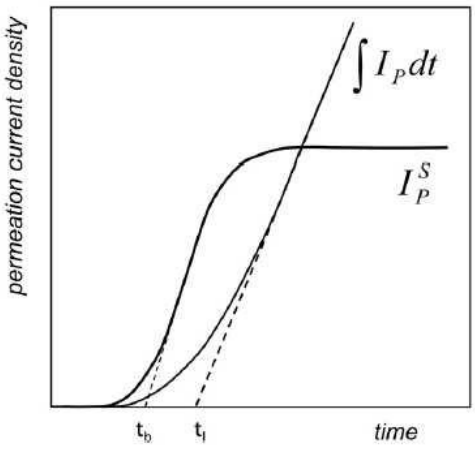

Figure 25. Determination of time-lag from the measurement of the permeation current density. "t_b" is the breakthrough time [89].

Gaseous and electrochemical permeation tests were performed using membranes obtained from the body and neck of a flange. It is aimed with these tests to characterize the hydrogen kinetics transportation through the chosen material by measuring the hydrogen solubility and diffusion coefficients.

The position in the flange of the samples used in the permeation tests is presented in **Figure 26**. The samples were prepared in a way that the permeation path follows the radial orientation in the component. This is the most probable direction the hydrogen coming from the environment is expected to follow. **Figure 27** shows the microstructure of sections of membranes obtained from the flange body and neck. These micrographs were obtained by optical microscopy after metallographic preparation and etching with 10 wt % KOH solution under a potential of 3V for 10s.

The permeation membranes were electrical discharge cut from the flange and machined to the final dimensions of 20 mm diameter and two goal thickness values: 0,2 and 0,5 mm. The membranes surfaces were submitted to grinding and polishing to a final step with 1µm diamond paste. One of the surfaces was covered with a 50-to-80 nm thick palladium layer. Physical vapour deposition (PVD) was used for the palladium layer deposition. The procedure was performed at pressure of 2,0 mTorr, using power of 40 W_{DC} for ca. 20 min.

Figure 26. Position of the permeation membranes in the flange body (left) and neck (right).

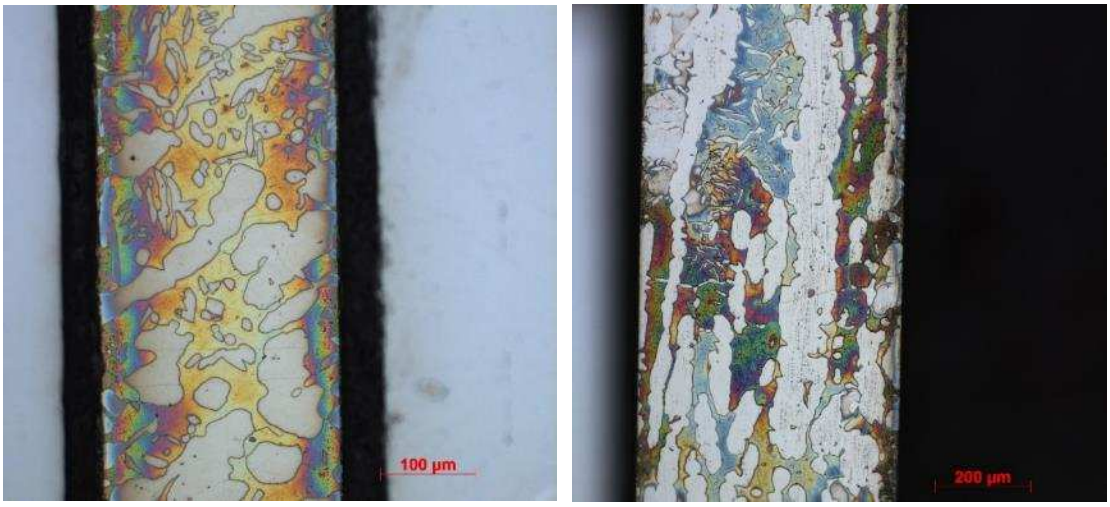

Figure 27. Microstructures of section of body (left) and neck (right) membrane used for permeation tests.

3.2.1.1. Hydrogen Gas Permeation Tests.

The gas-volumetric permeation tests were performed at CEA/Grenoble. On the tests performed in 2014, gas deuterium grade N30 was used, with maximum impurities of 10 ppm D_2O, 10 ppm O_2 and 25 ppm N_2. In 2015, a higher purity D_2 was used, with maximum impurity contents of 1,2 ppm H_2O, 0,2 ppm O_2 and 0,2 ppm N_2 (all values in ppm-mol). Deuterium was used because it is more easily detectable by the mass spectrometer, used to measure the permeation flux, and to mitigate spurious measurements from residual hydrogen present in the material or the stainless steel tubes of the permeation device before the tests or from contamination with air coming from the environment.

The measurement of the permeated gas was performed with a helium leak detector (Adixen ASM 142 D) or two different Pfeiffer Hi Cube mass spectrometers (indicated as

"old" - 2014 and "new" - 2015). The tests were performed at 80, 150, 200 and 280°C. **Figure 28** shows the sample assembled inside the test furnace. The tests should be performed below 300°C in order to avoid the lowest temperature transformation, which is formation of α_{Cr}' by spinodal decomposition of ferrite (occurring between 300 and 525°C).

Figure 28. Test furnace.

When using the helium detector, the response signals are obtained directly as volumetric flow rate "Q" in mbar.L.s^{-1}. The conversion of these results to Nm^3.s^{-1} may be done by the following expression:

$$Q(Nm^3.s^{-1}) = \frac{Q(mbar.L.s^{-1}).10^{-6}}{1{,}013}$$ **(Equation 42** – Helium detector**)**

The mass spectrometers enable the determination of the partial pressures of different species, improving thereby the results accuracy. As a disadvantage, previous calibration procedures are necessary. The mass spectrometer detector measures electric current intensities correspondent to each species, and these values are then converted to partial pressures through an algorithm that takes into account different factors: fragmentation, ionization, detection and transmission factors. It was measured the partial pressures of H_2O, D_2O, D_2, H_2, N_2, O_2, Ar, CO_2, HD and HDO, but only the partial pressure values of gas deuterium P_{D2} (mbar) were initially considered for the analyses and calculations. The conversion of these values to volumetric flow rate in mbar.L.s^{-1} was performed dividing them by 0,016 for the "old" mass spectrometer and by 0,002941 for the "new" mass spectrometer (**Equations 43** and **44**). These conversion factors were experimentally

obtained by the spectrometer manufacturer. The conversion of "Q" to $Nm^3.s^{-1}$ can be done through **Equation 42**.

$$Q(\mathrm{mbar.L.s^{-1}}) = \frac{P_{D_2}(\mathrm{mbar})}{0{,}016} \qquad \textbf{(Equation 43} – \text{"Old" mass spectrometer)}$$

$$Q(\mathrm{mbar.L.s^{-1}}) = \frac{P_{D_2}(\mathrm{mbar})}{0{,}002941} \qquad \textbf{(Equation 44} – \text{"New" mass spectrometer)}$$

The permeation flux "J" is the flow rate divided by the permeation area "A" of the tested membrane. In all cases, the average diameter was equal to 15,29 mm, i.e., $A = 1{,}836.10^{-4}$ mm^2. This corresponds to the actual area exposed to the permeation gas.

$$J(\mathrm{Nm^3.m^{-2}.s^{-1}}) = \frac{Q(\mathrm{Nm^3.s^{-1}})}{A(\mathrm{m^2})} \qquad \textbf{(Equation 45)}$$

The permeability coefficient P_e can be calculated using the following expression:

$$P_e(\mathrm{Nm^3 m.m^{-2}s^{-1}atm^{-0,5}}) = \frac{J.e}{\sqrt{P}} \qquad \textbf{(Equation 46)}$$

where:

- J: permeation flux ($Nm^3.m^{-2}.s^{-1}$)
- e: sample thickness (m)
- P: absolute pressure (atm)

The maximum (or effective initial) concentration on the upstream surface or solubility S_H is determined from the steady state permeation rate or flux and the diffusivity:

$$S_H(\mathrm{Nm^3 D_2/m^3}) = \frac{P_{e\infty}\sqrt{P}}{D} = \frac{J_\infty.e}{D} \qquad \textbf{(Equation 47)}$$

where:

- $P_{e\infty}$: steady state permeability coefficient.
- J_∞: steady state flux.
- D: apparent diffusion coefficient, calculated presently by the time-lag method.
- P: test pressure.

3.2.1.2. Electrochemical Hydrogen Permeation Tests.

The electrochemical hydrohen permeation tests were performed at UFRJ. General arrangement of the testing cell is presented in **Figure 29**. The tests were performed at room temperature. The test diameter was 7,5 mm.

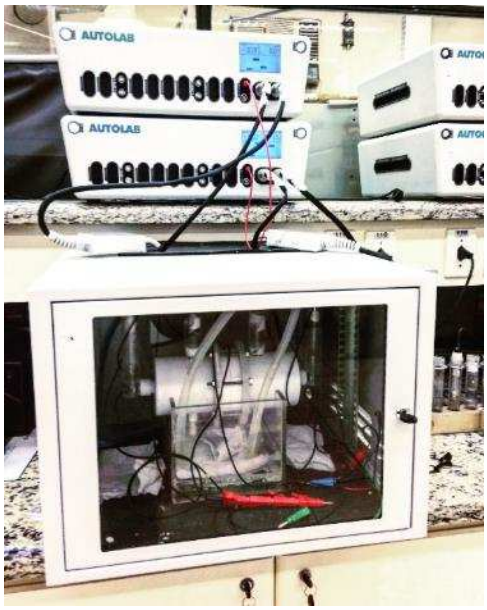

Figure 29. Electrochemical permeation test equipments.

The galvanostatic-potentiostatic technique was used. The charging semi-cell was filled with a 0,1 M H_2SO_4 + 2 mg/l As_2O_3 solution. The detection compartment was filled with a 0,1M NaOH solution. Before the permeation begins, the system is submitted to a waiting time until stabilization at the open circuit potential. Once the system is stabilized, the cathodic current is switched on the charging semi-cell, the open circuit potential is applied on the detection side, and the permeation current is recorded. A constant cathodic current equal to 0,6627 mA (current density of 1,5 mA/cm²) was applied for the generation of hydrogen which was reduced on the surface of galvanostatic side of the membrane. The open circuit potential (184-193 mV_{SCE}) was applied with the objective of maintaining a null concentration of hydrogen on the potentiostatic side. When the permeation current reaches the steady state, the cathodic current is switched off on the charging semi-cell, and the current decay with time continued to be recorded.

The charging current was selected after a cathodic potentiodynamic polarization test. This test was performed at room temperature in a 0,1 M H_2SO_4 solution using a sample removed from the flange body. The sample area was 0,51 cm². The polarization started 1h after the sample immersion in the solution. From the open circuit potential, a descending potential scan was performed at a continuous rate of 0,17 mV/s up to -2000 mV_{SCE}.

Figure 30 presents the result of the polarization test. According to this measurement,

the saturation density current verified was 28,67 mA/cm². The region of hydrogen reduction was in the range of density currents between ca. 0,1-4,0 mA/cm² (-1,04 to -1,4 V_{SCE}). The adopted current density of 1,5 mA/cm² is therefore a suitable value for hydrogen charging.

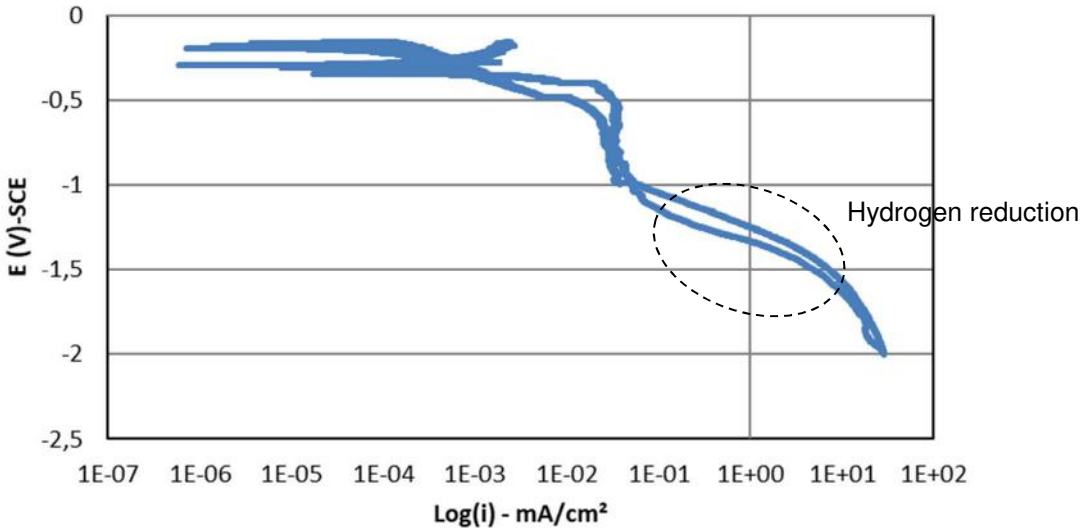

Figure 30. Cathodic potentiodynamic polarization curve.

3.2.2. Mechanical Tests

The effects of hydrogen on the mechanical properties of steels can be ascertained by performing mechanical tests using hydrogen-charged specimens and measuring the results in comparison to non-hydrogenated material. Several parameters are involved in these tests, such as hydrogen charging procedures and loading features. The mechanical properties most commonly used to quantify hydrogen embrittlement are tensile, fracture mechanics and fatigue properties.

Mechanical tests for evaluation of hydrogen susceptibility of metals and alloys can be classified in different manners:

- According to hydrogen charging conditions: (i) tests with hydrogen charging simultaneous to the mechanical loading application (“in-situ tests”) and (ii) tests in air after previous charging (“ex-situ tests”).
- According to the loading arrangement: (i) constant load tests, (ii) tests under controlled strain rate, including ripple load or step loading tests, (iii) fracture mechanics tests and (iv) indentation tests.

In general, tests in air after hydrogen charging are not suitable for ferritic steels, since the hydrogen desorption in these materials is rapid compared to the test duration, so that

a significant amount of the hydrogen can be released before or during the test. For austenitic stainless steels, tests with simultaneous hydrogen charging are in many cases not relevant, due to the low hydrogen diffusion rate in these materials. A proposed recommendation is that materials with hydrogen diffusivity greater than 10^{-10} m²/s, such as carbon and low alloy steels, should not be tested in air with previous hydrogenation. Tests with in-situ H-charging would not be necessary in materials with hydrogen diffusivity lower than 10^{-15} m²/s, like austenitic steels. With austenitic steels, simultaneous hydrogen charging is recommended for longer time tests, such as constant load test. In steels susceptible to deformation induced martensite formation during the test, concomitant hydrogen charging is recommended. Martensite increases considerably the material's effective hydrogen diffusivity [25].

Slow strain rate tests (SSRTs) use the application of dynamic straining of the specimen in the form of a slow increasing strain up to failure. They are based on the principle that by slowly deforming the specimens all environmentally-assisted cracking phenomena are allowed to occur. The advantage of slow strain rate testing over other techniques is the use of dynamic straining to mechanically accelerate cracking. This technique results in rupture of surface films and thus tends to eliminate initiation time required for surface crack to form. It then enables the use of more realistic environments and reduces the total time requirement for evaluating various metallurgical or environmental parameters. Duration of the tests depends on the strain rate and the ductility of the metal, but typical test durations for steels in hydrogenating media are about two to seven days.

A detailed description of this method is given in ASTM G129 (Standard Practice for Slow Strain Rate Testing to Evaluate the Susceptibility of Metallic Materials to Environmentally Assisted Cracking, 2013). The strain rate adopted is typically between 10^{-7} to 10^{-5} s^{-1}. The results obtained, such as time to failure, final elongation and reduction of area, are usually presented in comparison with tests performed in an inert environment. Values below 75 to 50% of those obtained in inert environment indicate high susceptibility to hydrogen-assisted cracking.

The evaluation of hydrogen embrittlement susceptibility is usually indicated by the generation of cracks of certain morphology as well as by measures such as time to failure, maximum load or stress and ductility parameters (reduction of area and elongation). Although somewhat less easily measured than those quantities, average crack velocity, from measurement of the deepest crack on the fracture surface, is a parameter that often has more direct relevance to defining HE susceptibility than some of the alternatives [90].

One of the most common complaints relating to SSRTs is that they do not provide threshold stress for use in engineering design. Different adaptations of SSRT procedures

were developed in order to obtain this information. SSRTs may be stopped at any time during the loading cycle and examined for cracks, so that by terminating tests at different maximum stresses some indication of the magnitude of the stress to initiate cracking can be obtained. When interrupted SSRTs are used for determining a threshold stress several specimens loaded to different stresses are required. It is possible however to use a single specimen by incorporating a tapered gage length. The taper creates a variation in stress along the gage length and from examination of a longitudinal section of the tested specimen the position at which cracks can just be detected allows the stress at that position to be defined [90].

Tensile tests were performed using smooth cylindrical specimens fabricated following standard NACE TM0198 (Slow Strain Rate Test Method for Screening Corrosion-Resistant Alloys for Stress Corrosion Cracking in Sour Oilfield Service, 2004), with gauge diameter of 3,70-3,87 mm and length of 16,67-18,23 mm (**Figure 31**). The specimen axial axis corresponds to the radial direction in the flange body and the longitudinal direction in the flange neck.

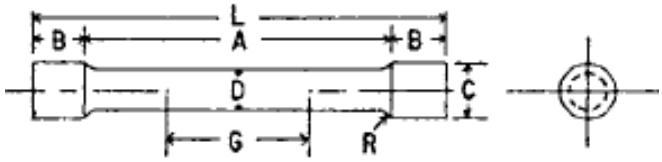

	(mm)
A	25,4
D	3,80
G	16,0
R	6,35
L	45
B	9,8
C	6,35

Figure 31. Nominal dimensions of the tensile specimens.

Different testing conditions were adopted:

a) Tests in air without previous hydrogen charging.

b) Tests with in-situ gaseous H_2 charging, without hydrogen pre-charging.

c) Tests with in-situ electrochemical hydrogen charging, without pre-charging.

d) Tests in air with specimens previously hydrogen charged (ex-situ charging).

The strain rates $\dot{\varepsilon}$ were determined based on the gauge length L_o of the specimen, and the crosshead displacement rate "v" according to the following expression:

$$\dot{\varepsilon} = \frac{v}{L_o} \qquad \textbf{(Equation 48)}$$

The tests of case (a), i.e. the evaluation of as-received material, were performed at initial strain rates of 10^{-3}, 10^{-5} and 10^{-6} s^{-1} to measure the reference mechanical properties.

In the tests with in-situ gaseous hydrogen-charging, H_2 grade N60 (H_2O < 0,6 ppm, O_2 < 0,1 ppm) was adopted. The testing gas pressures were 1, 10, 50 and 300 bar. The tests were performed in a servo-hydraulic machine (**Figure 32**) under constant displacement rate of 0,01 mm/min, corresponding to an initial strain rate of 10^{-5} s^{-1}. A specific procedure was applied in each test to ensure a reproducible atmosphere with a low oxygen and water vapor content. Moreover, the sample was kept under H_2 test pressure for 30 min prior to starting the mechanical loading.

In case (c), all tests were performed in 3,5%NaCl aqueous solution under galvanostatic control, with applied cathodic currents between 0,5 and 3000 mA, corresponding to current densities between 0,24 and 1428,6 mA/cm². Similarly to case (b), hydrogen pre-charging for 30 min was applied in the testing machine before application of the mechanical load in order to stabilize the medium conditions. Most of the tests were performed at initial strain rate of 10^{-5} s^{-1}, but some tests were also performed at 10^{-6} s^{-1} (displacement rate of 0,001 mm/min) to evaluate possible strain rate effects. **Figure 33** present aspects of the testing arrangement.

For case (d), tests were performed in air, at room temperature, under initial strain rates of 10^{-3}, 10^{-5} and 10^{-6} s^{-1} in a MTS servo-hydraulic machine. Specimens from the flange body were pre-charged at CNRS/Grenoble using gas hydrogen at 23,0-23,3 bar and 300±1 °C. The charging time, 120 h (5 days), was selected in order to ensure hydrogen saturation at the chosen temperature. The charged specimens were kept in air, at room temperature, for 14 to 25 days between the charging and the tests. In this period of time, part of the surface hydrogen was probably released from the specimens.

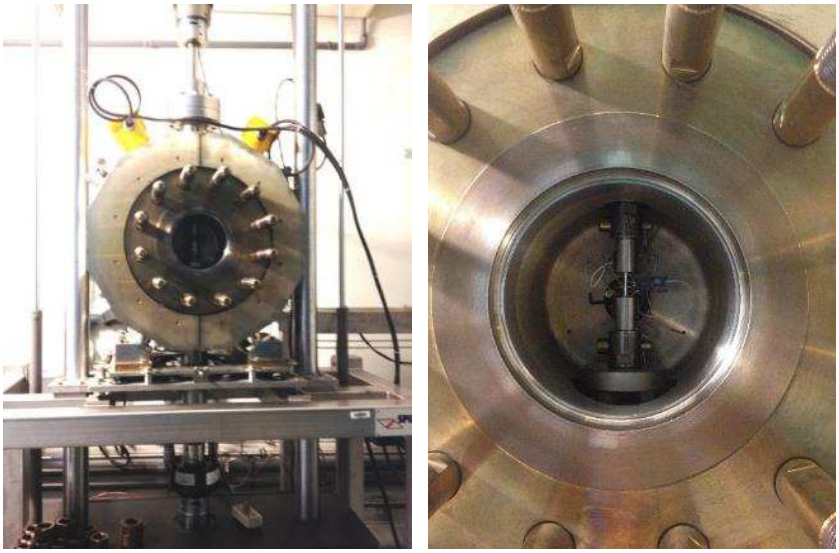

Figure 32. Tensile machine used in the in-situ hydrogen gas tests.

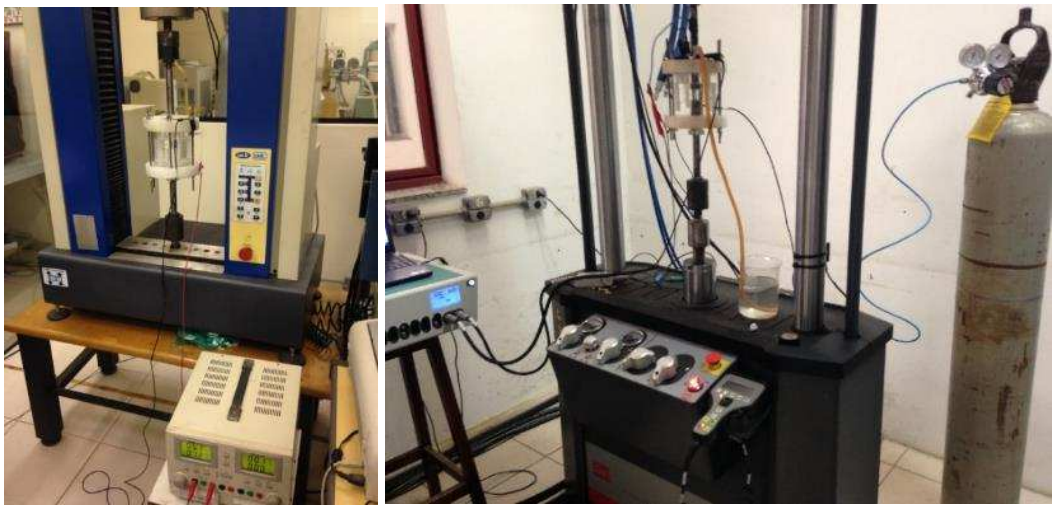

Figure 33. Tensile machines used in the in-situ electrochemical charging tests (EMIC DL 10000 and MTS model 370.25).

Different properties were measured according to definitions of NACE TM0198 (Slow Strain Rate Test Method for Screening Corrosion-Resistant Alloys for Stress Corrosion Cracking in Sour Oilfield Service, 2016) and ASTM A370 (Standard Test Methods and Definitions for Mechanical Testing of Steel Products, 2012):

a) Yield strength (YS): considering 0,2% offset.

b) Ultimate tensile strength (UTS).

c) Reduction of area (ROA): calculated by the following expression

$$\mathrm{ROA}\ (\%) = 100.\frac{D_o^2 - D_f^2}{D_o^2} \qquad \textbf{(Equation 49)}$$

where: "D_o" is the initial gauge section diameter, and "D_f" is the final gauge section diameter at fracture location.

d) Final elongation: relative gauge length variation after fracture.

e) Total fracture strain (ε_f).

f) Plastic strain to fracture (ε_{fp}): determined by subtracting the elastic strain at failure from the total strain at failure (ε_f).

g) Plastic strain at maximum load ($\varepsilon_{p\text{-}max}$): strain at maximum stress subtracted the elastic strain.

Fractographic analysis was performed in order to obtain indications of the fracture process, including crack propagation path and damage mechanisms. The fracture regions were examined visually and using low magnification stereoscopic microscope. The fracture surfaces were examined visually and by scanning electron microscopy

(SEM). Sections of the fracture surfaces were mounted, polished, electrochemically etched using oxalic acid 10% at 5 V and analyzed by optical microscopy.

3.2.3. Thermal Desorption Spectroscopy

Thermal desorption spectroscopy (TDS) is a non-isothermal technique to study the hydrogen desorption kinetics of hydrogen charged samples. TDS is used to obtain information on the different hydrogen traps active in a material, particularly their activation energies.

TDS measurements were performed at the testing apparatus of the Mechanical Properties Laboratory/UFRJ (**Figure 34**). It consists of a source of drag gas (helium), a turbomolecular pump Pfeiffer model TSU071, piping and valves, a quadrupole mass spectrometer Pfeiffer model QMS200, a furnace in which the reactor with the sample is placed (**Figure 35**) and a computer with software for pump pressure control and spectrometer acquisition (Quadstar). The testing procedure involves different steps:

- Specimen preparation and previous hydrogen charging.
- Reactor cleaning and placing the sample in the reactor.
- System purge.
- Test programming and measurements.
- End of test and save the data.

Figure 34. TDS testing apparatus.

Figure 35. Reactor of the TDS apparatus.

The specimens comprised rectangular membranes 0,26-0,30 mm thick for the material electrochemically charged and 0,5-0,8 mm thick for the specimens charged with gas hydrogen. The specimens of the flange body were obtained with their face normal to the component's longitudinal direction, while neck specimens were cut with their face normal to the circumferential direction of the flanges (**Figure 36**). **Figures 37** and **38** show the microstructure of sections of the TDS specimens obtained from the flange body and neck respectively. These micrographs were obtained by optical microscopy after metallographic preparation and etching with 10 wt % KOH solution under a potential of 3V for 10s.

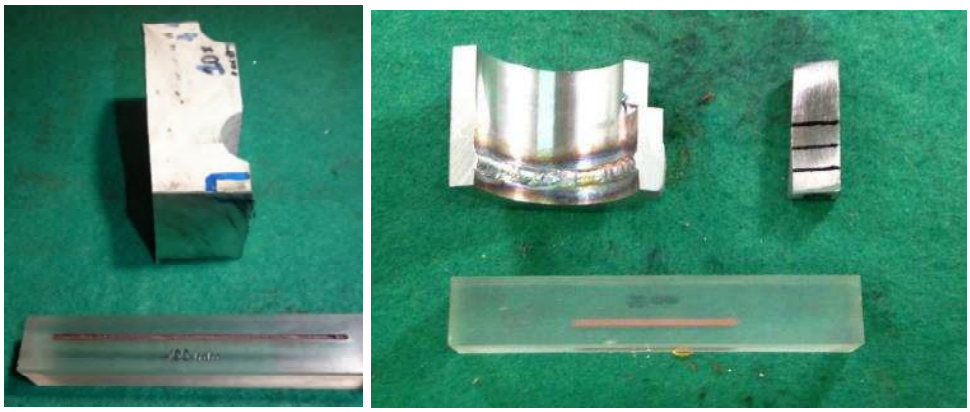

Figure 36. Position in the flanges of the TDS specimens from the body (left) and neck (right).

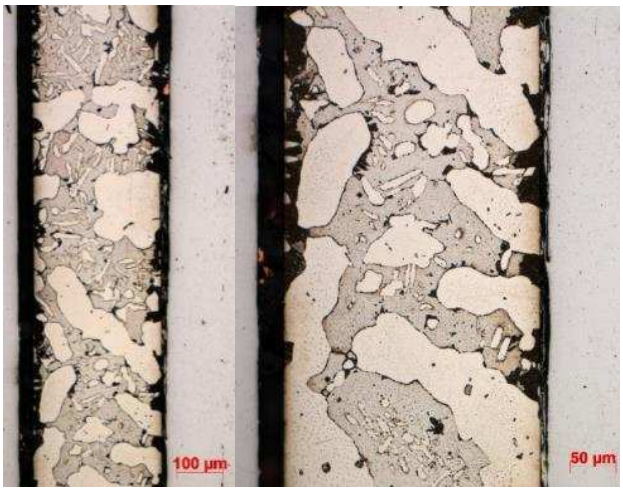

Figure 37. Microstructure of section of TDS specimen from the flange body.

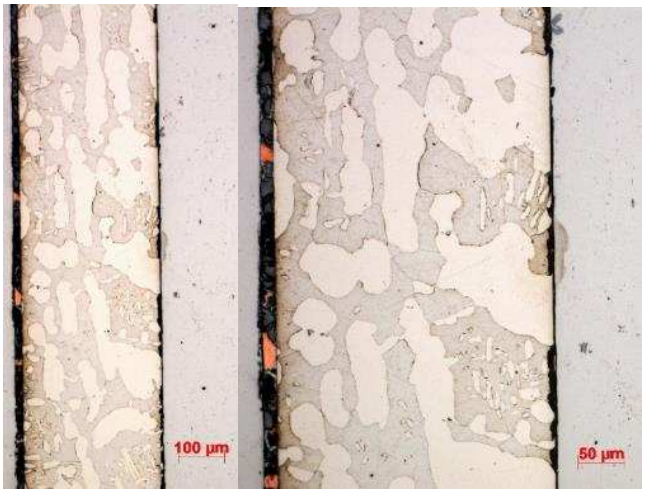

Figure 38. Microstructure of section of TDS specimen from the flange neck.

Electrochemical pre-charging was performed for 329-353 h in 3,5% NaCl solution with continuous replenishment (keeping pH around 6-8) under cathodic density current of 100 mA/cm² at 60ºC. Pre-charging with H_2 gas was performed under a pressure of 20 bar for 72h at 280ºC.

After hydrogen charging, the sample is subjected to the heating regime under different continuous heating rates. During heating, the gas flow that desorbs from the specimen is recorded by the mass spectrometer. In a quadrupole mass spectrometer (QMS), ionized gas particles are accelerated, separated and detected based on their mass-to-charge ratio. The QMS consists of three components: (i) the ionizer, where the molecules and atoms are ionized and focused into the quadrupole rods; (ii) the quadrupole analyser, which select the ions with a specific mass-to-charge ratio; and (iii) the electron amplifier, which improves the resolution of the signal.

The evolution of the amount of gas that desorbs from the sample with increasing temperature results in a TDS spectrum. A TDS spectrum usually consists of desorption

peaks that arise from different trap sites releasing the trapped hydrogen at a specific temperature during heating. While TDS is mechanically non-destructive, the thermal treatment might alter the microstructural characteristics of the metal. TDS is not an in situ experiment since it is generally performed in a machined specimen, obtained from a larger piece of material.

On desorption, hydrogen trapped in a trapping site S_A has to overcome an activation energy E_a (**Figure 39**). This energy is the sum of the binding energy of hydrogen to the trap (E_b) and the barrier energy (E_t). The barrier energy is the energy an atom in an ordinary interstitial site (S_N) must overcome to be trapped. The barrier energy can be bigger or smaller that the activation energy for lattice diffusion (E_m).

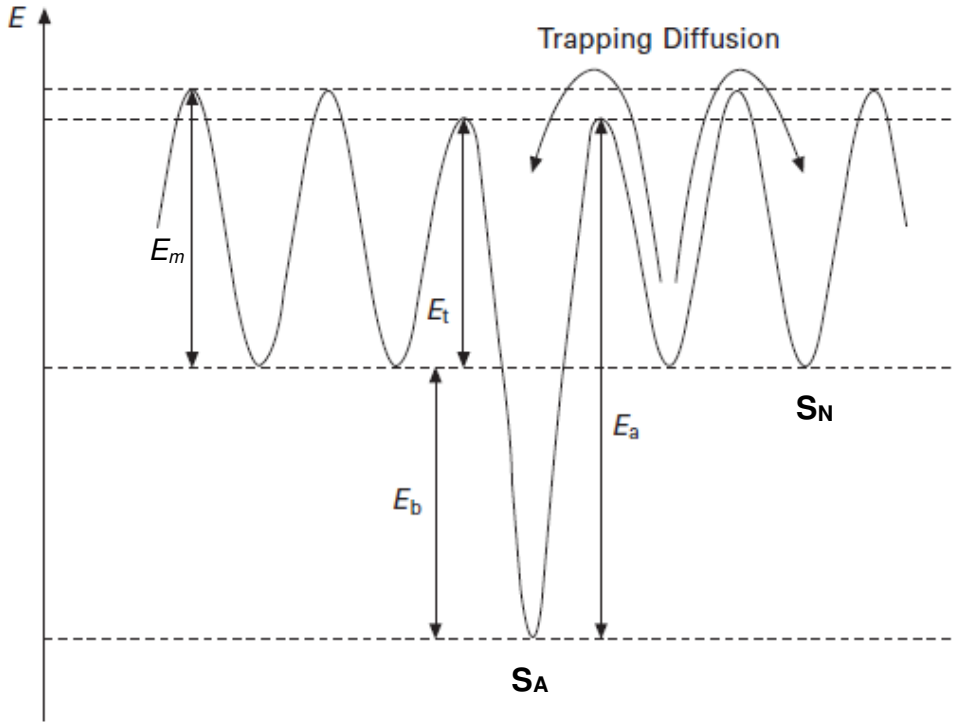

Figure 39. Profile of energies involved in the hydrogen desorption reaction [91].

According to the approach of Kissinger (1957), the desorption reaction kinetics can be described by the following equation [92]:

$$\frac{dX}{dt} = A(1-X)^n \exp\left(-\frac{E_a}{RT}\right) \qquad \textbf{(Equation 50)}$$

where:

- X: released hydrogen fraction
- t: time
- A: constant or frequency factor
- n: order of the reaction
- E_a: activation energy for hydrogen desorption
- R: universal gas constant

- T: absolute temperature.

If the temperature rises during the desorption reaction, dX/dt will rise to a maximum value, then return to zero as hydrogen is exhausted from a specific site. The maximum rate occurs when $d^2x/dt^2 = 0$. If the temperature rises at a constant rate Φ, then by differentiation of **Equation 50**, for a reaction of the first order:

$$\frac{d^2X}{dt^2} = \frac{dX}{dt}\left(\frac{E_a\Phi}{RT^2} - A\exp\left(-\frac{E_a}{RT}\right)\right) \quad \textbf{(Equation 51)}$$

The maximum rate occurs at the temperature T_m defined by setting **Equation 51** equal to zero:

$$\frac{E_a\Phi}{RT_m^2} = A\exp\left(-\frac{E_a}{RT_m}\right) \quad \textbf{(Equation 52)}$$

Linearizing **Equation 52** and differentiating by $1/T_m$, one obtains:

$$\frac{\partial \ln\left(\frac{\Phi}{T_m^2}\right)}{\partial\left(\frac{1}{T_m}\right)} = -\frac{E_a}{R} \quad \textbf{(Equation 53)}$$

After performing TDS measurements at at least two heating rates and determining the corresponding peak temperatures for a specific trap, the slope, when plotting $\ln(\Phi/T_m^2)$ vs. $(1/T_m)$, allows the activation energy corresponding to the trap to be obtained. **Table 7** lists data for reversible and irreversible hydrogen traps reported in the literature for different materials. This method is valid if the desorption is rate-limited by the dissociation of trapped hydrogen rather than by diffusion of hydrogen in the lattice [45].

Other models described in literature determine the activation energy from experimentally measured TDS spectra in conditions where the desorption is affected by diffusion of hydrogen. These models use numerical equations that include diffusion and (re)trapping characteristics. A first group of models is based on a modification of Fick's second law and in the theory of McNabb and Foster. Other models are built up from a simplified diffusion equation combined with Oriani's assumption of local equilibrium between hydrogen in crystal lattice and in the trapping sites [93].

Table 7. Activation energies of hydrogen traps and peak temperatures for hydrogen dessorption in iron and steels [22,94].

Type of trap	Peak temperature (ºC)	Activation energy (kJ/mol)	Heating rate (ºC/min)	Material
Reversible H traps				
Ordinary interstitial sites	-	8	-	Pure iron
Grain boundaries	112	17,2	3	Pure iron
Dislocations	215	26,8	3	Pure iron
Microvoids	305	35,2	3	Pure iron
Ferrite/Fe_3C interface	120	18,4	2,6	Medium carbon steel
V_4C_3 (coherent)	220	30	2,6 - 1,7	High and low carbon steel
Irreversible H traps				
TiC (incoherent)	710	86,9	3	Medium carbon steel
MnS	495	72,3	3	Low alloy steel
Retained austenite	600	55	4	Dual phase steel

The hydrogen concentration C_H may be derived from TDS measurements using the equation [95]:

$$C_H = \frac{v_{eff}}{RT}\int_0^{t_{meas}}(P - P_{bkg})dt \qquad \textbf{(Equation 54)}$$

where:

- v_{eff}: effective pumping speed
- t: time
- t_{meas}: duration of the experiment
- P: measured normalized hydrogen pressure
- P_{bkg}: background hydrogen pressure
- R: gas constant
- T: absolute temperature at the inlet of the pump.

The value of the integral is derived from the area under the curve of the plot of hydrogen pressure vs. time. Calibration experiments shall be used.

Different processes and effects should be considered in the analysis of the TDS spectra. Although it is generally assumed that the hydrogen trap sites are stable during the TDS measurement, heating might have actually impact on microstructural features. Recovery of the deformation structures, phase transformations, coarsening or dissolutions of precipitates can take place, resulting in hydrogen desorption and/or influencing the results.

Surface effects, hydrogen diffusion and retrapping (i.e. hydrogen released from one specific trap while diffusion out of the sample is trapped by another trapping site) can be complicating factors during the analysis of TDS results. One limitation of the analysis method is the assumption that the hydrogen evolution out of the specimen is the same as the hydrogen release rate from the trapping site, neglecting lattice diffusion. This assumption holds as long as no hydrogen accumulation occurs in the sample. At high heating rate, hydrogen degassing through lattice diffusion cannot keep up with the temperature change, causing accumulation in the sample. Also every trap is considered as an isolated microstructural feature, which implies that the trap characteristics do not influence each other and hydrogen retrapping is not considered. Therefore, it is important to plan the measurements in such a way that these effects are minimized. According to some authors, when a sample is sufficiently thin and receives an adequate surface treatment, these effects can be ignored.

Larger activation energies and trap densities shift the desorption peaks to higher temperatures. The curves tend to be shifted to higher temperatures as the grain size decreases [3].

3.2.4. Time-of-Flight Secondary Ion Mass Spectroscopy.

Time-of-flight SIMS is a technique that enables direct and precise mapping of hydrogen and/or its isotopes at sub-μm lateral resolution. The technique principle of SIMS involves the interaction of a primary ion beam of several hundred eV to several tens of keV with a sample, causing sputtering of atoms from the surface. The solid surface of the sample is bombarded with primary ions, which progressively lose their energy by colliding with atoms of the target. These atoms are permanently displaced above some critical energy transfer threshold. Neutral masses, radicals and ionized atoms or aggregates are then emitted from the surface, provided that they come to the solid/vacuum interface with an outward momentum and an energy exceeding the barrier potential [96].

The time-of-flight SIMS uses a pulsed primary ion beam to expel and ionize the sample surface. Each pulse is less than 1 ns in duration and corresponds to a primary

ion dose of less than 10^{12} ions/cm². Under such conditions, only a tiny fraction of surface atoms is hit by primary ions, thus ensuring that all secondary species originate from the first surface layers. In the static mode, the depth of analysis is typically of a few nm. A fraction of the sputtered atoms is ionized. It is possible to ionize remaining ejected neutral atoms with a laser. The ionized species are then accelerated by a difference of potential between the sample surface and the analyzer, which results in imparting to them distinct velocities depending on their individual mass-to-charge ratios. As the ion kinetic energy ($E = ½mv^2$) is determined by the extraction voltage, the time it takes to cross the analyzer is proportional to the square root of the ratio mass/charge (m/z). The analysis beam generates pulses of the order of ns, which allows to measure the time of flight of the ions and thus determine their mass (the fastest being the lighter) [48].

The pulsed primary ion beam flux is relatively low in this technique and, consequently, the sputter-induced effusion of hydrogen is reduced. Another advantage of ToF-SIMS is the high transmission of the mass spectrometer and its parallel mass detection capability. All secondary ions emitted into a solid angle per primary ion pulse are collected. For these reasons, ToF-SIMS has been applied for in-situ detection of hydrogen and deuterium in metallic materials [97].

Recently, ToF-SIMS image analysis has been improved by multivariate analysis of image data and by data fusion of the chemical and topographic information. Principal component analysis enables that all the deuterium related information in the ToF-SIMS spectra (e.g. D, OD, CrD ions) can be utilized for visualization of the deuterium distribution. This leads to an improved contrast and to more details in the image [97].

ToF-SIMS measurements were performed in samples removed from the flange body, with faces normal to the flange longitudinal direction. Preliminary evaluations were made at room temperature with samples 1-2 mm thick. Before hydrogen and deuterium charging, all specimens were polished mechanically and cleaned in an isopropanol ultrasonic bath. The specimens were submitted to gaseous deuterium charging at CEA in the following conditions: pressure and temperature of 19,5-19,8 bar and 276-278°C for 120 h (5 days). After deuterium charging, one of the samples was etched with oxalic acid 10% (5V, 10s). Etching was intended to enable better microstructural analysis by introducing a topographic difference between austenite and ferrite. Additional tests were performed with specimens 0,4 mm thick previously submitted to charging with gaseous D_2 at 280-290ºC, 19-21 bar for 120h. These tests were performed at cryogenic conditions (-100ºC).

Considering the diffusion coefficient values measured previously, the charging conditions were expected to provide a complete homogeneous penetration of deuterium through the specimens. In all cases, the gas D_2 used contained 0,40% HD, 1,2 ppm H_2O,

among other contaminants (max. 0,2 ppm of O_2, N_2, CO_2, CO and HC). Deuterium was used as a tracer of hydrogen to reduce confusions on the origin of hydrogen, i.e. to distinguish residual hydrogen in the samples and hydrogen introduced in the material from the rest gas in the analysis chamber from the deuterium introduced during pre-charging. Between charging and the tests, the samples were kept in a liquid N_2 bath.

The analyses were performed using the ToF SIMS (TOF.SIMS 5 from Ion Tof GmbH) of the *Plate-forme de Nano-caractérisation* (PFNC) of Minatec/Grenoble (**Figure 40**). The TOF.SIMS 5 is equipped with a reflectron type time-of-flight analyzer. In this type of analyzer ions are directed into a flight tube in which an electrostatic gradient exists. Ions of similar energies but different masses travel at different velocities and are therefore reflected back to the start of the flight tube at different times. The flight time depends solely on mass [98].

The primary species used for the analyses was Bi_1, with polarities positive and negative and accelerating voltage of 30 kV. All analyses have been achieved after several minutes of sputtering with Cs, with voltage of 2 kV for getting rid of surface contamination artifacts, such as hydroxides. The analyzed region was of 300x300 μm^2. The analyses were carried out under a vacuum of 2.10^{-10} mbar.

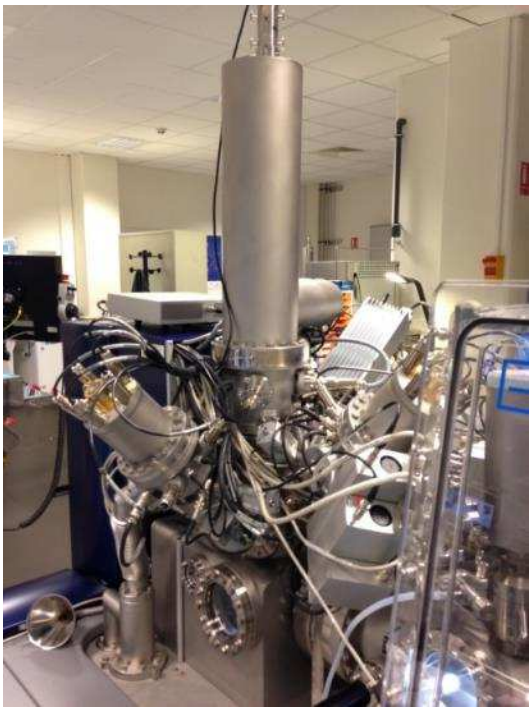

Figure 40. Time-of-flight SIMS used in the measurements.

For the tests at room temperature, a non pre-charged sample was first analyzed in both polarities. This sample contained only residual hydrogen. It was intended specially to distinguish properly the signals of deuterium and hydrogen. Considering positive polarity, the signal of mass 2 was found to be much higher than of mass 1, indicating

that recombination of hydrogen atoms took place, forming H_2^+ (**Figure 41**). At negative polarity, the ratio of the signals of mass 2 and 1 (D/H) was close to the natural occurring deuterium/hydrogen ratio (**Figure 42**). This indicates that hydrogen recombination was less important on this polarity, providing better conditions for detection of deuterium. It was further proved that besides better mass resolution, negative polarity provides also better spatial resolution than positive polarity, being then used for all following tests measurements.

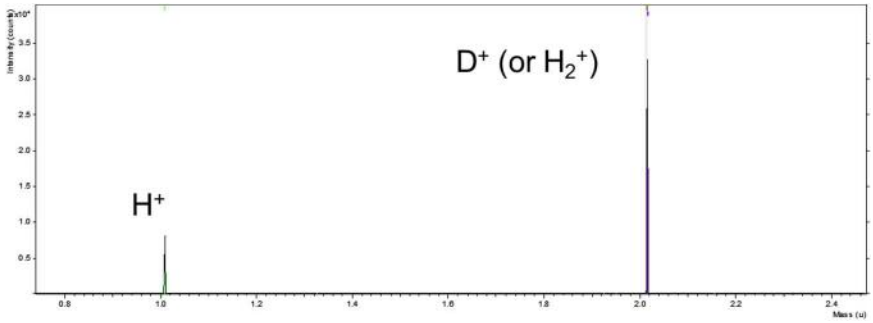

Figure 41. Mass spectrum of non charged specimen – Positive polarity.

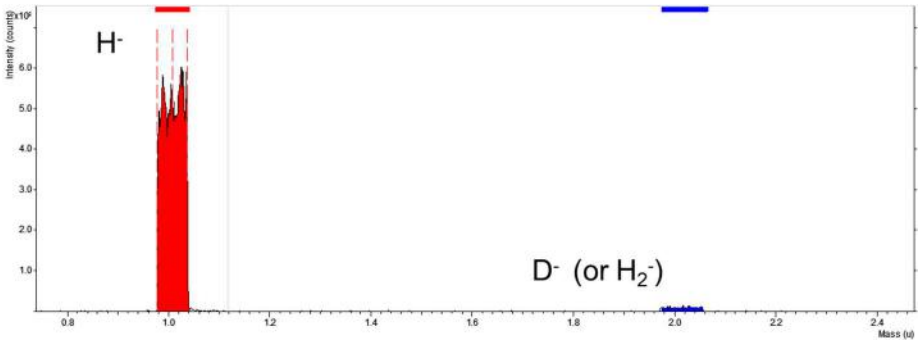

Figure 42. Mass spectrum of non charged specimen – Negative polarity.

3.2.5. Neutron Scattering

X-ray diffraction methods do not resolve light atoms in the presence of high proportion of heavy atoms. On the other hand, techniques involving neutrons can provide information on hydrogen distribution because they have the advantage of high sensitivity to light elements like hydrogen [99,100].

Neutrons have no charge and their electric dipole moment is either zero or too small to be measured. For these reasons, they can penetrate matter far better than charged particles. Furthermore, neutrons interact with atoms via nuclear rather than electrical forces, and nuclear forces are very short range. Thus, as far as the neutron is concerned, solid mater is not very dense because the “size” of a scattering center (a nucleus) is typically 10^5 times smaller than the distance between centers. Therefore, neutrons can go through mm to cm of most materials without being significantly scattered or absorbed.

The disadvantage of the neutron great penetrating power is that they are only weakly scattered once they penetrate. Furthermore, available neutron beams have inherently low brilliance (number of neutrons emitted from the source per second). For being a useful tool for investigating the structure of materials, neutrons used for scattering studies should have wavelengths of the same order of magnitude of interatomic distances, usually between 1 and 10 Å.

The scattering of a neutron by a free nucleus can be described in terms of a cross section σ, measured in barns (1 barn = 10^{-28} m²). Consider a neutron scattering experiment where a beam of neutrons of a given energy E is incident on a general collection of atoms. One can set up a neutron detector to count all the neutrons scattered into the solid angle Ω. The total scattering cross section can be defined as:

$$\sigma_s = \int \frac{d\sigma}{d\Omega} d\Omega = \frac{\text{total number of particles scattered in all directions per second}}{\Phi}$$

(Equation 55)

where:

- Φ: number of incident neutrons per unit area per second, referred to as the incident flux.

The quantity “b”, referred to as the scattering length of the nucleus, is equal to the amplitude of the scattered neutron beam at unit distance from the scattering nucleus, for an incident beam of unit amplitude [99]. It measures the strength of the interaction between the neutron and the nucleus or the efficacy of neutron scattering. The scattering length “b” can be defined as [101]:

$$b^2 = \frac{d\sigma}{d\Omega}$$ **(Equation 56)**

Integrating over all space (4π steradians), one obtains:

$$\sigma = 4\pi b^2$$ **(Equation 57)**

The value of “b” is mostly dependent of the incident neutron wavelength. The nuclear part of the scattering length is also independent of the scattering angle, allowing for better peak resolution at high angles. As can be noticed in **Figure 43**, there is no straightforward relation between the atomic number of the atoms and the scattering length “b” of the associated isotopic mixtures for neutrons. This property makes neutron diffraction a very helpful tool to detect light atoms such as hydrogen in its ^{1}H or ^{2}H forms, that exhibits a strong contrast. ^{1}H hydrogen (with 99.985% abundancy) has a large incoherent scattering length (25,18 fm) and a small coherent scattering length (-3,74 fm). Deuterium

has a small incoherent scattering length (3,99 fm) and a relatively large coherent scattering length (6,67 fm).

Positive values of the scattering length correspond to a phase change of 180° on scattered neutron beam. Negative values of “b” indicate a 0° phase change relative to the incident beam [99].

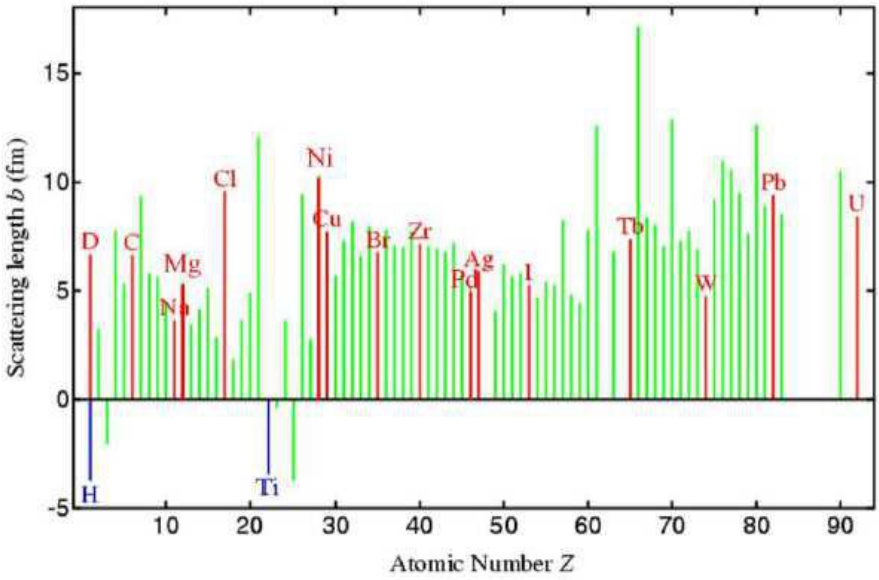

Figure 43. Coherent neutron scattering length “b” as a function of the atomic number Z [102].

Scattering is subdivided into elastic and inelastic. In elastic scattering, the total kinetic energy of the neutron and nucleus is unchanged by the interaction. In inelastic scattering the nucleus undergoes an internal rearrangement into an excited state from which it eventually releases radiation.

Scattering can also be coherent or incoherent. In coherent scattering neutron waves scattered from different nuclei interfere with each other. This type of scattering depends on the distances between atoms and on the scattering vector $\vec{Q}$, and it thus gives information about the structure of a material. Elastic coherent scattering tells about the equilibrium structure, whereas inelastic coherent scattering provides information about the collective motions of the atoms, such as those that produce phonons or vibrational waves in a crystalline lattice. In incoherent scattering there is no interference between waves scattered by different nuclei. Rather the intensities scattered from each nucleus just add up independently. Incoherent elastic scattering is the same in all directions, so it usually appears as unwanted background in neutron scattering experiments. Incoherent inelastic scattering, on the other hand, results from the interaction of a neutron with the same atom at different positions and different times, thus providing information about atomic diffusion [101].

A summarized mathematical description of the neutron scattering process is presented in **Annex A**.

The neutron diffraction experiments were performed on 3T2, a powder diffractometer of the Laboratoire Léon Brillouin, at CEA-Saclay (**Figure 44**). The neutrons source is the reactor Orphée.

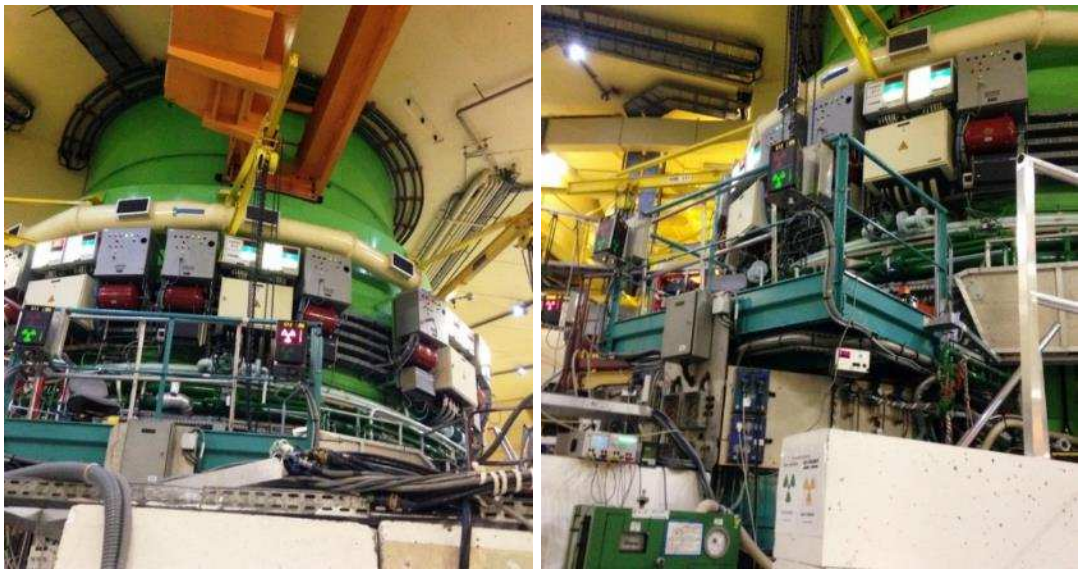

Figure 44. External view of 3T2 diffractometer.

The 3T2 spectrometer is a high resolution two-axis diffractometer dedicated to neutron powder diffraction studies of samples with primitive unit cell up to approx. 1000 Å. A scheme of this equipment is shown in **Figure 45**. The monochromator (vertically focusing Ge (335)) provides an incident beam of wavelength ca. 1,22 Å. The maximum beam size at the specimen is 20 x 60 mm². Fifty ^{3}He detectors, 2,4° apart, allows detection in the range of $4,5 < 2\theta < 122°$. The maximum flux at the specimens is 10^{6} neutrons/cm².s.

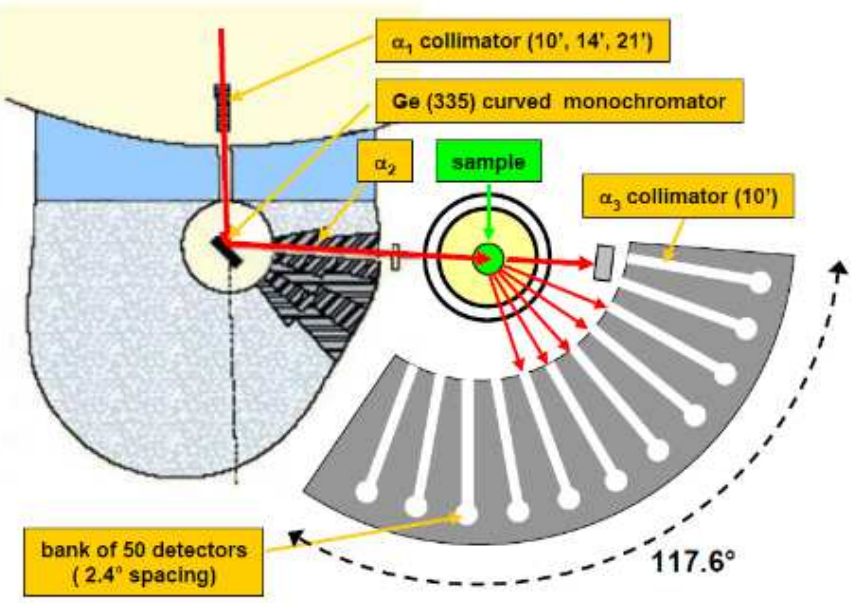

Figure 45. 3T2 diffractometer of the Laboratoire Leon Brillouin/CEA-Saclay (source: http://www-llb.cea.fr/fr-en/pdf/3t2-llb.pdf).

The cylindrical specimens used for the measurements were prepared from the flange body, with gauge height of 30 mm and diameter of 8 mm (**Figure 46**). The axis of the specimens corresponded to the longitudinal direction of the flanges (**Figure 47**). The specimens used for the tests of 2016 were surface covered with a 50-80 nm thick palladium layer. The Pd layer was aimed to improve the hydrogen/deuterium absorption during charging. Physical vapour deposition (PVD) was used for the palladium layer deposition. The procedure was performed at Ar pressure of 2,0 mTorr, using power of 75 W_{DC} for ca. 4 min.

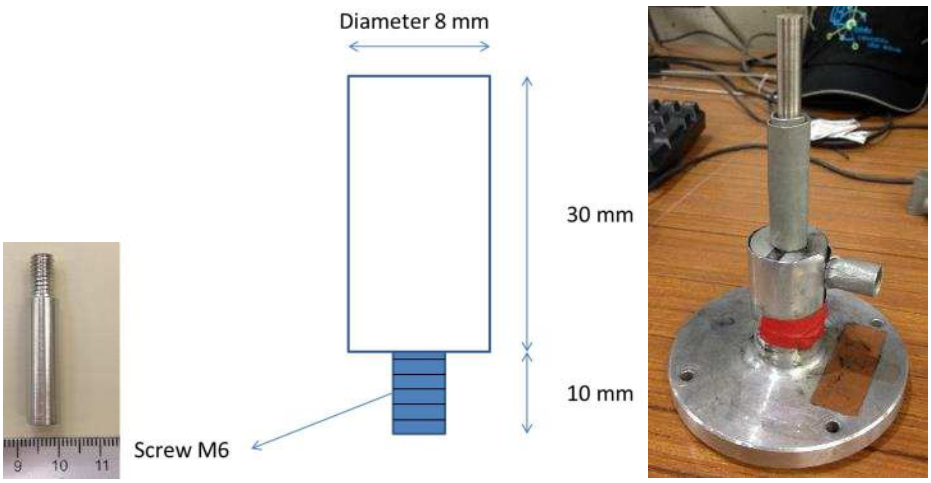

Figure 46. Specimens used for the neutron scattering experiments. Left: specimen placed in the testing holder.

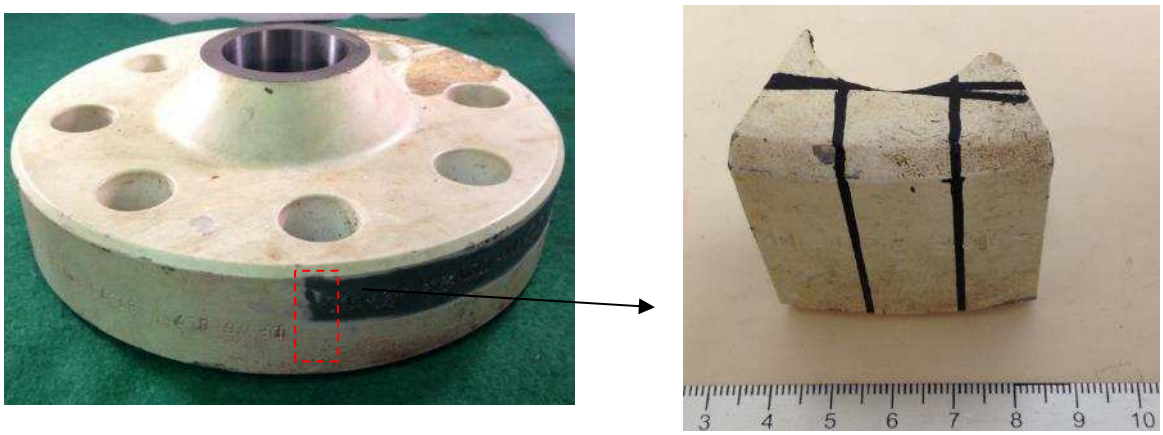

Figure 47. Position of the samples in the flange.

For the tests performed in 2015, specimens were pre-charged for 293 h with hydrogen gas (purity N55) at pressure of 16,7-18,1 bar and temperature of 290,3-291,9°C. For the tests of 2016, specimens were charged with hydrogen (125 bar, 295-300ºC, 8 days) and deuterium (285-290ºC, 29 bar, 12 days). In both cases, non pre-charged specimens, i.e. containing only residual hydrogen, were also tested.

Three measurements were performed in 2015: one non pre-charged specimen and two specimens pre-charged with hydrogen. In 2016, five measurements were performed: (i) one non pre-charged specimen, (ii) a specimen charged with H_2, (iii) a specimen charged with H_2 and submitted to partial degassing (1h, 200ºC), (iv) a specimen charged with D_2 and (v) a specimen charged with D_2 and submitted to partial degassing (1h 20min, 200ºC).

The measurement parameters are presented in **Table 8**.

Table 8. Parameters of the neutron scattering tests.

Test parameters	**2015**	**2016**
Wavelength	1,2256 Å	1,229186 Å
Divergence (primary collimator)	21’	
Angular range	4,5°-122°	4,5°-120,75°
Step size	0,05°	0,025°
Beam size	60 mm (height) x 12 mm (width)	
Test time for each experiment	12h	20h

The diffractograms obtained were further submitted to profile refinement using the software FullProf. The procedure followed is described in **Annex B**.

4. Results

4.1. Thermodynamic Simulations

The temperature ranges of stability of the different phases calculated using the software Thermocalc and considering the composition indicated in section **3.1.1** (without nitrogen) are presented in **Table 9** and **Figure 48**. Such calculations can only be used to show general behavior, as they describe equilibrium conditions, which are rarely attained in practice.

Table 9. Temperatures of stability of the phases.

Phase	**Range of stability (ºC)**
Liquid	>1416
Ferrite	<610, 903-1487
Austenite	<1200
Sigma	408-1028
$M_{23}C_6$	<294, 344-1017
μ	325-406
π	250-370
M_6C	250-340
Laves	<250

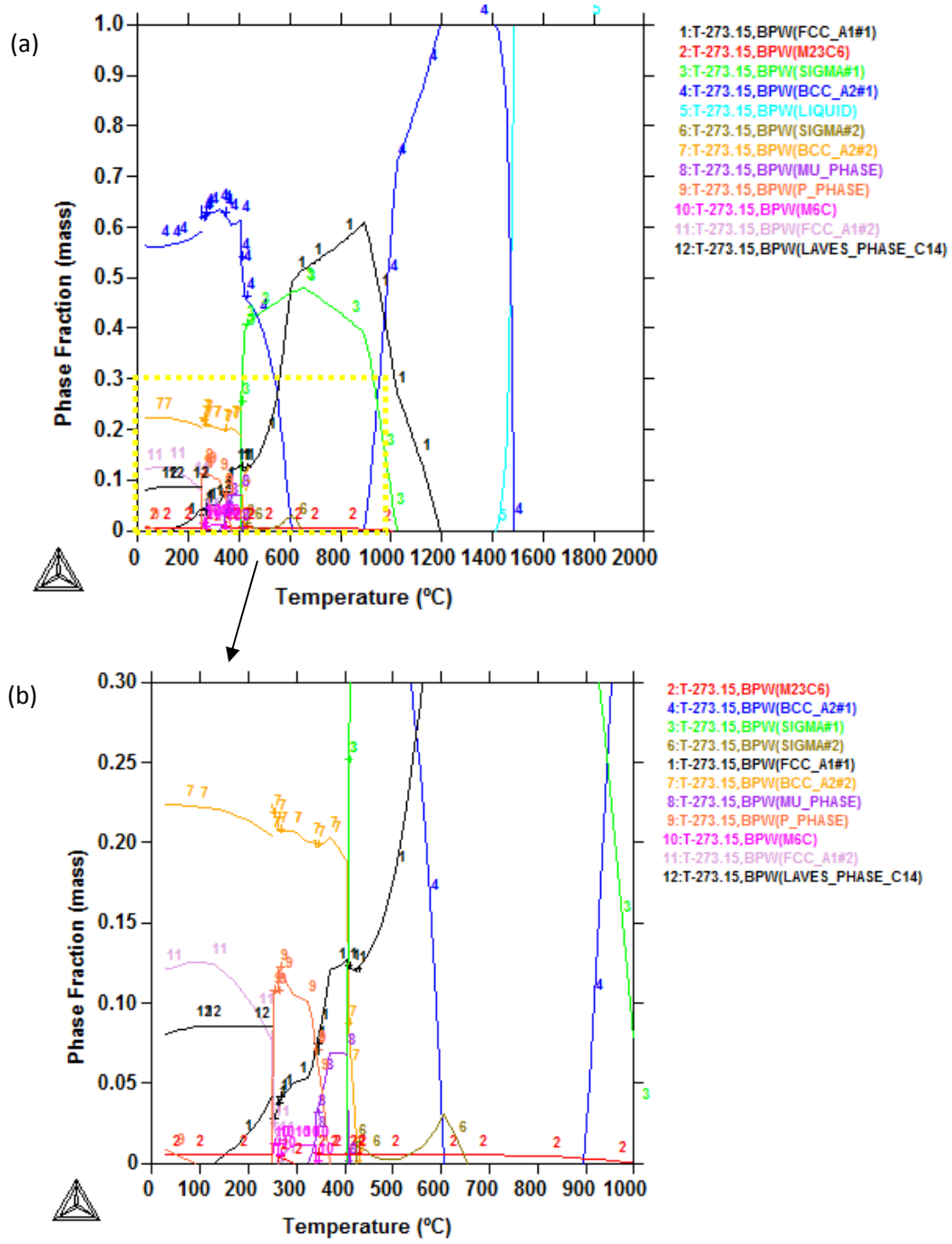

Figure 48. (a) Mass fraction of the phases as a function of the temperature. (b) Detail at lower fractions below 1000ºC.

The alloy solidifies in a ferritic structure and austenite forms in the solid state. The solidus predicted is 1416ºC. The formation of austenite starts below 1200ºC. Initially, austenite precipitates at the ferrite/ferrite grain boundaries and grows into the interior of the grains. Afterwards, austenite can also precipitate as intragranular islands. During hot working, which was performed between 1000 and 1230ºC, the formed microstructure has alternating ferrite and austenite lamellae. The fact that the α/γ interface energy is

lower that the α/α and γ/γ grain boundary energies induces the formation of the lamellar microstructure [8].

Figure 49 presents the calculations performed by adding 0,2%N to the original composition used in **Figure 48**. As nitrogen is a very strong austenite stabilizer, it is evident that the range of stability of austenite is expanded: austenite is stable below 1346ºC. Ferrite forms below 1464ºC. The hexagonal $(Cr,Mo)_2N$ phase is introduced, being stable below around 980ºC. The thermodynamically stable phases at room temperature are: ferrite, austenite, $(Cr,Mo)_2N$, M_6C and π.

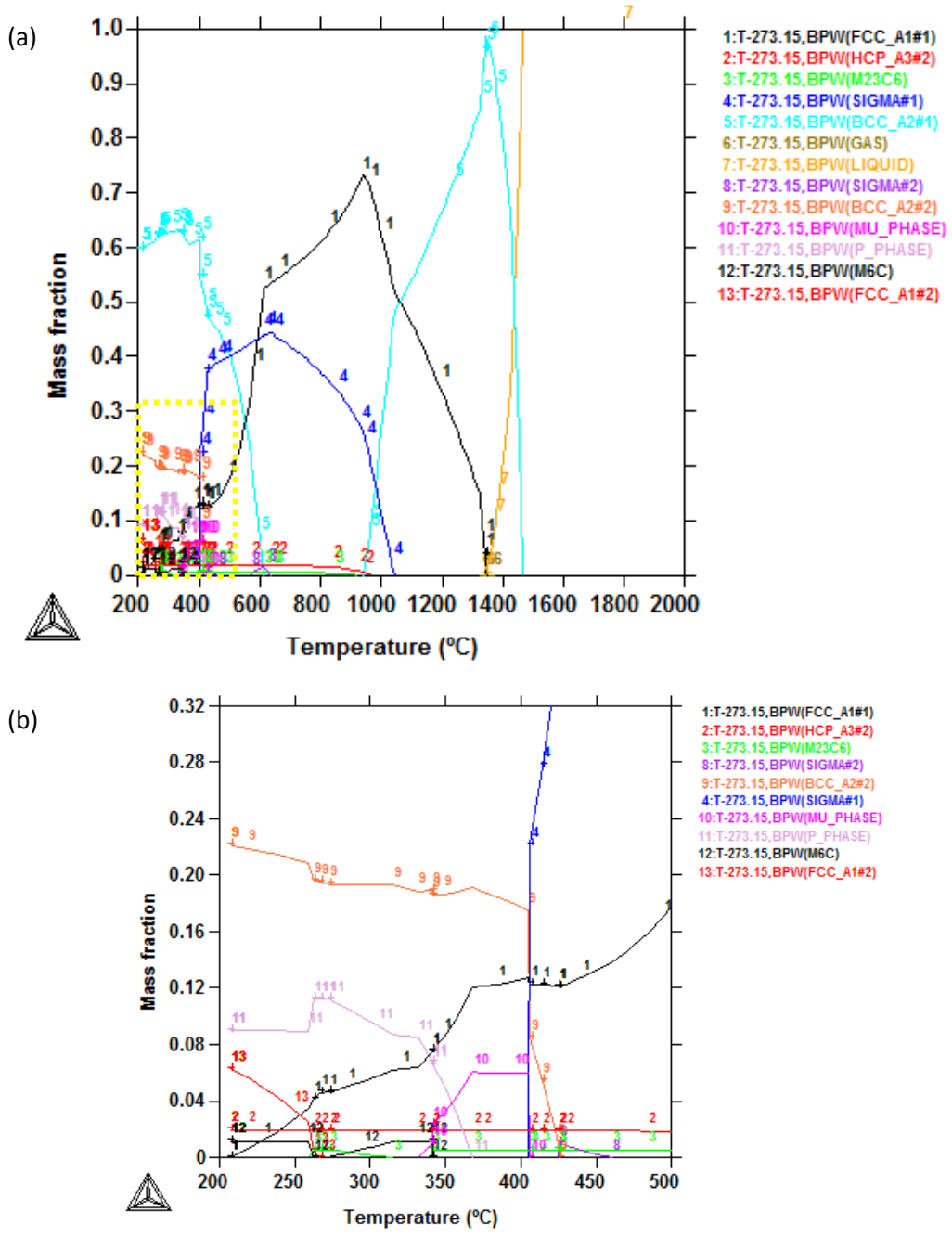

Figure 49. (a) Mass fraction of the phases as a function of the temperature – inclusion of 0,2%N. (b) Detail at lower temperatures and mass fractions.

Figure 50 shows the isothermal section at the solution annealing temperature (1100ºC), considering the composition with 0,2%N. It is evidenced the treatment is performed only in the presence of austenite and ferrite. The mass percentages of ferrite and austenite are estimated as 54% and 46% at this temperature.

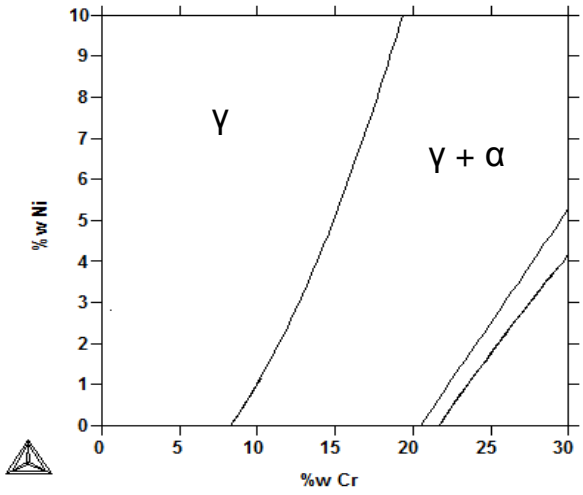

Figure 50. Isothermal section of the diagram %Cr vs %Ni at 1100°C. .

4.2. Microstructural Evaluation

4.2.1. Optical and Scanning Electron Microscopy

A bimodal distribution of equiaxial austenite grains can be verified throughout all regions, some having diameters bigger than 100 µm and austenitic grains smaller than 30 µm. While both the flange body and neck present similar average inter-austenitic spacing (55 µm) and ferrite fraction values (58%), the average size of the austenitic islands in the flange body is bigger than in the flange neck. Considering austenite grains of all dimensions, the average austenite grain diameter in the flange body is 24,7 µm, while in the neck is 18,3 µm. Excluding grains smaller than 30 µm, the austenitic average size in the body is 54,9 µm while in the neck is 43,3 µm. The flange neck also presented a more oriented microstructure, as can be seen by comparing **Figures 51** and **52**. These features can be attributed to the higher reduction ratio the flange neck is submitted to during the forging process.

Considering the coarser microstructure and the measured ferrite fraction, the tested material can be considered relatively more susceptible to hydrogen embrittlement in comparison with for instance rolled or hot isostatic pressed material of the same grade [38].

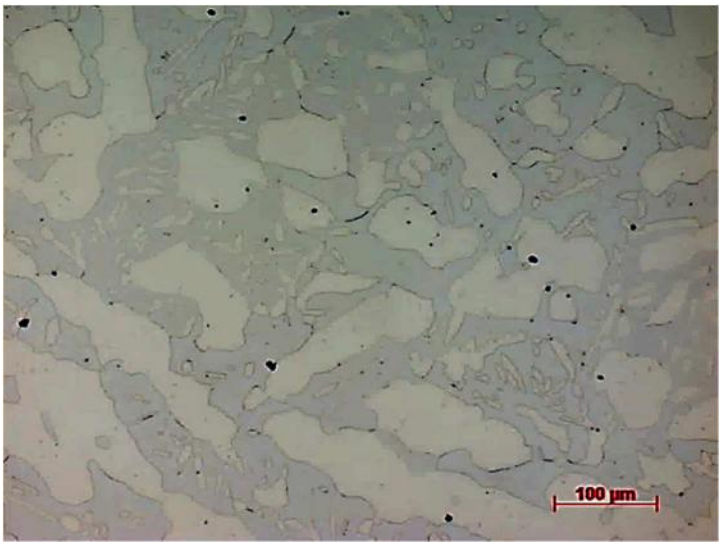

Figure 51. Microstructure of the flange body. Normal to the longitudinal direction. Etchant: oxalic acid.

Figure 52. Microstructure of the flange neck. Normal to the longitudinal direction. Etchant: oxalic acid.

According to the energy dispersive spectroscopy (EDS) composition measurements, in some cases, as shown in **Figure 53**, lower Cr content was verified in smaller austenite grains in comparison with larger austenite grains. **Figure 54** presents thermodynamic simulations performed with Thermocalc and the database TCFE6 (composition Fe + 0,027 wt%C, 0,477%Si, 1,010%Mn, 25,7%Cr, 4,36%Mo and 7,70%Ni) of the chemical composition of austenite between 200 and 1200ºC. Chromium contents in austenite decrease with temperature below 1000ºC. Thus the verified lower Cr content in some small austenite grains suggests they were formed at lower temperatures.

Great amount of nitride precipitates and intragranular secondary austenite clusters are clearly visible in **Figure 55**. Indications of the presence of intermetallic phases can be seen in **Figure 56**. The darker areas in phase or grain boundaries can indicate possible presence of intermetallic phases. The intermetallic phases could not be identified by optical microscopy, SEM and EDS. In general, they were isolated and in small amount.

(a)

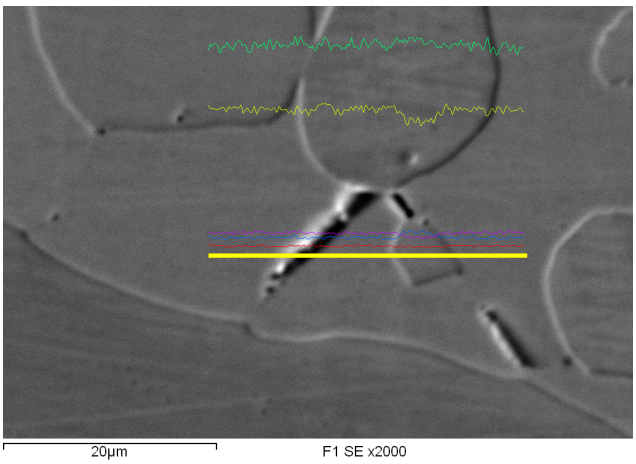

(b)

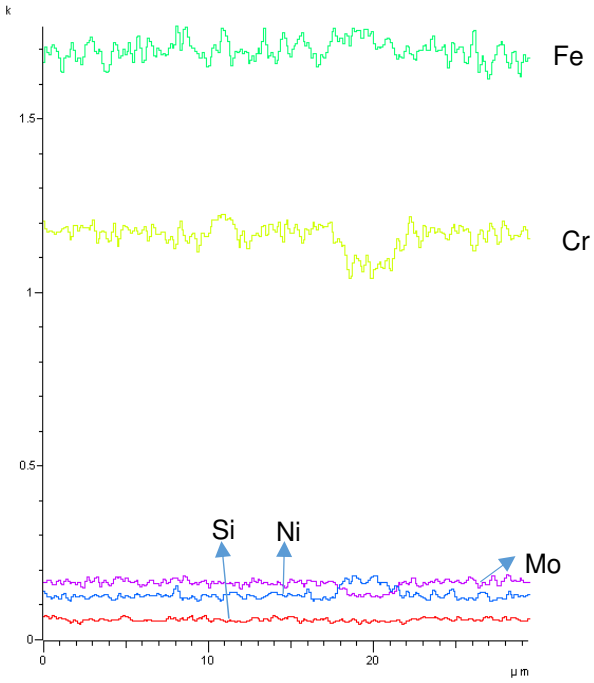

Figure 53. (b) EDS profile along the line shown in (a). Flange body, normal to the longitudinal direction.

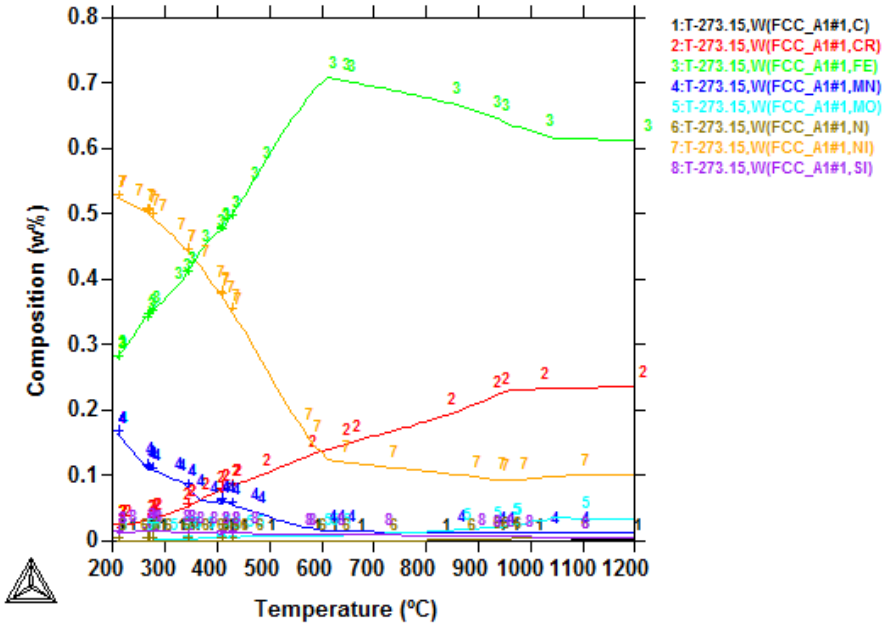

Figure 54. Simulated chemical composition of austenite as a function of temperature. Chromium content is shown in the red line.

(a)

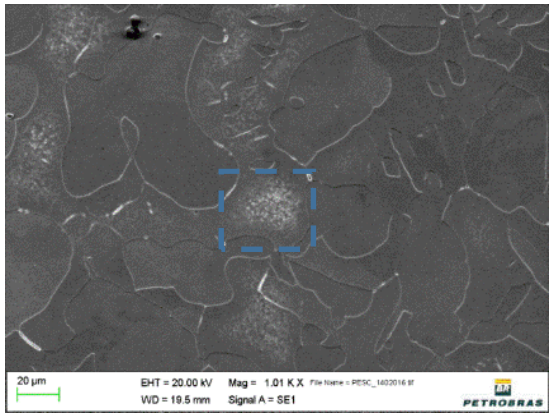

(b)

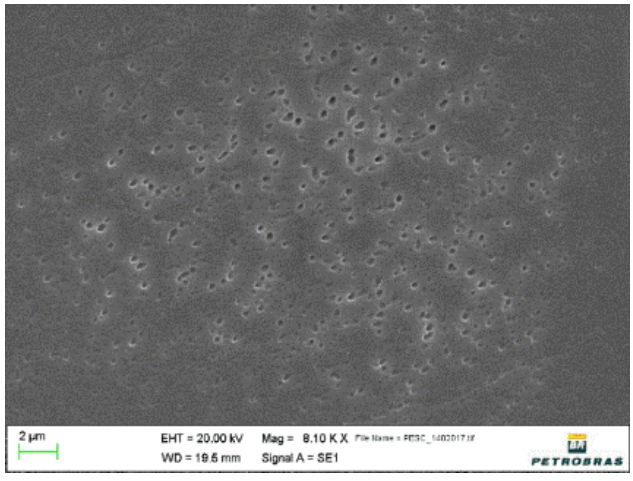

Figure 55. (a) SEM image of flange neck, section normal to the circumferential direction. (b) Detail of secondary austenite and nitride precipitates cluster.

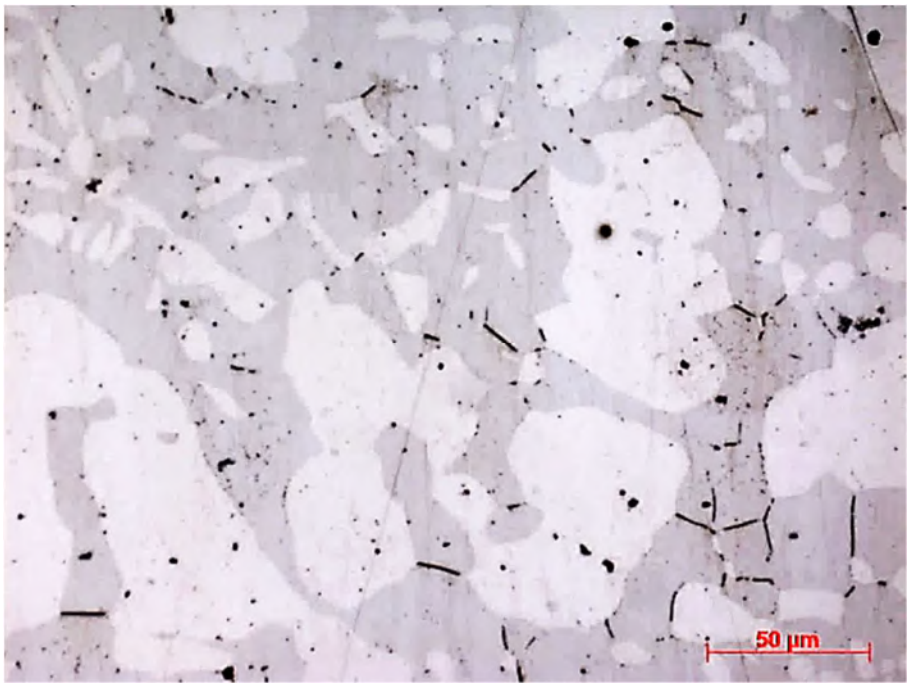

Figure 56. Microstructure of the flange body. Normal to the radial direction. Etchant: KOH.

4.2.2. Transmission Electron Microscopy

Figures 57 to **60** show bright field images obtained inside a ferrite grain and in ferrite/ferrite grain boundaries. Prolific nanometric precipitation is verified both inside ferrite grains (**Figures 57** and **58**) and along α/α grain boundaries (**Figures 59** and **60**). EDS profiles measured in a intragranular precipitate and in the ferritic matrix are shown superimposed in **Figure 58**. The main different is the higher nitrogen content in the precipitate. EDS mapping for a ferrite/ferrite boundary in the flange body shown in **Figure 60** also indicates higher N content in the precipitates. These results suggest the precipitates are chromium nitrides. Cr_2N is the predominating type of nitride in stainless steels [7]. Due to the size of the particles, the micro-analysis is partly affected by the chemical composition of the matrix.

Bright field and high-angle annular dark-field (HAADF) images of an austenite/ferrite phase boundary obtained in a section of the flange neck are displayed in **Figures 61** and **62**. Isolated precipitates at the phase boundary and growing into ferrite are visible. EDS profile measured in a precipitate (**Figure 61**) and EDS mapping of the region (**Figure 62**) indicate the precipitates are enriched in Cr and Mo. This result suggests it is probably σ or χ phases.

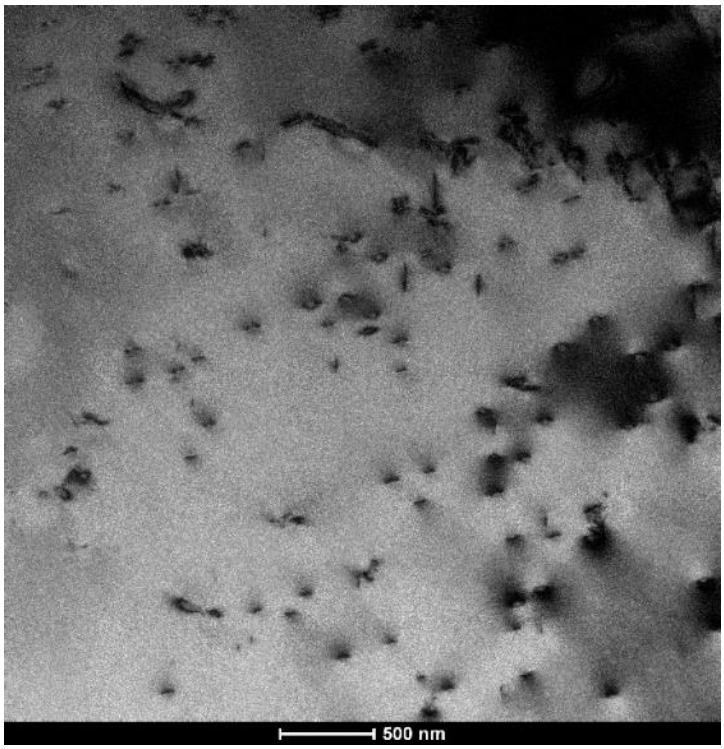

Figure 57. Microstructure inside a ferrite grain of flange body containing Cr_2N precipitates.

(a)

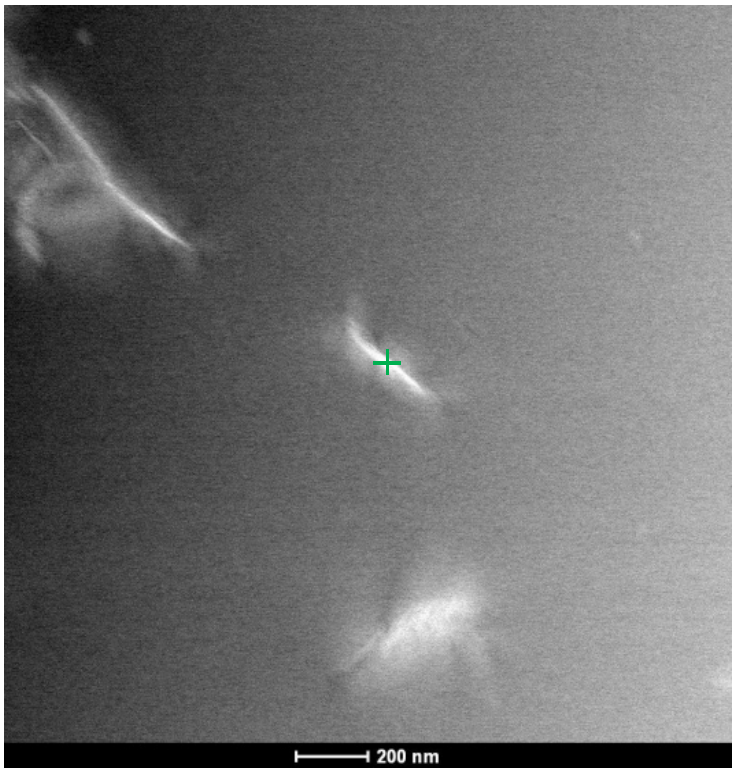

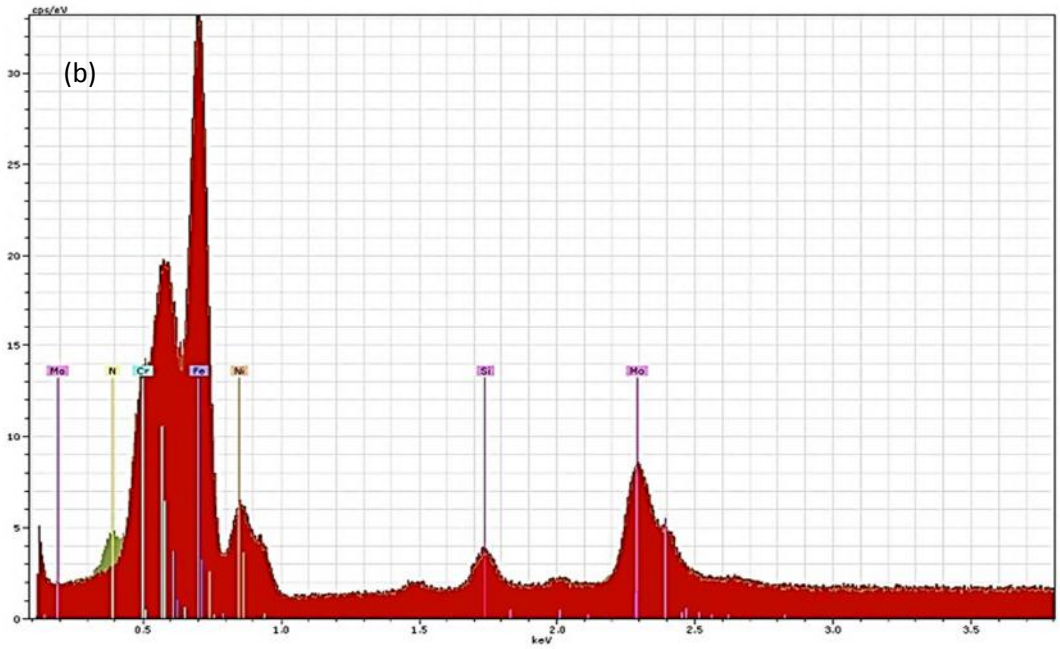

Figure 58. (a) Detail of intragranular Cr_2N precipitates in ferrite in flange body. (b) EDS profiles measured in ferrite (red) and on a particle (green).

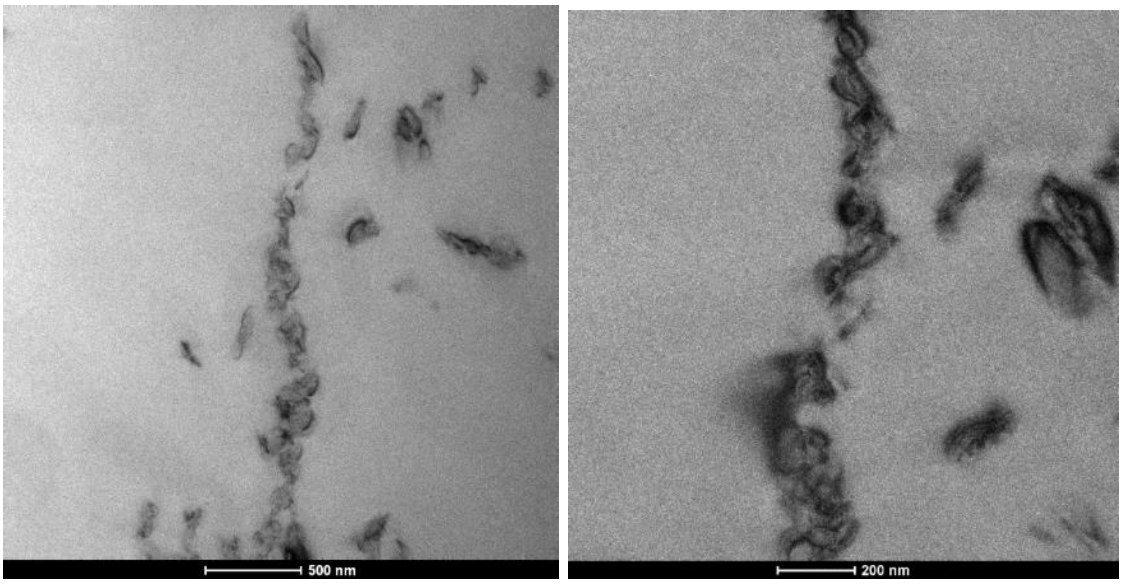

Figure 59. Detail of Cr_2N precipitates in an α/α grain boundary – flange body.

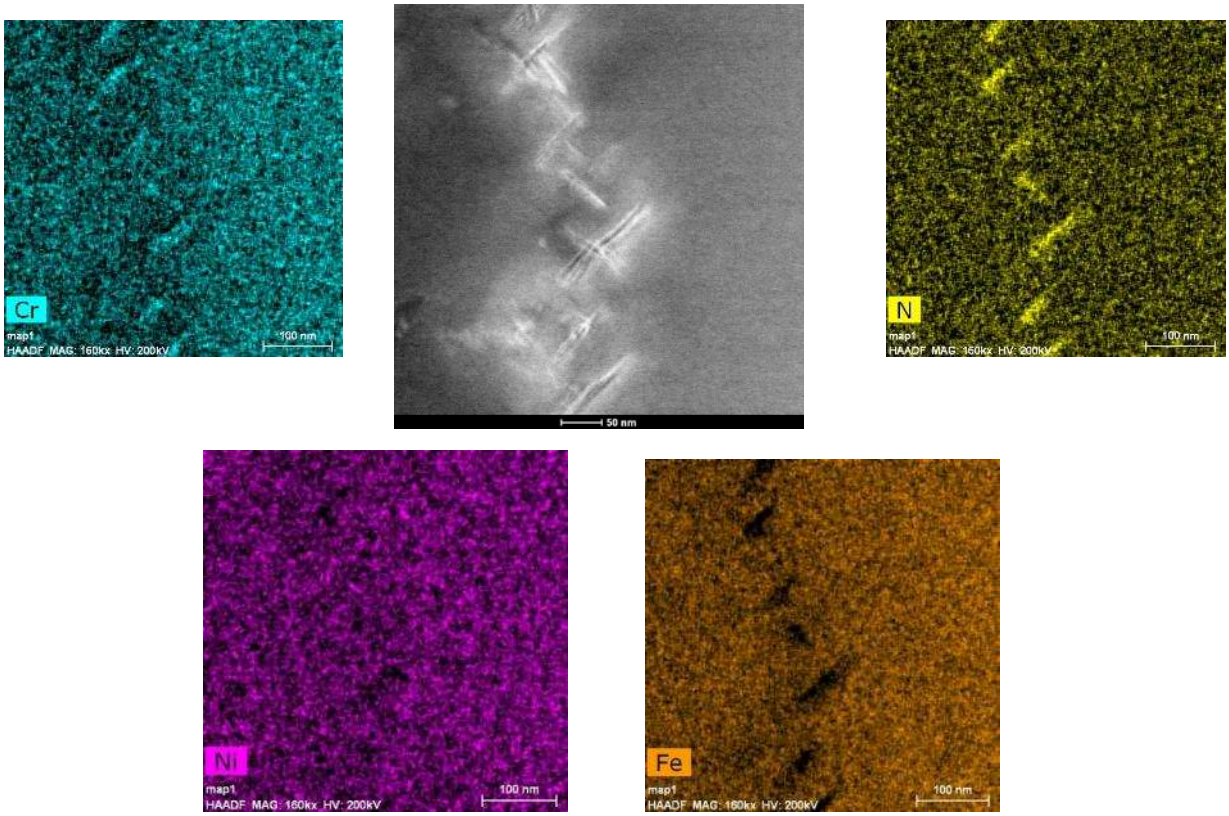

Figure 60. EDS mapping in a α/α boundary in the flange body.

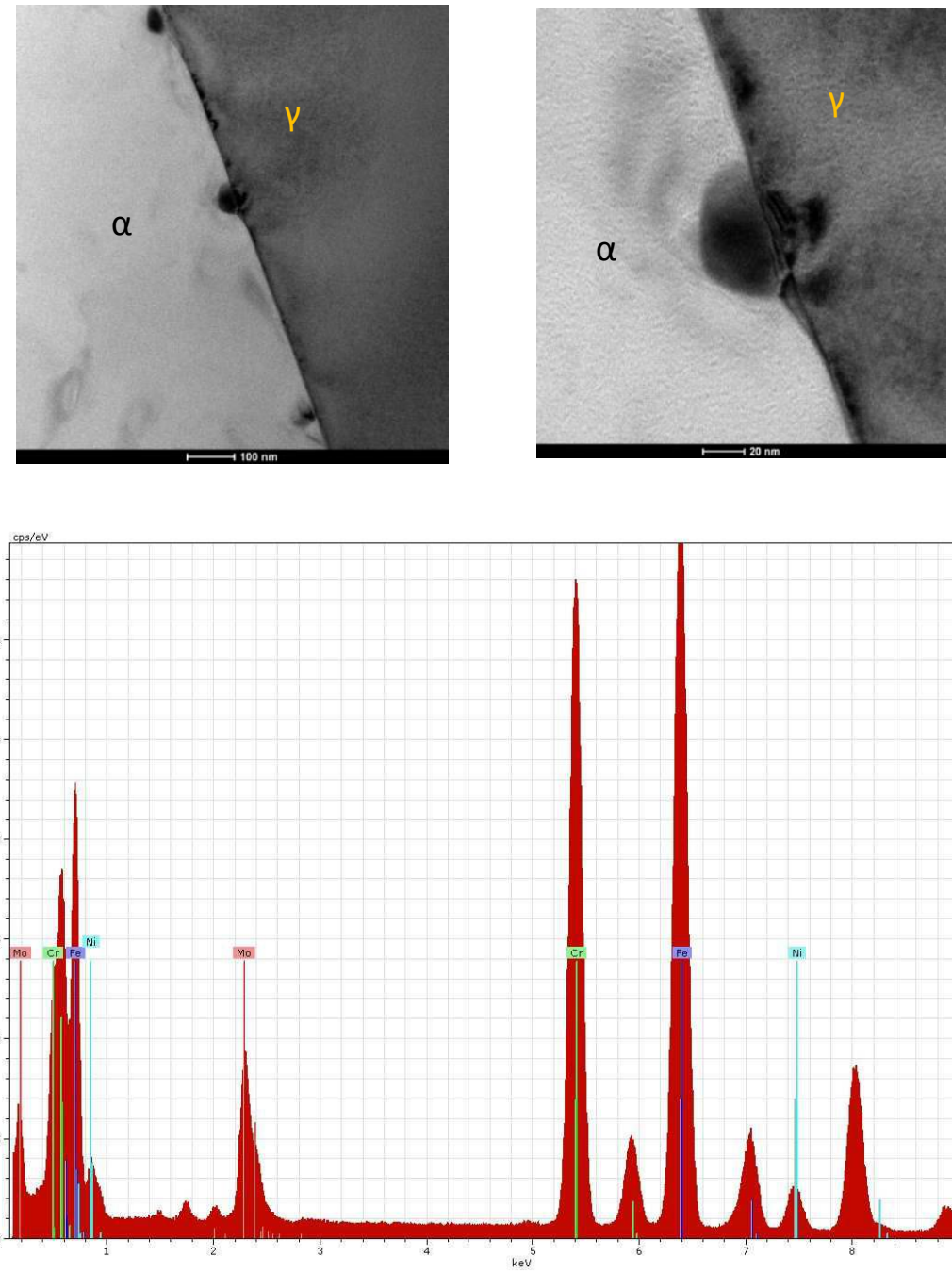

Figure 61. Bright field image of ferrite/austenite phase boundary in flange neck. EDS profile measured on a precipitate in the phase boundary.

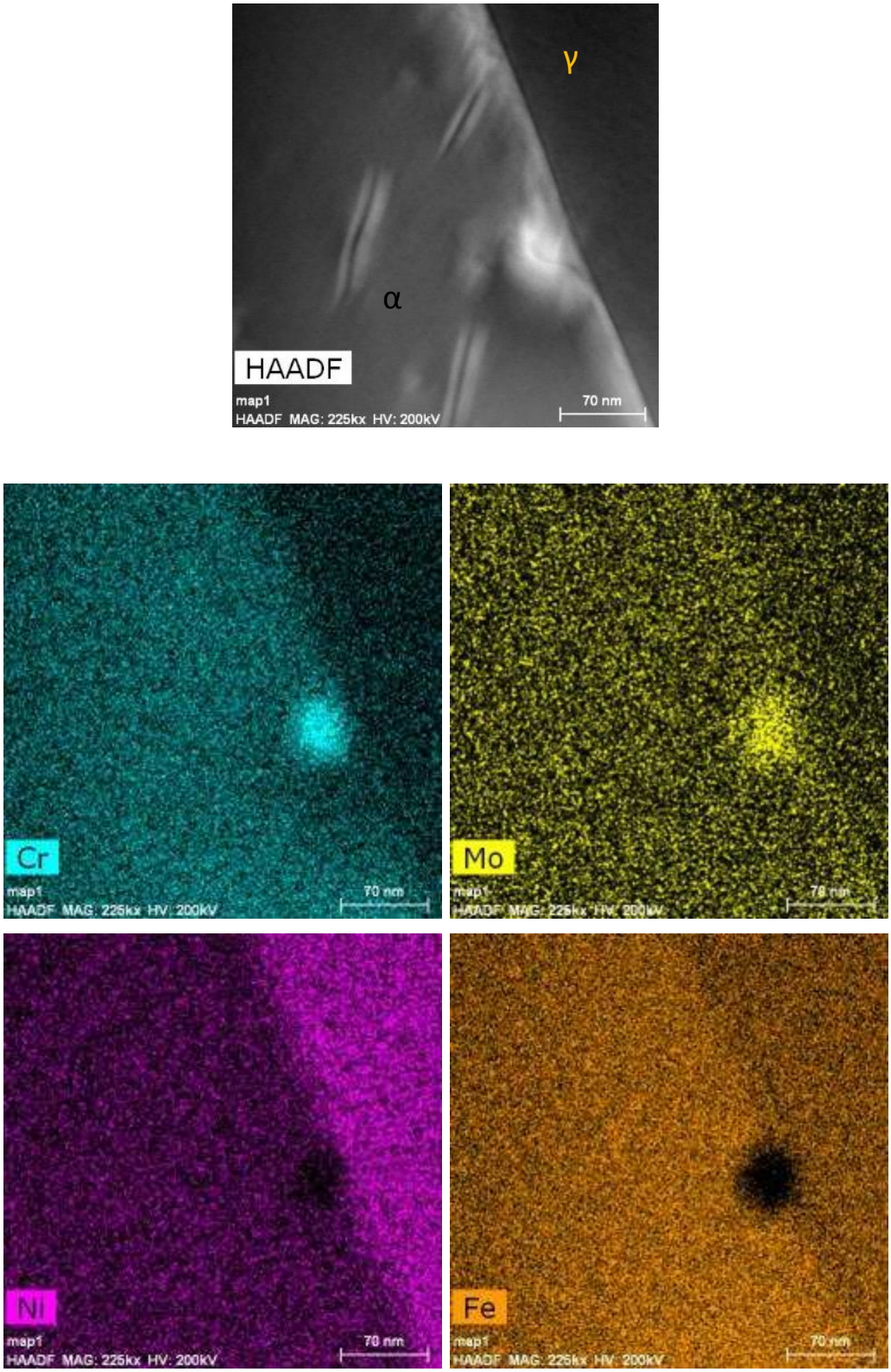

Figure 62. HAADF image and EDS mapping of ferrite/austenite phase boundary (flange neck).

4.3. X-Ray Diffraction

The measured diffraction patterns are presented in **Annex C**. Only characteristic peaks of ferrite and austenite are present. No sigma, chi, nitrides or martensitic phases were verified by XRD in either the non H-charged or the H-charged specimens.

Table 10 presents the calculated phase volume fractions. The average phase fractions estimated by metallography (58% ferrite, 42% austenite) is similar to the calculated values in the 2θ range of 20-100º. No statistically relevant difference between the specimens with and without previous hydrogen charging was verified considering these results.

The phase fractions varied greatly among all specimens. The obtained standard deviations were between 11 and 12%. The detectability limit of this technique is a phase fraction of 2%, while the typical error is usually smaller than ±4% [103,104]. Since the microstructure is rather coarse and the X-ray diffraction measurements are localized, it is believed that great part of the variability obtained comes from different regions measured.

Table 10. Phase fractions (%) estimated from the XRD results.

Specimen	2θ range considered			
	20-100º		20-50º	
	Austenite	Ferrite	Austenite	Ferrite
Non H-charged 1	48	52	48	52
Non H-charged 2	36	64	57	43
Non H-charged 3	63	36	73	27
Non H-charged 4	44	56	76	24
Average – Non H-charged	47,8	52,0	63,5	36,5
Hydrogen charged	60	40	53	47
Average - Total	50,2	49,6	61,4	38,6

4.4. Permeation Tests

4.4.1. Hydrogen Gas Permeation Tests

The general conditions of the gas volumetric permeation tests performed as well as some permeation (deuterium flux values vs time) curves obtained are shown in **Annex D**. Values clearly generated by acquisition errors, usually abnormally lower than immediately previous or subsequent measurements, were removed. These errors occurred typically when the electronic files were created or saved.

Verification of the applicability of equations and expressions based on Fick's laws, i.e. if the permeation transients were controlled by lattice diffusion, was performed according to standard BS EN ISO 17081. The measured and theoretical normalized flux ($J(t)/J_\infty$) vs normalized time τ ($D_{tL}t/L^2$) curves were compared. Diffusion coefficients calculated using the time-lag method were considered.

Where the normalized permeation transient is steeper than predicted from Fick's second law, as verified in the permeation step of tests 12 (**Figure 63**) and 14 (**Figure 65**), then trap occupancy is significant. A permeation transient less steep than predicted from Fick's law is an indication of unsteady surface conditions. This was verified e.g. on test 15 (**Figure 66**), in which the adsorption surface was not covered with Palladium. A rising plateau, present in tests 12, 16 and 17 (**Figure 66**), or peaks, such as in test 5 (**Figure 64**), can be due to changes in surface film.

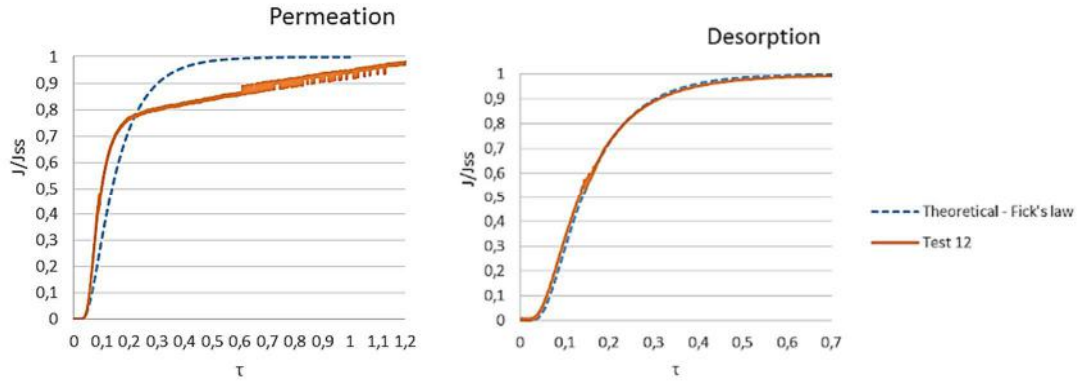

Figure 63. Permeation transient verification. Test 12 (flange neck, 280ºC, Pd on entry side).

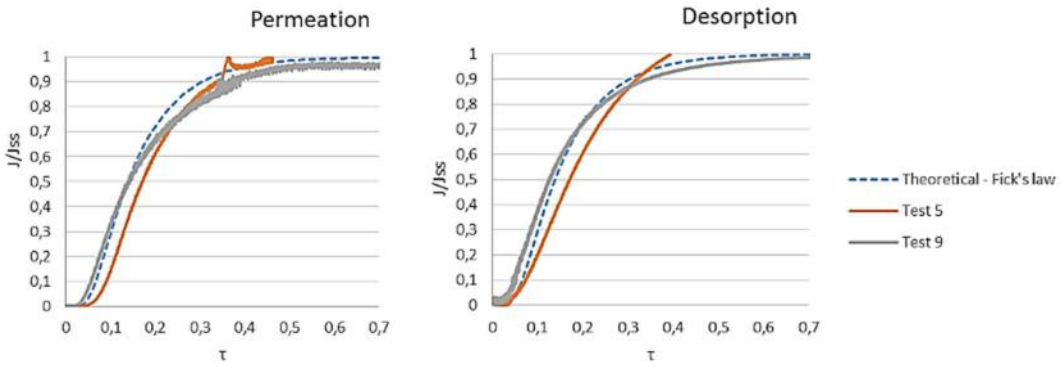

Figure 64. Permeation transient verification. Tests 5 and 9 (flange body, 200ºC).

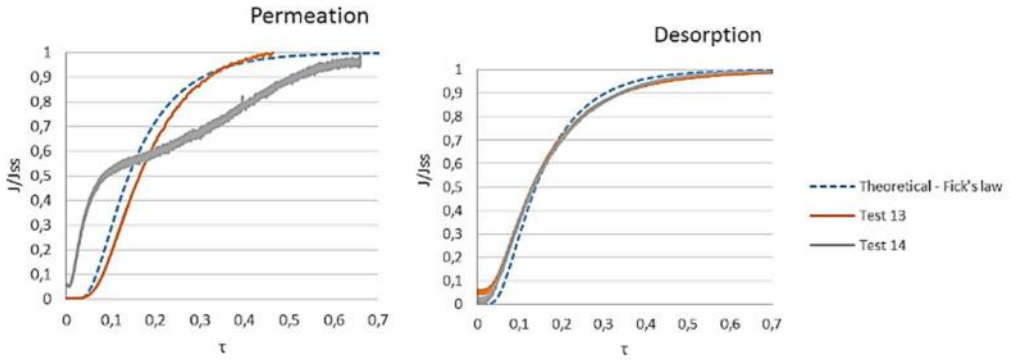

Figure 65. Permeation transient verification. Tests 13 and 14 (flange neck, 200ºC).

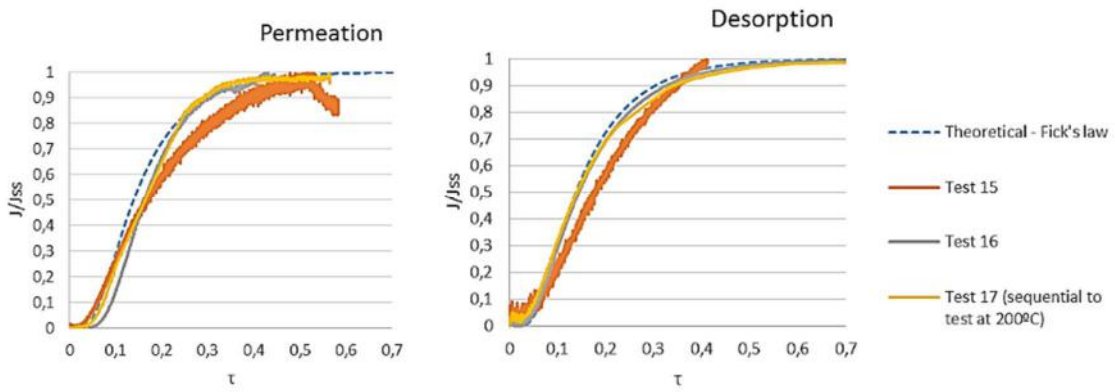

Figure 66. Permeation transient verification. Tests 15, 16 and 17 (flange neck, 150ºC).

Table 11 presents, according to described in section **3.2.1**, the deuterium diffusion coefficient values calculated using the time-lag method, as well as the solubilities. In all cases, the solubility was determined using only the data from the absorption step.

Table 11. Measured (deuterium) diffusion coefficients and solubilities.

Test	Flange position	Temperature (ºC)	Steady state flux (Nm^3/m^2s)	Diffusion coefficient D (time-lag method) - Permeation (m^2/s)	Solubility ($Nm^3.m^{-3}$)	Diffusion coefficient D (time-lag method) - Desorption (m^2/s)
1	Body	280	8,6E-08	5,2E-11	8,2E-01	4,7E-11
2	Body	280	8,6E-08	3,1E-11	1,4E+00	4,6E-11
3	Body	280	8,1E-08	3,5E-11	1,1E+00	4,3E-11
4	Body	280	2,2E-08	3,1E-11	3,5E-01	4,5E-11
5	Body	200	4,0E-09	6,8E-12	2,9E-01	9,7E-12
6	Body	150	6,0E-10	1,3E-12	2,2E-01	1,9E-12
7	Body	150	4,4E-09	1,7E-12	1,3E+00	2,1E-12
8	Body	150	3,5E-09	2,3E-12	7,6E-01	2,2E-12
9	Body	200	6,6E-09	2,8E-12	1,1E+00	4,6E-12
10	Body	150	8,3E-09	8,8E-13	4,5E+00	1,3E-12
11	Body	150	3,9E-10	6,3E-13	2,9E-01	1,1E-12
12	Neck	280	2,7E-07	1,5E-11	9,1E+00	3,8E-11
13	Neck	200	2,7E-08	4,9E-12	2,9E+00	4,9E-12
14	Neck	200	3,1E-10	1,1E-12	1,5E-01	4,1E-12
15	Neck	150	5,3E-11	6,4E-13	4,4E-02	1,8E-12
16	Neck	150	5,1E-09	1,5E-12	1,8E+00	1,6E-12
17	Neck	150	4,1E-09	1,0E-12	2,1E+00	1,1E-12
18	Body	80	1,2E-10	4,6E-14	5,6E-01	1,5E-13
19	Neck	80	9,0E-10	6,6E-14	3,4E+00	9,2E-14

As the permeation tests were executed using gas deuterium, the diffusivity was corrected to hydrogen (D_H) by multiplying the experimental values (D_D) by the square root of the mass ratio $\sqrt{2}$:

$$D_H = D_D\sqrt{2} \qquad \textbf{(Equation 58)}$$

This expression comes from the assumption that the ratio of diffusivity of hydrogen isotopes is equivalent to the inverse ratio of the square root of the masses of the isotopes. This relationship between isotopes stem from classical rate theory, which relates diffusivity to atomic vibrational frequencies and these frequencies are inversely proportional to mass [105].

Hydrogen diffusion coefficients converted from the measured data are presented in **Table 12.**

Table 12. Hydrogen diffusivities calculated from **Equation 58**.

Test	Flange position	Temperature (ºC)	Diffusion coefficient D (time-lag method) - Permeation (m^2/s)	Diffusion coefficient D (time-lag method) - Desorption (m^2/s)
1	Body	280	7,4E-11	6,6E-11
2	Body	280	4,4E-11	6,6E-11
3	Body	280	5,0E-11	6,0E-11
4	Body	280	4,5E-11	6,4E-11
5	Body	200	9,6E-12	1,4E-11
6	Body	150	1,9E-12	2,7E-12
7	Body	150	2,3E-12	2,9E-12
8	Body	150	3,2E-12	3,2E-12
9	Body	200	3,9E-12	6,5E-12
10	Body	150	1,2E-12	1,9E-12
11	Body	150	8,9E-13	1,5E-12
12	Neck	280	2,2E-11	5,3E-11
13	Neck	200	7,0E-12	7,0E-12
14	Neck	200	1,6E-12	5,8E-12
15	Neck	150	9,0E-13	2,5E-12
16	Neck	150	2,2E-12	2,3E-12
17	Neck	150	1,4E-12	1,5E-12
18	Body	80	6,5E-14	2,2E-13
19	Neck	80	9,4E-14	1,3E-13

4.4.2. Electrochemical Hydrogen Permeation Tests

The test conditions of the electrochemical permeation tests are shown in **Table 13**. The membrane thicknesses were 208 and 280 µm.

Table 13. Electrochemical permeation test conditions.

Test	Flange region	Pd layer side	Average thickness (mm)	Temperature (ºC)	Test current
1	Body	Charging side	0,280	23	0,6627 mA (1,5mA/cm²)
2	Neck	Charging side	0,208	23	0,6627 mA

Figures 67 presents the smoothed hydrogen flux values vs time measured in permeation tests with flange body and neck membranes.

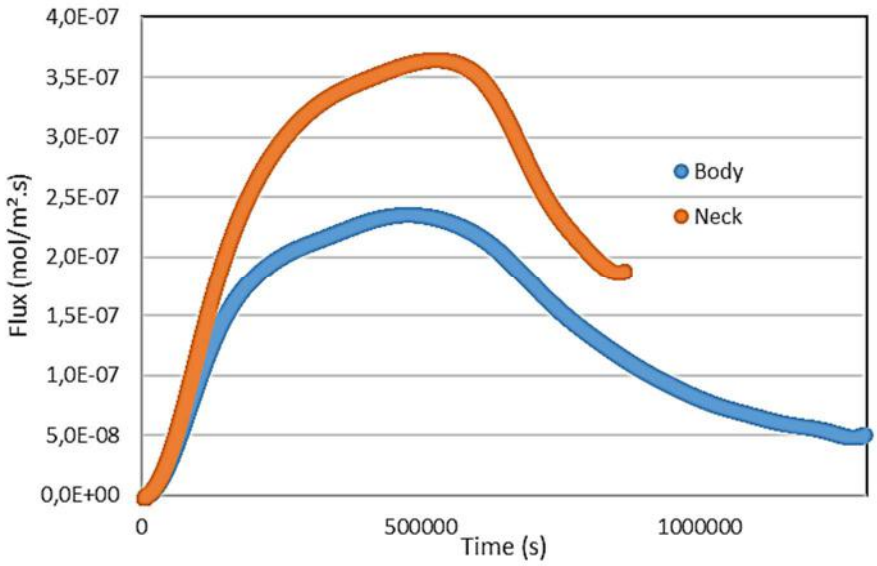

Figure 67. Permeation curves for flange body and neck specimens.

Verification of the applicability of Fick's second law to the permeation transients was performed similarly as done in gas-volumetric permeation analyses. As seen on **Figure 68**, the measured permeation transients were in general below than predicted from Fick's second law, indicating important effect of hydrogen trapping and that the trap occupancy was initially low.

(a)

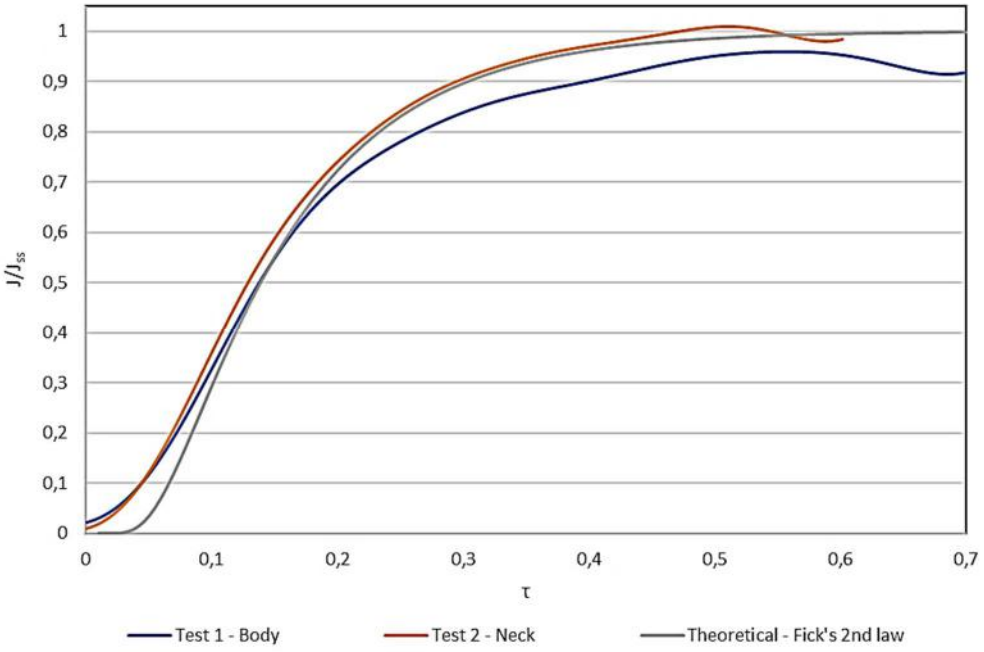

(b)

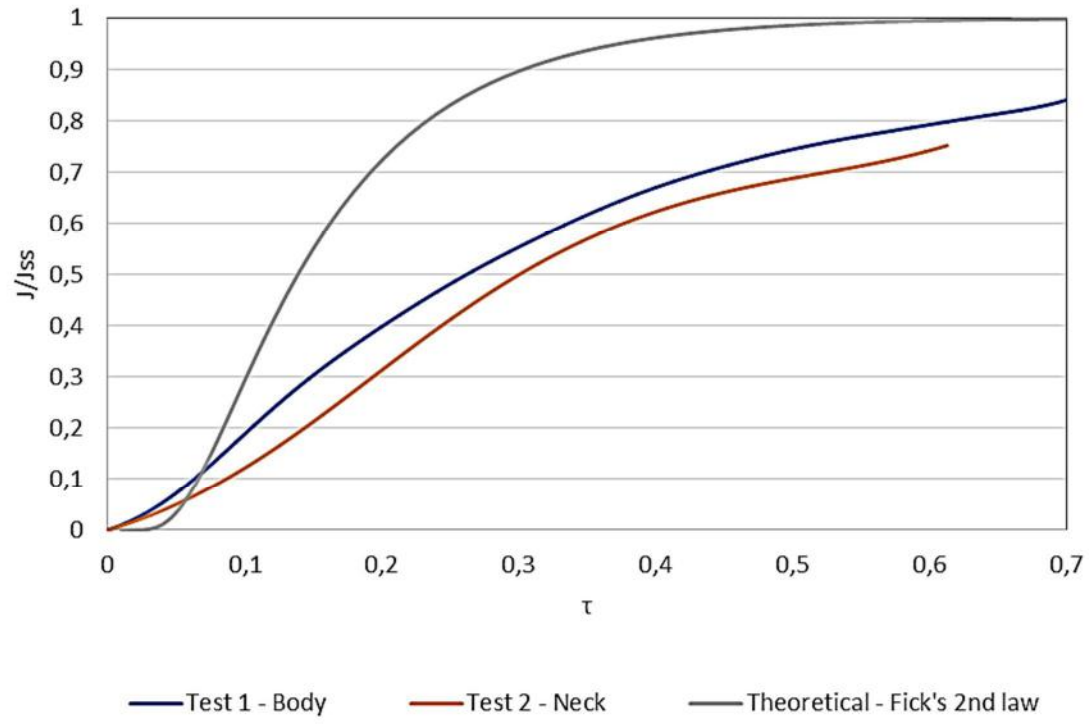

Figure 68. Transient verification. (a) Charging step. (b) Desorption step.

Table 14 presents the hydrogen diffusion coefficient values and solubilities.

Table 14. Measured hydrogen diffusion coefficients and solubilities.

Test	Flange position	Position of Pd layer	Temperature (ºC)	Steady state flux (mol/m²s)	Diffusion coefficient D_{tl} - Permeation (m²/s)	Diffusion coefficient D_{tl} - Desorption (m²/s)	Solubility (mol.m^{-3})
1	Body	Entry side	23	2,5E-07	9,3E-14	7,9E-14	749,36
2	Neck	Entry side	23	3,6E-07	4,3E-14	1,0E-13	1737,56

4.5. Mechanical Tests

The general conditions of the tensile tests are presented in **Annex E**. All tests were performed at room temperature (20-25ºC). The results are presently displayed in four condition groups, as described in section **3.2.2**:

a) Tests in air without previous hydrogen charging.

b) Tests with in-situ gas H_2 charging, without previous hydrogen charging.

c) Tests with electrochemical charging, without previous hydrogen charging.

d) Tests in air with specimens previously charged.

A sequential specimen designation is adopted.

4.5.1. Tests in Air of Non Pre-Charged Samples

The stress-strain curves obtained for the tests in air (group “a”) are shown in **Figures 69** and **70**. **Tables 15** and **16** list the measured tensile properties.

In all tests, the elasticity modulus was assumed as 197,1 GPa. The average values of the flange body tests were calculated excluding test F1B32 that was performed at a lower strain rate (10^{-6} s^{-1}). The mean values were used for the embrittlement ratio calculations in tests with hydrogen. Except for the test F1B32, the measured properties in general met the minimum requirements of ASTM A182 grade F53 (UTS > 730 MPa, YS > 515 MPa, elongation > 15%). The yield strength of F1B16 was slightly below the minimum required. For both the body and the neck, the scatter is quite large. The coarse microstructure is considered the main cause for this scatter in mechanical properties.

As expected from the finer microstructure, flange neck presented in average greater tensile properties (YS 620 MPa, UTS 788 MPa) than the body (YS 529 MPa, UTS 758 MPa).

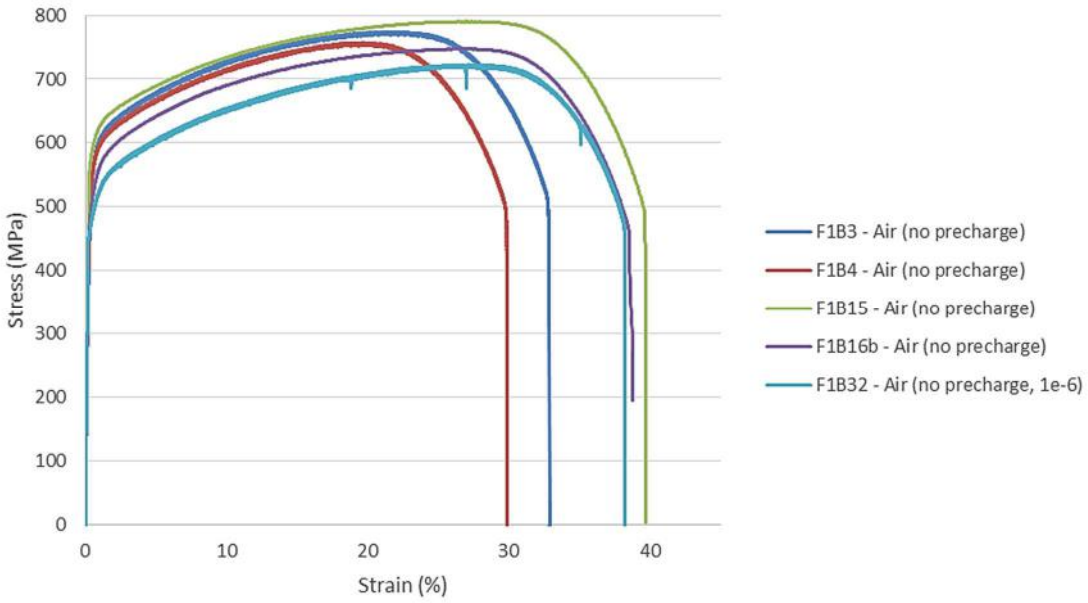

Figure 69. Tests in air – Flange body.

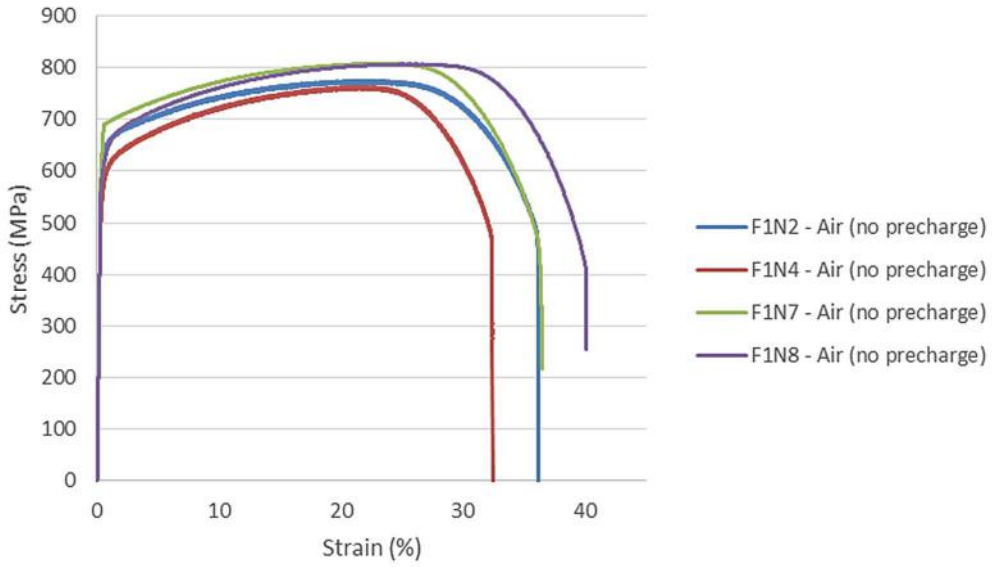

Figure 70. Tests in air – Flange neck.

Table 15. Tensile properties in air – Body samples.

Property	F1B32	F1B15	F1B16	F1B3	F1B4	Average (excluded F1B32)
Yield strength (MPa)	478,0	587,8	503,2	532,5	543,0	541,6
Ultimate strength (MPa)	723,0	789,9	746,9	773,8	757,0	766,9
Reduction of area (%) - ROA	69,7	66,0	54,6	64,5	67,5	63,2
Final elongation (%)	32,3	38,3	36,8	26,5	30,7	33,1
Fracture strain (%) - ε_f	38,3	39,7	38,8	32,9	29,9	35,3
Plastic fracture strain (%) - ε_{fp}	38,0	39,4	38,5	32,6	29,6	35,1
Plastic strain at maximum load (%) - $\varepsilon_{p\text{-}max}$	27,4	27,7	27,0	21,9	19,4	24,0

Table 16. Tensile properties in air – Neck samples.

Property	F1N2	F1N4	F1N7	F1N8	Average
Yield strength (MPa)	625,0	565,0	684,6	605,4	619,9
Ultimate strength (MPa)	775,0	762,7	807,8	806,3	787,9
Reduction of area (%) - ROA	69,9	75,8	78,8	86,8	77,8
Final elongation (%)	41,8	29,5	40,6	34,0	36,5
Fracture strain (%) - ε_f	36,2	32,4	36,5	40,1	36,3
Plastic fracture strain (%) - ε_{fp}	35,9	32,2	36,2	39,8	36,0
Plastic strain at maximum load (%) - $\varepsilon_{p\text{-}max}$	21,7	21,1	23,0	26,3	23,1

Vickers micro-hardness measurements were performed according to ASTM E384 (2011) on sections normal to the circumferential direction of both the flange body and neck (without previous hydrogen charging). The measurements were performed with a load of 25 gf and indentation time of 10 seconds, using the tester Buehler Micromet 2104. The average values from 5 measurements (**Table 17**) indicate ferrite is always harder than austenite. The flange neck is also slightly harder than the body.

Table 17. Vickers microhardness (HV0,025) of non pre-charged specimens.

	Austenite	**Ferrite**
Neck	243,2	273,6
Body	243,0	263,4

4.5.2. Tests with In-situ Hydrogen Charging

The stress-strain curves obtained for the tests performed with in-situ gas H_2 charging (group "b") are shown in **Figures 71** and **72**. The measured tensile properties are presented in **Annex E.**

Three ratios between the ductility parameters measured in the hydrogen-rich environments and the average properties measured in air were used for the embrittlement degree evaluation:

a) Relative reduction of area (%):

$$\mathrm{ROA_R} = 100\frac{\mathrm{ROA}}{\mathrm{ROA_{air}}} \qquad \textbf{(Equation 59)}$$

b) Plastic strain at maximum load ratio (%):

$$\varepsilon_{\mathrm{p-max_R}} = 100\frac{\varepsilon_{\mathrm{p-max}}}{\varepsilon_{\mathrm{p-max_{air}}}} \qquad \textbf{(Equation 60)}$$

c) Plastic strain-to-failure ratio (or plastic fracture strain ratio) (%):

$$\varepsilon_{\mathrm{p-F_R}} = 100\frac{\varepsilon_{\mathrm{p-F}}}{\varepsilon_{\mathrm{p-F_{air}}}} \qquad \textbf{(Equation 61)}$$

Values close to 100% indicate high resistance to hydrogen damage or low degree of hydrogen damage/embrittlement, whereas low values generally indicate elevated embrittlement degree.

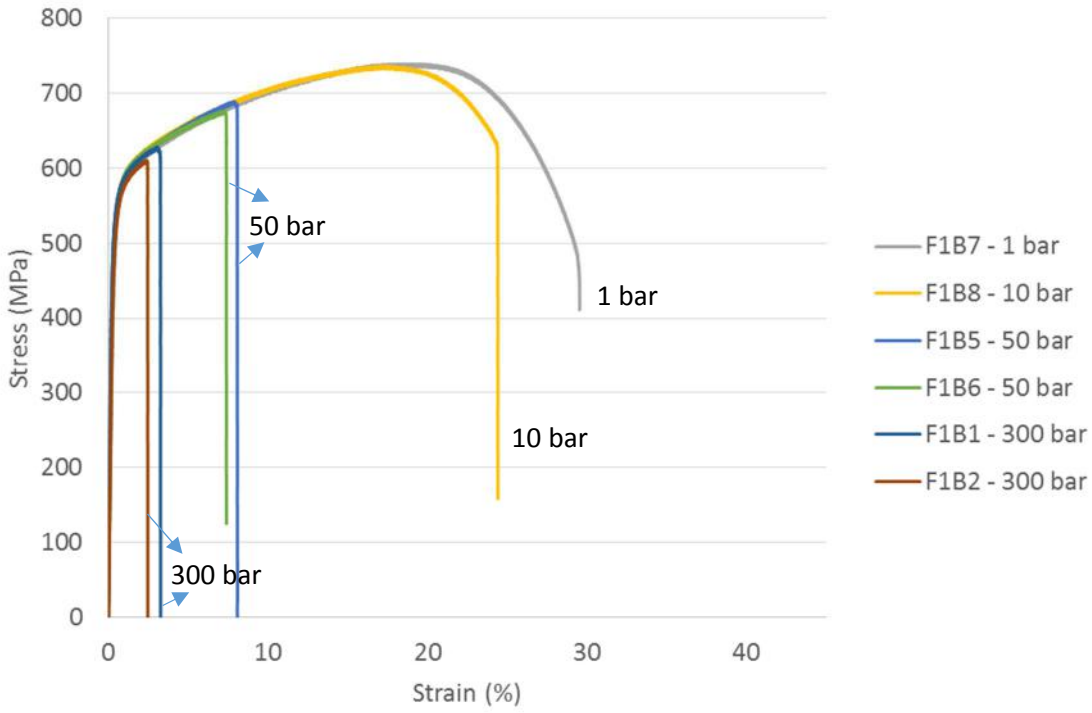

Figure 71. Tests with in-situ gaseous H charging – Flange body. Strain rate: $10^{-5}\,s^{-1}$.

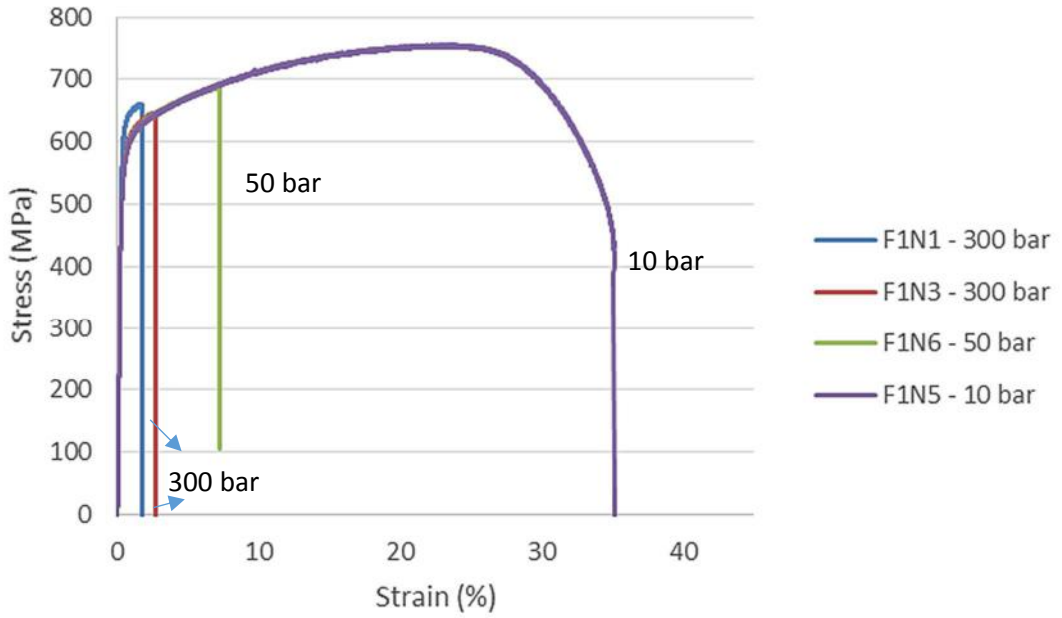

Figure 72. Tests with in-situ gaseous H charging – Flange neck. Strain rate: $10^{-5}\,s^{-1}$.

The stress-strain curves obtained for the tests on flange body specimens performed with in-situ cathodic hydrogen charging (group “c”) are shown **Figures 73** and **74**. The flange neck results are shown in **Figures 75** and **76**. The measured tensile properties are displayed in **Annex E**.

Data of tests F1B21 and F1B22 were removed from the embrittlement analyses. These tests were performed with a cathodic current of 3000 mA (current density of 1430 mA/cm²). This charging condition caused excessive bubble formation, so that important dispersion resulted. The variations obtained in other tests performed at the same conditions, e.g. F1B19 and F1B20, are within the experimental error, so that relatively good repeatability was verified on these tests.

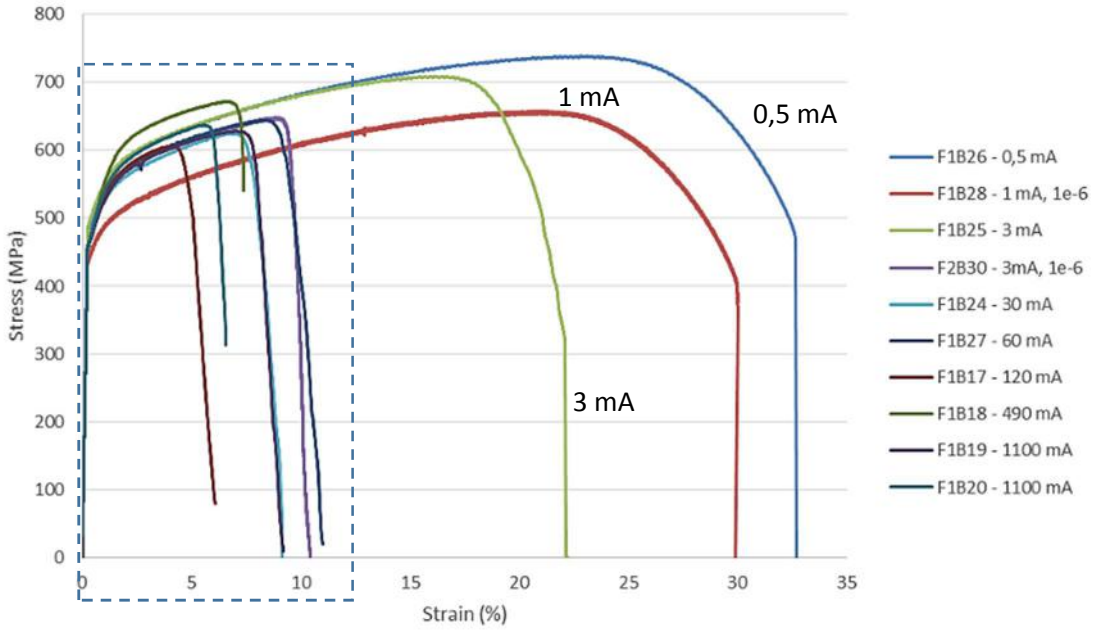

Figure 73. Tests with in-situ cathodic H charging – Flange body.

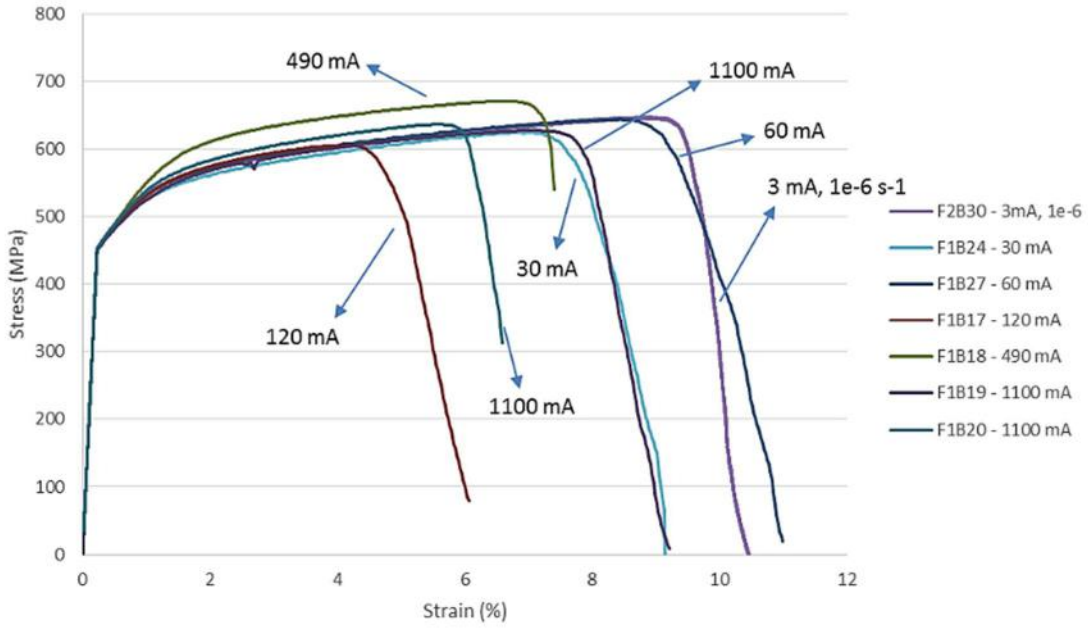

Figure 74. Detail of **Figure 73** at ε < 12%.

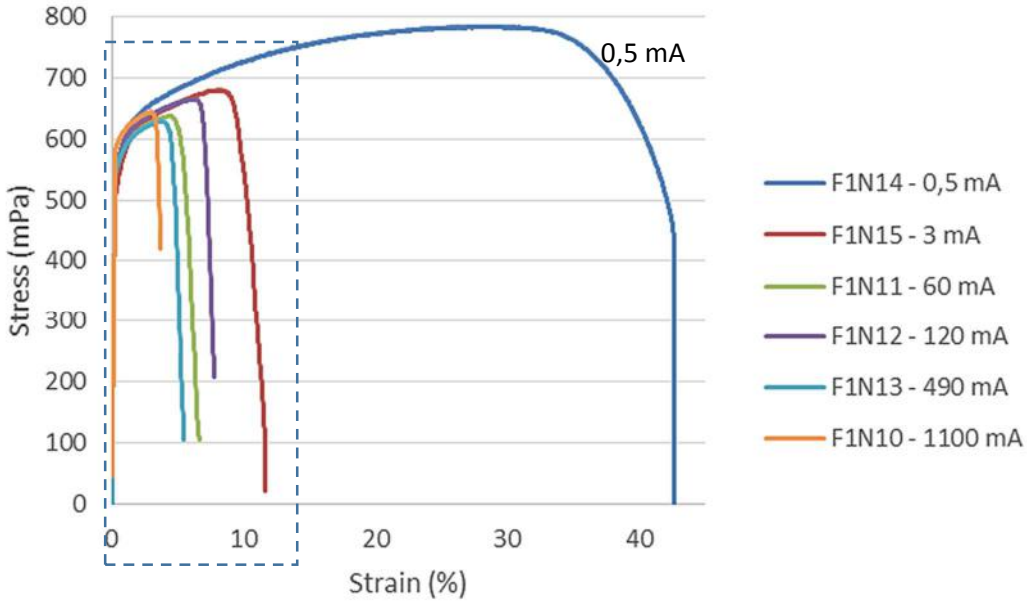

Figure 75. Tests with in-situ cathodic H charging – Flange neck.

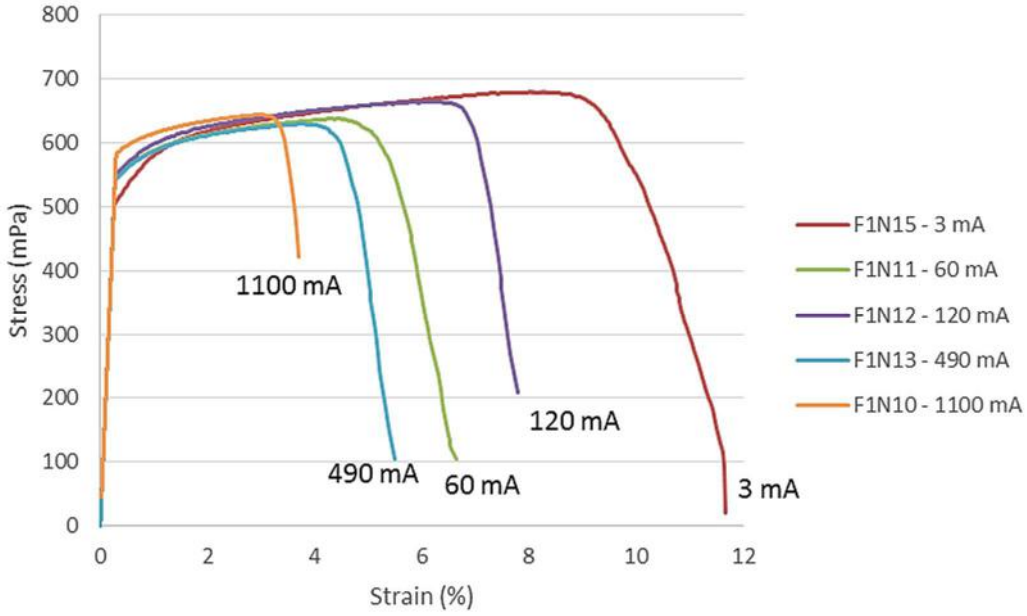

Figure 76. Detail of **Figure 75** at ε < 12%.

Figures 77 to **79** present the values of ductility ratios measured in the tests with in-situ gas hydrogen. A ductility loss above 60% was measured at pressures equal to or above 50 bar for both flange body and neck specimens. The level of embrittlement was nearly constant above the 50 bar pressure threshold. The existence of such a plateau of embrittlement as a function of the hydrogen activity can be verified under different hydrogen-rich environments and charging conditions [25].

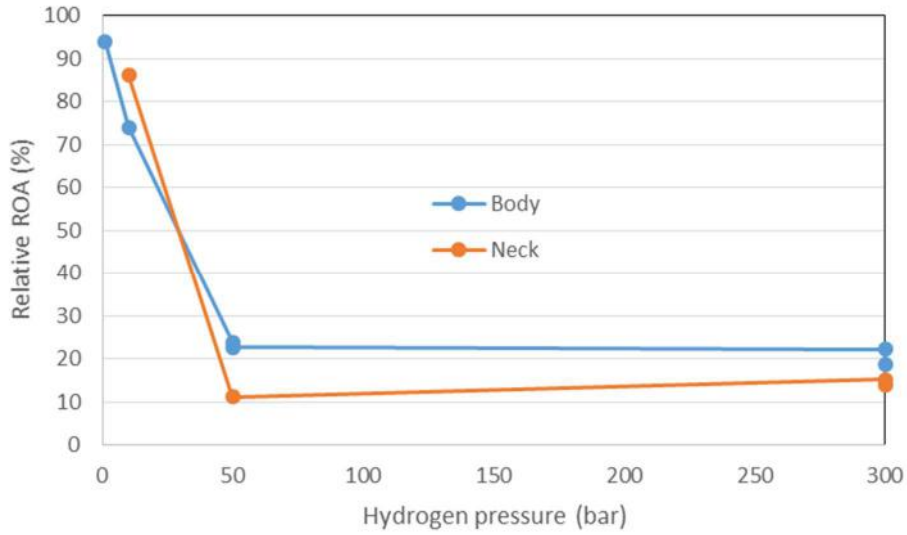

Figure 77. Relative reduction of area as function of pressure with in-situ gaseous H charging – Flange body and neck.

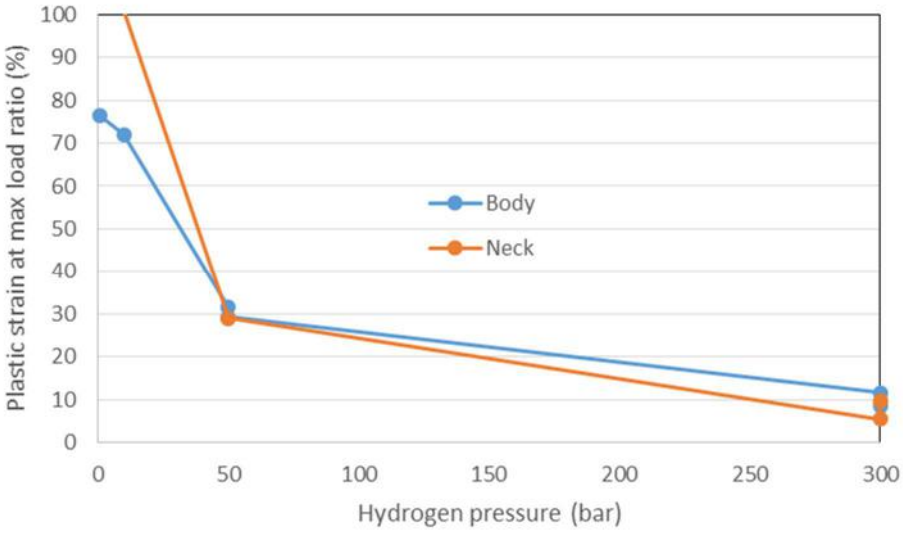

Figure 78. $\varepsilon_{pmax\text{-}r}$ as function of pressure with in-situ gaseous H charging – Flange body and neck.

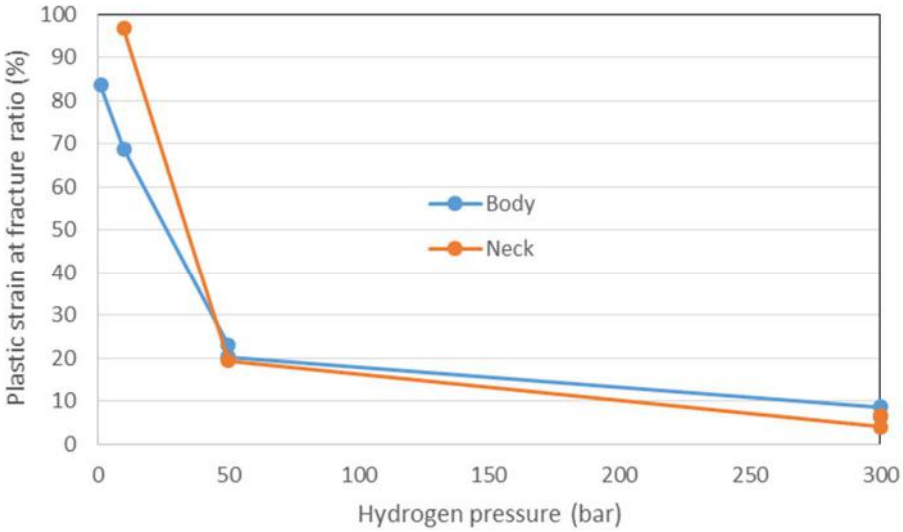

Figure 79. $\varepsilon_{pf\text{-}r}$ as function of pressure with in-situ gaseous H charging – Flange body and neck.

Figures 80 to **82** present values of ductility ratios measured in the tests with in-situ electrochemical charging. There is an enhancement of the embrittlement degree from 0,5 mA to 3 mA at the strain rate of 10^{-5} s^{-1}. At currents equal to and more cathodic than ca. 30-60 mA (at $\dot{\varepsilon} = 10^{-5}$ s^{-1}), there is no clear trend on the embrittlement degree. The embrittlement ratios at currents between 30 and 1100 mA fall within a dispersion range of low ductility values, similarly to the behavior observed in in-situ gaseous tests above 50 bar.

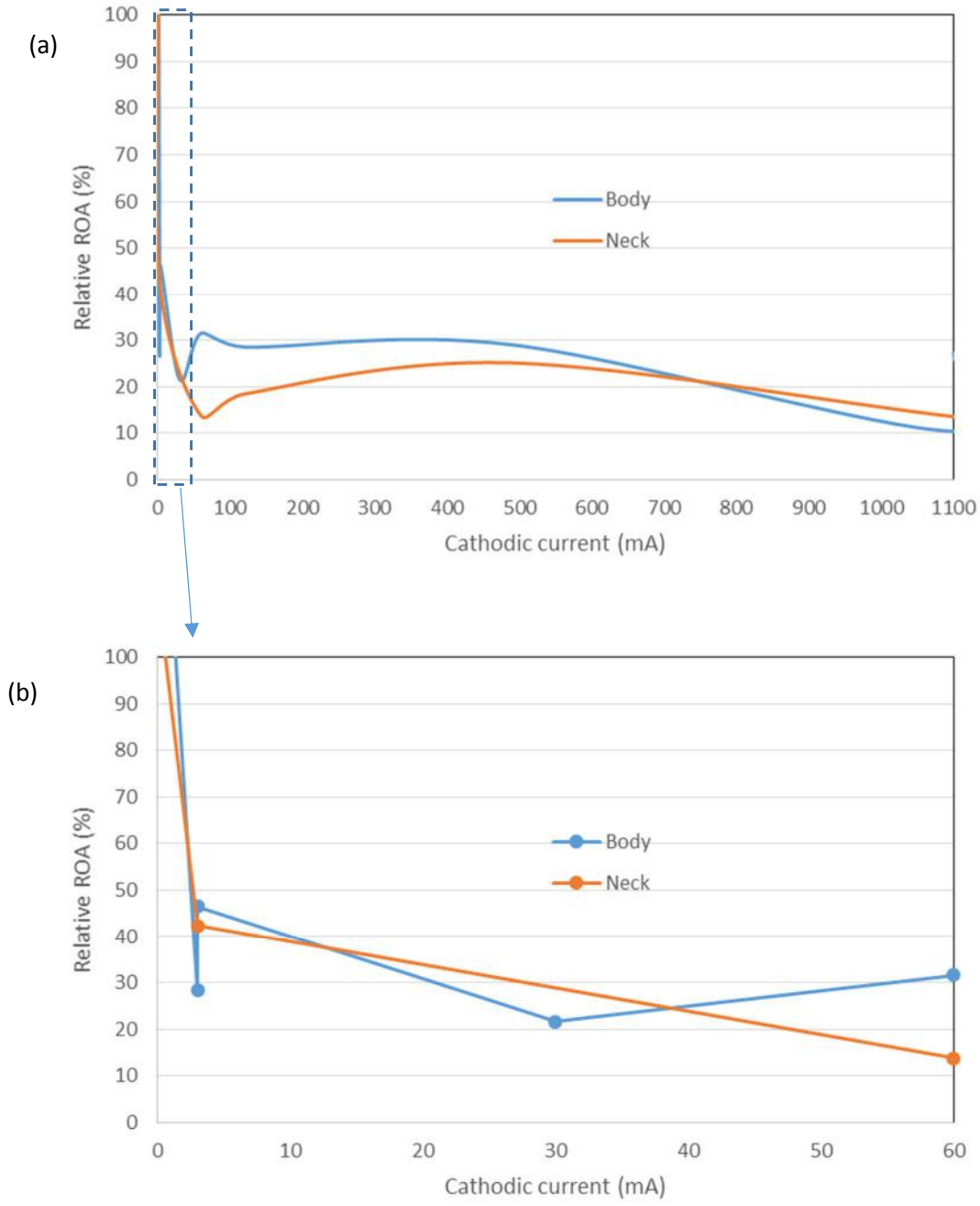

Figure 80. (a) Relative reduction of area as function of current with in-situ cathodic charging – Flange body and neck. (b) Detail at low currents.

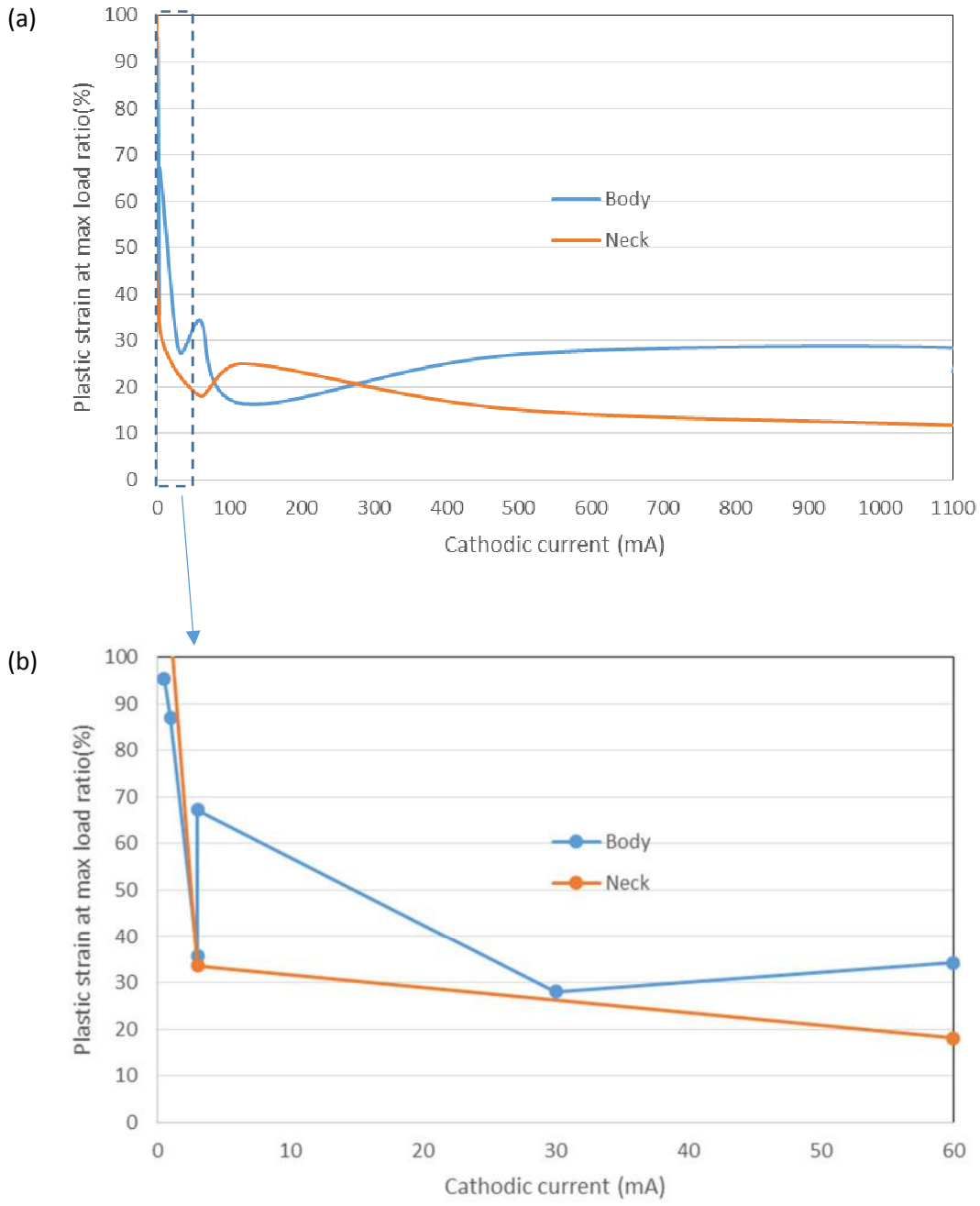

Figure 81. (a) $\varepsilon_{pmax\text{-}r}$ as function of current with in-situ cathodic charging – Flange body and neck. (b) Detail at low currents.

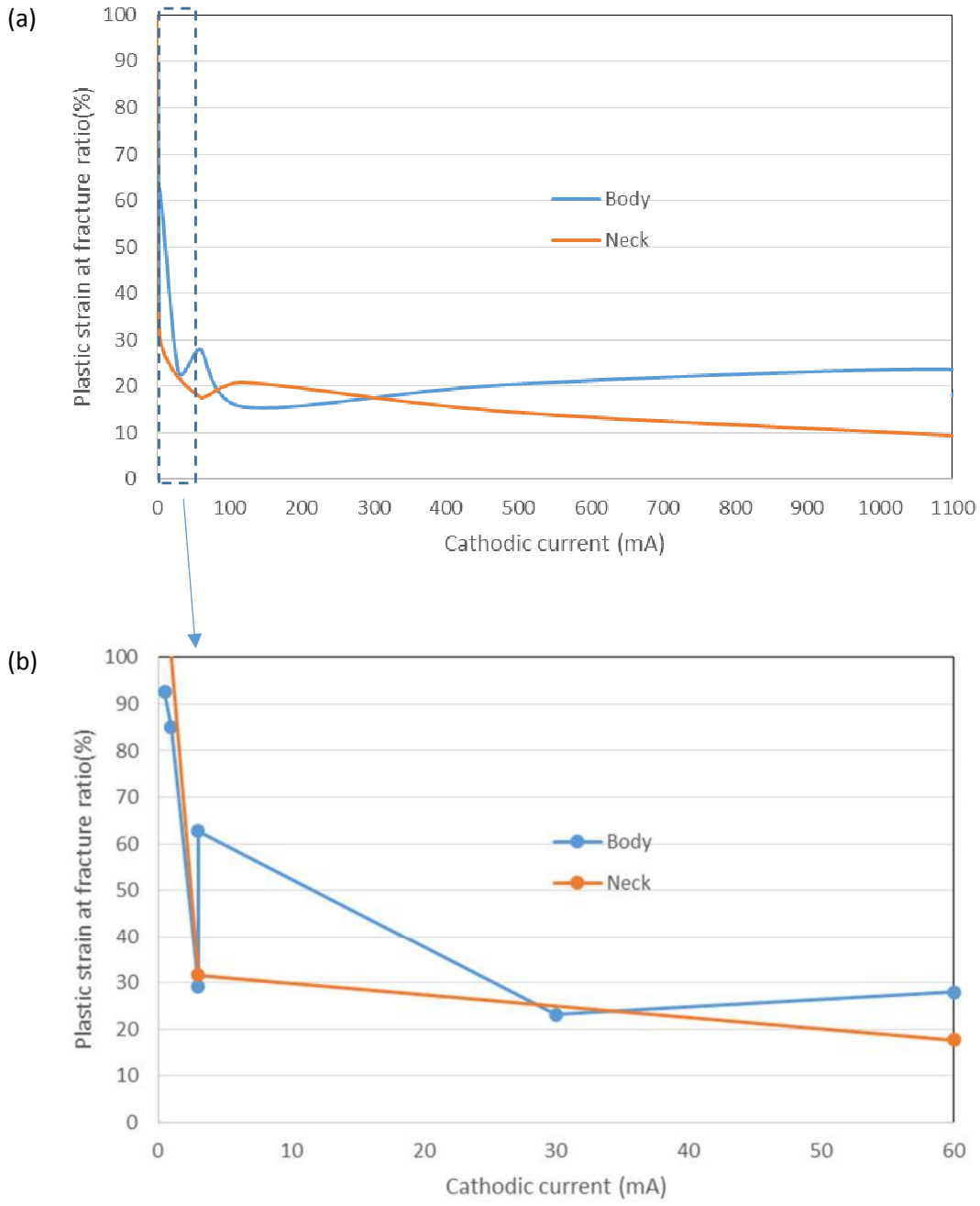

Figure 82. (a) $\varepsilon_{pf\text{-}r}$ as function of current with in-situ cathodic charging – Flange body and neck. (b) Detail at low currents.

Figures 83 and **84** display the values of yield and ultimate tensile strength as a function of hydrogen pressure and cathodic current. It is evident that the presence and activity of hydrogen implied no relevant difference on the yield stress level in the in-situ charging tests. A slight reduction of UTS occurred at high hydrogen activities.

(a)

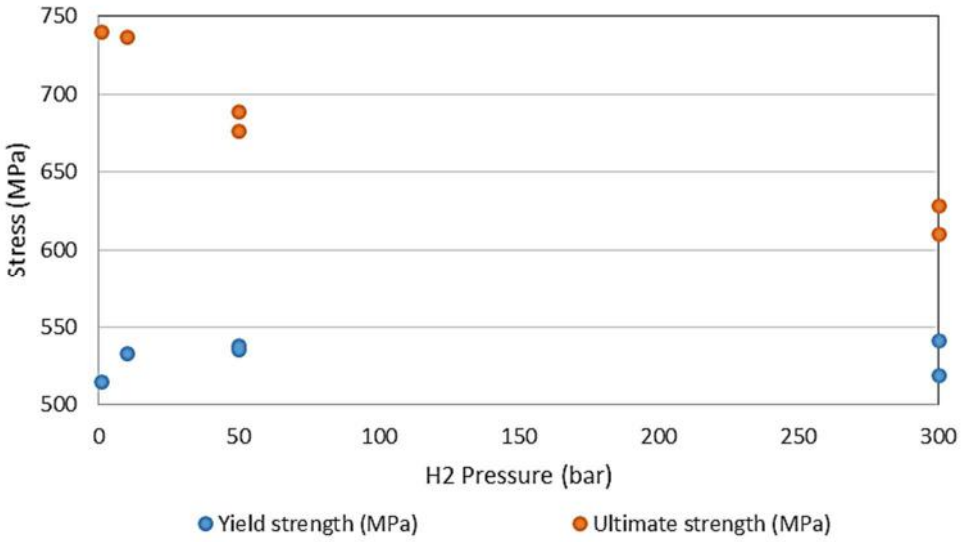

(b)

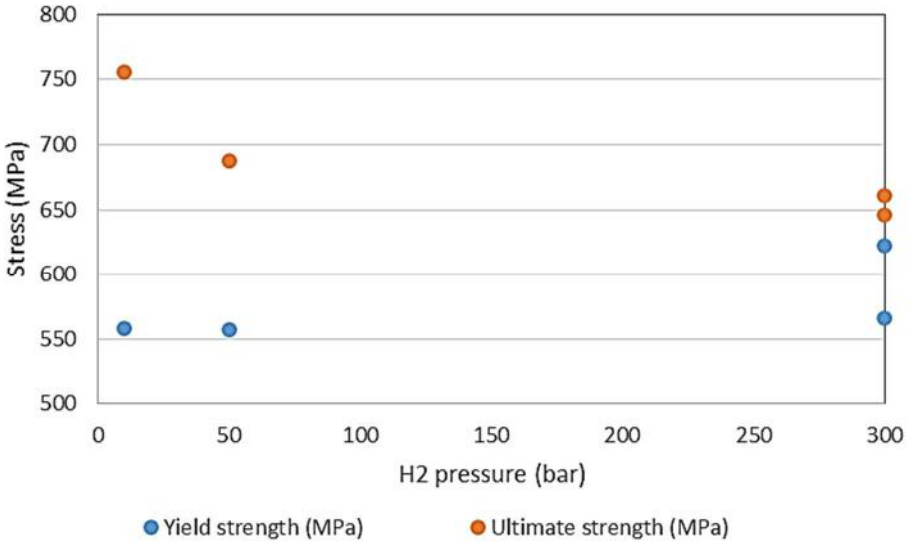

Figure 83. Variation of YS and UTS with hydrogen pressure. (a) Body. (b) Neck.

(a)

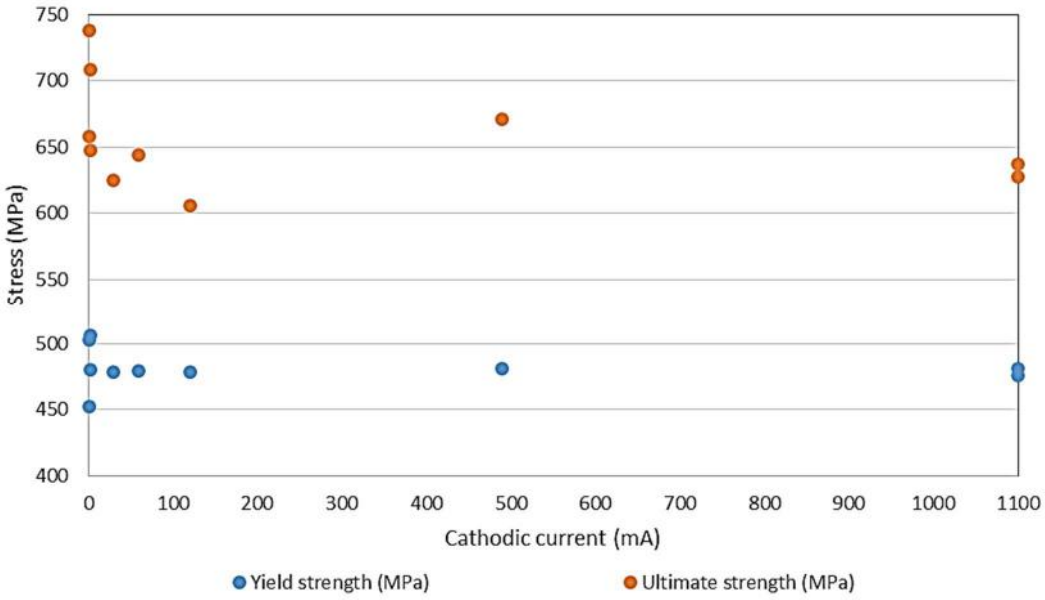

(b)

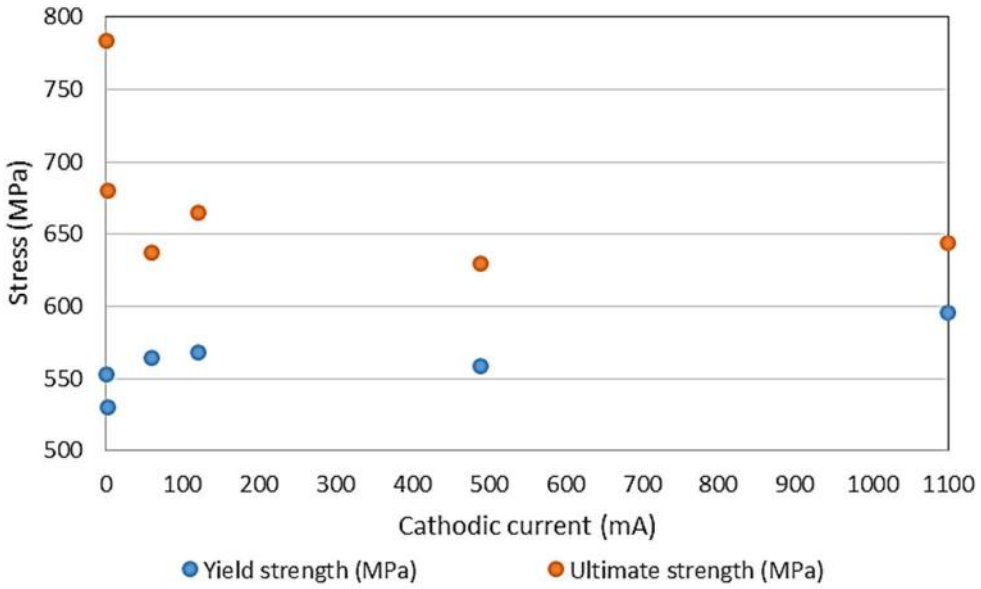

Figure 84. Variation of YS and UTS with cathodic current. (a) Body. (b) Neck.

4.5.3. Tests in Air of Hydrogen Pre-charged Samples

The stress-strain curves obtained for the tests performed in air with specimens pre-charged (group “d”) are shown in **Figure 85**. **Table 18** list the measured tensile properties.

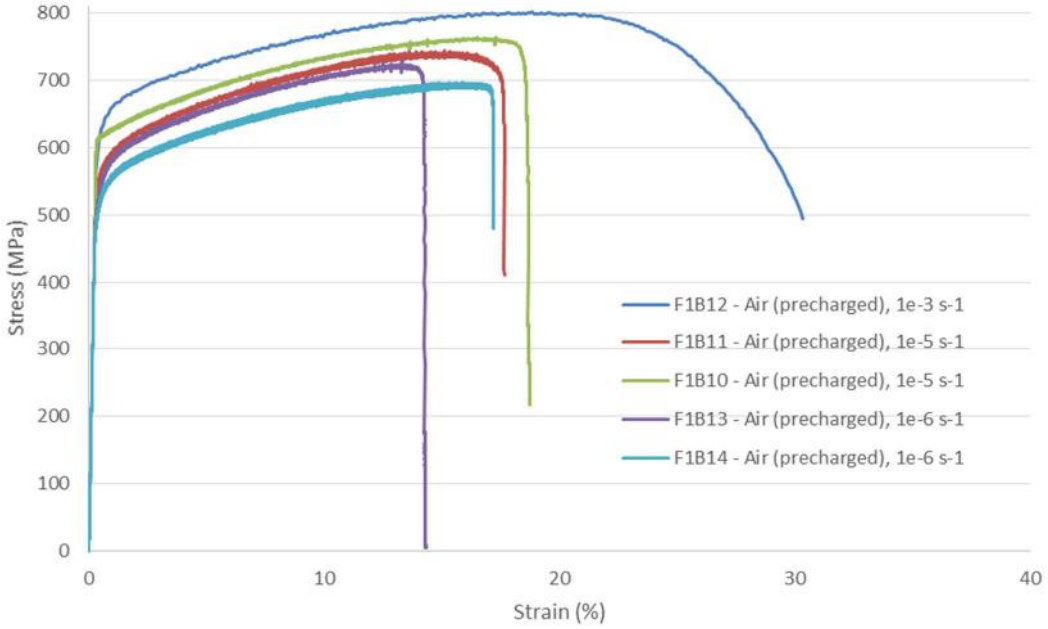

Figure 85. Tests in air with pre-charged body specimens.

Table 18. Tensile properties obtained in tests in air with pre-charged samples.

	F1B10	F1B11	F1B12	F1B13	F1B14
Yield strength (MPa)	616,0	559,5	624,0	538,0	518,0
Ultimate strength (MPa)	763,2	743,6	800,3	729,1	696,3
Reduction of area (%) - ROA	21,60	33,37	64,69	20,57	22,92
Final elongation (%)	23,32	22,57	41,07	15,89	7,85
Fracture strain (%) - ε_f	18,73	17,66	30,31	14,31	17,2
Plastic fracture strain (%) - ε_{fp}	18,42	17,38	29,99	14,04	16,94
Plastic strain at maximum load (%) - $\varepsilon_{p\text{-}max}$	16,95	14,82	18,50	13,03	15,61
Relative ROA (%)	34,20	52,84	102,4	32,57	36,29
Plastic strain at maximum load ratio (%)	70,63	61,76	77,09	54,3	65,03
Plastic fracture strain ratio (%)	52,55	49,57	85,57	40,05	48,32

Measured yield and ultimate strength values as a function of the strain rate for the flange body (tests F1B10 to F1B14) are displayed in **Figure 86**. The relationship between stress and strain rate is given by the Hollomon equation [106]:

$$\sigma = K\dot{\varepsilon}^{m} \qquad \textbf{(Equation 62)}$$

The calculated values of the strain-rate sensitivity factor "m" and the material constant "K" are shown in **Table 19**.

Table 19. Strain-rate parameters calculated for body specimens tested in air.

	Yield strength	**Ultimate stress**
m	0,0242	0,0168
K	752,63	905,03

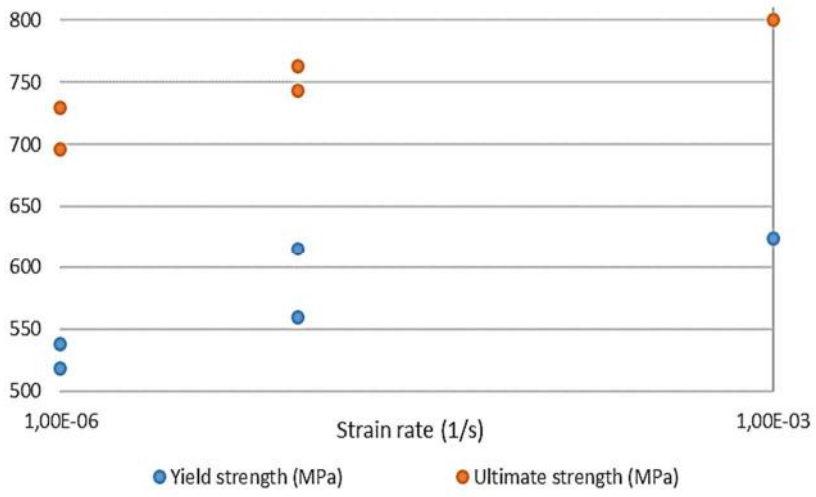

Figure 86. Variation of YS and UTS with strain rate.

Figure 87 shows the variation of the ductility ratios as a function of the strain rate. Major ductility losses occurred in the ex-situ charging tests at strain rates equal or lower than 10^{-5} s^{-1}. The level of embrittlement was nearly constant below the strain rate of 10^{-5} s^{-1}.

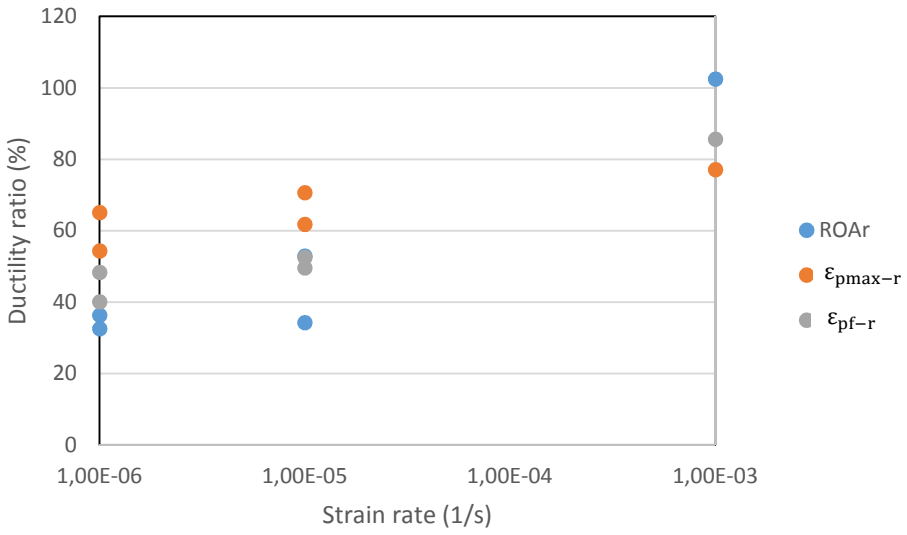

Figure 87. Effect of strain rate on the embrittlement degree of pre-charged samples tested in air.

4.5.4. Fractographic Characterization

Figures 88 displays typical low magnification image of a non pre-charged specimen tested in air. Cup-and-cone fracture and extensive plastic deformation were evident both in body and neck specimens. **Figure 89** shows the microstructure of sections of representative fractures. The fractures propagated indiscriminately through ferrite and austenite.

Figure 90 shows secondary electron images of the fracture surface of a non pre-charged specimen tested in air. All non pre-charged samples tested in air presented similar fractures, composed by ductile dimples initiated at small inclusions or precipitates.

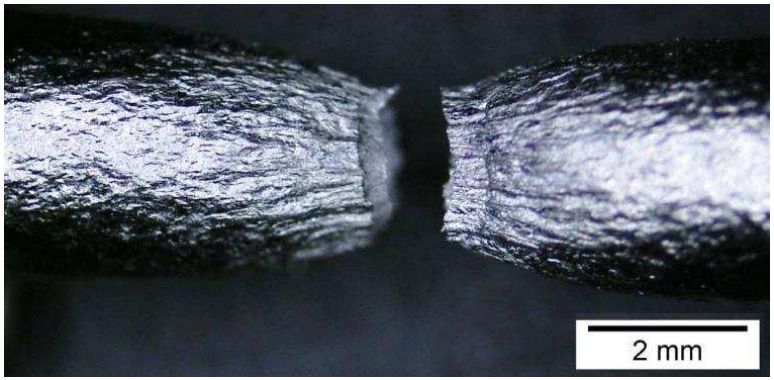

Figure 88. Low magnification image of non pre-charged body specimen tested in air (F1B3). Ductile aspect is evident.

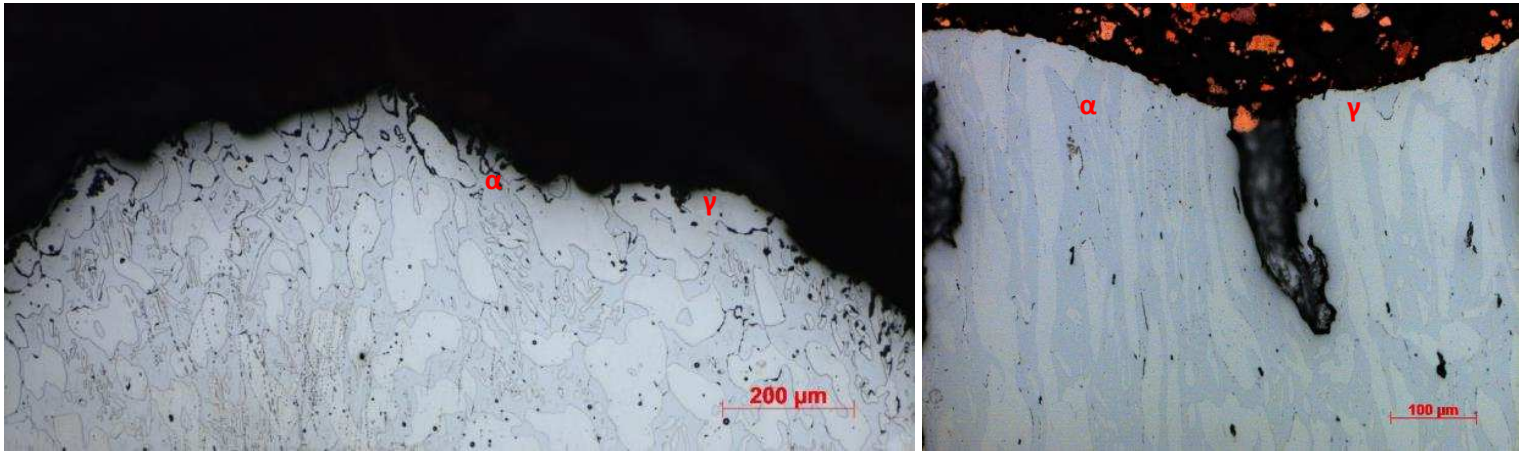

Figure 89. Micrographs of fracture sections – non pre-charged body specimens tested in air (left: F1B3, right: F1B16b). Fractures crossed both ferrite and austenitic islands.

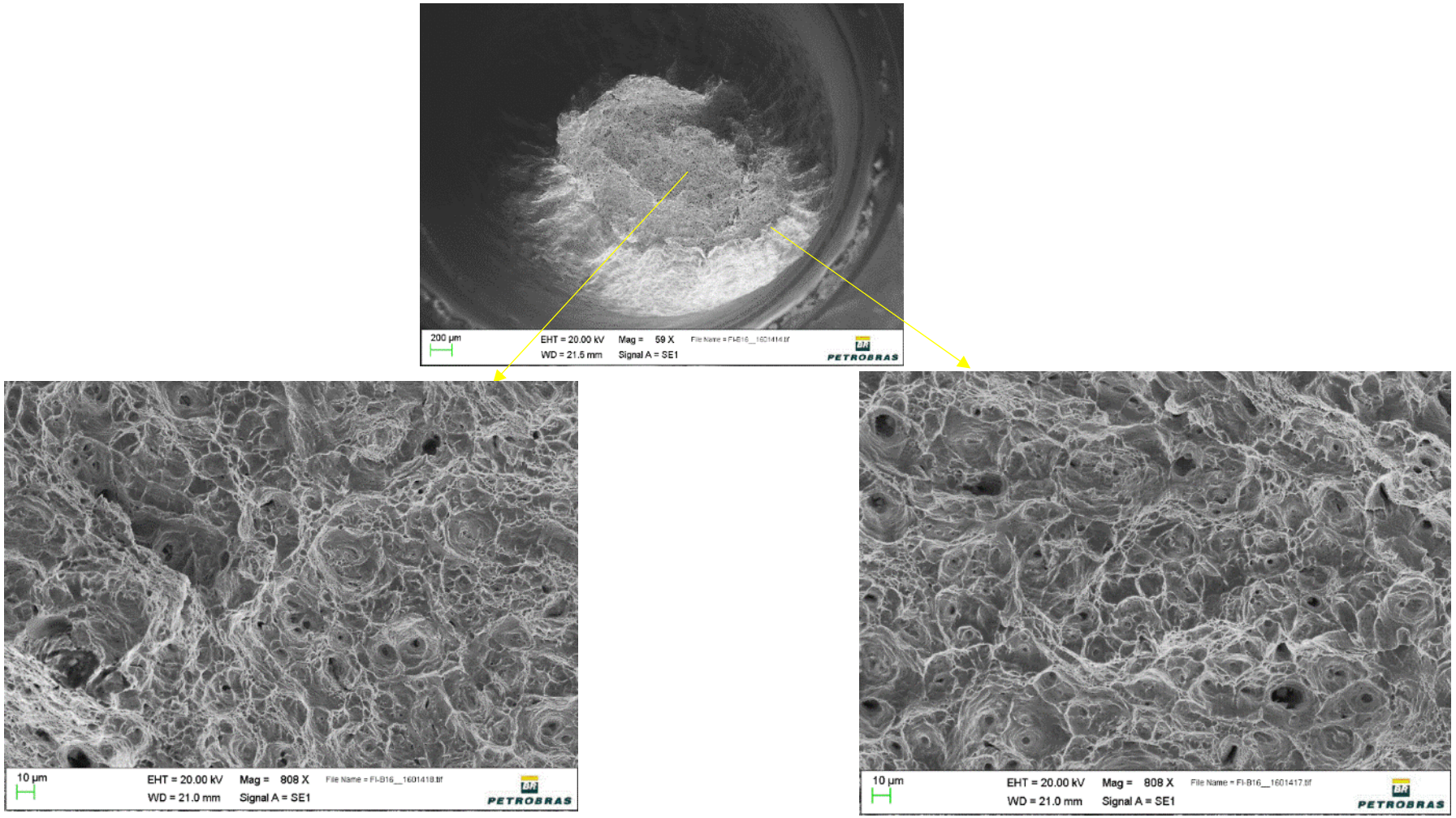

Figure 90. SEM images of non pre-charged body specimen tested in air (F1B16b). Characteristic ductile fracture composed dimples.

Fracture features of specimens tested with in-situ hydrogen gas below the threshold values of 50 bar H_2 and 30 mA are depicted in **Figures 91** to **95**.

As can be seen from **Figure 91**, more severely embrittled appearance is verified at higher hydrogen pressures and cathodic currents. The fractures propagated transgranularly predominantly through ferrite, especially at higher hydrogen activities, as shown in **Figure 92**. Sometimes the fractures crossed austenite grains and sometimes propagated along the phase boundaries.

From **Figures 93** to **95**, most of these specimens' fracture surfaces are characterized by mixed appearance, i.e. cleavage and secondary cracks present together with dimples. Cleavage becomes more important at higher hydrogen activities. Dimples are more predominant at lower hydrogen activities, for instance at cathodic current of 0,5 mA. Dimples were verified at different positions along the fracture surface, both on the section core and close to the outer surface.

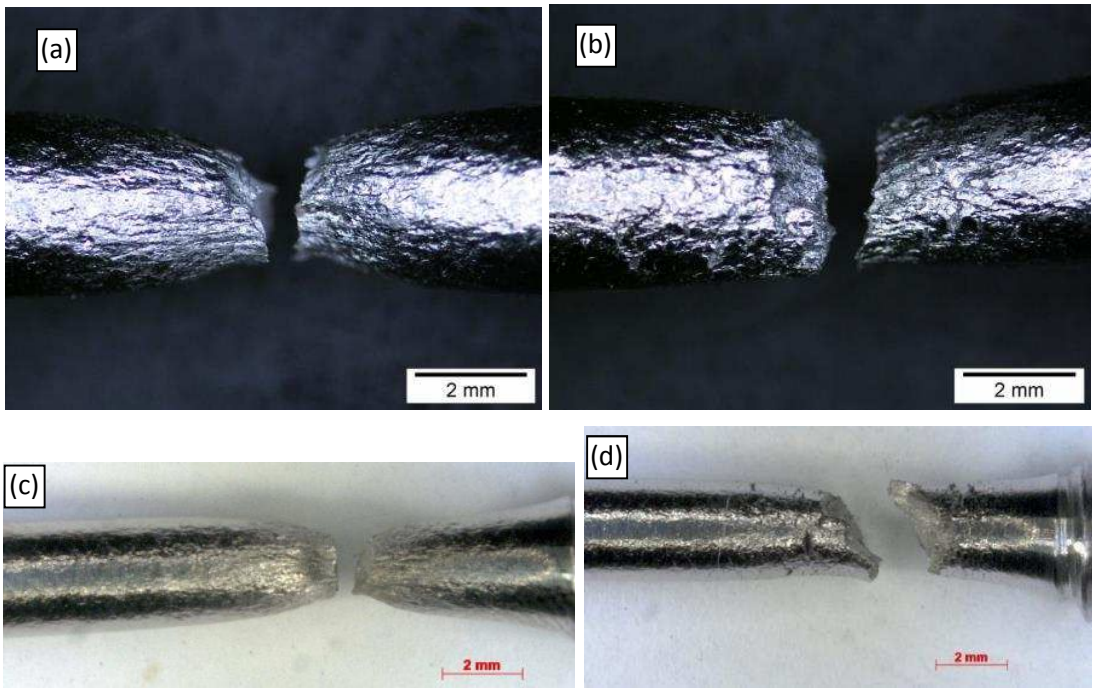

Figure 91. Low magnification images. (a) Flange body, 1 bar H_2 (F1B7). (b) Flange body, 10 bar H_2 (F1B8). (c) Flange body, 1 mA (F1B28). (d) Flange body, 3 mA (F1B25). Mixed brittle-ductile aspect is verified.

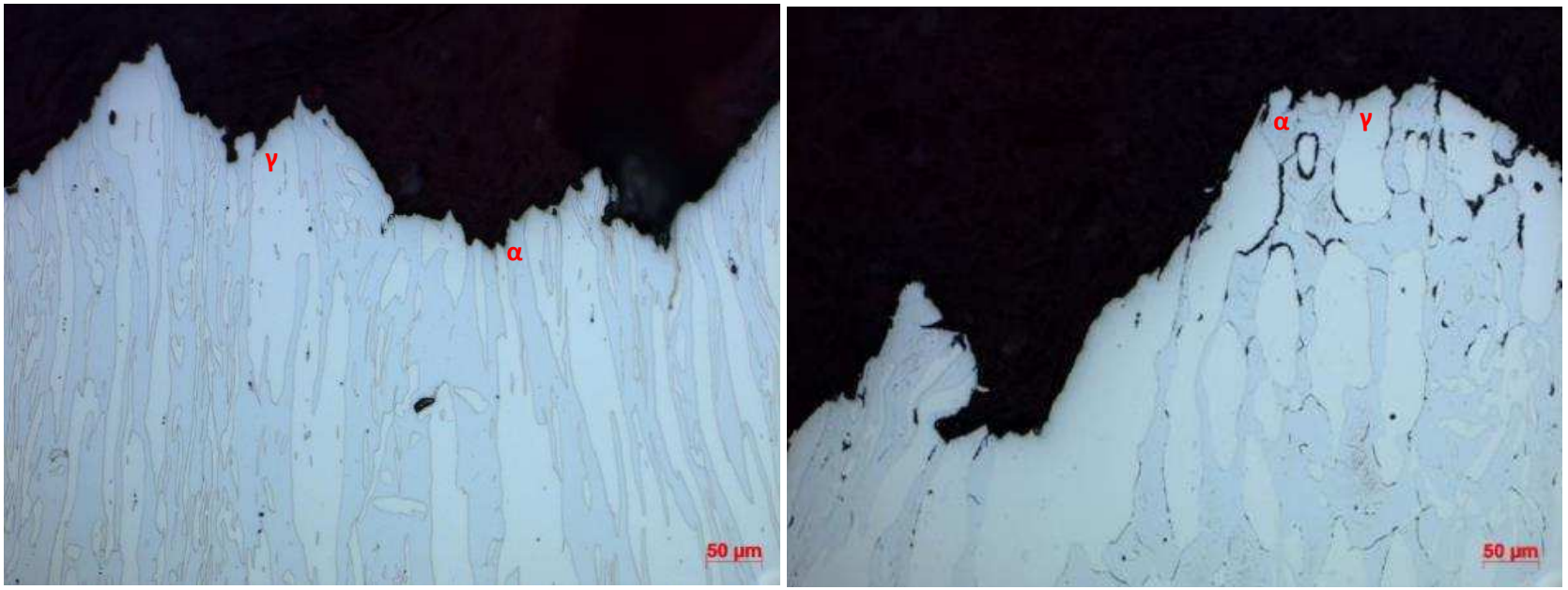

Figure 92. Low magnification image and fracture section micrographs. Left: flange body, 1 mA (F1B28). Right: flange body, 3 mA (F1B25).

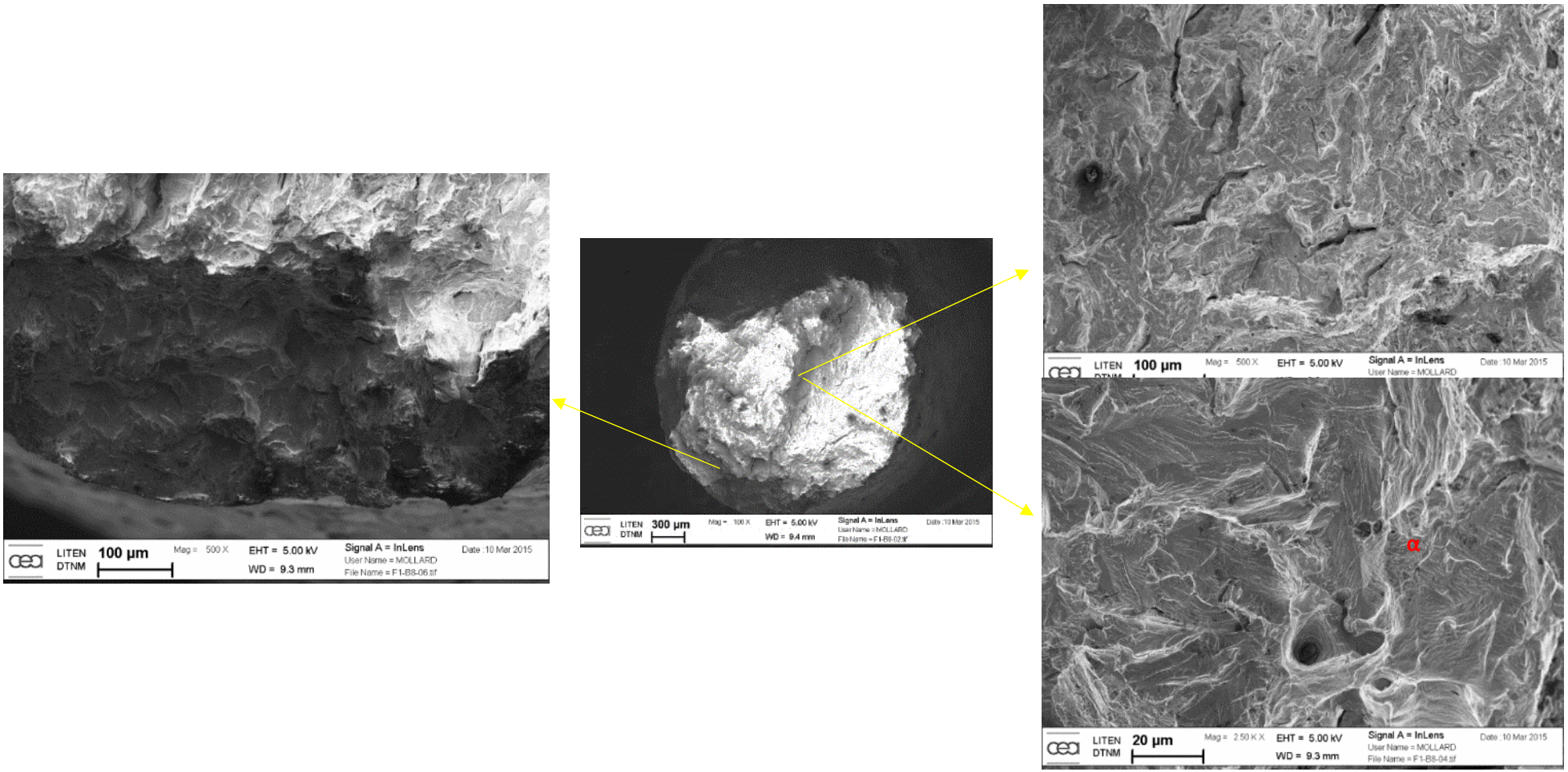

Figure 93. SEM images of the fracture surface. Flange body, 10 bar H_2 (F1B8). Predominant cleavage aspects are evident, with minor regions composed by dimples.

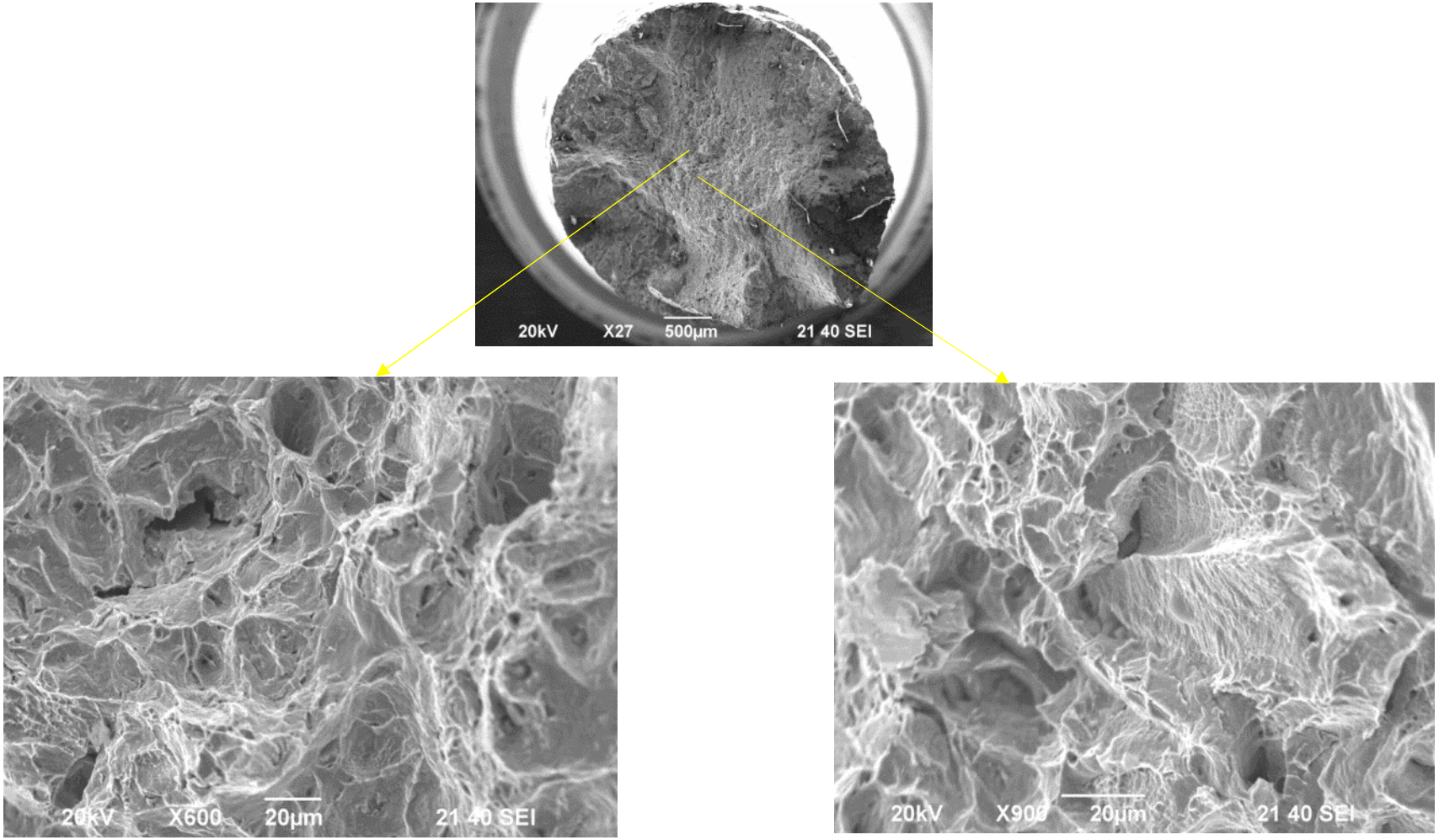

Figure 94. Flange body, 3 mA (F1B25). SEM images of the fracture surface close to the section core. Mixed cleavage and dimple characteristics are verified.

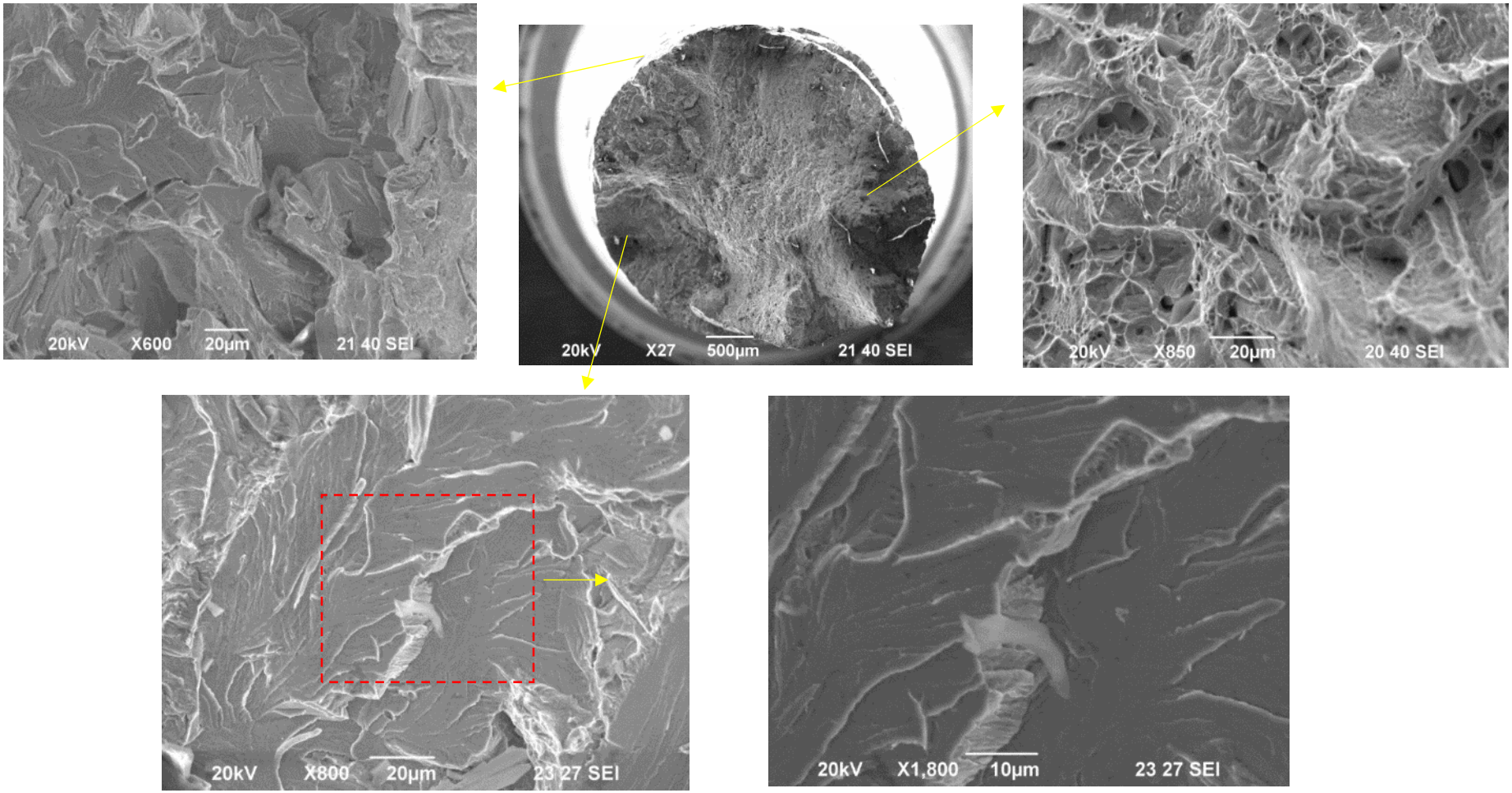

Figure 95. Flange body, 3 mA (F1B25). SEM images of the fracture in regions between core and outer surface. Cleavage was dominant close to the outer surface, while closer to the core, dimples were displayed.

Fracture characteristics of the specimens tested with in-situ hydrogen gas at pressures equal and above the threshold of 50 bar and with in-situ cathodic charging at currents more cathodic than the threshold of 30 mA are presented in following pictures. These specimens were highly embrittled, as seen in **Figure 96**. The fracture paths followed predominantly the ferrite phase, eventually crossing smaller austenite grains, as shown in **Figure 97**. Cracking of bigger austenite grains was less common at these conditions of higher hydrogen activity; when reaching bigger austenite grains, the cracks tended mostly to follow the α/γ phase boundaries, and decohesion between austenite and ferrite took place. This fracture propagation path was more tortuous than in fractures without action of hydrogen. This behavior was also verified by other authors [107].

Features of the fracture surfaces obtained by scanning electron microscopy are displayed in **Figures 98** to **102.** The fracture surfaces consisted usually of multi-facets composed by riverlike patterns, separated by steps of different slopes. The facets are associated with cleavage of the ferritic phase. Many secondary cracks were present in the ferritic phase, as shown for instance on **Figure 100**. Secondary cracks and cleavage in ferrite were confirmed by EDS measurements (**Figure 102**). These aspects were verified by different authors [27, 29, 32, 36, 53; 107-111].

The steps are related to fracture propagation through austenitic grains. These steps presented a serrated aspect at higher magnification (e.g. **Figures 99** and **101**). These micro-ridges were ill defined, indicating a higher absorption energy during fracture. According to different authors, the surface ridges are associated with failure along slip bands, which have experienced localized deformation probably along the (111) plane. The localization of the deformation as well as the accompanying reduction in cross-slip is consistent with the localized plasticity associated with the shielding model of hydrogen embrittlement [26,71,108,112]. Hydrogen reduces the stacking fault energy of austenite, which induces the change of the deformation mode from cross slip to planar slip [16]. In some cases, also small and shallow dimples were verified (e.g. **Figure 99**). These characteristics suggest plastic micro-mechanisms (dislocation slip, microvoid coalescence) are acting.

According to model proposed by different authors and mentioned on section **2.5.3.1**, the first fracture event comprises the formation of cleavage microcracks in the ferrite phase. As cleavage microcracks form in ferrite, stress is concentrated in austenite and then ductile fracture of austenite or along austenite/ferrite interfaces links the cleavage cracks [53,109].

It was verified rather homogeneous characteristics along the entire fracture surfaces, i.e. regions close to the outer surface and at the fracture core presented similar aspects.

This fracture appearance is different from literature results, e.g. in a 22Cr duplex stainless steel [27], in which specimens tested without pre-charging showed distinguished brittle and ductile regions in the fracture surfaces.

This homogeneity on fracture appearance can be explained by considering the crack tip is continuously submitted to a high hydrogen activity generated by environment. As the effective diffusion coefficient of SDSS at the test temperature is very low, the hydrogen atoms absorbed at the crack tip tend to be concentrated there during the entire crack propagation. Other aspects are further discussed.

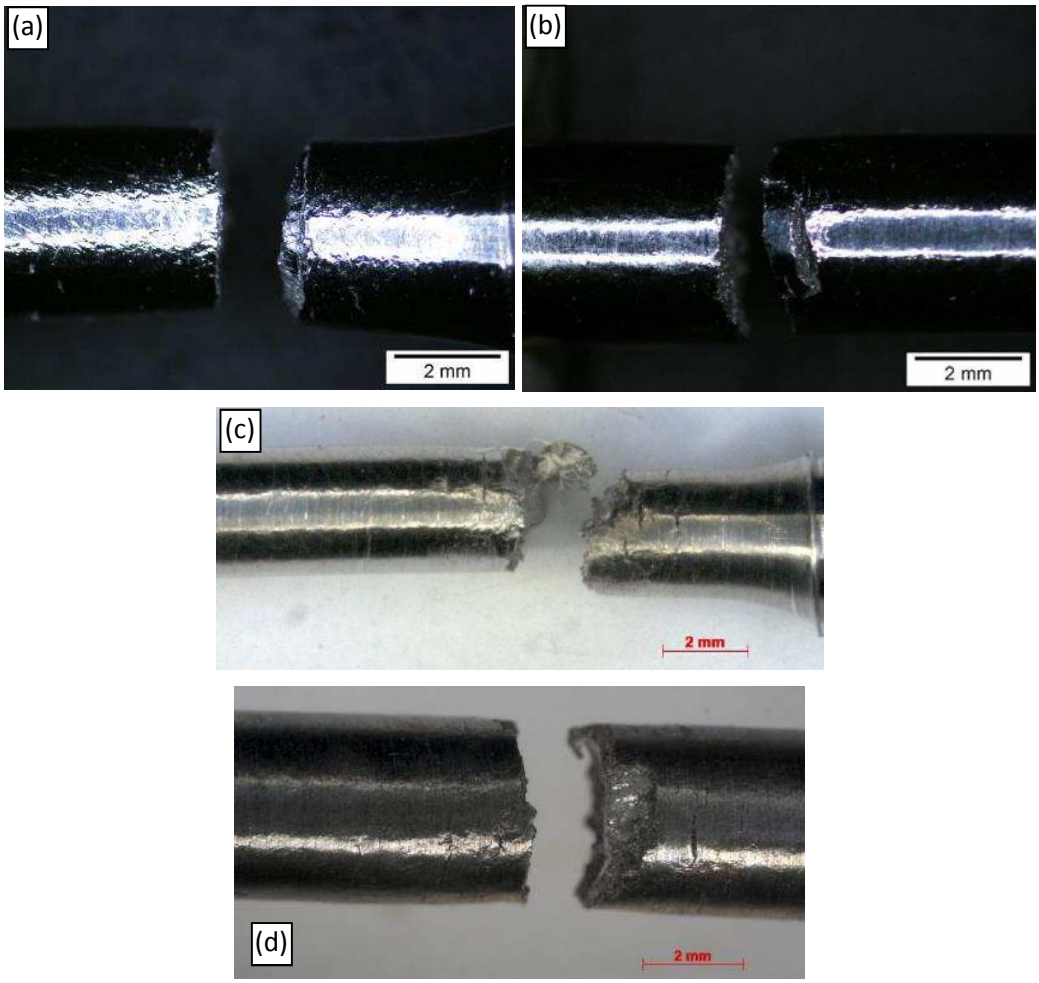

Figure 96. Low magnification images of highly embrittled specimens. (a) Flange body, 50 bar H_2 (F1B5). (b) Flange neck, 300 bar H_2 (F1N1). (c) Flange neck, 60 mA (F2N11). (d) Flange neck, 1100 mA (F1N10).

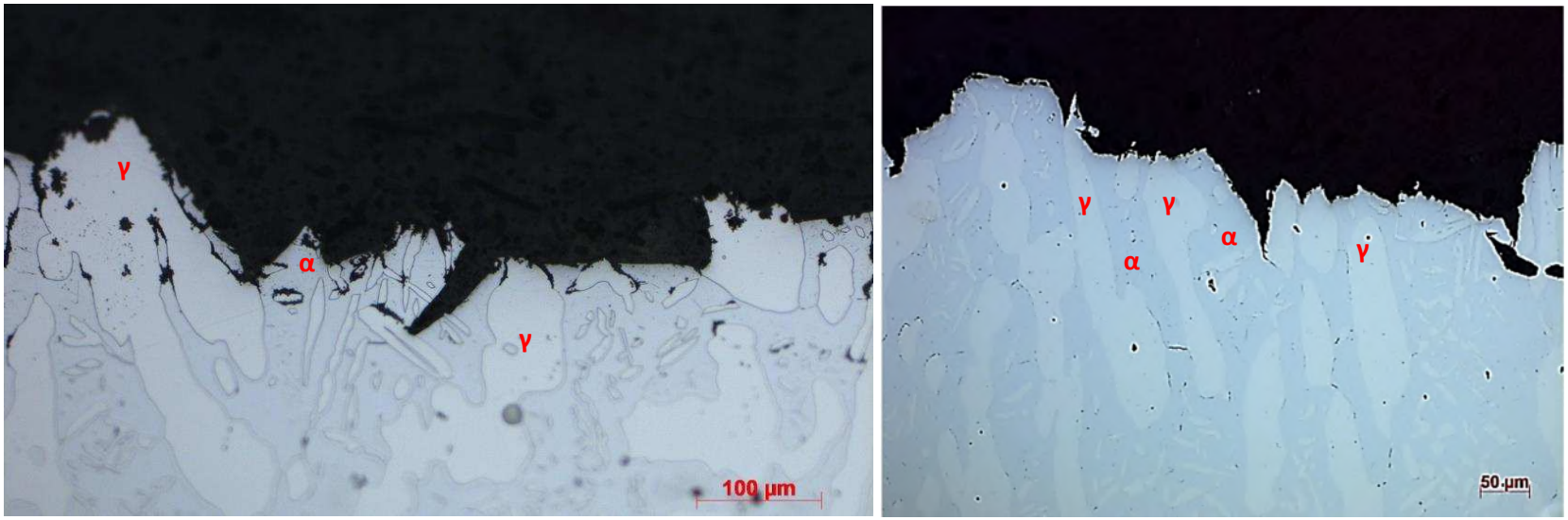

Figure 97. Micrograph of fracture sections. Left: flange body, 300 bar H_2 (F1B2). Right: Flange body, -60 mA (F1B27). Fractures followed preferentially the ferritic matrix.

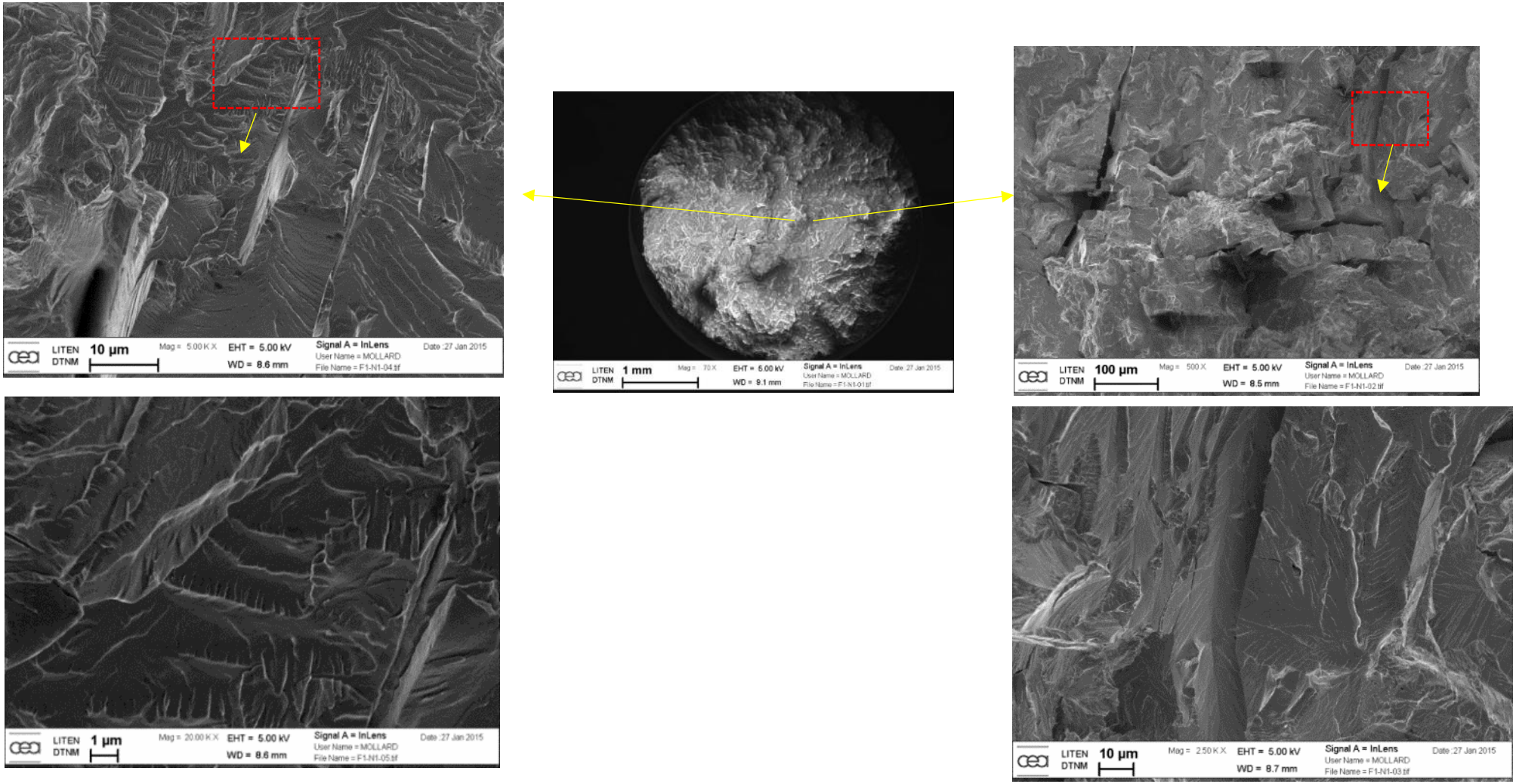

Figure 98. Flange neck, 300 bar H_2 (F1N1). SEM images of the fracture surface close to the section core. Cleavage and secondary cracks are predominant.

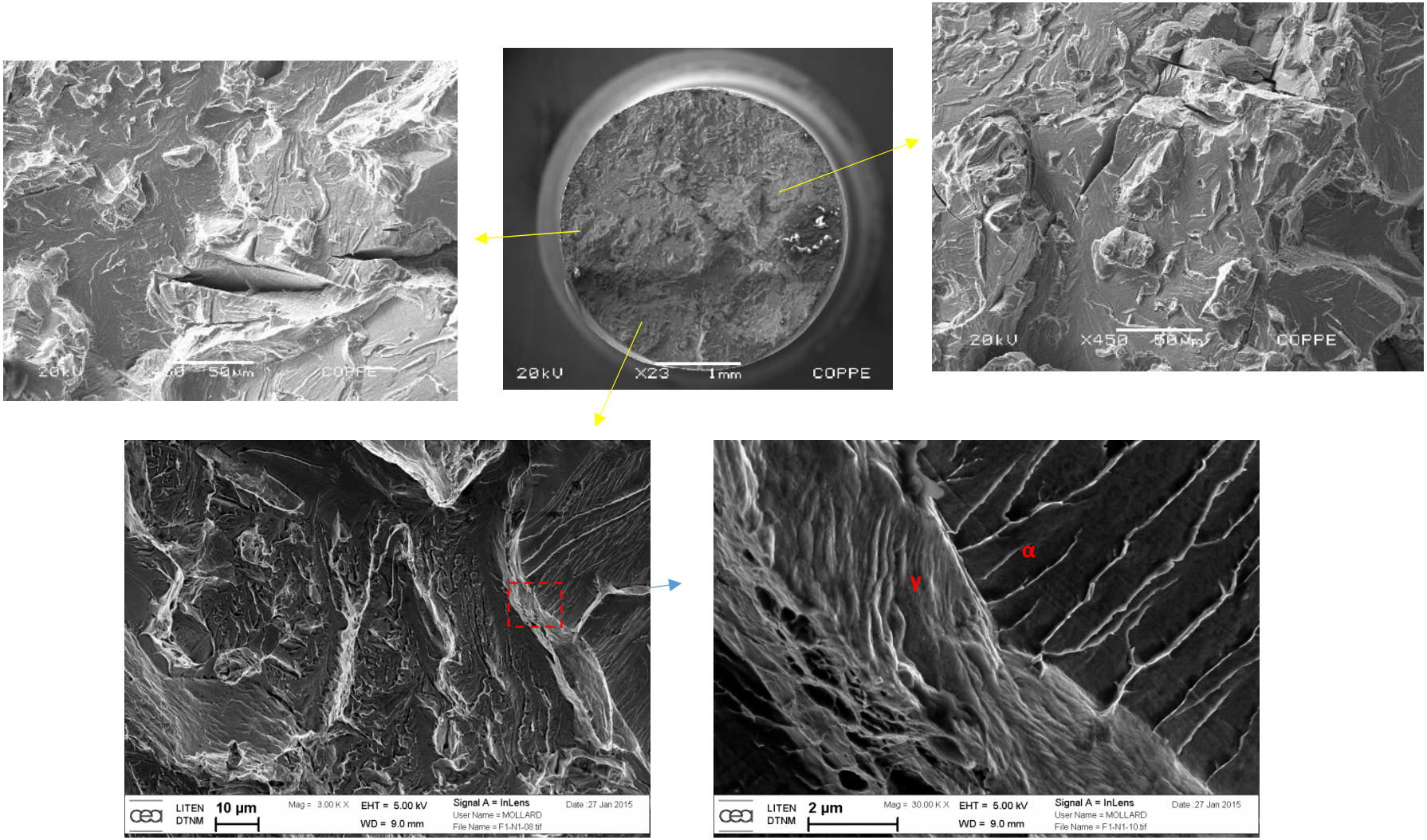

Figure 99. Flange neck, 300 bar H_2 (F1N1). SEM images of the fracture at regions between core and outer surface. Cleavage facets separated by steps are evidenced.

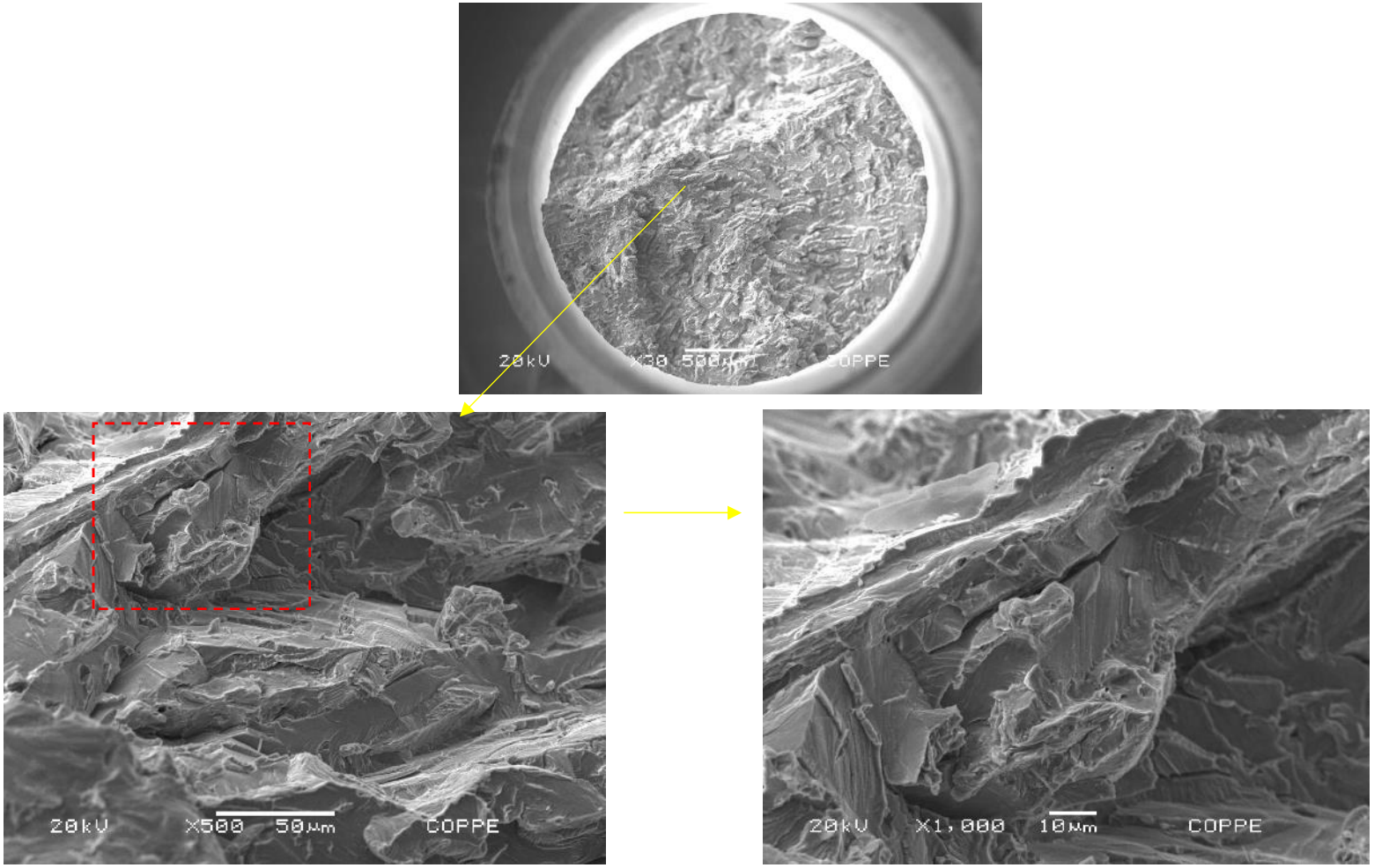

Figure 100. Flange body, 1100 mA (F1B20). SEM images of the fracture surface close to the section core. Detail of secondary cracks.

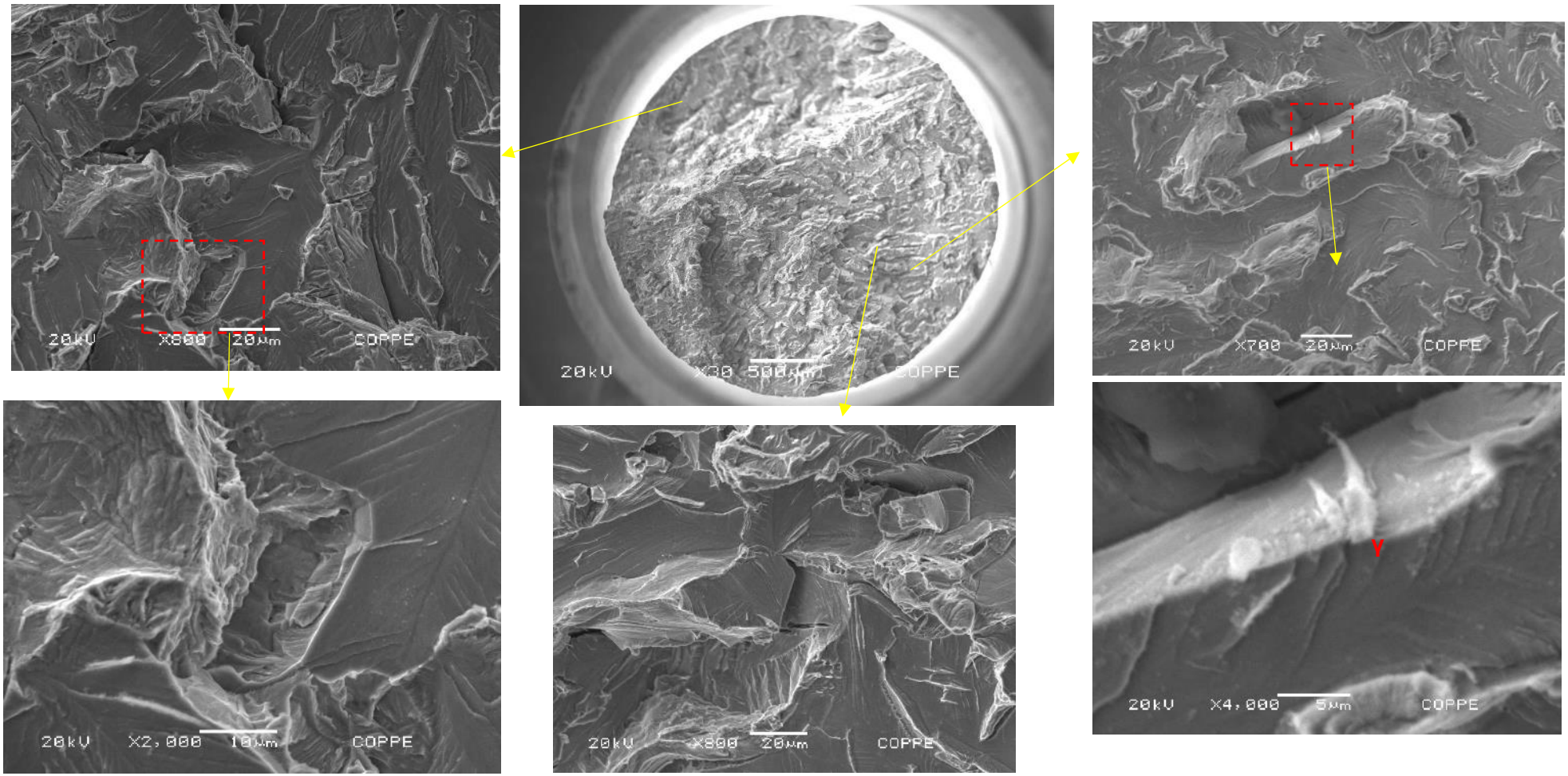

Figure 101. Flange body, 1100 mA (F1B20). SEM images of the fracture at regions between core and outer surface. Cleavage facets separated by steps

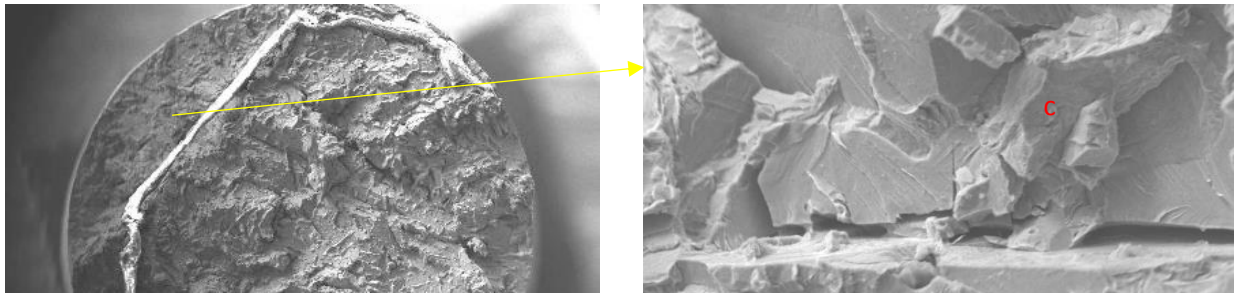

a

b

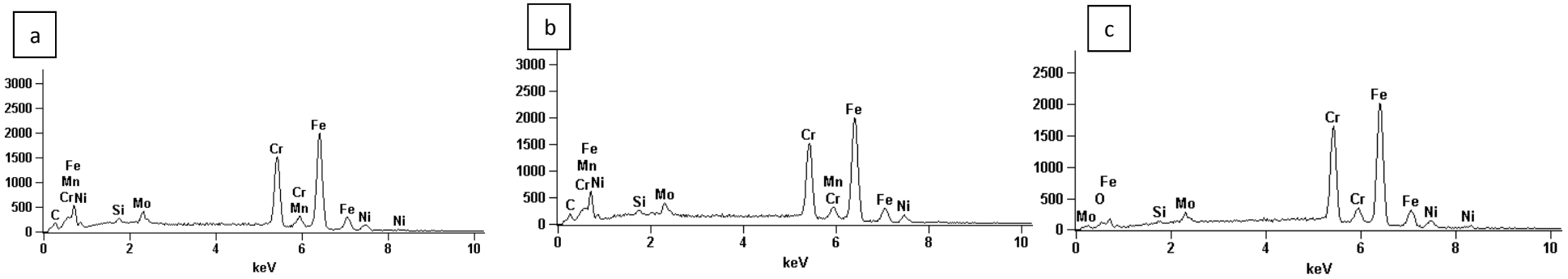

Figure 102. Flange neck, 1100 mA (F1N10). SEM images of the fracture and EDS measurements performed in a region close to the outer surface.

Figures 103 to **106** show aspects of the fractures of the hydrogen pre-charged (ex-situ) samples. Mixed ductile-brittle aspect is evident. Similar features to those verified in the in-situ charged material were observed in the specimens cores. However, a higher density of dimples was verified closer to the external surface. This can be associated to eventual release of surface hydrogen during the delay time between the charging process and during the tests theirselves.

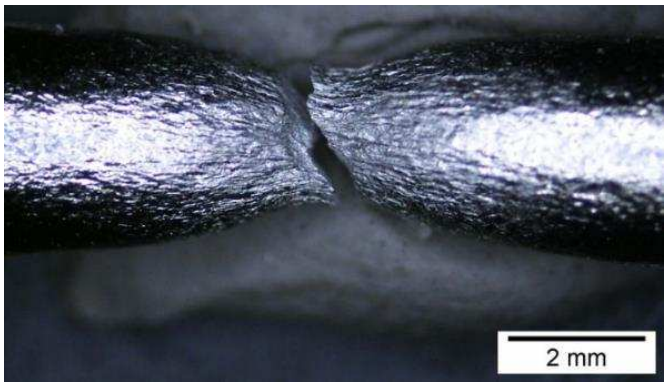

Figure 103. Low magnification images. $\dot{\varepsilon}=10^{-3}$ s^{-1} (F1B12).

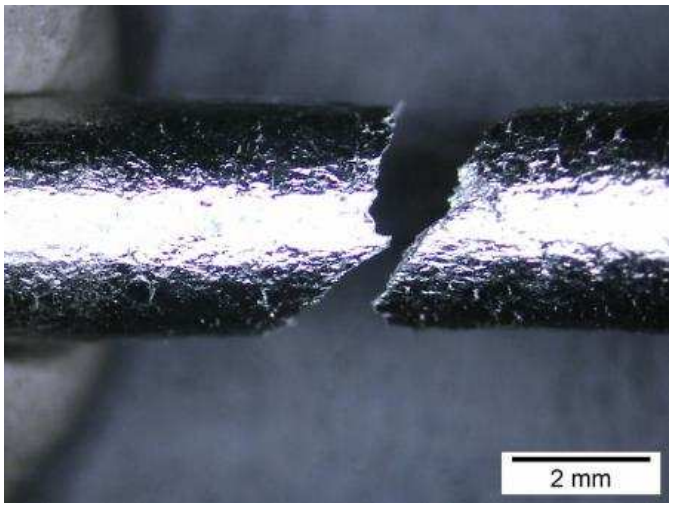

Figure 104. Low magnification images. $\dot{\varepsilon}=10^{-5}$ s^{-1} (F1B10).

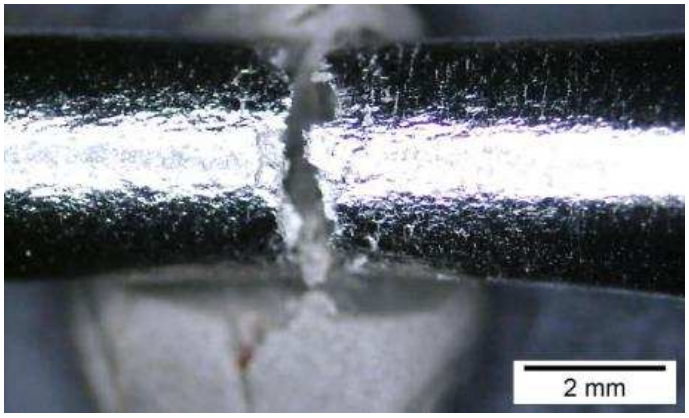

Figure 105. Low magnification images. $\dot{\varepsilon}=10^{-6}$ s^{-1} (F1B13).

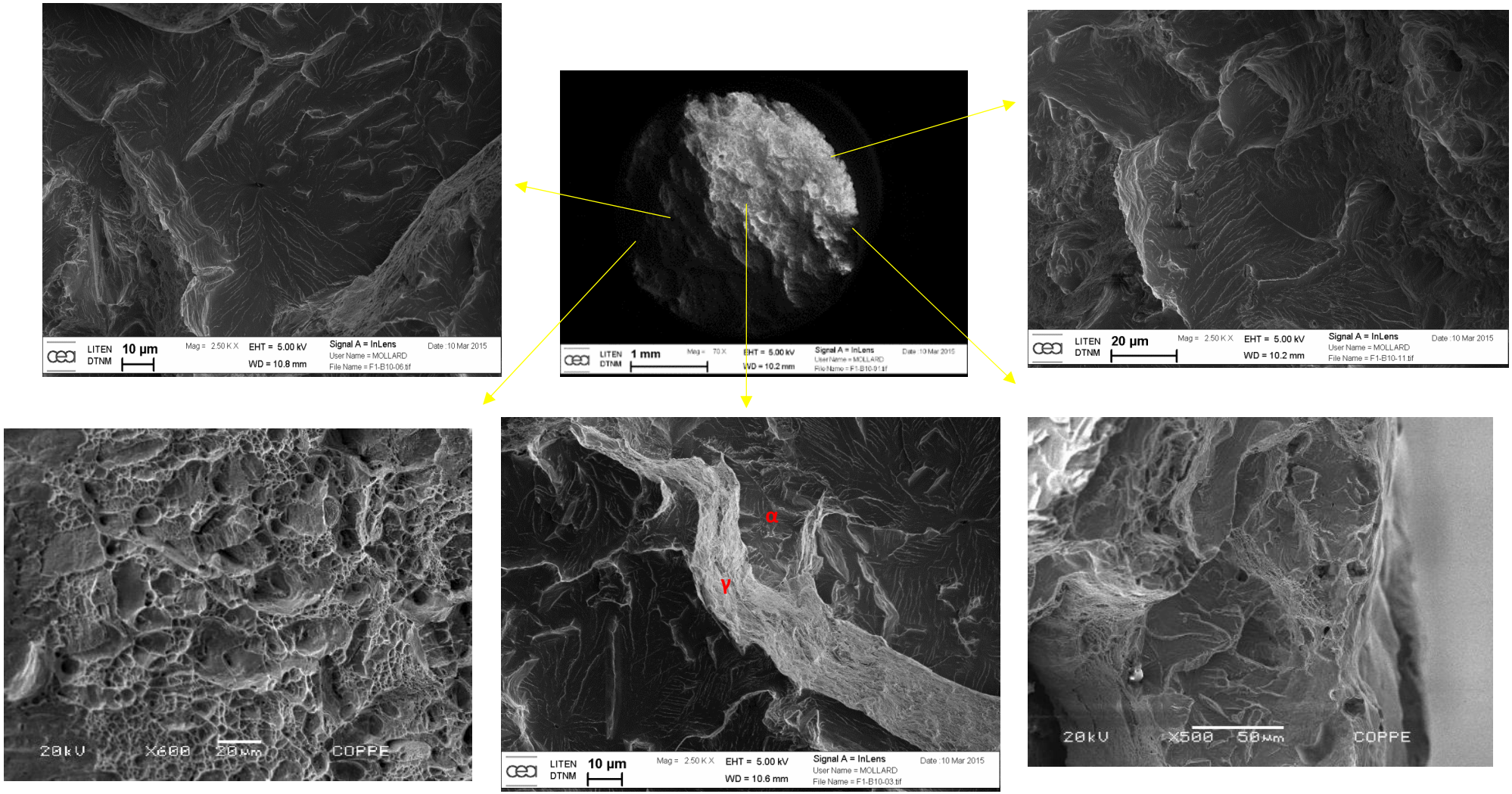

Figure 106. Hydrogen pre-charged and tested in air – flange body (F1B10). SEM images of the fracture surface. Dimples were dominant close to the outer surface, while in the core cleavage facets were displayed.

4.6. Thermal Desorption Spectroscopy

TDS was aimed to describe the hydrogen desorption kinetics and to obtain information about hydrogen traps. The TDS test conditions are listed on **Annex F**. **Figures 107** to **109** present the hydrogen desorption spectra measured at different heating rates from all samples. Despite temperatures as high as 840ºC were reached, only the results up to 600ºC are considered. Signals at temperatures higher than 600ºC were disregarded as these temperatures are outside the accuracy limit of the mass spectrometer.

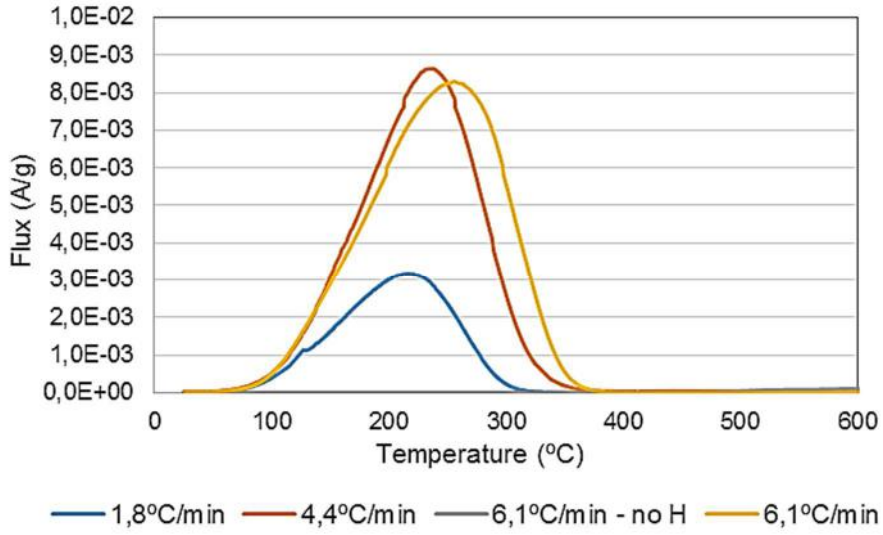

Figure 107. TDS results – Flange body samples pre-charged cathodically (329-353 h, 3,5% NaCl, 100 mA/cm², 60ºC).

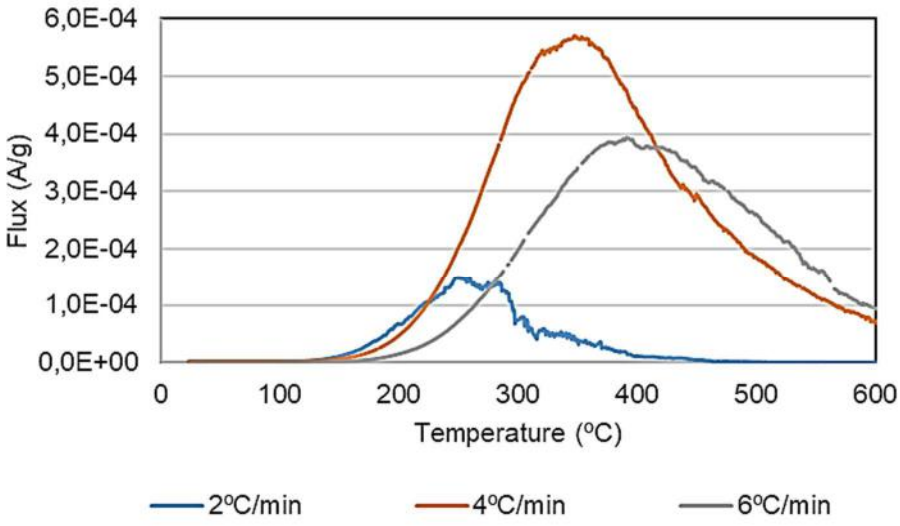

Figure 108. TDS results – Flange neck samples pre-charged cathodically (329-353 h, 3,5% NaCl, 100 mA/cm², 60ºC).

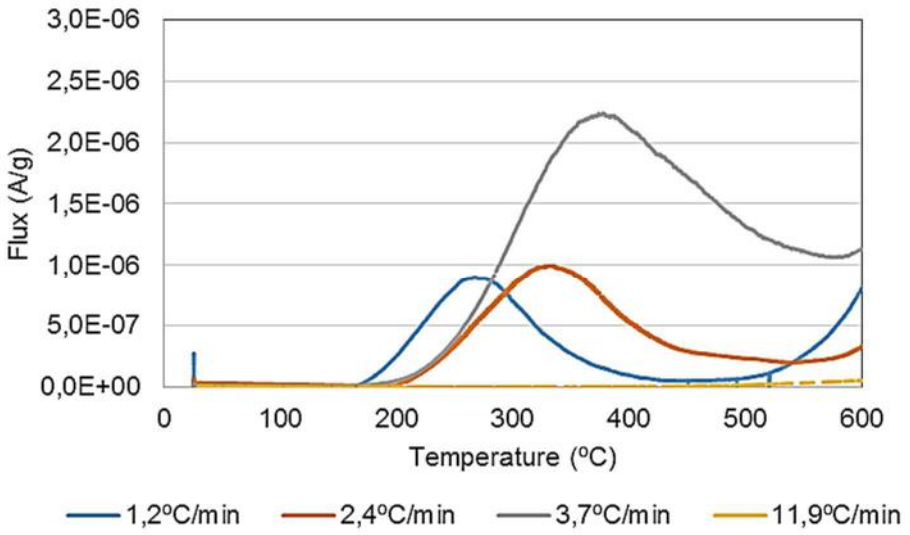

Figure 109. TDS results – Flange body samples pre-charged with gaseous hydrogen (72h, 20 bar 280ºC).

The deconvolution of the desorption peaks was first performed considering Gaussian curves, according to the form given in **Equation 63**.

$$Y = Y_o + \frac{A}{w\sqrt{\pi/2}} \exp\left[\frac{-2(T-T_m)}{w^2}\right] \qquad \textbf{(Equation 63)}$$

where:

- A: area of the peak.
- T_m: peak temperature.
- w: width of the peak.

Table 20 lists the peaks deconvoluted considering Gaussian curves and the measured activation energies associated to each peak according to Kissinger's method, as described in section **3.2.3**. **Figures 110** to **112** show the respective graphs of $\ln(\Phi/T_m^2)$ vs. $(1/T_m)$ used to obtain the activation energies according to this method.

Table 20. Desorption peaks deconvoluted using Gaussian fitting and calculated activation energies.

Peak	**Flange body - Electrochemical charging**			**Ea (kJ/mol)**	**Body - Gaseous charging**			**Ea (kJ/mol)**	**Neck - Electrochemical charging**			**Ea (kJ/mol)**
Heating rate (ºC/min)	1,8	4,4	6,1		1,2	2,4	3,7		2,0	4,0	6,0	
T (ºC)	182	176	216	24,6	266	329	362	21,8	260	333	369	18,4
T(ºC)	234	244	277	46,3	340	491	507	11,1	278	445	466	6,7
									306	588	-	-

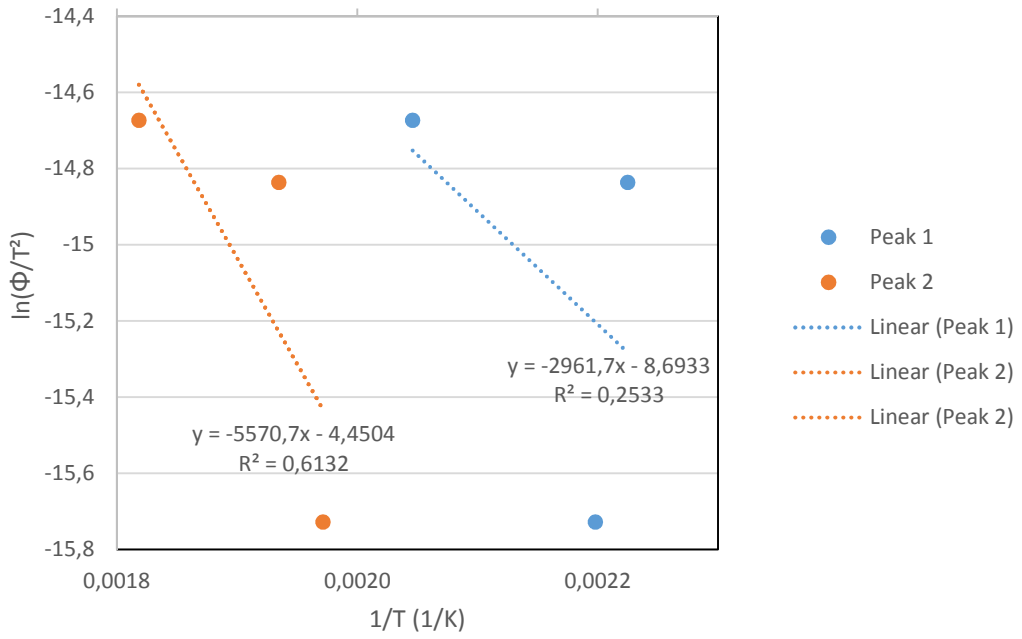

Figure 110. Curves for activation energy calculation, flange body, electrochemical charging – Gaussian curves.

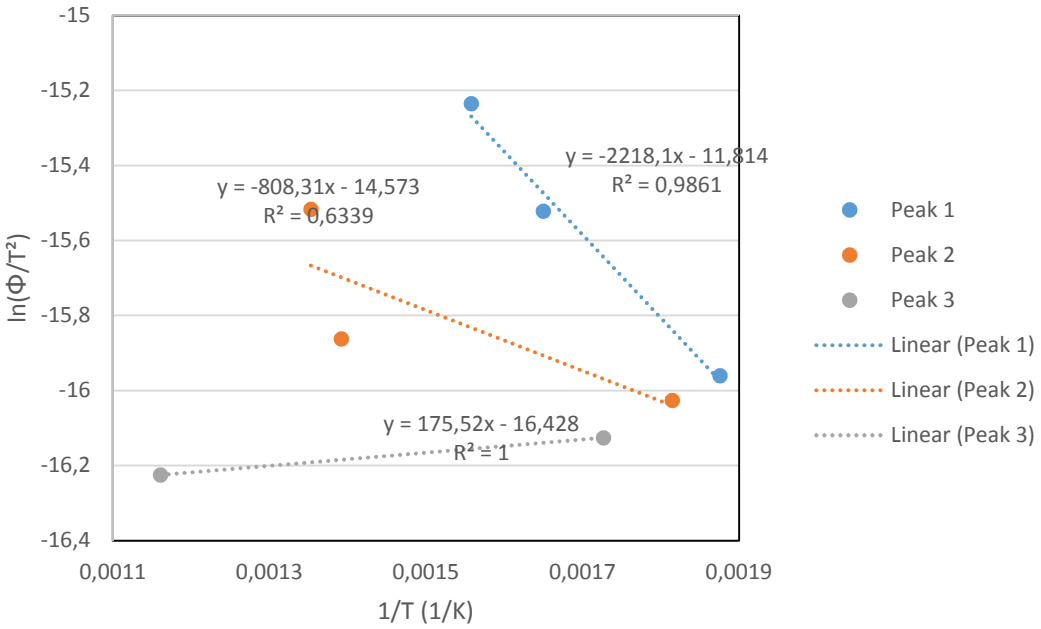

Figure 111. Curves for activation energy calculation, flange neck, electrochemical charging – Gaussian curves.

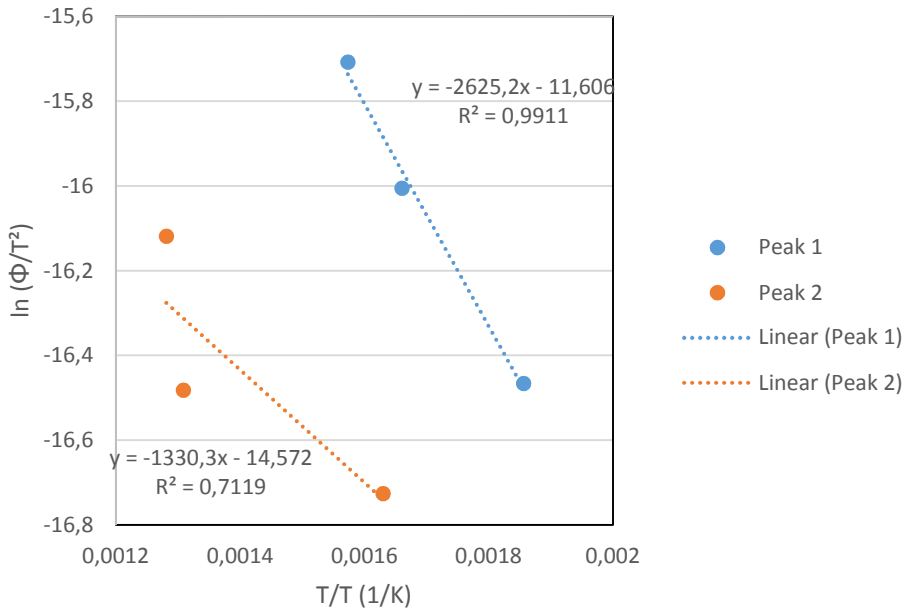

Figure 112. Curves for activation energy calculation, flange body, gaseous charging – Gaussian curves.

The body samples cathodically pre-charged presented only two clear peaks partially overlapped, at peak temperatures of 176-216 and 234-277ºC. Example of the deconvolution at Φ = 4,4ºC/min is presented in **Figure 113**. These peaks were associated to activation energies of 24,6 and 46,3 kJ/mol respectively. As seen in **Figure 110**, important nonlinearity was verified in some cases.

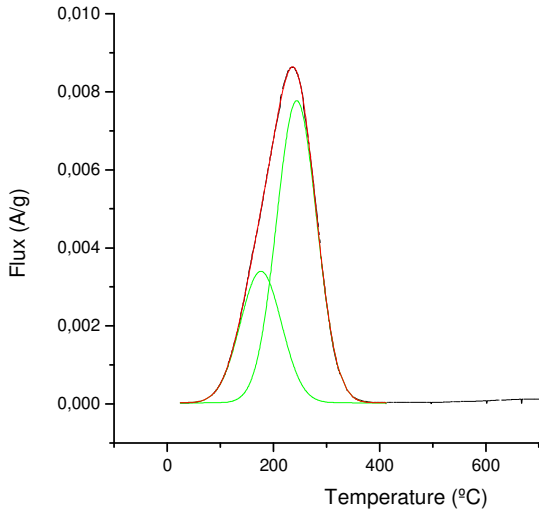

Figure 113. Deconvolution of the peak for the spectrum obtained for the body sample cathodically pre-charged at heating rate of 4,4ºC/min.

The neck samples electrochemically charged presented in all heating rates two peaks partially overlapped at higher peak temperatures than in the body samples: at 260-369 and 278-466ºC. These peaks were associated to activation energies of 18,4 and 6,7 kJ/mol. A third peak also partially overlapped with these first two peaks was verified only at the heating rates of 2 and 4ºC/min, in the range of 306-588ºC. This peak presented an anomalous $\ln(\Phi/T_m^2)$ vs. $(1/T_m)$ relationship, suggesting a very low activation energy, close to the experimental error.

The specimens from the flange body that were charged with gaseous hydrogen at 280ºC presented also two partially overlapped peaks at 266-362 and 340-507ºC, associated to activation energies of 21,8 and 11,1 kJ/mol respectively. In all heating rates, a peak was also measured at temperatures higher than 600ºC (697-763º°C), being associated to an activation energy of 89,2 kJ/mol. As mentioned, this temperature range presents lower accuracy, so that these peaks were disregarded.

According to LEGRAND *et al.* [110] the trapped hydrogen evolution rates may not follow Gaussian distributions, but an asymmetric double sigmoidal (ADS) distribution. This curve is described by the **Equation 64**:

$$Y = Y_o + A.\left(\frac{1}{1+\exp\left(-\frac{T-T_m+w_1/2}{w_2}\right)}\right).\left(1-\frac{1}{1+\exp\left(-\frac{T-T_m+w_1/2}{w_3}\right)}\right)$$

(Equation 64)

being:

- A: area of the peak.
- T_m: peak temperature.
- w_1, w_2, w_3: weights to adjust the asymmetry of the peak.

Following the deconvolution on ADS curves, **Table 21** lists the peaks identified and the measured activation energies associated to each peak according to Kissinger's method. **Figure 114** shows the $\ln(\Phi/T_m^2)$ vs. $(1/T_m)$ curves used to obtain the activation energies for all experiments.

Table 21. Desorption peaks deconvoluted using asymmetric double sigmoidal fitting and calculated activation energies.

Peak	Flange body - Electrochemical charging			Ea (kJ/mol)	Body - Gaseous charging			Ea (kJ/mol)	Neck - Electrochemical charging			Ea (kJ/mol)
Heating rate (ºC/s)	1,8	4,4	6,1		1,2	2,4	3,7		2,0	4,0	6,0	
T (ºC)	208	230	243	64,1	248	299	312	31,0	241	299	407	9,0

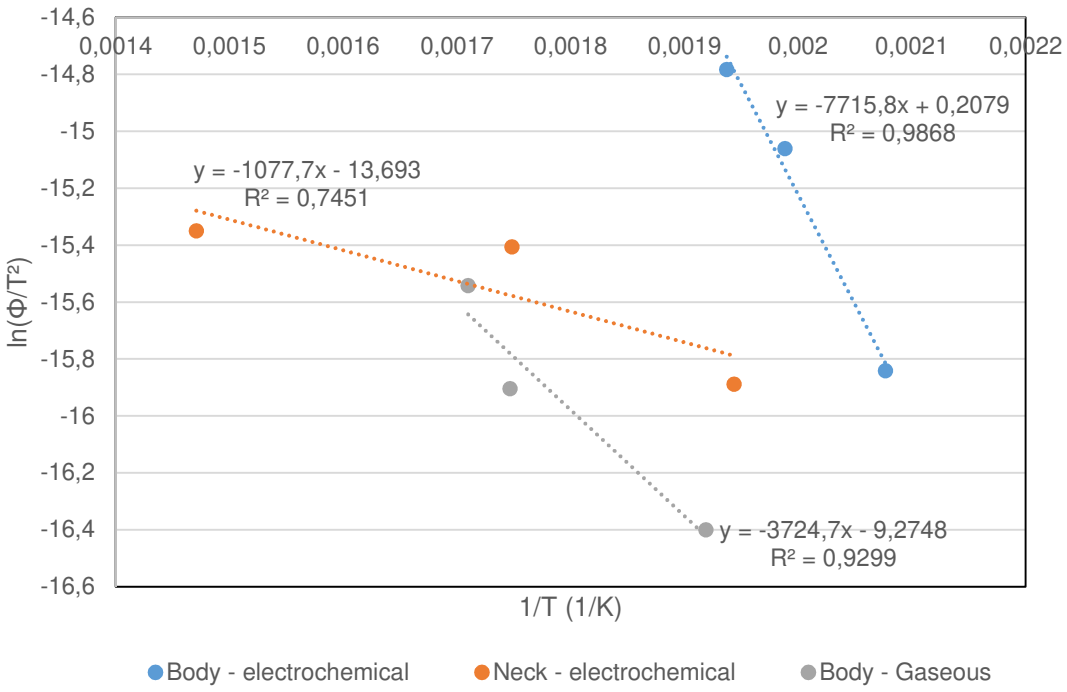

Figure 114. Curves for activation energy calculation for all specimens – ADS curves.

Under ADS deconvolution, only one peak below 600ºC was identified in all cases. The body samples that were cathodically pre-charged presented the peak in the temperature range of 208-243ºC. An activation energy of 64,1 kJ/mol was estimated, a value more elevated than those obtained for the same peaks by the Gaussian deconvolution (24,6 and 46,3 kJ/mol). For this case, the $\ln(\Phi/T_m^2)$ vs. $(1/T_m)$ relationship using the ADS convolution was more linear (R^2 = 0,99) than for the first same peaks in the Gaussian convolution (R^2 = 0,25-0,61), indicating a better accuracy of the Kissinger's method using the deconvolution by asymmetric double sigmoidal distribution. That means the

activation energy of 64,1 kJ/mol is more accurate than those obtained by the Gaussian deconvolution.

The neck samples electrochemically charged presented a peak in the range of 241-407ºC, with an activation energy of 9,0 kJ/mol. This activation energy lies within the range calculated using Gaussian fitting (6,7-18,4 kJ/mol). The specimens from the flange body that were charged with gaseous hydrogen at 280ºC presented the peak at 248-312ºC. It was associated to an activation energy of 31 kJ/mol, relatively close to the values obtained using the Gaussian deconvolution (11-22 kJ/mol). For these specimens, the values of reduced chi-squared using Gaussian and ADS deconvolutions were quite similar (average from all heating rates: χ^2 = 4,2-4,3.10^{-16}), indicating that both fittings (Gaussian and ADS curves) are adequate.

In summary, the samples cathodically pre-charged from the flange body and neck presented peaks related to different hydrogen trapping sites. Spectra from the body samples indicated E_a of 64 kJ/mol (peaks at 208-243ºC). For neck samples, the estimated activation energies for hydrogen desorption are in the range of 7-18 kJ/mol (peaks at 260-466ºC). The activation energy of 64 kJ/mol relates to irreversible traps, such as α/γ interfaces. Similar results are mentioned in the literature. DABAH *et al.* [111] obtained from 2507 samples cathodically charged a peak at 175-237ºC with activation energies of 50-57 kJ/mol. SILVERSTEIN [113,112] estimated for the same material from a peak at 210-365ºC E_a values between 43-63 kJ/mol. SEQUEIRA [76] obtained by testing specimens 2507 manufactured by hot isostatic pressing a peak at 497-511ºC associated to a value of 71 kJ/mol.

The values of E_a below 60 kJ/mol as measured in the neck (7-18 kJ/mol) and gas-charged body specimens (11-31 kJ/mol) are related typically to reversible traps at room temperature, such as ferrite/ferrite grain boundaries and dislocations. A wide range of E_a values for reversible traps are mentioned in the literature, as shown in **Table 7**. (**section 3.2.3**). SILVERSTEIN [113] indicates that elastic stress fields of dislocations present E_a ≤ 20 kJ/mol, screw dislocation cores and grain boundaries have E_a between 20–30 kJ/mol. For ferrite (in pure iron), CHOO *et al.* [114] measured activation energies of 17 and 27 kJ/mol respectively for detrapping from grain boundaries and dislocations. According to SONG [115], typical values of E_a for hydrogen desorption from grain boundaries and dislocation elastic stress fields and cores in ferrite lie between 17 and 59 kJ/mol.

The shape of the desorption curve can be used to determine the order of the desorption reaction and whether the activation energy is constant or a function of surface coverage.

In the approach of READHEAD [115], it was proved that the peak temperature T_m is independent of hydrogen surface coverage for a first-order reaction (with constant E_a), i.e. in which the reaction rate is directly proportional to the atomic hydrogen activity. For second-order desorption reaction, i.e. in which the rate determining step for desorption is the recombination of atomic hydrogen to molecules at the surface, T_m depends on the surface coverage. Redhead also verified that, for first-order desorption, the desorption curve is asymmetric about the maximum at T_m. For the second-order case, it is shown that the desorpion curve is symmetric about the maximum at T_m.

A better fitting using ADS curves was clearly verified only in the cathodically-charged body samples, suggesting, according to the Redhead description, first-order hydrogen desorption kinetics is dominant. In case of the neck and gas-charged samples, similar fitting quality was verified for both Gaussian and ADS deconvolution, so that preferential first- or second-order desorption kinetics was not possible to be established using this approach.

4.7. Time-of-flight Secondary Ion Mass Spectroscopy

ToF SIMS was aimed to obtain information on the spatial distribution of hydrogen atoms in the microstructure close to the surface. The tests performed at room temperature are presented in **Figures 115** and **116**. The specimens were submitted to gaseous deuterium at 19,5-19,8 bar and 276-278°C for 120 h (5 days). **Figure 115** shows the overlay of two images obtained from the etched pre-charged sample: the sum of signals of Fe+Cr+Ni and the signals of deuterium (mass 2) normalized to this sum (red dots). **Figure 116** displays the same results for the non etched pre-charged sample. The regions in green with higher brightness are austenite islands, and the darker regions are the ferritic matrix. A good resolution was obtained with both samples, indicating that surface etching would not be necessary.

The obtained results from the tests at room temperature indicate higher deuterium content in ferrite. Fewer D atoms were identified in austenite.

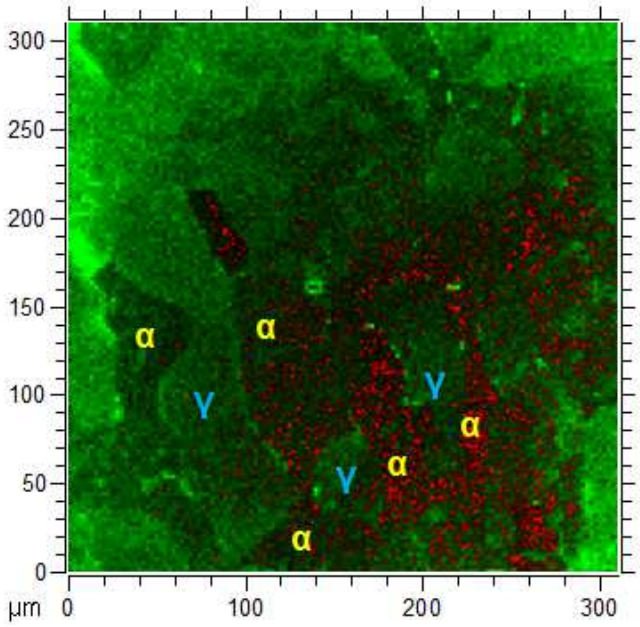

Figure 115. Overlay of sum of Fe/Cr/Ni and signal of D (red dots) for the etched sample. Negative polarity.

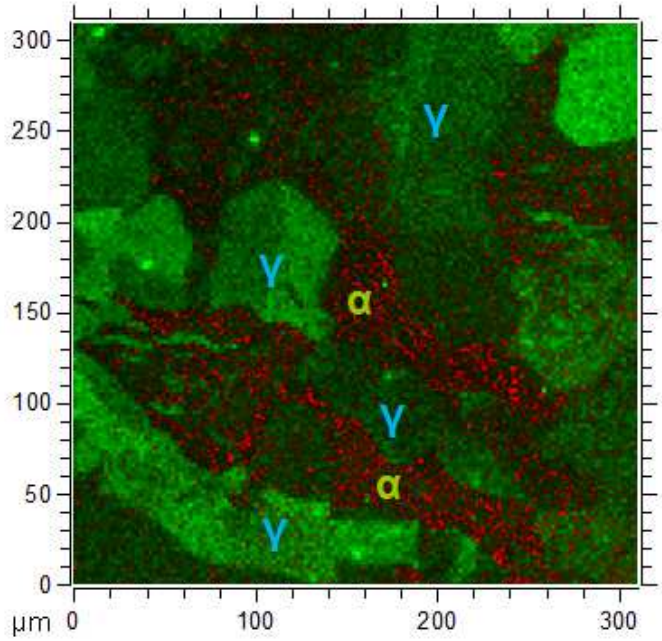

Figure 116. Overlay of sum of Fe/Cr/Ni and signal of D for the non etched sample. Negative polarity.

Figure 117 shows the sum of the signals of all atomic species obtained in the test in cryogenic conditions. This specimen was submitted to charging with gaseous D_2 at 280-290ºC, 19-21 bar for 120h. The brightest spots throughout **Figure 117** are mainly contamination by chlorides. **Figure 118** displays only the signals of deuterium. A larger amount of D is indicated by a brighter signal.

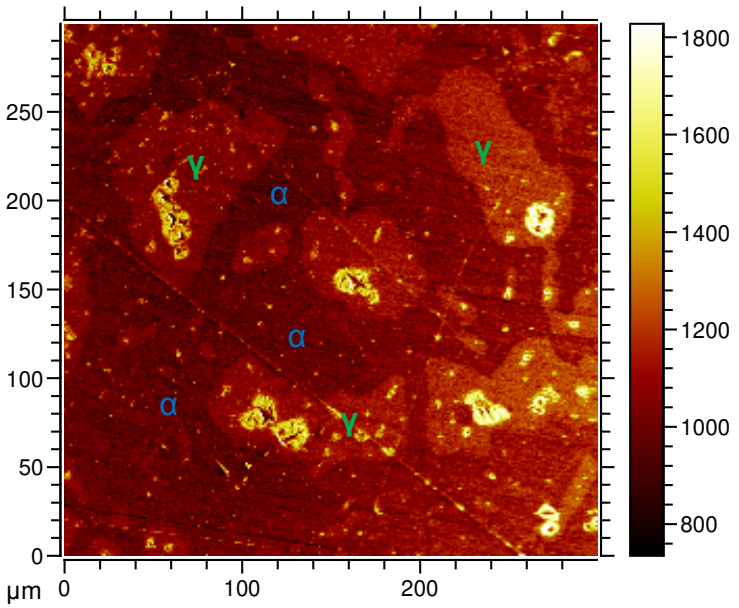

Figure 117. Sum of signals from all elements.

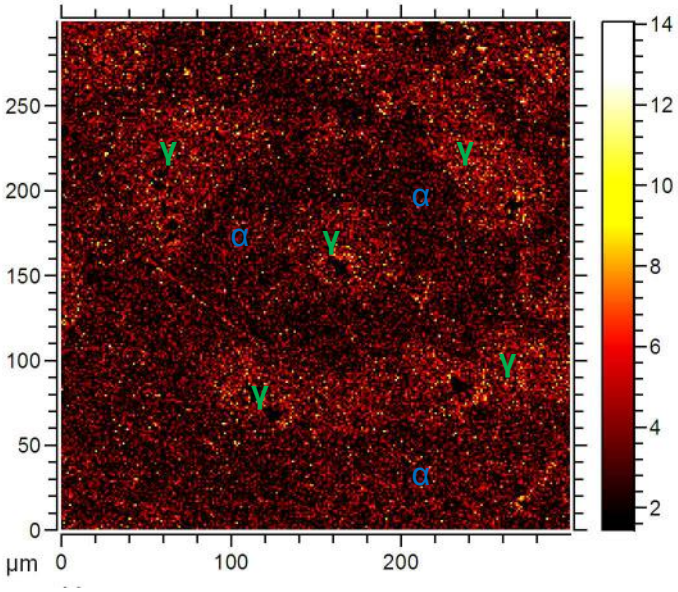

Figure 118. Only signal from deuterium of the same area of **Figure 117**.

Considering the charging conditions, deuterium is estimated to have penetrated all the specimen thickness both in ferrite and in austenite.

At cryogenic conditions, it is better captured the effect of microstructural localization of deuterium. At -100ºC, a clear contrast was verified in D concentration and higher signal of D at austenite islands was measured. Hydrogen/deuterium diffusivity decreases exponentially with temperature according to an Arrhenius relationship (**Equation 23**). In cryogenic conditions, diffusion of deuterium during the measurements is highly reduced both in austenite and in ferrite, so that the results in such conditions indicate the deuterium distribution more similarly to the one verified right after charging. As the

solubility of H or D in austenite is much higher than in ferrite, the observed pattern is expected. The results at cryogenic conditions agreed with the work of SOBOL *et al.* [97] on 2205 specimens pre-charged electrochemically tested at -120ºC.

At room temperature, the measurements relate to the flux of deuterium escaping via the ferrite phase. At room temperature one verified poorer contrast and higher deuterium content in ferrite. A possible explanation for this is that in fact at room temperature hydrogen flux is being measured. This result is similar to the hydrogen microprint technique. As the deuterium diffusivity in ferrite is much higher than in austenite at room temperature, deuterium flux from the surface in ferrite is thus more important than in austenite, where it is almost immobile. The results at room temperature were similar to those obtained by TANAKA *et al.* [116] using samples of 2205 duplex stainless steel electrochemically charged with deuterium.

In a sample non pre-charged, the ratio of the peak intensities of D/H was measured as equal to 0,2%. The natural occurring D/H ratio is equal to 0,0115%. In **Figure 117**, the ratio of the peak intensities of D/H was estimated as equal to 8% in austenitic grains, and 6,4% in ferrite. Therefore the amount of deuterium in austenite was measured as 25% higher than in ferrite in the tests performed in cryogenic conditions. At room temperature, the hydrogen solubility in austenite is ca. 2500 times higher than in ferrite [73].

In an additional measurement performed at room temperature, the D/H ratio was 8,8% in austenite and 14,9% in ferrite, i.e. the amount of deuterium in austenite was 41% smaller in austenite than in ferrite. This result at room temperature agrees with the qualitative results shown in **Figures 115** and **116**.

It was not observed important variations on D signal inside the γ grains, i.e. there was not observed higher deuterium segregation at the phase boundaries. The spatial resolution of the applied technique is not sufficient to obtain information about the smaller austenite grains. Resolution could be improved by e.g. decreasing the primary ion impact speed. However probably another technique is necessary, such as nano SIMS or atom probe tomography.

4.8. Neutron Scattering

Neutron scattering was performed in an exploratory way intending to verify its potential for hydrogen content measurements and identification of hydrogen position in the steel lattice.

The neutron diffraction profiles obtained in the tests performed in 2015 and 2016 are shown in **Figures 119** and **120**. Only austenite and ferrite were verified. The peaks identified for each phase are shown in the profiles.

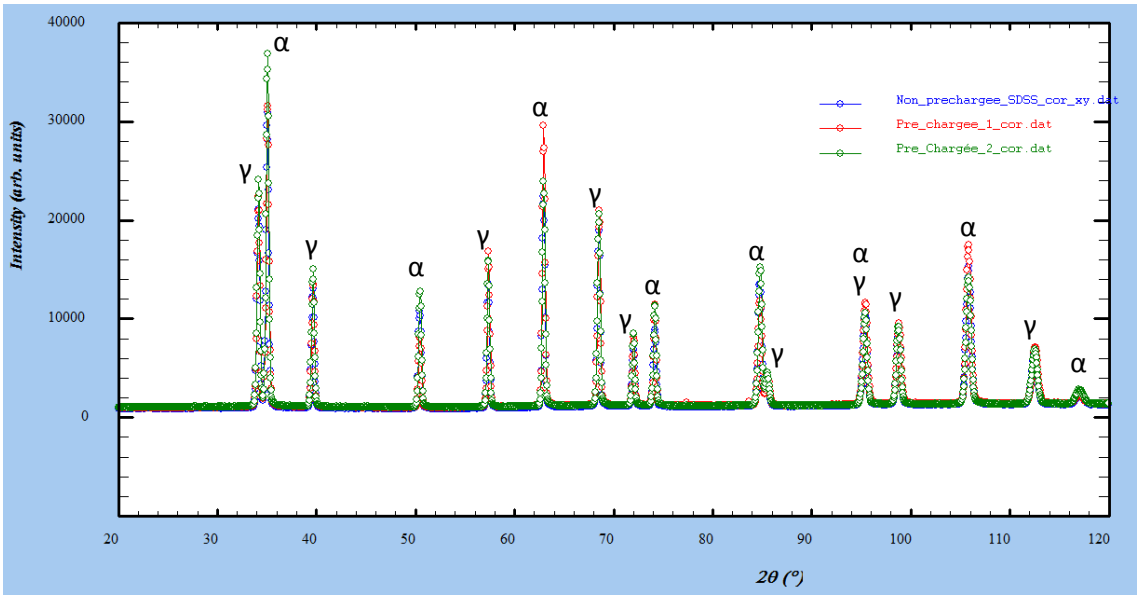

Figure 119. Neutron diffraction profile – Tests of hydrogen-charged specimens (2015) (λ = 1,2256 Å).

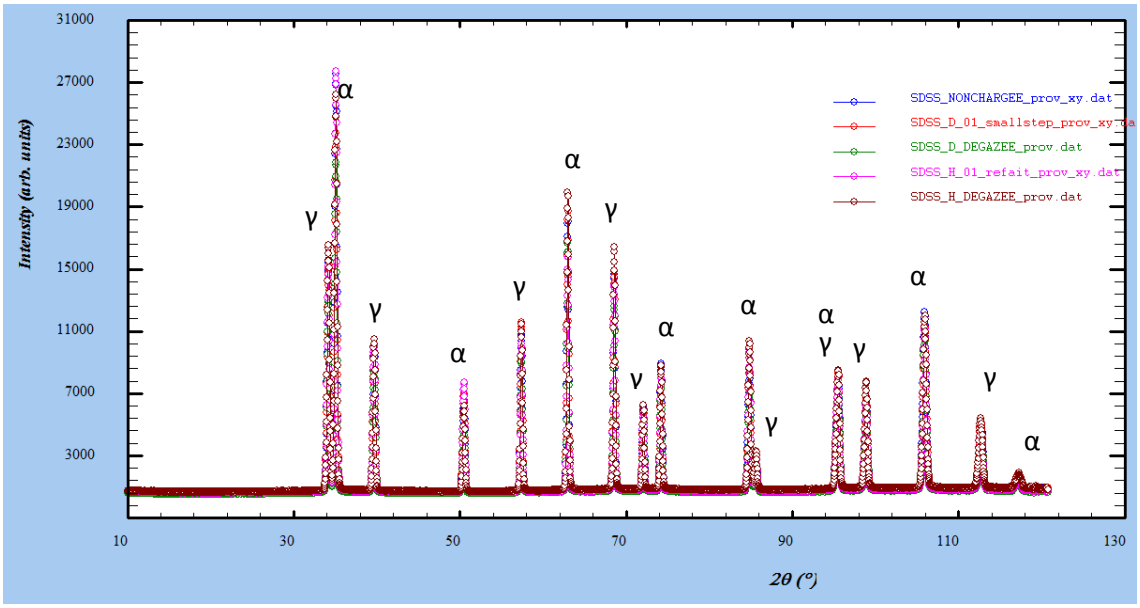

Figure 120. Neutron diffraction profile – Tests of H- and D-charged specimens (2016) (λ = 1,229186 Å).

Coherent scattering (diffraction peaks) enables localization of the hydrogen atoms ordered in the crystal lattice, while the incoherent scattering (background) is proportional to the total amount of hydrogen in the sample, whether it is segregated or not. These two components of the obtained results are analyzed separately.

4.8.1. Analysis of Incoherent Scattering

The coherent and incoherent cross sections of hydrogen, deuterium, vanadium and iron (defined in section **3.2.5**) are presented in **Table 22**. The coherent cross section of Fe (and Cr, Ni, Mo) is much larger than the incoherent one, so that the majority of the incoherent scattering intensity in the measured samples comes from hydrogen or deuterium.

Table 22. Scattering cross sections

	Coherent σ_{coh} (barn)	**Incoherent σ_{incoh} (barn)**
H	1,7583	80,27
D (^{2}H)	5,592	2,05
V	0,0184	5,08
Fe	11,22	0,4

Source: https://www.ncnr.nist.gov/resources/n-lengths/list.html

For vanadium, the incoherent cross section is much larger than the corresponding coherent cross section. Also, Bragg peaks from the sample holder are not visible from the neutron diffraction experiments. Therefore, using the vanadium background (**Figure 121**) obtained in a specific scattering measurement, it is possible to estimate the total content of hydrogen or deuterium present in the specimens.

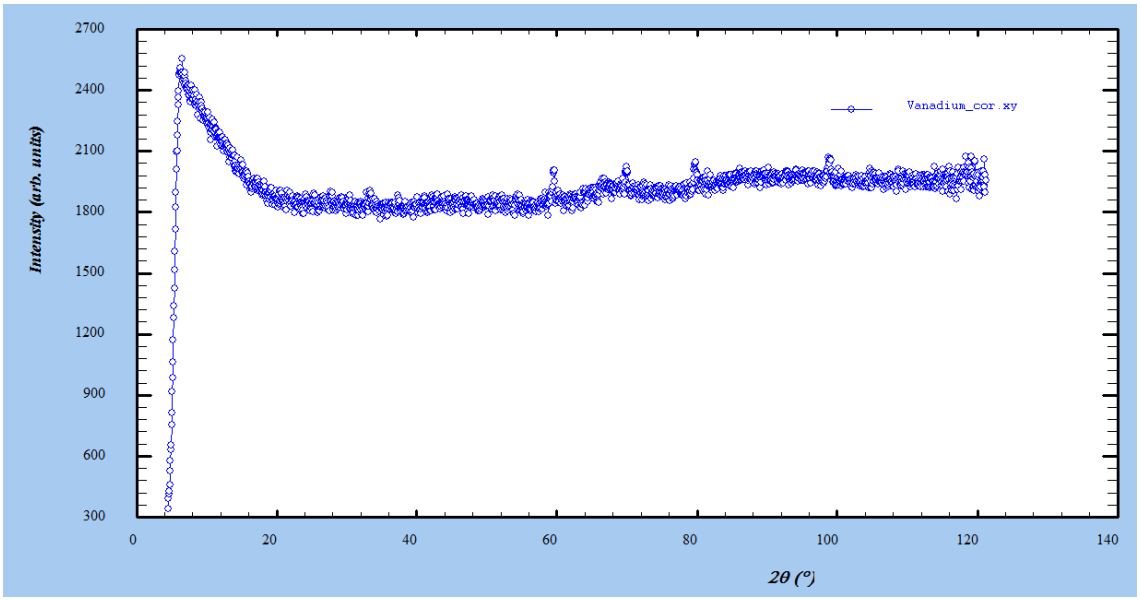

Figure 121. Vanadium scattering profile.

The incoherent scattering intensity from a sample is proportional to the number of atoms (n) and the incoherent cross section:

$$\mathrm{I(incoh)} \sim \mathrm{n}.\sigma(\mathrm{incoh}) \qquad \textbf{(Equation 65)}$$

The ratio of incoherent scattering intensities of vanadium and of the measured samples is thus given by **Equation 66**. It is assumed that the incoherent scattering from the super duplex stainless steel samples are generated only by hydrogen atoms.

$$\frac{\mathrm{I(incoh)_V}}{\mathrm{I(incoh)_{SDSS}}} = \frac{\mathrm{n_V}}{\mathrm{n_H}}.\frac{\sigma(\mathrm{incoh})_\mathrm{V}}{\sigma(\mathrm{incoh})_\mathrm{H}} \qquad \textbf{(Equation 66)}$$

The ratio $\sigma(\mathrm{incoh})_\mathrm{V}/\sigma(\mathrm{incoh})_\mathrm{H}$ is equal to 0,063.

Calculations using deuterium-charged specimen results are inaccurate because, unlike vanadium and hydrogen, the coherent cross section (5,59 b) is higher than the incoherent cross section (2,05 b). So that the results concerning the number of deuterium atoms should be disregarded.

The number of atoms of vanadium n_V can be estimated from the volume of the test specimen V_{cyl} (cylinder with diameter of 10 mm and height of 52 mm), the volume of the Vanadium unit cell V_{cell} (303^3 pm³) and the number of atoms per unit cell n_{cell} (bcc structure, 2 atoms/unit cell). From **Equation 67**, it comes $n_V = 2{,}936.10^{23}$ atoms.

$$\mathrm{n_V} = \frac{\mathrm{V_{cyl}.n_{cell}}}{\mathrm{V_{cell}}} \qquad \textbf{(Equation 67)}$$

So, **Equation 68** turns to:

$$\frac{\mathrm{I(incoh)_V}}{\mathrm{I(incoh)_{SDSS}}} = \frac{2{,}936.10^{23}}{\mathrm{n_H}}.0{,}063 \qquad \textbf{(Equation 68)}$$

From the values of incoherent scattering intensities of vanadium and of the samples (i.e. the backgrounds from the scattering profiles) shown in **Figure 122**, it is possible from **Equation 68** to obtain the total number of hydrogen atoms in the specimens (n_H). These hydrogen atoms are expected to be distributed in ferrite, austenite as well as in traps, such as in phase boundaries.

Similarly to **Equation 67**, the number of Fe atoms can be estimated. From **Equation 68**, assuming equal fractions of austenite and ferrite, n_{Fe} is equal to $1{,}293.10^{23}$ atoms.

$$\mathrm{n_{Fe}} = \mathrm{V_{specimen}}\left(0{,}5\frac{\mathrm{n_\gamma}}{\mathrm{V_{cell-\gamma}}} + 0{,}5\frac{\mathrm{n_\alpha}}{\mathrm{V_{cell-\alpha}}}\right) \qquad \textbf{(Equation 69)}$$

being:

- $V_{specimen}$: considering the dimensions mentioned in section **3.2.5**, it is equal to $1{,}508.10^{-6}$ m³.
- $\mathrm{n_\gamma}, \mathrm{n_\alpha}$: number of Fe atoms per unit cell of austenite (4 atoms) and ferrite (2 atoms).

- $V_{cell-\gamma}$, $V_{cell-\alpha}$: volume of the unit cell of austenite (3,591³ A³) and ferrite (2,863³ A³).

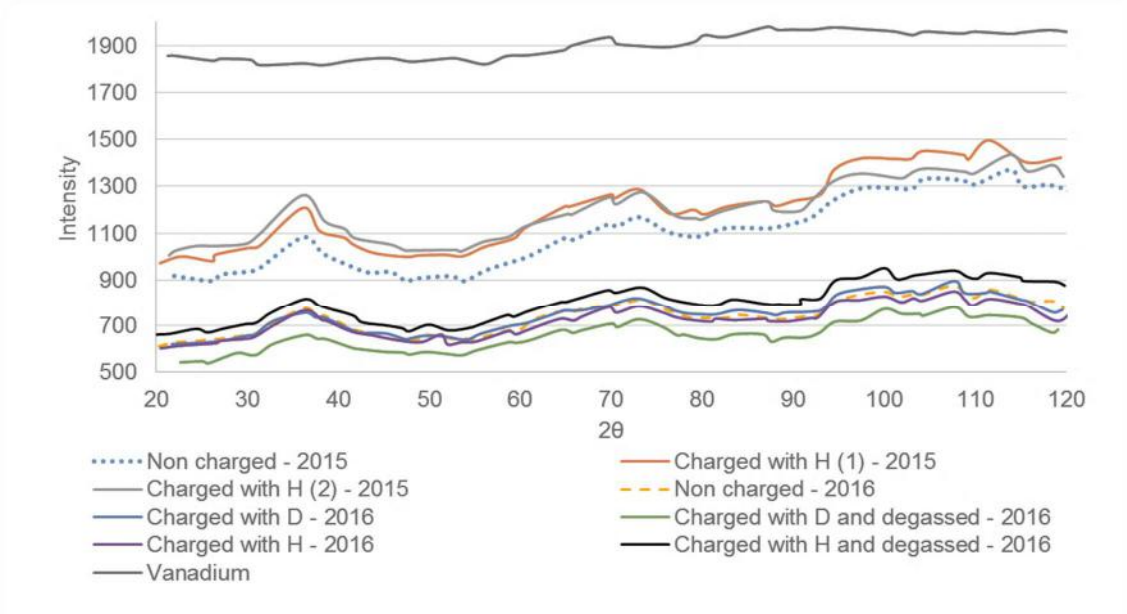

Figure 122. Background measured in all neutron scattering tests.

Table 23 presents the calculated total amount of hydrogen present in the samples in all microstructural and crystalline positions. The estimated number of H atoms in the pre-charged samples was around 8-10% higher than in the non pre-charged samples. However, the estimated number of hydrogen atoms corresponds to 5,4 to 9,1% of the number of atoms of iron, which is several orders of magnitude higher than the hydrogen equilibrium solubility indicated in section **2.6.3** (0,028 at-ppm in ferrite and 70 at-ppm in austenite).

These results indicate that the adopted procedure presents important inaccuracy for duplex stainless steels. Further developments are necessary in order to obtain reliable values of hydrogen content using neutron scattering.

Table 23. Calculated number of H atoms.

	2015			2016			
	Non charged	Charged with H (1)	Charged with H (2)	Non charged	Charged with H	Charged with H and degassed	Vanadium
Average incoherent scattering (background)	1095,46	1200,37	1190,21	737,23	720,43	798,66	1898,39
Standard deviation	151,70	162,89	29,85	29,55	29,52	29,63	57,34
Number of H atoms (10^{22} at)	1,07	1,17	1,18	0,72	0,70	0,78	-
Ratio H/Fe (%)	8,2	9,0	9,1	5,5	5,4	6,0	-

4.8.2. Analysis of Coherent Scattering

The cell parameters and phase fractions estimated by the Rietveld refinement using the Fullprof software are shown in **Table 24**. **Figures 123** and **124** depict the unit cell volumes of ferrite and austenite.

Variation of the lattice parameters of the pre-charged material in comparison with the non-charged samples was within the range of ±0,02%. Austenite presented the greater relative variations on cell parameters, which is unexpected. As austenite presents higher hydrogen solubility, it is not expected that the presence of hydrogen in equilibrium contents provokes important changes in the lattice parameter.

Table 24. Information obtained by the Rietveld analysis.

Test	**Cell parameters (A)**		**Weight fractions (%)**	
	Austenite	**Ferrite**	**Austenite**	**Ferrite**
Non pre-charged - 2015	3,609835	2,874442	47,73	52,27
Pre-charged with H (1) - 2015	3,609819	2,874708	49,97	50,03
Pre-charged with H (2) - 2015	3,610613	2,874356	47,26	52,74
Non pre-charged - 2016	3,617567	2,880979	46,58	53,42
Pre-charged with H - 2016	3,618062	2,881109	46,57	53,43
Pre-charged with H and partially degassed - 2016	3,617821	2,880737	47,84	52,16
Pre-charged with D - 2016	3,617380	2,880840	47,55	52,45
Pre-charged with D and partially degassed	3,616728	2,881291	46,84	53,16

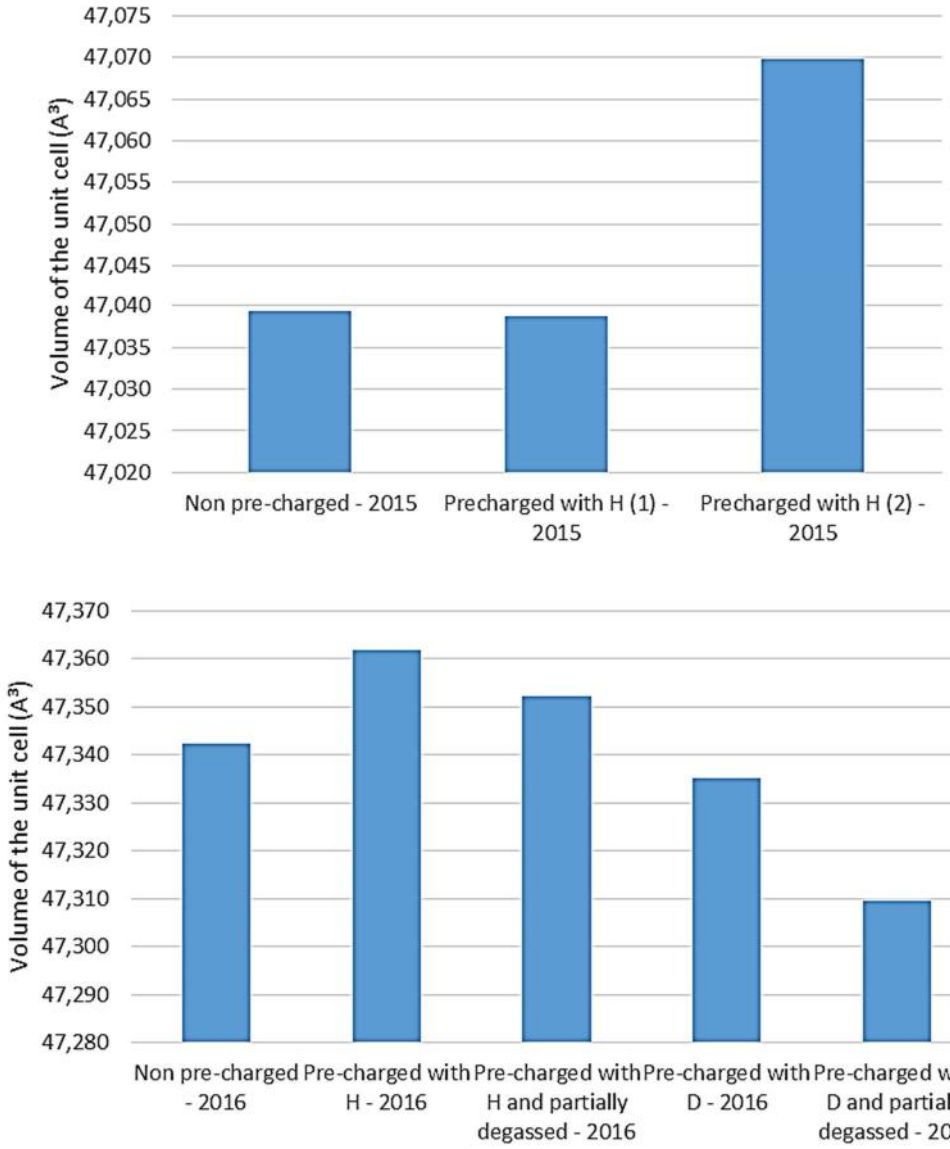

Figure 123. Volume of the unit cell of austenite for all tests.

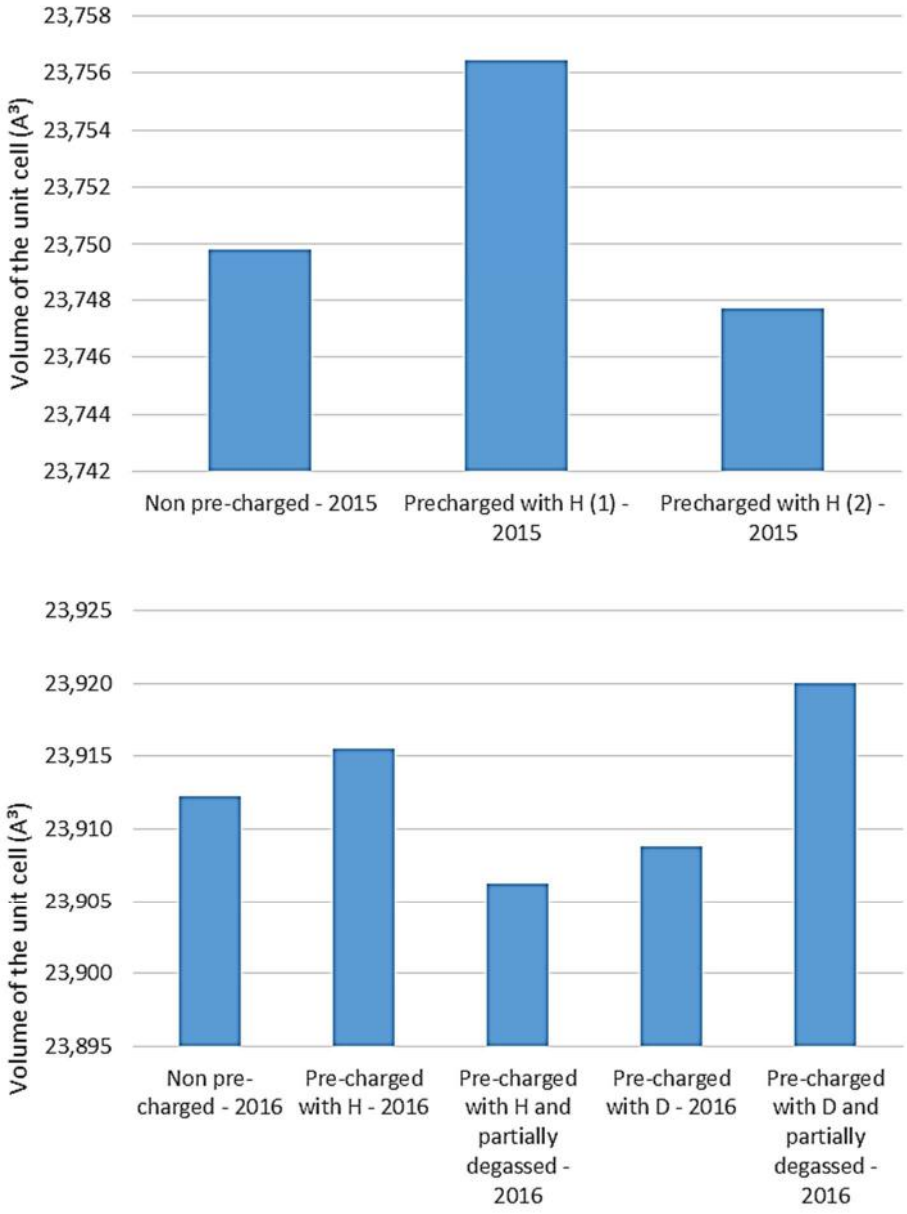

Figure 124. Volume of the unit cell of ferrite for all tests.

In order to try to localize the positions of H and D in the lattice, one approach is to introduce these elements manually in the phase lattices during the profile refinement. Then the reliability indices are compared with the original refinement without H or D.

For hydrogen/deuterium in fcc metals essentially two types of interstitial sites are identified: octahedral sites (e.g. coordinates ½, 0, 0 and ½, ½, ½) and tetrahedral sites (e.g. coordinates ¼, ¼, ¼). For H and D in bcc metals two types of interstitial sites are also usual: octahedral sites (e.g. coordinates ½, 0, 0 and ½, ½, 0) and tetrahedral sites (e.g. coordinates ½, ¼, 0). Besides, also other sites like hexahedral sites (¼, ¼, ¼) and triangular sites (3/8, 3/8, 0 and 1/8, 1/8, ½) have been proposed, partially as intermediate

sites during hydrogen diffusion [117]**.** Fcc metals tend to absorb hydrogen in octahedral sites. In bcc metals, H atom at low concentration occupy tetrahedral sites [118].

Hydrogen or deuterium was introduced in the position (½ 0 0) in austenite, indicated schematically in **Figure 125**. **Table 25** indicates the values of profile R-factor (R_p), weighted profile R-factor (R_{wp}) and χ^2 obtained in the original refinements and after introducing H or D in the interstitial position of austenite. The Rietveld parameters decreased in all cases by the introduction of H and D. This indicates a better modelling, suggesting the presence of H and D at the proposed interstitial site agrees with the measurements obtained.

Table 25. Comparison between Rietveld error indices.

Test	**Rietveld discrepancy values**		
	R_p	**R_{wp}**	**χ^2**
Pre-charged with H (1) - 2015	5,53	8,44	66,8
Pre-charged with H (1) - 2015 - H in austenite (1/2 0 0)	5,46	8,30	64,3
Pre-charged with H (2) - 2015	6,02	8,21	63,0
Pre-charged with H (2) - 2015 - H in austenite (1/2 0 0)	6,00	8,12	61,6
Pre-charged with H - 2016	5,43	7,70	51,8
Pre-charged with H - 2016 - H in austenite (1/2 0 0)	5,31	7,56	48,4
Pre-charged with H and partially degassed - 2016	3,51	5,04	24,3
Pre-charged with H and partially degassed - 2016 - H in austenite (1/2 0 0)	3,32	4,88	22,0
Pre-charged with D - 2016	4,30	5,62	28,0
Pre-charged with D - 2016 - D in austenite (1/2 0 0)	4,03	5,34	24,6
Pre-charged with D and partially degassed	5,97	8,39	54,2
Pre-charged with D and partially degassed - D in austenite (1/2 0 0)	5,83	8,28	51,0

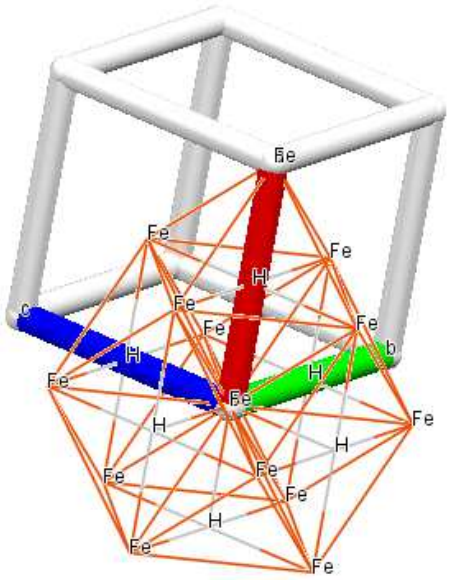

Figure 125. Hydrogen or deuterium at the interstitial position (½ 0 0).

Attempts were made considering other interstitial positions. **Table 26** presents the χ^2 and R_{wp} values obtained in the profile refinements of tests performed in 2015 in which H atoms were placed at two interstitial positions: sites (½ ½ ½) and (0 ½ 1) in austenite and sites (½ ¼ 1) and (1 ½ ¼) in ferrite.

The quality factors obtained when H is placed in both positions in ferrite were one order of magnitude higher than without hydrogen in the refinement. This suggests hydrogen was not present at these positions. Assuming hydrogen is in austenite, the obtained residuals were also not lower than in the refinements without H. Because of this, it is believed the (½ ½ ½) and (0 ½ 1) interstices tend not to be the more probable positions for H in austenite.

Table 26. Profile refinement results after adding hydrogen in chosen interstitial sites.

	R_{wp}		**χ^2**
Sample	**Austenite**	**Ferrite**	
Pre-charged 1 - not considering H	5,0	5,9	61,3
Pre-charged 1 - H in austenite (½ ½ ½)	8,9	5,0	86,5
Pre-charged 1 - H in austenite (0 ½ 1)	7,2	2,9	73,3
Pre-charged 1 - H in ferrite (½ ¼ 1)	12,2	99,7	965
Pre-charged 1 - H in ferrite (1 ½ ¼)	14,5	99,6	603
Pre-charged 2 - not considering H	6,8	4,9	63,1
Pre-charged 2 - H in austenite (½ ½ ½)	10,7	9,8	85,2
Pre-charged 2 - H in austenite (0 ½ 1)	10,6	10,2	84,4
Pre-charged 2 - H in ferrite (½ ¼ 1)	13,4	99,5	735
Pre-charged 2 - H in ferrite (1 ½ ¼)	14,0	99,6	753

Additional analyses were performed using Fourier maps, calculated by the application GFOURIER of Fullprof. Fourier maps provide the scattering (nuclear) density inside the unit cell. **Figures 126** to **128** give the bi- and tri-dimensional (x-y) Fourier maps of three tests performed in 2016: specimens non pre-charged, charged with H and with D.

The (½ 0 0) interstitial positions presented lower density in the specimen with hydrogen (0,725) than in the specimens non-charged and with deuterium (0,809 and 0,822 respectively). This can be explained by the fact that the coherent scattering length of hydrogen is negative (-3,74 fm), while the value for deuterium is positive (+6,68 fm). The Fourier maps analyses confirm this (½ 0 0) octahedral interstitial position is the preferable site for hydrogen occupation in austenite in the tested material.

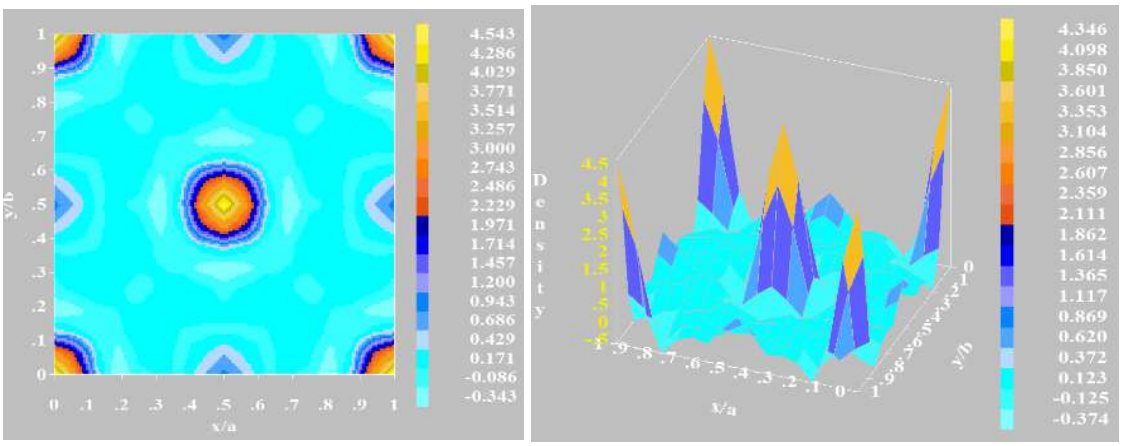

Detail at (½ 0 0):

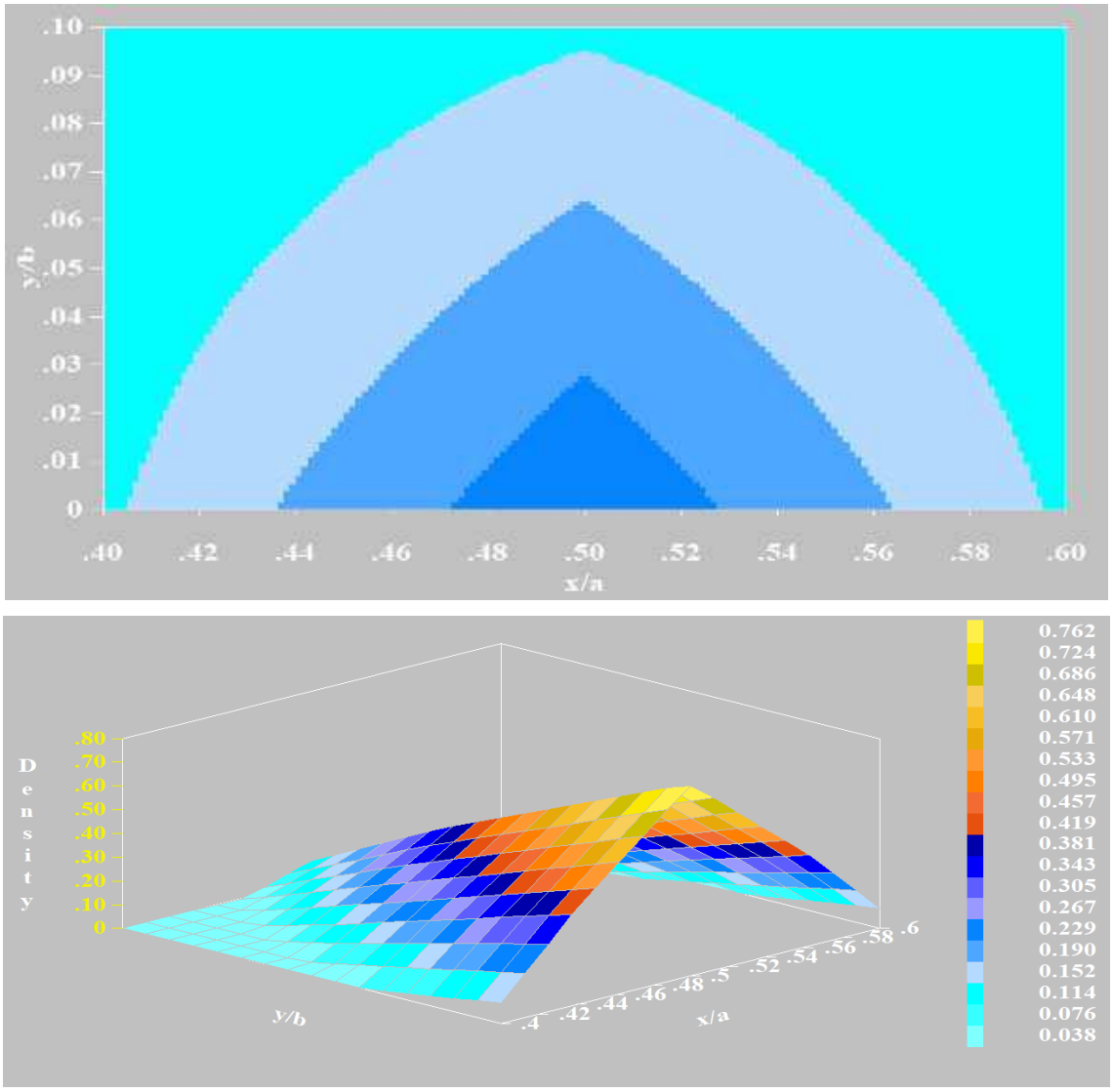

Figure 126. Fourier maps, z = 0. Non pre-charged (2016). Below: detail at (½ 0 0), with scattering density of 0,809.

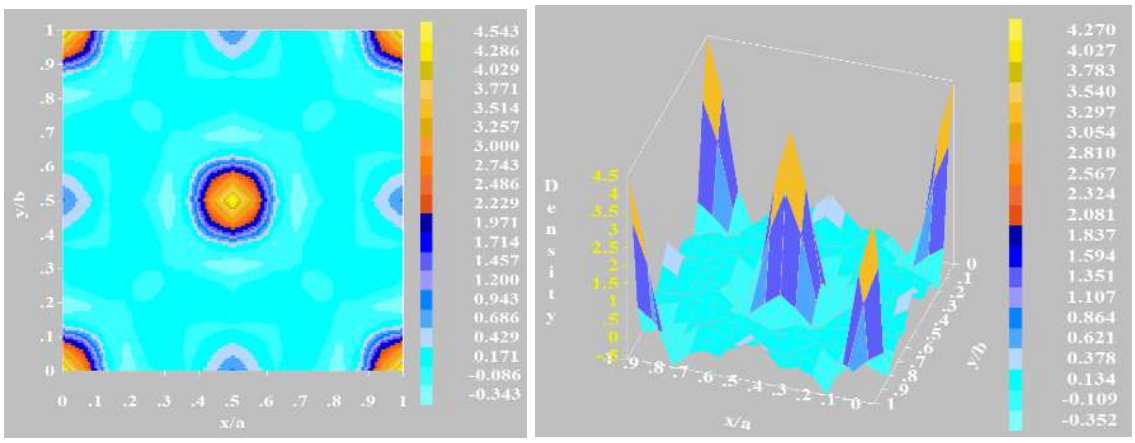

Detail at (½ 0 0):

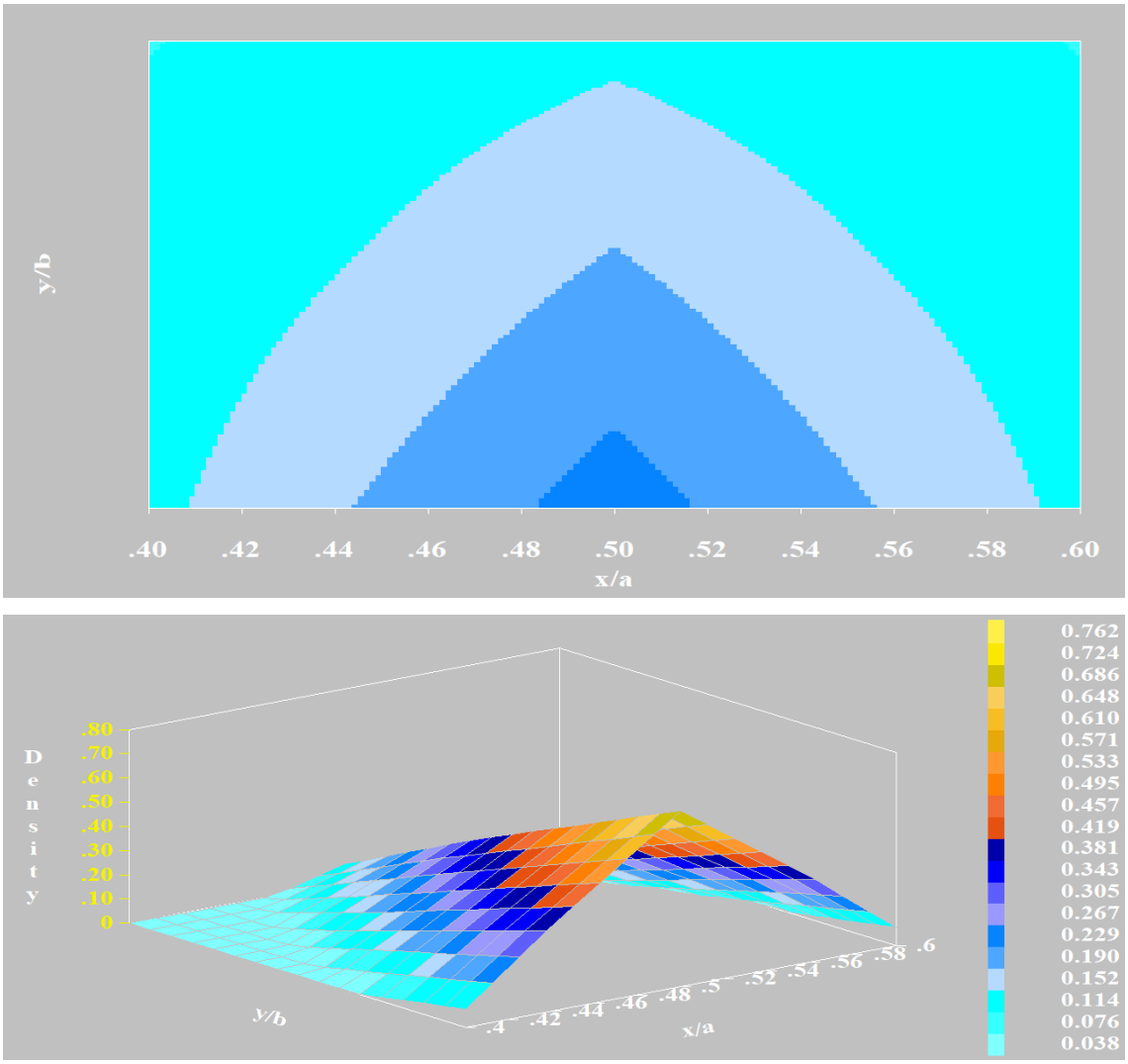

Figure 127. Fourier maps, z = 0. Pre-charged with H (2016). Below: detail at (½ 0 0), with scattering density of 0,725.

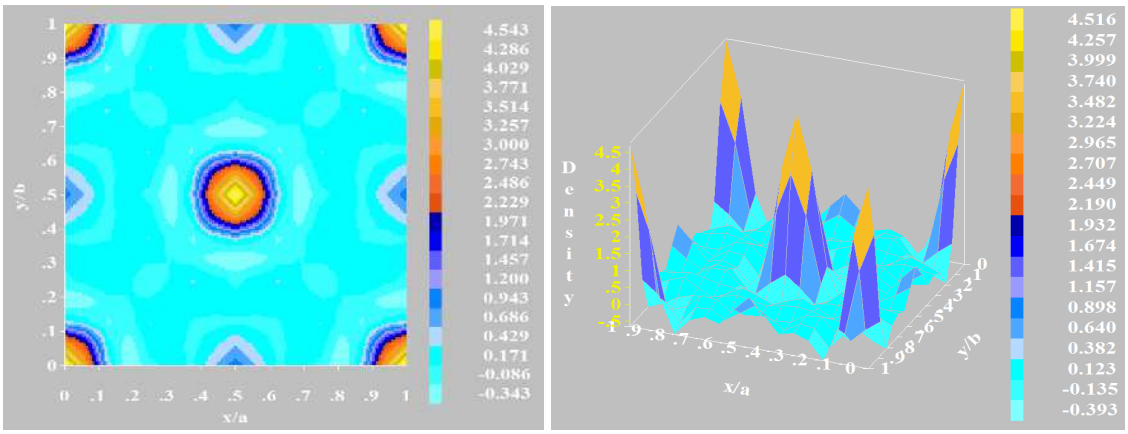

Detail at (½ 0 0):

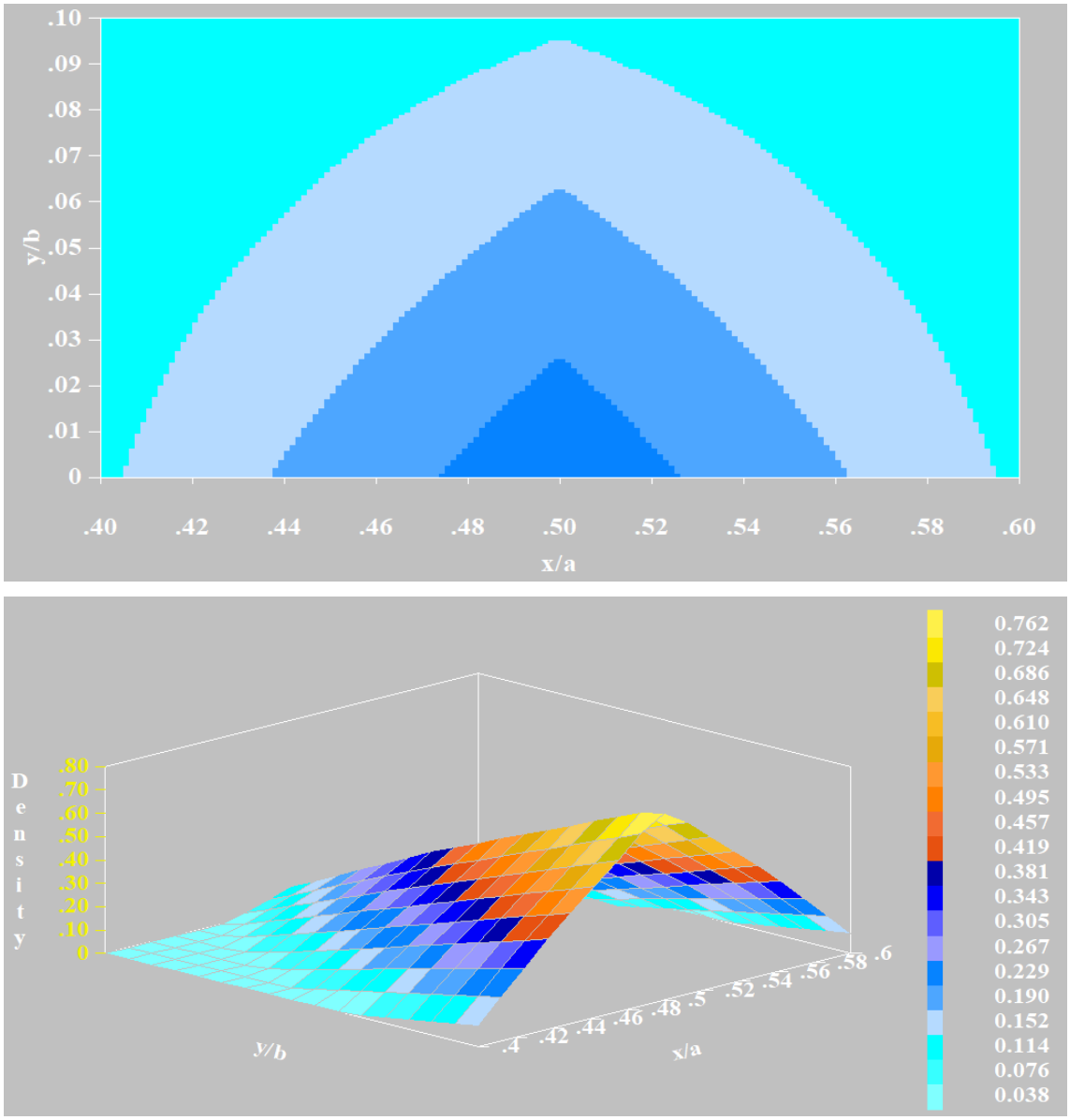

Figure 128. Fourier maps, z = 0. Pre-charged with D (2016). Below: detail at (½ 0 0), with scattering density of 0,822.

5. Discussion

In view of the obtained results and analyses for the tested material and conditions, for the improvement on the understanding of hydrogen embrittlement, a relationship between gas and cathodic hydrogen embrittlement as well as the parameters describing and variables affecting hydrogen diffusion will be discussed. Possible interactions between hydrogen and microsctructure (especially dislocations) as a contributor for the hydrogen damage process are proposed.

5.1. Hydrogen Embrittlement in Different Environments.

Figures 129 to **134** present ductility parameters as a function of H_2 pressure and cathodic current obtained in the tensile tests with in-situ charging, as described in section **4.5.2**.

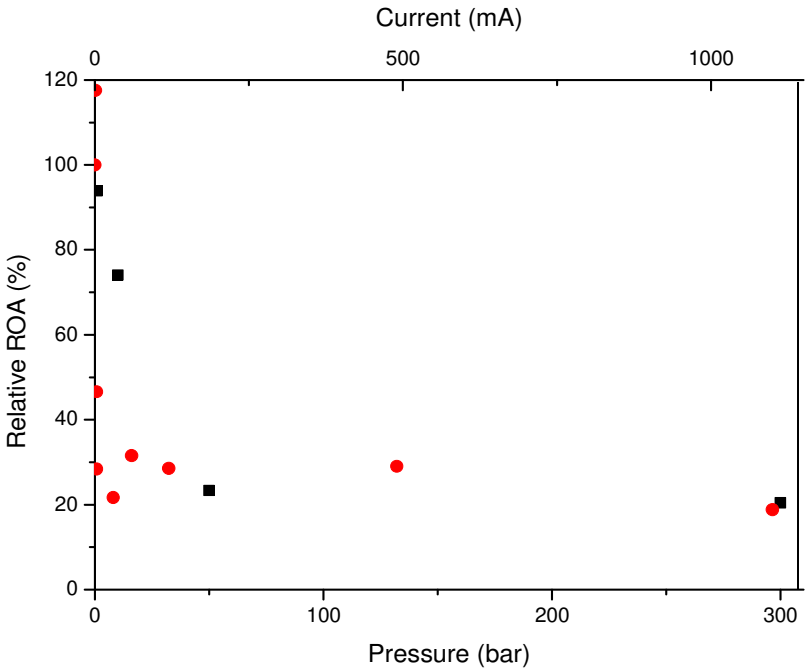

Figure 129. Relative reduction of area obtained in the tensile tests with in-situ hydrogen charging – Flange body. ■: Gas charging, pressure ●: Cathodic charging, current.

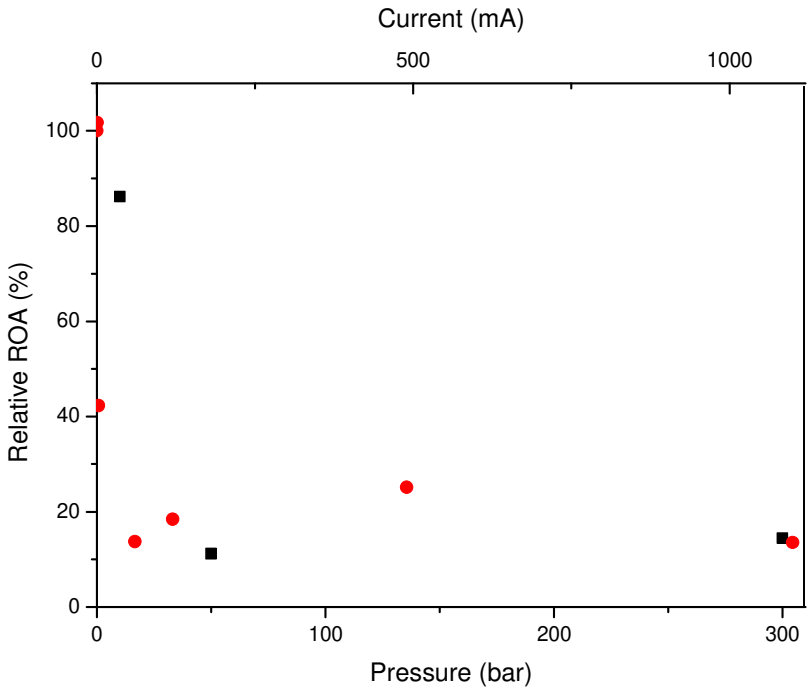

Figure 130. Relative reduction of area obtained in the tensile tests with in-situ hydrogen charging – Flange neck. ■: Gas ●: Cathodic.

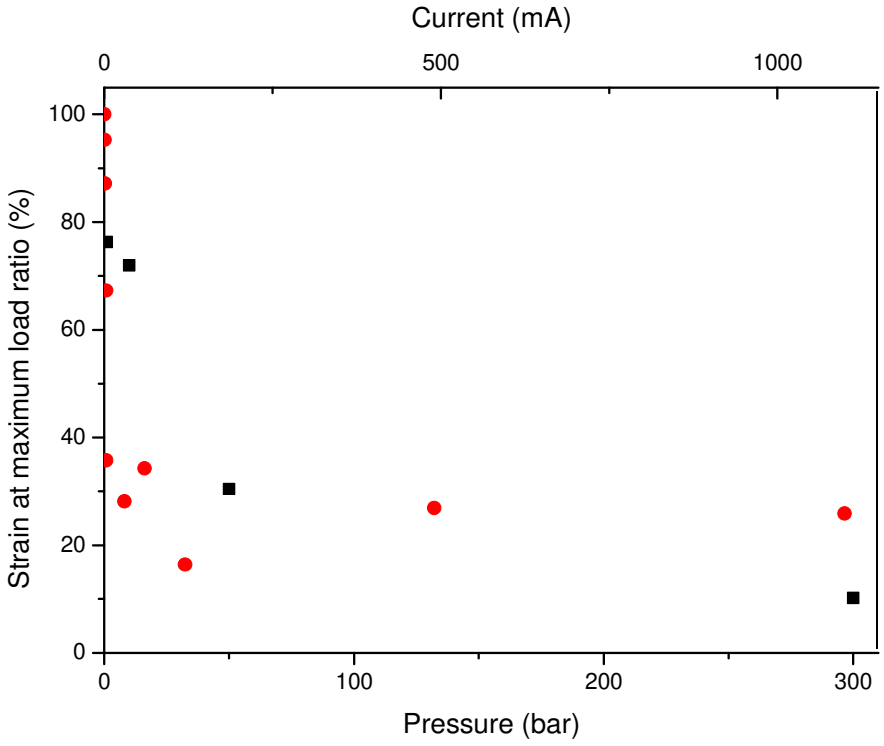

Figure 131. Relative plastic strain at maximum load measured in the tensile tests with in-situ hydrogen charging – Flange body. ■: Gas ●: Cathodic.

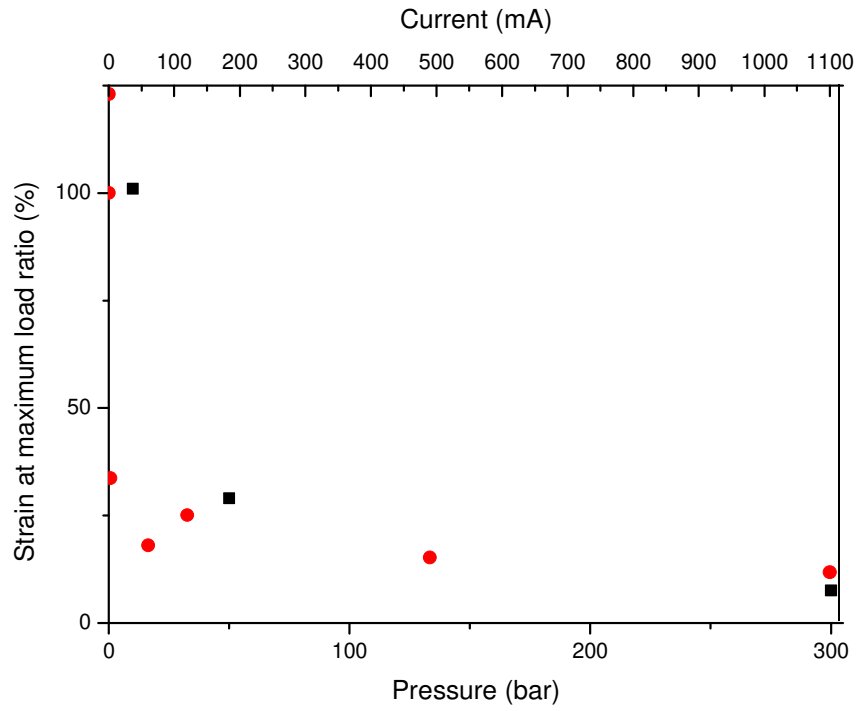

Figure 132. Relative plastic strain at maximum load measured in the tensile tests with in-situ hydrogen charging – Flange neck. ■: Gas ●: Cathodic.

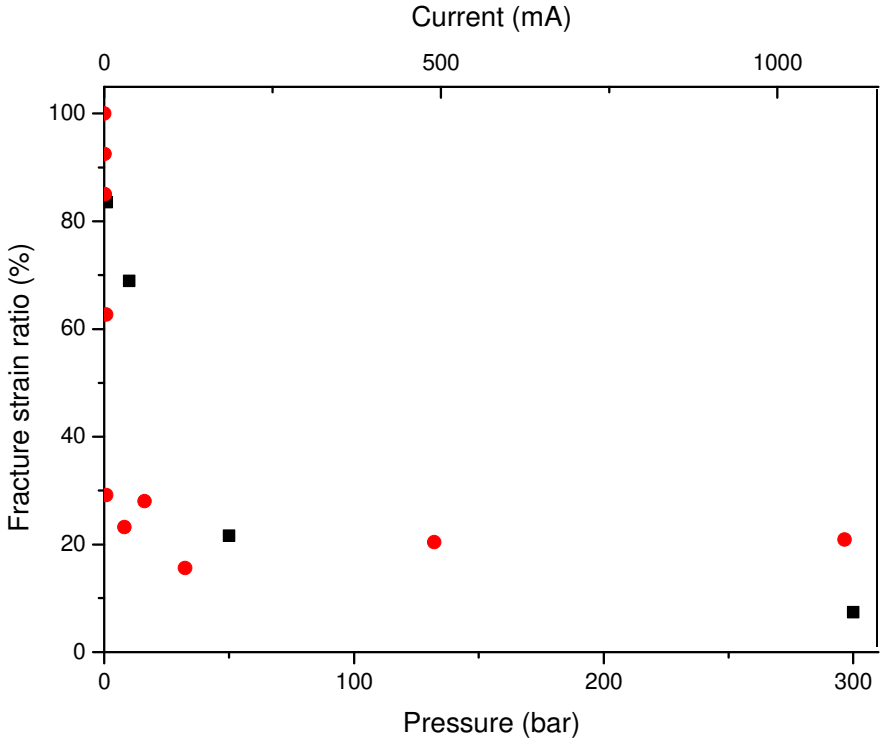

Figure 133. Relative plastic strain at fracture measured in the tensile tests with in-situ hydrogen charging – Flange body. ■: Gas ●: Cathodic.

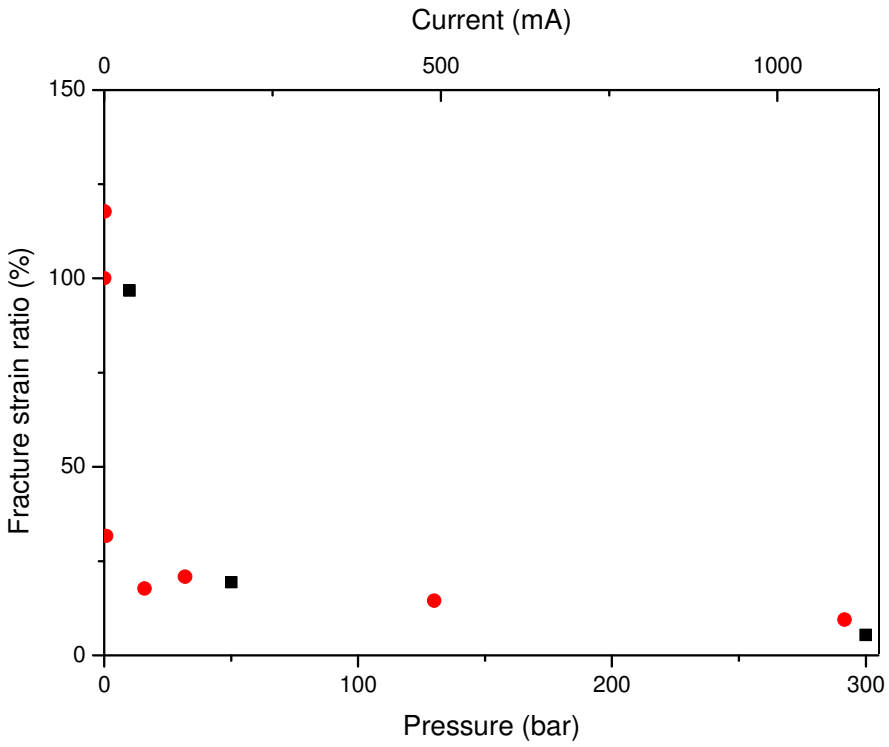

Figure 134. Relative plastic strain at fracture measured in the tensile tests with in-situ hydrogen charging – Flange neck. ■: Gas ●: Cathodic.

Regression equations of the ductility ratios as a function of hydrogen pressure "P" obtained from the curves shown in these figures up to the threshold of 50 bar are shown below. In all equations, the adjusted R^2 values were above 99%.

a) Flange body (P≤ 50 bar):

$ROA_r = 310,0-66,4\ln(P+24,88)$ **(Equation 70)**

$\varepsilon_{pmax-r} = 6757,6-970,8\ln(P+971,61)$ **(Equation 71)**

$\varepsilon_{pf-r} = 481,3-98,7\ln(P+55,11)$ **(Equation 72)**

b) Flange neck (P≤ 50 bar):

$ROA_r = 242,6-57,7\ln(P+5)$ **(Equation 73)**

$\varepsilon_{pmax-r} = 251,1-55,4\ln(P+5)$ **(Equation 74)**

$\varepsilon_{pf-r} = 257,9-59,5\ln(P+5)$ **(Equation 75)**

Regression equations of the ductility ratios as a function of current density "i" up to current densities of 60 mA (30 mA/cm²) are shown below. The adjusted R^2 values were higher for the neck (98-99%) than for the body (58-62%).

a) Flange body:

$$ROA_r = 63,6-14,6\ln(i-0,22) \quad \textbf{(Equation 76)}$$

$$\varepsilon_{pmax-r} = 61,1-10,5\ln(i-0,21) \quad \textbf{(Equation 77)}$$

$$\varepsilon_{pf-r} = 56,7-11,0\ln(i-0,21) \quad \textbf{(Equation 78)}$$

b) Flange neck:

$$ROA_r = 42,4-7,0\ln(i-0,24) \quad \textbf{(Equation 79)}$$

$$\varepsilon_{pmax-r} = 33,2-3,0\ln(i-0,24) \quad \textbf{(Equation 80)}$$

$$\varepsilon_{pf-r} = 31,6-3,3\ln(i-0,24) \quad \textbf{(Equation 81)}$$

Considering these expressions, the relationships experimentally obtained between hydrogen pressure "P" (up to 50 bar) and the absolute cathodic density current "i" (up to 30 mA/cm²) that correspond to equal ductility indices are shown in **Equations 82** to **87**.

- Equivalent relative reduction of area (ROA_r):

a) Flange body: $P = \exp(3,71).(i-0,22)^{0,22} - 24,88$ **(Equation 82)**

b) Flange neck: $P = \exp(3,47).(i-0,24)^{0,12} – 5$ **(Equation 83)**

- Equivalent relative maximum plastic strain (ε_{pmax-r}):

a) Flange body: $P = \exp(6,90)\ (i-0,21)^{0,011} - 971,61$ **(Equation 84)**

b) Flange neck: $P= \exp(3,93)\ (i-0,24)^{0,05} – 5$ **(Equation 85)**

- Equivalent relative plastic strain at fracture (ε_{pf-r}):

a) Flange body: $P = \exp(4,30)\ (i-0,21)^{0,11} - 55,11$ **(Equation 86)**

b) Flange neck: $P = \exp(3,80)(i-0,24)^{0,055} – 5$ **(Equation 87)**

Figures 135 to **137** present the curves of **Equations 82** to **87**. These curves and equations have applicability for the tested material and conditions, and can be used to determine the hydrogen pressure and cathodic current density (within the mentioned ranges), that should generate equal embrittlement levels.

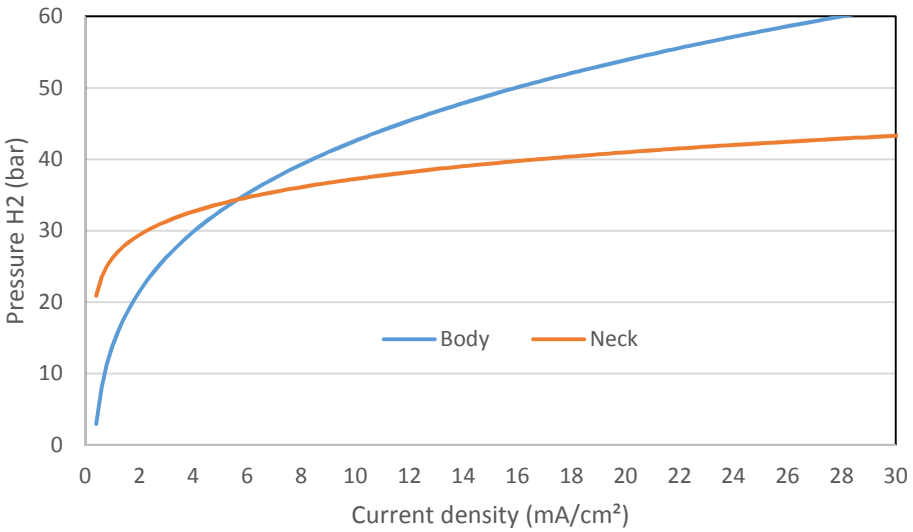

Figure 135. Relative ROA – Equivalence between gas and cathodic in-situ tests.

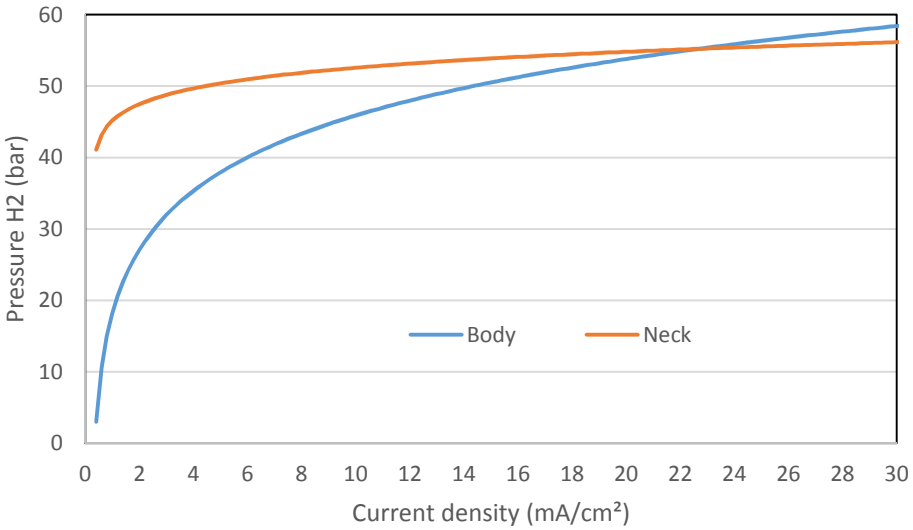

Figure 136. Relative ε_{pmax} – Equivalence between gas and cathodic in-situ tests.

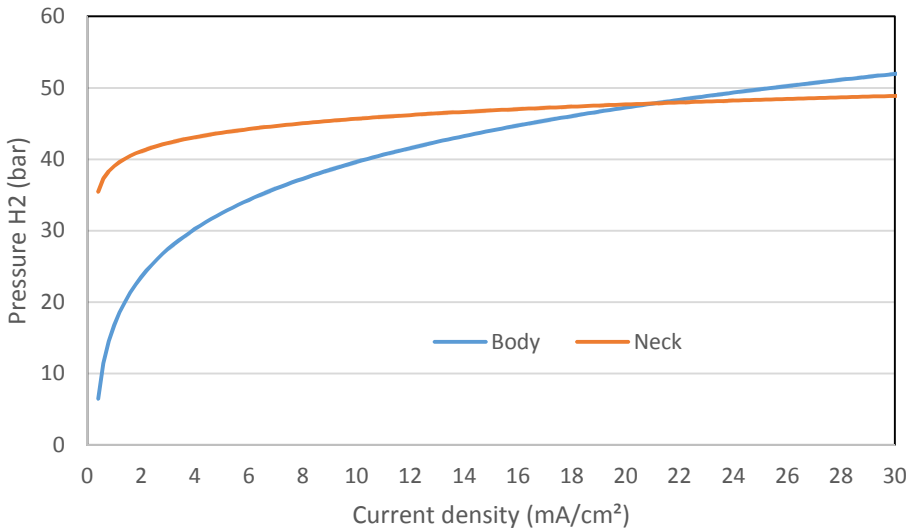

Figure 137. Relative ε_{pf} – Equivalence between gas and cathodic in-situ tests.

Consider for instance one intends to evaluate the embrittlement of the flange body at 15 bar H_2. According to **Equation 70**, the relative reduction of area should be close to 65%. Following **Equations 82** or **76**, or using the graph of **Figure 135**, one can check this value or evaluate the fracture characteristics by testing at a current density of 1,1 mA/cm².

The obtained relationships between hydrogen pressure and cathodic current density are analyzed in view of a theoretical description assuming that these two hydrogen-bearing environments generate equal absorbed hydrogen concentrations in the material.

5.1.1. Cathodic Charging.

In a solution under cathodic polarization, the hydrated hydrogen cations H_3O^+ are transported by diffusion or migration towards the cathode. There the cation undergoes reduction and becomes atomic hydrogen H. The most probable mechanisms followed by hydrogen reduction on iron and steels are (a) coupled electrochemical reduction and chemical combination (Volmer-Tafel mechanism) or (b) slow reduction and fast electrochemical recombination (Volmer-Heyrovsky mechanism) [119].

The electrochemical reduction of hydrogen ions is given by the Volmer reaction:

$$H^+_{hydrated} + e^- \overset{k_1/k_{-1}}{\Longleftrightarrow} H_{adsorbed} \qquad \textbf{(Equation 88)}$$

The potential-current density dependency for the Volmer reaction can be expressed as:

$$i_1 = k_1[H]\exp\left(\frac{\alpha_V F}{RT}\eta\right) - k_{-1}[H^+]\exp\left(-\frac{(1-\alpha_V)F}{RT}\eta\right) \quad \textbf{(Equation 89)}$$

with:

- [H], [H⁺]: concentration of adsorbed H and H⁺ at the electrode-electrolyte interface.
- α_v: symmetry of the energy barrier ($0 < \alpha < 1$)
- η: overpotential for the hydrogen evolution reaction i.e. the difference between the actual local potential and the standard electrode potential for hydrogen evolution on the substrate.

In a noncorrosive environment, the rate constant k_1 depends on the exchange current density of hydrogen evolution on the metal [120]. The concentration of atomic hydrogen adsorbed on the surface, [H] is proportional to the degree of hydrogen coverage, θ. The coverage θ is the fraction of the metal surface occupied by a monoatomic layer of hydrogen. It depends on the rate of hydrogen recombination reactions, the presence of ions or molecules present in the electrolyte that compete with hydrogen on adsorption on the metal, agitation intensity, hydrogen partial pressure and concentration and temperature [121]. The reduction of hydrogen cation H⁺ occurs only on the sites that are not covered by absorbed hydrogen atoms. This part is equal to (1-θ). Then the current-potential relationship becomes:

$$i_1 = k_1\theta\exp\left(\frac{\alpha_V F}{RT}\eta\right) - k_{-1}(1-\theta)\exp\left(-\frac{(1-\alpha_V)F}{RT}\eta\right) \quad \textbf{(Equation 90)}$$

After the reduction of hydrogen cations, part of the hydrogen atoms that are adsorbed on the metallic surface will recombine to form molecular hydrogen that leaves the surface. According to the Volmer-Tafel mechanism, the chemical recombination of atomic hydrogen is given by the Tafel reaction:

$$H_{adsorbed} + H_{adsorbed} \overset{k_2/k_{-2}}{\Longleftrightarrow} H_2 \quad \textbf{(Equation 91)}$$

The Tafel reaction is a purely chemical reaction, so its rate constant does not depend on the potential. The reaction rate is given by:

$$i_2 = k_2(1-\theta)^2 - k_{-2}\theta^2 \quad \textbf{(Equation 92)}$$

At equilibrium, i.e. when the overall rate is zero, the degree of coverage reaches the equilibrium value θ_o, given by:

$$i_{0,2} = k_2(1-\theta_o)^2 = k_{-2}{\theta_o}^2 \quad \textbf{(Equation 93)}$$

Part of adsorbed hydrogen atoms that do not recombine will undergo an absorption reaction inside the material. The direct reaction of passage of atomic hydrogen through

the interface depends on the surface coverage "θ" and on the number of available sites in the subsurface that hydrogen can occupy. The consequence is the accumulation of hydrogen under the metallic surface, leading to a concentration C_o. The reversal reaction – hydrogen passage from the subsurface towards the surface – can take place. The rate for the reversal reaction is proportional to the subsurface concentration and to the concentration of empty sites on the surface through which hydrogen can be desorbed, (1-θ). The rate of the overall reaction is:

$$i_{abs} = k_{abs}\theta\left[1 - \frac{N_o}{N_s}\right] - k_{des}C_o(1-\theta) \qquad \textbf{(Equation 94)}$$

being:

- N_o: number of interstitial sites occupied by hydrogen
- N_s: number of interstitial sites in the matrix
- C_o: subsurface hydrogen concentration.

At equilibrium (i_{abs} = 0) and for small coverage degree θ and small degree of occupation, the subsurface concentration of hydrogen C_o is proportional to the degree of coverage:

$$C_o = K\theta \qquad \textbf{(Equation 95)}$$

being $K = k_{abs}/k_{des}$.

Assuming that the passage of hydrogen through the interface is the slowest step, then for the Volmer-Tafel mechanism the relationship between the subsurface concentration and the charging current can be found considering that Volmer and Tafel reactions are at equilibrium. A simplistic way is to combine the rate of the Tafel reaction ($i_{0,2} = k_2\theta_o^2$, **Equation 93**) with the expression $C_o = K\theta$ (**Equation 95**), so that one obtains the following relationship between the subsurface concentration C_o with the charging current density (i) and the kinetics of hydrogen evolution (k_2):

$$C_o = K\sqrt{\frac{i}{k_2}} \qquad \textbf{(Equation 96)}$$

The square root dependence on the charging current density is followed up to certain value of the current density. Above a limiting value, the subsurface concentration of hydrogen becomes independent of the charging current. This corresponds to the saturation of the surface (θ=1). In the presence of promoters or poisons this square root dependency is followed up to higher values of charging current density.

The value of the parameter k_2 for iron was estimated by RAMASUBRAMANIAN *et al.* [120] as equal to $1{,}8.10^{-11}$ mol/m²s and in general $k_{abs} \geq k_{des}$ (thus $K \geq 1$).

5.1.2. Gas Charging.

The model proposed for the dissociative chemisorption of gaseous hydrogen involves several steps [119,122]. The gas molecule at pressure P strikes the material surface and splits into atoms that adhere there ($H_2 \leftrightarrow 2H_{adsorbed}$). The flux of adsorbing atoms can be expressed by:

$$J_{ads} = k_{ads}(1-\theta)^2 P \qquad \textbf{(Equation 97)}$$

The adsorption kinetic constant k_{ads} can be given by the following expression:

$$k_{ads} = 2\alpha_m.\mu \qquad \textbf{(Equation 98)}$$

where

- α_m: adsorption probability for incident molecules
- $\mu = (2\pi mkT)^{-1/2}$
- m: gas molecule mass
- k: Boltzmann constant ($1{,}3806.10^{-23}$ J/K)
- T: temperature of the molecular gas.

There is a reversal reaction of recombination of adsorbed atoms with the formation of molecular hydrogen, which leaves the metallic surface. The desorbing flux is expressed by:

$$J_{des} = k_{des}\theta^2 \qquad \textbf{(Equation 99)}$$

The desorption kinetic constant k_{des} can be given by:

$$k_{des} = 2\delta \qquad \textbf{(Equation 100)}$$

where “δ” is the rate constant for desorption.

The adsorbed atoms could cross the metallic interface and become absorbed atoms. The corresponding flux is:

$$J_{abs} = \gamma\theta \qquad \textbf{(Equation 101)}$$

where “γ” is a proportionality constant

The atoms inside the material can diffuse out to the surface and the flux is proportional to the subsurface hydrogen concentration C_o and the fraction of unoccupied surface sites, though which hydrogen can diffuse out:

$$J_{dsb} = \beta(1-\theta)C_o \qquad \textbf{(Equation 102)}$$

where “β” is a proportionality constant.

The net atomic flux values J_p in the interfaces can be given by:

$$J_p = J_{ads} - J_{des} = 2\alpha_m.\mu(1-\theta)^2 P - 2\delta\theta^2 \qquad \textbf{(Equation 103)}$$

and

$$J_p = J_{abs} - J_{dsb} = \gamma\theta - \beta(1-\theta)C_o. \quad \textbf{(Equation 104)}$$

Considering the equilibrium case where $J_p = 0$, from these equations one obtains the following relation between H_2 gas pressure and concentration of atoms in the bulk, equivalent to Sievert's law:

$$C_o = (\gamma/\beta)(\alpha_m\mu/\delta)^{1/2}P^{1/2} = s.P^{1/2} \quad \textbf{(Equation 105)}$$

The Sievert's law in terms of pressure is only correct if the hydrogen gas behaves like an ideal gas, in general at high temperatures or lower pressures, typically below 200 bar [64,123]. Under frequently occurring conditions, hydrogen does not behave ideally, in which case it must be used the fugacity instead of pressure, i.e.:

$$C_o = s.f^{1/2} \quad \textbf{(Equation 106)}$$

The use of the fugacity "f" is theoretically correct, but it is not a quantity that can be measured directly, and it therefore has to be related to the pressure. The following expression can be employed for the pressure-fugacity relation:

$$f = \xi P \quad \textbf{(Equation 107)}$$

with the fugacity coefficient ξ. For an ideal gas, ξ is equal to 1.

The fugacity coefficient can be determined when the equation of state of the gas is known. Simulations were performed with software OLI version 9.5 using the Soave-Redlich-Kwong (SRK) equation of state. This equation is described in [124]. **Figures 138** and **139** present the calculated hydrogen fugacity factor and fugacity as a function of pressure at 23ºC using the SRK EOS.

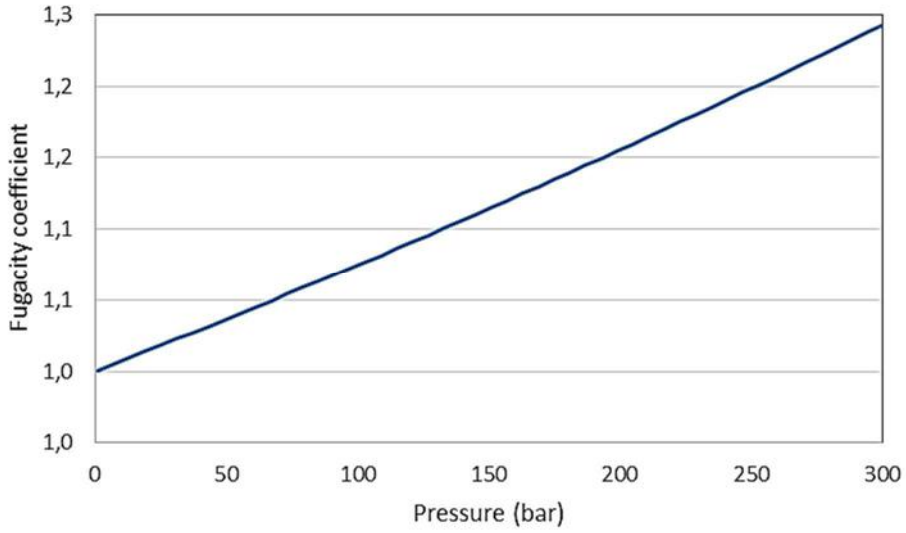

Figure 138. Fugacity factor as a function of pressure at 23ºC calculated with the software OLI using SRK EOS.

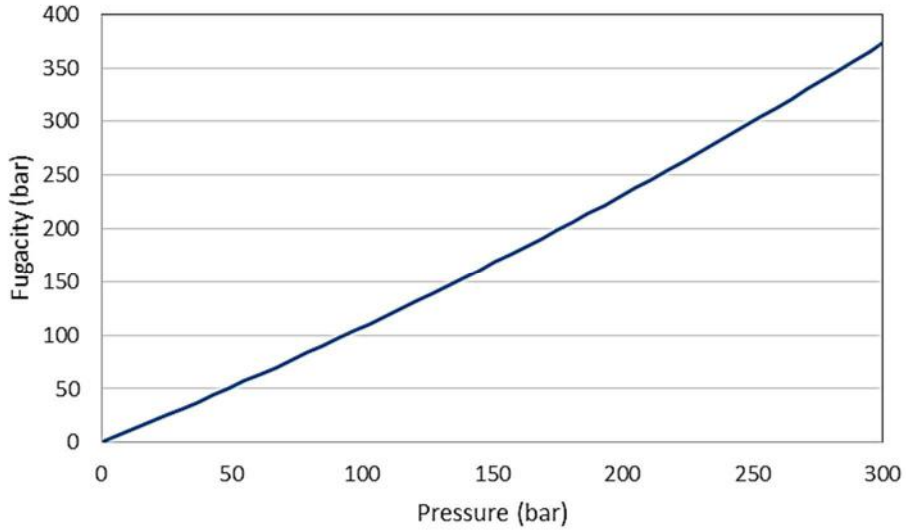

Figure 139. Fugacity as a function of pressure at 23ºC calculated with the software OLI using SRK EOS.

From **Figure 139**, a quadratic relationship between fugacity and pressure is kept up to 300 bar:

$$f = 8{,}58.10^{-4}P^2 + 0{,}9826P + 0{,}4278 \quad \textbf{(Equation 108)}$$

Considering a maximum value of 50 bar, a linear relationship is valid:

$$f = 1{,}0365P - 0{,}2828 \quad \textbf{(Equation 109)}$$

5.1.3. Comparison between Gas and Electrochemical Hydrogen Embrittlement.

According to the previous descriptions, the subsurface hydrogen concentration relates to hydrogen pressure and current density by the following expressions:

- For electrochemical hydrogen: $C_o = K\sqrt{\frac{i}{k_2}}$. **(Equation 96)**

- For gaseous hydrogen (Sievert's law) for P ≤ 50 bar:

$$C_o = S.(1{,}0365P - 0{,}2828)^{1/2} \quad \textbf{(Equations 106 and 109)}$$

Under equal subsurface concentration, the following relationship is thus valid:

$$1{,}0365P - 0{,}2828 = \left(\frac{K^2}{k_2 s^2}\right) I \quad \textbf{(Equation 110)}$$

being: "$K = k_{abs}/k_{des}$" the ratio of the rate constants for the hydrogen absorption and desorption reactions, "k_2" the rate constant of the chemical recombination reaction (Tafel reaction) and "s" the Sievert's parameter.

All these parameters follow an Arrhenius-type relationship with temperature and activation energy. The proposed relationship is valid up to and around the threshold values of hydrogen pressure and cathodic current. Above the critical values, the plateau of severe embrittlement does not allow for valuable analyses.

Equations 82 to **87** indicate the conditions of similar hydrogen damage considering the tested materials and the tensile tests procedures adopted, while **Equation 110** only determines the conditions of equal subsurface hydrogen concentration. These relationships differ considerably.

The value of $\left(\frac{K^2}{k_2 s^2}\right)$ is estimated to be a large number, especially because of the expected very low values of the rate constant of the recombination reaction k_2. Since the density current exponents of the experimentally obtained relationships are lower than the unity, between 0,05 and 0,22, for a given current density, these relationships provide much smaller values of pressure "P" than estimated by **Equation 110**. This means that the hydrogen pressures that generate equal ductility loss for a certain value of current density are a fraction of the value expected to generate the same absorbed hydrogen concentration at the same certain "i" value.

Explanations may be proposed for this disparity. **Equation 122** is theoretically developed considering equilibrium conditions and small hydrogen coverage. The tensile tests in which **Equations 82** to **87** were obtained are not equilibrium processes. The surface conditions of the specimens changed during the experiments as result of straining. As the solution was not replenished during the tests, the environment conditions also varied. More importantly, however, the damage process is not controlled

entirely by the subsurface hydrogen content. It is proposed the hydrogen-assisted fracture phenomenon comprises an interaction between hydrogen and dislocations moving during the fracture process. This interaction is discussed in section **5.3**.

5.2. Hydrogen Diffusion

Different aspects related to hydrogen diffusion in the tested material are analyzed: the diffusivity parameters (pre-exponential factor D_o and activation energy E_L) and hydrogen trapping.

5.2.1. Parameters of the Diffusion Coefficients.

Figures 140 and **141** display the hydrogen apparent diffusion coefficients calculated by the time-lag method as a function of 1000/T (T is the absolute temperature) measured from the permeation tests in the flange neck and body.

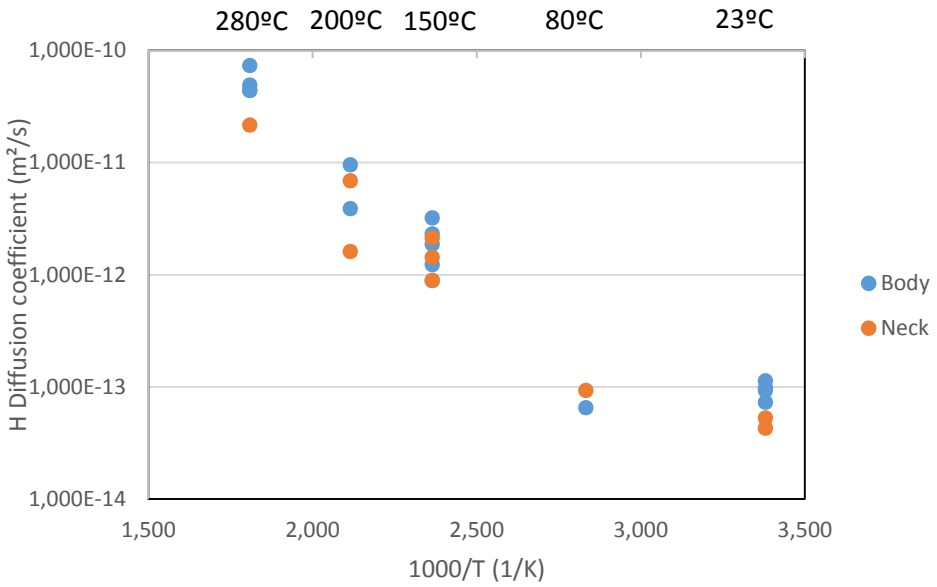

Figure 140. Hydrogen diffusivities as a function of temperature – Absorption step.

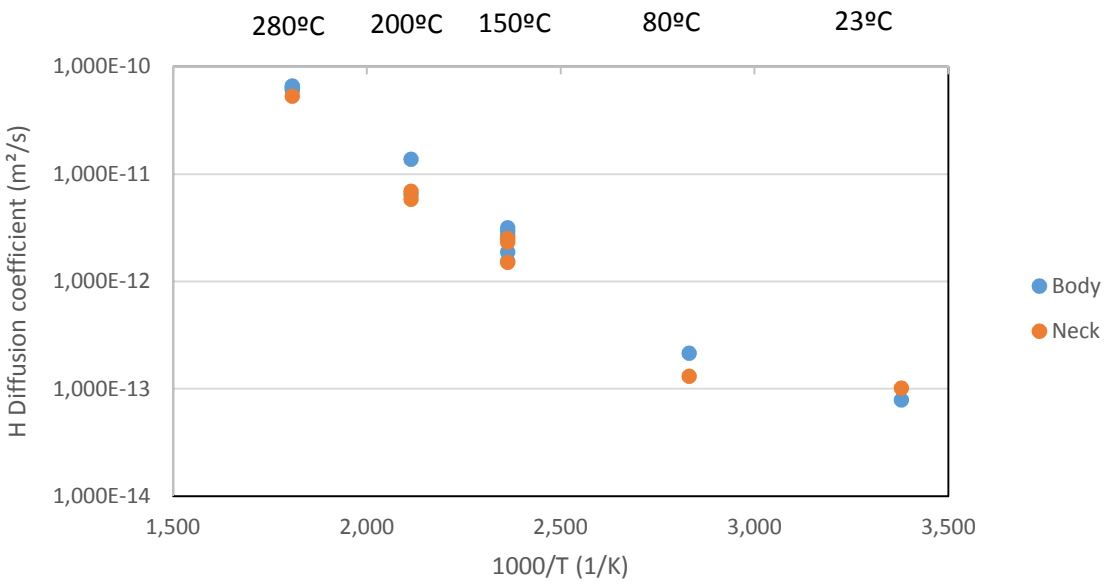

Figure 141. Hydrogen diffusivities as a function of temperature – Desorption step.

The diffusion coefficients measured at lower temperatures are about one order of magnitude higher than predicted by extrapolation of the higher temperature results. This suggests that different hydrogen diffusion paths occur at high and low temperatures.

The equations for hydrogen diffusivities as a function of temperature obtained follow an Arrhenius-type relationship shown in **Equation 23**. The pre-exponential factor D_o and activation energy E_L obtained by regression from the measured values shown in **Figures 140** and **141** are listed in **Table 27**. Two temperature ranges were considered: 80-180 and 23-80ºC. The ranges shown for D_o and E_L refer to the values obtained from the charging and desorption steps of the permeation tests.

Table 27. Diffusivity parameters of the equation $D = D_o.\exp\left(\frac{-E_L}{RT}\right)$.

	D_o (m²/s)	E_L (kJ/mol)
Flange body	80-280ºC: $(1,8\text{-}4,7).10^{-6}$ 23-80ºC: $3,9.10^{-11}$	80-280ºC: 49,9±2,5 23-80ºC: 15,3
Flange neck	80-280ºC: $2,0.10^{-7}$-$1,3.10^{-6}$ 23-80ºC: $4,7.10^{-13}$-$3,0.10^{-12}$	80-280ºC: 44,8±2,4 23-80ºC: 7±3,2

Different values of activation energy and pre-exponential factor for hydrogen diffusion in duplex and super duplex stainless steels are mentioned in the literature.

In the range between 144-600ºC, IACOVIELLO *et al.* [125] obtained for a 2205 duplex stainless steel, with 40% austenite D_o equal to $6,5.10^{-8}$ m²/s and E_L equal to 33,7 kJ/mol.

SEQUEIRA [76] measured an activation energy of 86,4 kJ/mol in 2507 SDSS manufactured by hot isostatic pressing (48% austenite) in the range of 350-500ºC. SALVIO [126] obtained for UNS S33207, a hyper duplex stainless steel with 51% austenite, between 150 and 250ºC activation energy of 44,74 kJ/mol [126].

Between room temperature and 80-84ºC, more data are available. TURNBULL [127] obtained for Uranus 50 duplex stainless steel (22Cr 6Ni 2,5Mo) with 44% austenite D_o equal to $4{,}6.10^{-8}$ m²/s and E_L equal to 36,6 kJ/mol. HSU [129] obtained for a SAF 2205 with 55% austenite activation energy of 40 kJ/mol [128]. For a 2507 super duplex stainless steel with 49% austenite, TURNBULL *et al.* [73] indicated for lattice diffusion, i.e. in which the traps were completely filled, $D_o = 1{,}3.10^{-7}$ m²/s and E_L = 45,6 kJ/mol. For conditions in which hydrogen trapping had an effect on the diffusion (low trap occupancy), they obtained $D_o = 4{,}3.10^{-6}$ m²/s and E_L = 55,8 kJ/mol.

At temperatures between 80 and 280ºC, the estimated activation energies from the body samples (47,4-52,5 kJ/mol) were higher than the neck samples (42,4-47,2 kJ/mol). Literature mentioned for (S)DSS E_L values between 33,7 and 44,7 kJ/mol in this temperature range, so that the obtained values agree approximately with published ones.

At lower temperatures (23 and 80ºC), a greater dispersion was verified. Several causes may explain the higher dispersion obtained from the results closer to room temperature, such as a higher relevance of strong traps and diffusion through oxide layers. The little significant difference between the results at 23 and 80ºC implied low E_L values. For the specimens from the body region, the activation energy measured was 15,3 kJ/mol from the desorption step. The value estimated for the charging step from the body samples was not reliable, since the diffusivities at 23ºC were slightly higher than at 80ºC. For the neck samples, at 80-23ºC, the activation energies were 10,2 kJ/mol for the permeation step and 3,8 kJ/mol for the desorption step.

The activation energy obtained by SEQUEIRA [76] at 350-500ºC, 86 kJ/mol, is explained by the hydrogen diffusion at this range within austenite. This value is higher than the activation energies measured at 80-280ºC (42-52 kJ/mol). At this temperature range, diffusion through ferrite and also in phase boundaries and austenite is believed to occur. On the other hand, E_L values measured at 23-80ºC (4-15 kJ/mol) are close to the activation energy for ferrite, 12,5 kJ/mol [129]. It is thus suggested that at lower temperatures lattice diffusion in ferrite is more relevant than at higher temperatures.
For purely interstitial diffusion of hydrogen in metals, the pre-exponential or frequency factor D_o can be defined by [130]:

$$D_o = n\alpha a^2 \upsilon \qquad \textbf{(Equation 111)}$$

where:

- n: number of adjacent interstitial sites. This is equal to 12 for a fcc metal and 4 for a bcc metal.
- α: coefficient whose value depend upon the location of the interstitial position. It is equal to 1/12 for a fcc metal and to 1/24 for a bcc metal.
- a: lattice parameter (m)
- v: oscillation frequency of the hydrogen atoms (s^{-1}).

The parameter α is obtained by modelling of tridimensional diffusion of hydrogen along interstitial sites. It can be proved that for both fcc and bcc lattices, the diffusivity of a single H atom along octahedral sites can be given by $D = l^2v/6$, being "l" the jump distance. While the jump distance "l" for bcc is equal to "a/2", for fcc structures it is $\sqrt{2}$ times larger [130].

The most reliable D_o values were those measured at 80-280ºC since they were obtained using the same testing procedure, i.e. via gas permeation tests. In this range, the body samples presented much smaller difference on D_o between the charging and desorption steps (1,8-4,7.10^{-6} m^2/s) than the neck specimens. Considering more data are available for the flange body, these results are considered more reliable. According to [129], the D_o values lie in the ranges of 1,1-1,5.10^{-6} m^2/s for austenite and 0,76-2,2.10^{-7} m^2/s for ferrite. The measured values are then relatively similar to the austenite value, indicating hydrogen diffusion in austenite takes place at in the 80-280ºC temperature range. Considering the parameters for austenite, and the D_o values for the flange body at 80-280ºC, oscillation frequency between (1,4-3,6).10^{13} s^{-1} is obtained. The vibration frequency of hydrogen can be estimated by [131]:

$$\upsilon = \frac{1}{2\pi}\left(\frac{aE}{m}\right)^{\frac{1}{2}} \qquad \textbf{(Equation 112)}$$

where:
- a: lattice parameter (3,61 Å for austenite and 2,88 Å for ferrite).
- m: mass of the hydrogen atom (1,66.10^{-24} g).
- E: Young's modulus.

In the range of 80-280ºC, E varies between 176-186 GPa for austenite [132]. For austenite, the estimated frequency using **Equation 111** is around (3,1-3,2).10^{13} s^{-1}, which is close to the experimentally obtained values.

It should be emphasized that the permeation tests have limited resolution for the determination of diffusion parameters as activation or trap binding energies. A considerable number of tests would be necessary for the accurate calculation of these properties.

5.2.2. Effects of Traps.

In almost all permeation tests, the diffusion coefficients measured by the time-lag method in the absorption step were consistently lower than the values on the desorption step at the same temperatures. This can be related to the process of filling and saturation of traps with hydrogen that take place during the charging step. At the desorption step, higher trap occupancy implies on a higher diffusivity, closer to the lattice diffusion coefficient. The effect of surface processes cannot be excluded. Hydrogen ion reduction or atomic hydrogen recombination on the outflow surface is more energetically favorable than the dissociation reactions taking place in charging step, resulting in general on higher apparent diffusion coefficient in the desorption step.

As shown in section **4.4.1** and **Annex D**, a clear anomalous permeation transient was verified only in the permeation of the flange neck membrane at 200ºC (test 14). It was measured an approximate double sigmoidal curve, i.e. two steady state rising plateaus. For permeation time up to ca. 10^5 s, D_{tL} was calculated as $1{,}1.10^{-12}$ m²/s. From this time until the second steady state, the diffusivity was $3{,}3.10^{-12}$ m²/s. This behavior suggests that the trap occupancy enhanced relatively rapidly during this test.

The diffusion coefficients were also determined in the transient regime according to the procedure described in **Annex G**. In some cases, the diffusivities increased during the transient on the charging step (**Figure 142**). In another cases, the diffusivities decreased during the charging transient (**Figure 143**). As mentioned for test 14, increasing of the diffusivities in the charging step transient may be a result of the trap occupancy increment, so that lattice diffusion progressively dominates. Their decrease may indicate that the trap occupancy is still far from approaching a relevant value, so that trapping still dominates. During desorption, in general the transient diffusivities tended to decrease. This indicates that hydrogen trapping was also acting during desorption.

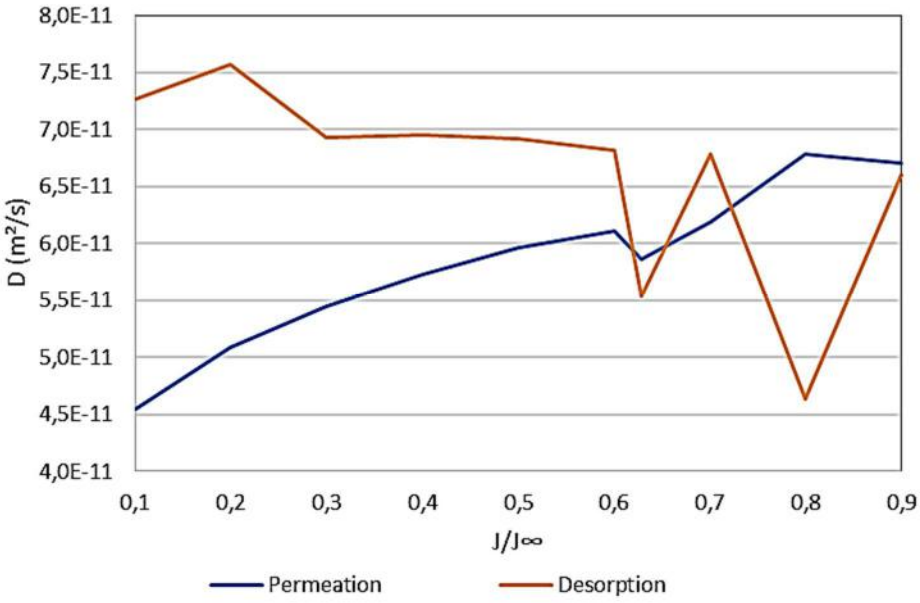

Figure 142. Transient diffusivities at 280ºC (flange body, Pd on entry side).

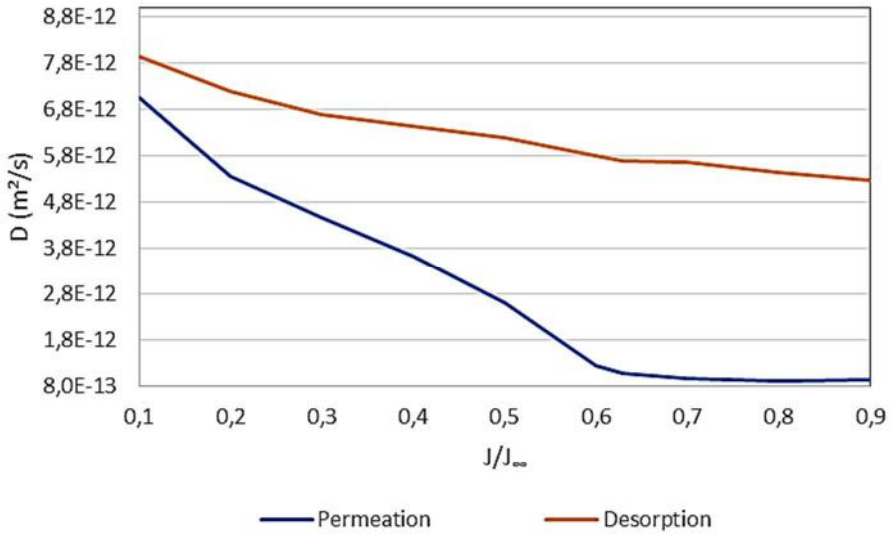

Figure 143. Transient diffusivities at 200ºC (flange body, Pd on exit side).

On sequential permeation runs, it is expected the second and subsequent runs provide higher diffusivity values (in comparison to the first run) due to saturation of trapping sites. Interstitial diffusion would be in these cases relatively dominant. This hypothesis was not verified clearly in any test, suggesting that the main trapping sites were not completely saturated or that the hydrogen atoms were in some grade detrapped during desorption on every run.

5.3. Hydrogen-Microstructure Interactions in the Diffusion Process.

Different results indicate that the major trapping sites in the tested material are α/γ phase boundaries, α/α grain boundaries, dislocations, nitride/α interfaces as well as austenite grains.

From the TDS experiments (section **4.6**), the body samples cathodically pre-charged presented activation energy for desorption equal to 64 kJ/mol, related probably to α/γ interfaces. For neck samples charged in the same conditions, the estimated E_a values were lower, in the range of 7-18 kJ/mol. These values in the neck were related to ferrite/ferrite grain boundaries and/or dislocations.

A great amount of nanometric nitride precipitates was verified by TEM at α/α grain boundaries and inside ferritic grain (section **4.2.2**). These precipitates are usually coherent with the ferrite matrix, as mentioned in section **2.2.4**, so that, although no published data for E_a concerning nitrides in duplex stainless steels is available, a small activation energy is expected. Thus, trapping at nitride/α interfaces is a possibility.

Hydrogen trapping in austenite was not ascertained by TDS, probably because in the tested material it is related to desorption peaks above 600ºC. However, hydrogen segregation to austenite was verified by other techniques. In ToF-SIMS experiments the amount of deuterium in austenite was measured as 25% higher than in ferrite in the tests performed in cryogenic conditions (section **4.7**). Analysis of Rietveld refinement and Fourier maps from neutron diffraction results indicated that the (½ 0 0) octahedral interstitial position in austenite is the preferable site for hydrogen occupation in the tested material (section **4.8**).

Considering the discussion on section **5.2.1**, from the activation energies measured on permeation tests, it was proposed that at higher temperatures hydrogen diffusion through ferrite, phase boundaries and austenite is believed to occur, while closer to room temperature, lattice diffusion in ferrite dominates, i.e. phase boundaries present smaller relevance.

The neck samples presented diffusivities in general lower than the body samples. As shown in section **4.2.1**, the microstructure of the neck membranes was finer and more oriented as a result of the forging process. In the neck, the austenitic islands were elongated perpendicularly to the diffusion trajectory, acting more efficiently to hinder the hydrogen diffusion. In the body, a more isotropic microstructure generated lower tortuosity diffusion paths, related to higher diffusivities.

5.4. Hydrogen-Microstructure Interactions in the Embrittlement Process.

In section **5.1.3**, it is proposed that the damage process is not controlled entirely by the subsurface hydrogen content, since the experimentally obtained relationships between pressure and cathodic current density for equal ductility loss differ greatly from theoretical relationship for equal subsurface concentration. There are other indications that ordinary lattice diffusion does not explain completely the embrittlement process. The fracture surfaces of embrittled specimens presented uniform features throughout the sections, as described in section **4.5.4**. Considering the diffusivities measured at room temperature (4.10^{-14} to 1.10^{-13} m²/s), ordinary hydrogen diffusion throughout the entire section would take many days. As can be seen on **Figures 77** to **82**, in most of the conditions, neck samples presented slightly more severe loss of ductility than the body samples under similar hydrogen activities. As the flange neck presents a finer microstructure and lower hydrogen diffusivities, a better resistance against hydrogen could be expected.

Considering these evidences, it is suggested not only lattice diffusion but also hydrogen transportation assisted by dislocations takes place. Moving dislocations can act as rapid and efficient carriers of hydrogen. This was verified by different authors in nickel and stainless steels using techniques such as autoradiography, tritium release and hydrogen permeation measurements during plastic deformation [133,134]. There is a considerable body of evidence to show that hydrogen accumulates at dislocations, both in the core and in the stress field [71]. Indications of plastic micro-mechanisms in highly hydrogen-embrittled specimens, as shown in section **4.5.4**, suggest dislocations and hydrogen interact during the fracture process.

Dislocation-assisted hydrogen transport can be divided into two cases: when hydrogen is present before the plastic deformation start, and when hydrogen penetrates during the plastic deformation. If hydrogen charging is simultaneous to the plastic deformation, as in most of the tests performed, the dislocations that move from the surface can transport hydrogen to a concentration similar to the surface in contact with the hydrogen-bearing environment. As dislocations move, depending on their speed, they drag the surrounding hydrogen atmosphere, exchanging hydrogen with other trapping sites they encounter on the way. This phenomenon is known as dynamic trapping. In finer microstructures, such as in the flange neck, higher grain boundary density can mean more trapped hydrogen available for this exchange with dislocations, so that this effect on the fracture process tends to be enhanced [135].

A hydrogen atom can follow the motion of a dislocation with a velocity derived through the Einstein-Stokes relationship [3]:

$$V^d = \left(\frac{D}{RT}\right) F \qquad \textbf{(Equation 113)}$$

where:

- D: hydrogen lattice diffusivity.
- R: gas constant (8,314 J/mol.K)
- F: effective driving force per atom of hydrogen on the dislocation.

A critical dislocation velocity V_c^d can be defined for hydrogen to move along with a dislocation, associated to a critical driving force F_c. This driving force corresponds to a gradient of the hydrogen-dislocation binding energy E_B, assumed to be distributed over a distance of 30 Burgers vector modules [3]: $F_c = E_B/30b$. According to other authors, a better value for iron would be $E_B/75b$ [135].

Above V_c^d, or at a strain rate greater than $\dot{\varepsilon} = \rho_m b V_c^d$ (ρ_m is the mobile dislocation density) - Orowan equation, the dislocation line can be expected to break away from its hydrogen cloud, and dislocation sweeping is no longer effective [136].

For austenite and ferrite, estimated values of critical dislocation velocity and maximum strain rate (considering the range of $F_c = E_B/75b$ to $E_B/30b$) are shown in **Table 28**. Hydrogen transportation by dislocations can occur in ferrite at very rapid deformations. In austenite, it is required strain rates below 10^{-4} s^{-1} for transport of hydrogen by dislocations. This is related to the lower hydrogen diffusivity and binding energy between hydrogen and dislocations in austenite.

The tensile test durations for embrittled specimens were between ca. 1 and 10 hours for initial strain rate of 10^{-5} s^{-1}, depending on the hydrogen activity. Considering the calculated dislocation velocities, the penetration distance of hydrogen transported by dislocations is in all cases above 100 µm for austenite. Therefore, the dislocations enabled hydrogen to cross entirely most of the austenite grains, which would not be possible by ordinary diffusion in the test conditions. Ordinary interstitial diffusion in ferrite is faster, so that hydrogen transport by dislocations can be considered to be less critical for the embrittlement phenomenon in ferrite.

Table 28. Estimation of critical dislocation velocity and strain rates at 20ºC.

Parameter	Ferrite	Austenite	Source
Dislocation binding energy E_B (kJ/mol)	26	13,5	[3,70]
Burgers vector module b (lattice parameter - Å)	2,88	3,61	Measured in neutron scattering tests
Hydrogen diffusion coefficient D (m^2/s)	10^{-10}	10^{-16}	[73]
Dislocation density ρ_m (m^{-2})	8.10^{14}	10^{13}	[136]
Critical dislocation velocity V_c^d (m/s)	0,05-0,12	$(2,0\text{-}5,1).10^{-8}$	Calculated
Maximum strain rate $\dot{\varepsilon}_c$ (1/s)	11385-28462	$7,4.10^{-5}$ - $1,8.10^{-4}$	

From observations performed by transmission electron microscopy on as-received material (**Figure 144**), it is qualitatively clear that the initial dislocation density in ferrite is higher than in austenite. A reason of this high dislocation density could be the thermal expansion difference between the ferrite and austenite during thermo-mechanical manufacturing process [137]. While ordinary diffusion in ferrite is faster, so that hydrogen transport by dislocations is usually deemed to be less critical in ferritic steels, considering this higher dislocation density in ferrite than in austenite, it is possible the hydrogen transportation by dislocations acquires a higher relevance.

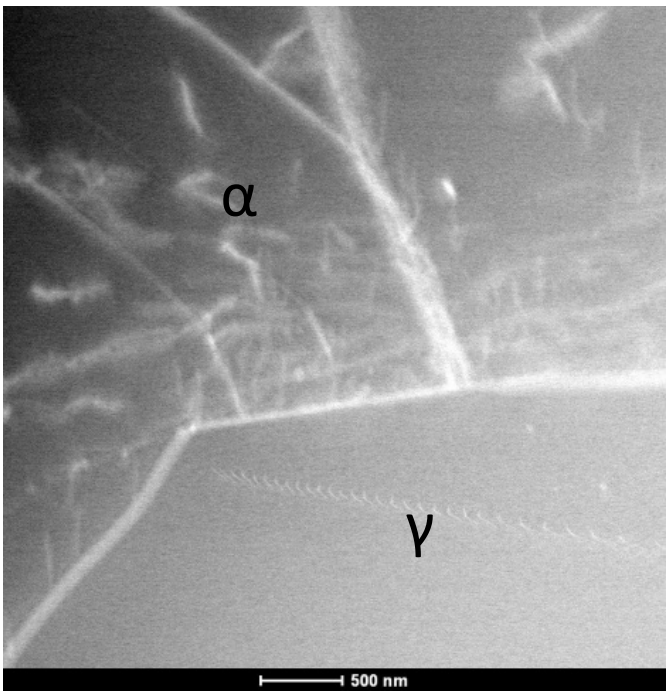

Figure 144. Bright field image obtained by TEM of ferrite/austenite phase boundary in the flange body.

The value of mobile dislocation density can be as low as 1% of the total dislocation density [136]. Therefore, it is estimated that the calculated $\dot{\varepsilon}_c$ can be approximately two to three orders or magnitude lower than the values shown in **Table 28**. Even under this degree of uncertainty, hydrogen transportation by dislocations is still possible in ferrite at conventional tensile tests, while in austenite, low strain rates are required.

Different parameters can influence the value of dislocation density. In pure iron, the dislocation density increases sharply with deformation at low deformation levels and then increases more gradually with further deformation [66]. In tensile tests performed with 2205 DSS specimens, it was verified that the dislocation density in austenite increased from the onset of necking whereas the increase in the dislocation density in ferrite was not significant. This coincides with the lower strain hardening in ferrite and its higher sensitivity to brittle cracking [138]. As described in the models for the HELP and AIDE mechanisms (section **2.5.3**), the presence of hydrogen itself can affect the dislocation density and mobility [16].

At strain rates up to the critical value $\dot{\varepsilon}_c$, higher loading or plastic strain rates are associated with larger fluxes of mobile dislocations and hence larger amounts of hydrogen transported by them. Considering the upper critical value for austenite is estimated around 10^{-4} s^{-1}, it is possible that hydrogen transportation assisted by dislocations occurred in austenite during the tensile tests performed.

The higher dislocation density introduced during the test and the phenomenon of dislocation-assisted hydrogen transportation explains part of the accelerated character of slow-strain rate tensile tests. Plastic deformation is expected usually at stress raisers such as geometry transitions and weld toes. For such regions, evaluation by constant load tests at elastic regime using smooth specimens may be excessively mild. Other testing procedures that generate high density of mobile dislocations may also be developed, such as ripple load tests, in which an alternating load is superimposed to a constant load close to the yield stress.

6. Conclusion

As a result of the manufacturing process of the analyzed flanges made of UNS S32750, specifically the hot forging procedure, their microstructure is coarse, with average inter-austenitic spacing of 55 µm. The flange body presented a more equiaxed microstructure and bigger austenitic grains (average diameter of 55 µm), while the flange neck presented a more oriented microstructure, with austenitic islands smaller (average diameter of 43 µm) and more elongated in the longitudinal direction. While the average phase fractions estimated by metallography are similar to the calculated values by X-ray diffraction (52-58% ferrite, 42-48% austenite), they varied greatly among all specimens as a result of the coarse microstructure.

The average mechanical properties in air of the flanges in general met the minimum requirements of ASTM A182 grade F53. For both the body and the neck, the scatter was quite large, also as a consequence of the coarse microstructure. As expected from the finer microstructure, flange neck presented in average greater tensile properties (YS 620 MPa, UTS 788 MPa) than the body (YS 529 MPa, UTS 758 MPa), as was as higher hardness values.

Gas and electrochemical hydrogen permeation tests were performed with specimens from the flange body and neck in the range from 23 to 280ºC. For the flange neck, the following expressions of hydrogen diffusivity as a function of absolute temperature were obtained (permeation step) in two ranges:

$$80\text{-}280ºC:\ D\ (m^2/s) = 2{,}0.10^{-7}\exp(-42403/RT)$$

$$23\text{-}80ºC:\ D\ (m^2/s) = 3{,}0.10^{-12}\exp(-10226/RT)$$

At temperatures between 80 and 280ºC, the estimated activation energies of the hydrogen diffusivity Arrhenius equation for the body samples were 47,4-52,5 kJ/mol, while for the neck they were 42,4-47,2 kJ/mol. In the range 23-80ºC, for the body region, the measured activation energy was 15,3 kJ/mol, while for the neck samples, it varied between 3,8 to 10,2 kJ/mol. These activation energies suggest that lattice diffusion through ferrite and austenite as well as in phase boundaries occurs at higher temperatures, while closer to room temperature lattice diffusion in ferrite is dominant. The measured values of the pre-exponential factor in the 80-280ºC range (1,8-4,7.10^{-6} m^2/s) are similar to obtained for austenitic steels, indicating hydrogen lattice diffusion in austenite takes place at these temperatures.

The neck samples presented diffusivities in general lower than the body samples. In the neck, the austenitic islands were elongated perpendicularly to the diffusion trajectory,

acting more efficiently to hinder the hydrogen diffusion. In the body, a more isotropic microstructure generated lower tortuosity diffusion paths, related to higher diffusivities.

Different results indicate that the major trapping sites in the tested material are α/γ phase boundaries, α/α grain boundaries, dislocations in ferrite, nitride/α interfaces as well as austenite grains. From the TDS experiments, the body samples cathodically pre-charged presented activation energy for desorption equal to 64 kJ/mol, related to α/γ interfaces. For neck samples charged in the same conditions, the estimated E_a values were lower, in the range of 7-18 kJ/mol. These values in the neck relate to α/α grain boundaries and/or dislocations in ferrite. A great amount of nanometric nitride precipitates was verified by TEM at α/α grain boundaries and inside ferrite grains ferrite. These precipitates are usually coherent with the ferrite matrix, so that a small activation energy is expected. Thus, trapping at nitride/α interfaces is a possibility.

Hydrogen trapping in austenite was not ascertained by TDS, however hydrogen segregation to austenite was verified by other techniques. In ToF-SIMS experiments the amount of deuterium in austenite was measured as 25% higher than in ferrite in the tests performed in cryogenic conditions. Analysis of Rietveld refinement and Fourier maps from neutron diffraction results indicated that the (½ 0 0) octahedral interstitial position in austenite is the preferable site for hydrogen occupation in the tested material.

In tensile tests performed in air at strain rates between 10^{-6} and 10^{-3} s^{-1} with pre-charged specimens, major ductility losses occurred at strain rates equal or lower than 10^{-5} s^{-1}. The level of embrittlement was nearly constant below the strain rate of 10^{-5} s^{-1}. In tensile tests performed at initial strain rates of 10^{-5} s^{-1} under in-situ hydrogen gas at pressures between 1 and 300 bar H_2 without hydrogen pre-charging, a ductility loss above 60% was measured at pressures equal to or above 50 bar for both flange body and neck specimens. The level of embrittlement was nearly constant above the 50 bar pressure threshold. Under in-situ cathodic hydrogen charging at currents between 0,5 and 1100 mA, similar embrittlement degree was observed at currents equal to and more cathodic than ca. 30-60 mA at 10^{-5} s^{-1}. The embrittlement ratios at currents between 30 and 1100 mA fell within a dispersion range of low ductility values, equivalently to the behavior observed in in-situ gaseous tests above 50 bar.

The non pre-charged specimens tested in air presented fractures composed by ductile dimples that propagated indiscriminately through ferrite and austenite. Specimens tested with in-situ hydrogen gas at pressures equal and above the threshold of 50 bar and with in-situ cathodic charging at currents more cathodic than the threshold of 30 mA were highly embrittled. The fracture paths followed predominantly the ferrite phase. Cracking of bigger austenite grains was less common at these conditions of higher hydrogen activity; when reaching bigger austenite grains, the cracks tended

mostly to follow the phase boundaries, and decohesion between austenite and ferrite took place. The fracture surfaces consisted of secondary cracks in the ferritic phase, multi-facets composed by riverlike patterns, separated by steps of different slopes. The facets are associated with cleavage of the ferritic phase, while the steps are related to fracture propagation through austenitic grains. These steps presented a serrated aspect at higher magnification and, in some cases, also small and shallow dimples were verified. These micro-ridges were ill defined, indicating a higher absorption energy during fracture and planar slip through austenite. These characteristics suggest plastic micro-mechanisms are acting. It was verified rather homogeneous characteristics along the entire fracture surfaces, i.e. regions close to the outer surface and at the fracture core presented similar aspects.

Regression equations of the ductility ratios as a function of hydrogen pressure “P” up to the threshold of 50 bar and as a function of current density “i" up to current densities of 60 mA (30 mA/cm²) were obtained. Considering these expressions, the relationships experimentally obtained between hydrogen pressure “P” and the absolute cathodic density current “i” that correspond to equal ductility indices were derived. For instance, the expression that determines the hydrogen pressure and cathodic current density that should generate equal values of relative ROA for the flange body is:

$$P = \exp(3{,}71).(i-0{,}22)^{0{,}22} - 24{,}88$$

A theoretical description assuming that gaseous and cathodic hydrogen-rich environments generate equal absorbed hydrogen concentrations in the material establishes a linear relationship between “i” and “P” (up to threshold of 50 bar). However, the relationships obtained from SSRT tests for equal embrittlement differ considerably from the theoretical expression, which suggests that the damage process is not controlled entirely by the subsurface hydrogen content.

Considering other evidences, such as from fractographic analysis, the hydrogen-assisted fracture phenomenon is suggested to comprise not only lattice diffusion but also an interaction between hydrogen and moving dislocations. The upper critical strain rate for hydrogen to move along with a dislocation in austenite is estimated around 10^{-4} s^{-1}. Thus, it is possible that hydrogen transportation assisted by dislocations occurred in austenite during the tensile tests performed.

7. Suggested Future Works

Several issues arose from the developed research, which should be analyzed in future works. Among them, one can mention the following:

- Improved direct observation of hydrogen positions in the microstructure by the enhancement of the spatial resolution of ToF-SIMS measurements (e.g. through decreasing of the primary ion impact speed and using of nano SIMS), the use of APT and calibration in order to obtain quantitative measurements.
- Experimental studies for direct evaluation of dislocation-assisted H transportation: measurement of H profiles of strained specimens (e.g. SIMS), permeation tests under mechanical stress, nanoidentation etc.
- Development of reliable procedures for hydrogen content measurement using neutron scattering.
- Use of numerical modelling procedures for analysis of TDS and permeation data, in order to better describe hydrogen diffusion and trapping.
- Development/improvement of numerical models integrating hydrogen transportation, stresses/strains and crack growth.
- Experimental and theoretical studies on hydrogen phase/grain boundary diffusion in duplex stainless steels.

8. References

1. BESENBACHER, F. . M. S. . N. J. Interaction of Hydrogen with Defects in Metals. **Nuclear Instruments and Methods in Physics Research**, B7/8, 1985.

2. JOHNSON, W. On some remarkable Changes produced in Iron and Steel by the Action of Hydrogen and Acids. **Proceedings of the Royal Society of London**, 1875.

3. MAROEF, I. . O. D. . E. M. . E. G. Hydrogen trapping in ferritic steel weld metal. **International Materials Reviews**, 47, 2002.

4. GUNN, R. **Duplex stainless steels – Microstructure, properties and applications**. [S.l.]: Abington Publishing, 1997.

5. KNYAZEVA, M. . P. M. Duplex Steels: Part I: Genesis, Formatiom Structure. **Metallography, Microstruture, and Analysis**, 2, n. PP. 112-121, 2013.

6. ISO. ISO 17781 - Petroleum, petrochemical and natural gas industries – Test methods for quality control of microstructure of ferritic/austenitic (duplex) stainless steels, 2017.

7. LO, K. . S. C. . L. J. Recent developments in stainless steels. **Materials Science and Engineering R**, 65, n. PP. 39-104, 2009.

8. PADILHA, A. . P. R. Phase Transformation and Microstructure. In: ALVAREZ-ARMAS, I. . D.-M. S. **Duplex Stainless Steels**. [S.l.]: Wiley, 2009.

9. NILSSON, J. Super duplex stainless steels - Overview. **Materials Science and Technology**, 8, n. PP. 685-700, 1992.

10. REDJAÏMIA, A. . M. G. Diffusion controlled precipitation of austenitic bi-crystals possessing twin related orientation in the ferrite of a duplex stainless steel. **Journal of Materials Science**, 36, n. PP. 1717-1725, 2001.

11. SHEK, C. . D. C. . L. J. . W. K. Early-Stage Widmanstätten Growth of the γ Phase in a Duplex Steel. **Metallurgical and Materials Transactions A**, 31A, n. PP. 15-19, 2000.

12. CHEN, C. . Y. H. . Y. J. Sympathetic nucleation of austenite in a Fe-22Cr-5Ni duplex stainless steel. **Scripta Materialia**, 56, n. PP. 673-676, 2007.

13. POHL, M. . S. O. . G. T. Effect of intermetallic precipitation on the properties of duplex stainless steel. **Materials Characterization**, 58, n. PP. 65-71, 2007.

14. DAS, A. Revisiting Stacking Fault Energy of Steels. **Metallurgical and Materials Transactions A**, 47, n. P. 748-768, 2015.

15. HERMIDA, J. . R. A. Stacking Fault Energy Decrease in Austenitic Stainless Steels Induced by Hydrogen Pairs Formation. **Scripta Materialia**, 39, n. PP. 1145-1149, 1998.

16. GLOWACKA, A. . S. W. Effect of hydrogen charging on the microstructure of duplex stainless steel. **Journal of Alloys and Compounds**, 356-7, n. PP. 701-704, 2003.

17. EEMUA. **EEMUA 194 - Guidelines for materiais selection and corrosion control for subsea oil and gas production equipment**. [S.l.]: EEMUA. 2012.

18. CHAI, G. . R. S. . K. P. R. . J. S. Mechanisms of Hydrogen Induced Stress Crack Initiation and Propagation in Super Duplex Stainless Steels. **Materials Technology**, 80, n. PP. 482–487, 2009.

19. PARDAL, J. **Efeitos dos Tratamentos Térmicos nas Propriedades Mecânicas, Magnéticas e na Resistência à Corrosão de Aços Inoxidáveis Superduplex.** [S.l.]: Universidade Federal Fluminense, 2009.

20. GUTIERREZ, I. . I.-M. A. Process: Hot Workability. In: ALVAREZ-ARMAS, I. . D.-M. S. **Duplex Stainless Steels**. [S.l.]: Wiley, 2009.

21. FACCOLI, M. . R. R. Study of hot deformation behaviour of 2205 duplex stainless steel through hot tension tests. **Journal of Materials Science**, 48, n. P. 5196-5203, 2013.

22. TORRES, L. **Influência da Microestrutura na Interação do Hidrogênio com o Aço 2,25Cr-1Mo Envelhecido**. [S.l.]: Universidade Federal do Rio de Janeiro, 2011.

23. FUKAI, Y. . M. K. . S. H. The phase diagram and superabundant vacancy formation in Fe–H alloys. **Journal of Alloys and Compounds**, 348, n. PP. 105-109, 2003.

24. ASSIS, K. **Aspectos Metalúrgicos e Susceptibilidade à Corrosão Localizada do Aço Inoxidável Superduplex UNS S32760**. [S.l.]: Universidade Federal do Rio de Janeiro, 2011.

25. SAN MARCHI, C. . S. B. **Technical Reference for Hydrogen Compatibility of Materials - Report SAN2012-7321**. [S.l.]. 2012.

26. MARTIN, M. . F. J. . L. G. . S. P. . R. I. On the formation and nature of quasi-cleavage fracture surfaces in hydrogen embrittled steels. **Acta Materialia**, 59, n. PP. 1601–1606, 2011.

27. ASBJøRNSEN, I. **The effect of microstructure on hydrogen induced stress cracking (HISC) of stainless steels**. [S.l.]: NTNU, 2006.

28. POURBAIX, M. **Atlas of Electrochemical Equilibria in Aqueous Solutions**. Houston: NACE International Cebelcor, 1974.

29. FRANCIS, R. . B. G. . W. G. Effects of Cathodic Protection on Duplex Stainless Steels in Seawater. **Corrosion**, 53, n. PP. 234-240, 1997.

30. ZAKROCZYMSKI, T. . G. A. . S. W. Effect of hydrogen concentration on the embrittlement of a duplex stainless steel. **Corrosion Science**, 47, n. PP. 1403-1414., 2005.

31. VITIELLO, R. **Trincamento sob Tensão Induzido pelo Hidrogênio em Aços Superduplex Submetidos à Proteção Catódica**. [S.l.]: Universidade Federal do Rio Grande do Sul, 2009.

32. ALSARRAF, J. **Hydrogen Embrittlement Susceptibility of Super Duplex Stainless Steels**. [S.l.]: Cranfield University, 2010.

33. AURSAND, M. . R. G. . M. L. . K. I. Experiences with Hydrogen Induced Stress Cracking of Duplex Stainless Steel Components in Subsea Service with Cathodic Protection. **NACE Conference & Expo**, Paper nº 2490, 2013.

34. COTTIS, R. Hydrogen Embrittlement. In: _____ **Shreir's Corrosion**. [S.l.]: Elsevier, 2010.

35. KOBRIN, G. Materials Selection. In: _____ **ASM Handbook, V. 13 - Corrosion**. [S.l.]: ASM International, 1983.

36. ZHENG, W. . H. D. The effect of hydrogen on the fracture of a commercial duplex stainless steel. **Corrosion Science**, 32, n. PP. 23-36, 1991.

37. BEACHEM, C. A New Model for Hydrogen-Assisted Cracking (Hydrogen "Embrittlement"). **Metallurgical Transactions**, 3, n. PP. 437-451, 1972.

38. CASSAGNE, T. . B. F. A Review on Hydrogen Embrittlement of Duplex Stainless Steels. **Corrosion Conference & Expo**, n. Paper 05098, 2005.

39. OLSEN, S. . H. S. Hydrogen Embrittlement form CP on Supermartensitic Stainless Steels – Recommendation for New Qualification Methods. **Corrosion Conference & Expo**, n. Paper nº 04546, 2004.

40. FESTY, D. Cathodic protection of steel in deep sea: hydrogen embrittlement risk and cathodic protection criteria. **NACE Conference & Expo**, n. Paper nº 01011, 2001.

41. MIKKELSEN, A. . W. S. . J. R. . N. B. . R. R. Influence of ambient pressure on Hydrogen Induced Stresss Cracking (HISC) of Duplex Stainless Steels under Cathodic Protection. **Corrosion - NACExpo**, Paper 0699, 2006.

42. PEREIRA, Y. Avaliação da Criticidade de Trincas Superficiais em Aços Inoxidáveis Superduplex Fragilizados pelo Hidrogênio devido ao Efeito Colateral da Proteção Catódica. **Master Dissertation**, 2009.

43. LYNCH, S. Hydrogen embrittlement phenomena and mechanisms. In: RAJA, V. . S. T. (.). **Stress corrosion cracking:** theory and practice. [S.l.]: Woodhead Publishing, 2012.

44. BARNOUSH, A. **Hydrogen embrittlement, revisited by in situ electrochemical nanoindentation.** [S.l.]: Universität des Saarlandes, 2007.

45. NAGUMO, M. **Fundamentals of Hydrogen Embrittlement**. [S.l.]: Springer, 2016.

46. DICK, L. Estudos eletroquímicos de permeação de hidrogênio e determinação de concentrações críticas de hidrogênio em um aço de alta dureza. **Thesis (in portuguese)**, 1986.

47. GAVRILJUK, V. . S. V. . F. J. Diagnostic experimental results on the hydrogen embrittlement of austenitic steels. **Acta Materialia**, 51, n. PP. 1293-1305, 2003.

48. STRAUB, F. . B. T. . U. W. . M. T. **In-situ Detection of Deuterium in Duplex Stainless Steels by Time-of-Flight Secondary Ion Mass Spectrometry**. [S.l.]: [s.n.], 2012.

49. KIRCHHEIM, R. Revisiting hydrogen embrittlement models and hydrogen-induced homogeneous nucleation of dislocations. **Scripta Materialia**, 62, n. PP. 67-70, 2010.

50. TAKAI, K. . S. H. . S. H. . N. M. Lattice defects dominating hydrogen-related failure of metals. **Acta Materialia**, 56, n. PP. 5158-5167, 2008.

51. PETCH, N. Lowering of the fracture stress due to surface adsorption. **Philosophical Magazine**, 1, n. PP. 331-337, 1956.

52. OLDEN, V. . T. C. . B. T. . Ø. E. . N. B. Influence of hydrogen from CP on the fracture susceptibility of 25%Cr duplex stainless steel – FE modelling of constant load testing using hydrogen influenced cohesive zone elements. **International Offshore and Polar Engineering Conference**, 2008.

53. SAN MARCHI, C. . S. B. . Z. J. . T. X. . S. G. Mechanical Properties of Super Duplex Stainless Steel 2507 after Gas Phase Thermal Precharging with Hydrogen. **Metallurgical and Materials Transactions A**, 38A, n. PP. 2763-2775, 2007.

54. CASKEY, G. Hydrogen Effects in Stainless Steel. In: ORIANI, R. . H. J. . S. M. **Hydrogen Degradation of Ferrous Alloys**. [S.l.]: Noyes Publications, 1985.

55. OLTRA, R. . B. C. . M. T. Localized hydrogen cracking in the austenitic phase of a duplex stainless steel. **Scripta Materialia**, 35, n. PP. 1101-1105, 1996.

56. BARNOUSH, A. **Hydrogen embrittlement**. [S.l.]. 2011.

57. GUEDES, D. . O. A. . F. S. . C. G. . C. S. . G. P. . C. J. . B. J. . M. A. . T. F. . D. L. K. D. . F. X. The influence of hydrostatic stress states on the hydrogen solubility in martensitic steels. **Scripta Materialia**, 84-85, n. P. 23-26, 2014.

58. BOURGEON, A. Effect of the hydrogen content and the test environment on the formation of HISC on smooth surface superduplex stainless specimens. **Stainless Steel World Conference**, 2011.

59. MORO, I. **Fragilisation par l'hydrogène gazeau d'un acier ferrito-perlitique de grade API X80**. [S.l.]: Université de Toulouse, 2009.

60. MORO, I. **Etude de la perméation de l'hydrogène dans les aciers martensitiques inoxydables**. [S.l.]. 2010.

61. MOLI-SANCHEZ, L. Role of tempering temperature on the hydrogen diffusion in a 34CrMo4 martensitic steel and the related embrittlement, 2012.

62. LEGRAND, E. . B. J. . F. X. . G. H. Computational analysis of geometrical factors affecting experimental data extracted from hydrogen permeation tests: II – Consequences of trapping and an oxide layer. **International Journal of Hydrogen Energy**, 37, n. PP. 13574-13582, 2012.

63. BRUZZONI, P. . R. E. On the mechanism of hydrogen transport through the passive oxide film on iron. **Corrosion Science**, 36, n. PP. 1597-1614, 1994.

64. HIRTH, J. Effects of Hydrogen on the Properties of Iron and Steel. **Metallurgical Transactions A**, 11A, n. PP. 861-890, 1980.

65. SIQUARA, P. **Influência da Microestrutura nas Propriedades Físicas e Mecânicas de Aços 2,25Cr-1Mi usados em Ambientes Ricos em Hidrogênio**. [S.l.]: Universidade Federal do Rio de Janeiro, 2006.

66. JOHNSON, H. Hydrogen in Iron. **Metallurgical Transactions B**, 19B, n. PP. 691-707, 1988.

67. ROSADO, D. **Comparação do Efeito da Fragilização por Hidrogênio em Aços com Resistência à Tração acima de 1000 MPa.** [S.l.]: Universidade Federal do Rio Grande do Sul, 2011.

68. IINO, M. A more generalized analysis of hydrogen trapping. **Acta Metallurgica**, 30, n. PP. 367-375, 1982.

69. GANGLOFF, R. Hydrogen Assisted Cracking of High Strength Alloys. In: MILNE, I. . R. R. . K. B. (.). **Comprehensive Structural Integrity**. [S.l.]: Elsevier Science, 2003.

70. ENOMOTO, M. . C. L. . M. H. . W. Y. . O. T. . S. J. . Y. K. . S. H. . O. R. Hydrogen Absorption into Austenitic Stainless Steels under High-Pressure Gaseous Hydrogen and Cathodic Charge in Aqueous Solution. **Metallurgical and Materials Transactions**, 1E, n. PP. 331-340, 2014.

71. ROBERTSON, I. . M. M. . F. J. Influence of hydrogen on the behavior of dislocations. In: GANGLOFF, R. . S. B. (.). **Gaseous hydrogen embrittlement of materials in energy technologies V. 2**. [S.l.]: Woodhead Publishing, 2012.

72. SONG, E. . B. H. S. D. E□ect of hydrogen on the surface energy of ferrite and austenite. **Corrosion Science**, n. P. 379-384, 2013.

73. TURNBULL, A. . H. R. Analysis of hydrogen atom transport in a two-phase alloy. **Materials Science and Engineering A**, 177, n. PP. 161-171, 1994.

74. BEYLEGAARD, E. **Hydrogen transport in duplex stainless steels**. [S.l.]: NTNU, 1996.

75. SILVA, B. . S. F. . S. D. Hydrogen Embrittlement in Super Duplex Stainless Steel Tubes UNS S32750 under Mechanical Stress. **International Hydrogen-Materials Interactions Conference**, n. PP. 245-253, 2012.

76. SEQUEIRA, T. **Estudo da Fragilização pelo Hidrogênio em Aço Inoxidável Super Duplex SAF 2507 Processado por Pressão Isostática a Quente**. [S.l.]: Universidade Federal do Rio de Janeiro, 2016.

77. LEBLOND, J. . D. D. A General Mathematical Description of Hydrogen Diffusion in Steels - I. Derivation of Diffusion Equations from Boltzmann-type Transport Equations. **Acta metallurgica**, 31, n. PP. 1459-1469, 1983.

78. DEVAUX, J. . D. D. . L. J. Computer Simulation of Hydrogen Diffusion in Stainless Clad Low-Alloy Steels. **Proceedings of the First International Conference on "Current Solution to Hydrogen Problems in Steels"**, n. PP. 45-52, 1982.

79. MCNABB, A. . F. P. A New Analysis of the Diffusion of Hydrogen in Iron and Ferritic Steels. **Transactions of the Metallurgical Society of AIME**, 227, n. PP. 618-627, 1963.

80. KHARIN, V. . T. J. A generalized model of hydrogen diffusion in metals with multiple trap types. **Philosophical Magazine**, 95, n. PP. 3429-3451, 2015.

81. PRESSOUYRE, G. A Classification of Hydrogen Traps in Steels. **Metallurgical Transactions A**, 10A, 1979. 1571-1573.

82. LUKAS, H. . F. S. . S. B. **Computational Thermodynamics - The Calphad Method**. [S.l.]: Cambridge University Press, 2007.

83. CULLITY, B. . S. S. **Elements of X-ray diffraction**. [S.l.]: Prentice Hall, 2001. ISBN 3rd ed.

84. DEVANATHAN, M. . S. Z. The Adsorption and Diffusion of Electrolytic Hydrogen in Palladium. **Proceedings of the Royal Society**, 270, n. PP. 90-102, 1962.

85. BOES, N. . Z. H. Electrochemical Methods for Studying Diffusion Permeation and Solubility of Hydrogen in Metals. **Journal of the Less-Common Metals**, 49, n. PP. 223-240, 1976.

86. SANTOS, D. Novos Desenvolvimentos para Avaliação das Propriedades Mecânicas e Evolução Microestrutural de Aços Sujeitos a Contaminação com Hidrogênio na Indústria do Petróleo. **Conferência sobre Tecnologia de Equipamentos**, 2011.

87. FRAPPART, S. . F. X. C. J. . T. F. . D. L. . M. H. Study of the hydrogen diffusion and segregation into Fe-C-Mo martensitic HSLA steel using electrochemical permeation test. **Journal of Physics and Chemistry of Solids**, 71, n. PP. 1467-1479, 2010.

88. VIYANIT, E. **Numerical Simulation of Hydrogen Assisted Cracking in Supermartensitic Stainless Steel Welds**. [S.l.]: Helmut-Schmidt-Universität, 2005.

89. EVERS, S. . S. C. . R. M. Hydrogen detection in metals a review and introduction of a Kelvin probe approach. **Science and Technology of Advanced Materials**, 14, n. PP. 1-12, 2013.

90. PARKINS, R. Slow Strain Rate Testing – 25 Years Experience. In: _____ **STP 1210 – Slow Strain Rate Testing for the Evaluation of Environmentally Induced Cracking. Research and Engineering Applications**. [S.l.]: ASTM, 1993.

91. VERBEKEN, K. Analysing hydrogen in metals: Bulk thermal desorption spectroscopy (TDS) methods. In: GANGLOFF, R. . S. B. (.). **Gaseous Hydrogen Embrittlement of Materials in Energy Technologies:** Mechanisms, Modelling and Future Developments. [S.l.]: Woodhead Publishing, 2012.

92. KISSINGER, H. Reaction Kinetics in Differential Thermal Analysis. **Analytical Chemistry**, 29, n. PP. 1702–1706, 1957.

93. HURLEY, C. . M. F. . M. L. . C. J. . B. C. . A. E. Numerical modeling of thermal desorption mass spectroscopy (TDS) for the study of hydrogen diffusion and trapping interactions in metals. **International Journal of Hydrogen Energy**, 40, n. PP. 3402-3414, 2015.

94. SZOST, B. . V. R. . R.-D.-D.-C. B. Hydrogen-Trapping Mechanisms in Nanostructured Steels. **Metallurgical and Materials Transactions A**, 44, n. PP. 4542-4550, 2013.

95. VENEZUELA, J. . G. E. . L. Q. . Z. Q. . T.-B. C. . Z. M. . A. A. Equivalent hydrogen fugacity during electrochemical charging of some martensitic advanced high-strength steels. **Corrosion Science**, 127, n. PP. 45-58, 2017.

96. HASSEL, A. . M. S. . M. A. . G. C. . F. J. . B. K. . T. A. . M. A. . Z. F. **Methodology of hydrogen measurements**. [S.l.]. 2010.

97. SOBOL, O. . H. G. . N. G. . W. T. . E. D. . B. T. . U. W. Time-of-flight Secondary Ion Mass Spectrometry (ToF-SIMS) imaging of deuterium assisted cracking in a 2205 duplex stainless steel microstructure. **Materials Science & Engineering A**, 676, n. PP. 271-277, 2016.

98. SMITH, G. **Quantitative Surface Analysis for Material Science**. [S.l.]: The Institute of Metals, 1991.

99. BACON, G. . L. K. Neutron Diffraction. **Reports on Progress in Physics**, 16, n. PP. 1-61, 1953.

100. TROCELLIER, P. Analyzing hydrogen in metals: surface techniques. In: GANGLOFF, R. . S. B. **Gaseous hydrogen embrittlement of materials in energy technologies – Volume 2**. [S.l.]: Woodhead Publishing, 2012.

101. PYNN, R. Neutron Scattering - A Non-destructive Microscope for Seeing Inside Matter. In: _____ **Neutron Application in Earth, Energy and Environmental Sciences**. [S.l.]: Springer Science + Business Media, 2009.

102. PONTHIEU, M. **Novel Mg-rich materials for hydrogen storage:** bulk and nanoconfined Mg6Pd1-xTMx (TM = Ni, Ag, Cu) compounds and MgH2-TiH2 nanocomposites. [S.l.]: Université Paris Est, 2013.

103. ASTM. ASTM E975 - Standard Practice for X-Ray Determination of Retained Austenite in Steel with Near Random Crystallographic Orientation, 2013.

104. KHOKHAR, F. **Quantitative analysis of multi-phase systems - steels with mixture of ferrite and austenite**. [S.l.]: Linköping University, 2005.

105. SAN MARCHI, C. . S. B. . R. S. Permeability, solubility and diffusivity of hydrogen isotopes in stainless steels at high gas pressures. **International Journal of Hydrogen Energy**, 32, n. P. 100-116, 2007.

106. HERTZBERG, R. **Deformation and Fracture Mechanics of Engineering Materials**. [S.l.]: John Wiley & Sons, 1996. ISBN 4th ed.

107. MICHALSKA, J. . S. M. . H. M. Application of quantitative fractography in the assessment of hydrogen damage of duplex stainless steel. **Materials Characterization**, 60, n. PP. 1100-1106, 2009.

108. ULMER, D. . A. C. Hydrogen-induced strain localization and failure of austenitic stainless steels at high hydrogen concentrations. **Acta Metallurgica et Materialia**, 39, n. PP. 1237-1248, 1991.

109. SILVA, B. . S. F. . S. D. Hydrogen induced stress cracking in UNS S32750 super duplex stainless steel tube weld joint. **International Journal of Hydrogen Energy**, 40, n. PP. 17091-17101, 2015.

110. LEGRAND, E. . O. A. . S. C. . B. J. . F. X. Towards a better understanding of hydrogen measurement obtained by thermal desorption spectroscopy using FEM modellling. **International Journal of Hydrogen Energy**, 40, n. PP. 2871-2881, 2015.

111. DABAH, E. . L. V. . E. D. Performance of hydrogen trapping and phase transformation in hydrogenated duplex stainless steel. **Materials Science and Engineering A**, 527, n. PP. 4851-4857, 2010.

112. SILVERSTEIN, R. . E. D. . G. B. . E. S. . M. D. Evaluation of hydrogen trapping mechanisms during performance of different hydrogen fugacity in a lean duplex stainless steel. **Journal of Alloys and Compounds**, 648, n. PP. 601-608, 2015.

113. SILVERSTEIN, R. . E. D. Hydrogen trapping mechanism of different duplex stainless steel alloys. **Journal of Alloys and Compounds**, 644, n. PP. 280-286, 2015.

114. CHOO, W. . L. J. Thermal Analysis of Trapped Hydrogen in Pure Iron. **Metallurgical Transactions A**, 13A, n. PP. 135-140, 1982.

115. READHEAD, P. Thermal Desorption of Gases. **Vacuum**, 12, n. PP. 203-211, 1962.

116. TANAKA, T. . K. K. . H. S. Visualization of deuterium flux and grain boundary diffusion in duplex stainless steel and Fe-30%Ni alloy, using secondary ion mass spectrometry equipped with Ga focused ion beam. **Journal of Materials Science**, 49, n. PP. 3928-3935, 2014.

117. CARSTANJEN, H. Interstitial positions and vibrational amplitudes of hydrogen in metals investigated by fast ion channeling. **Physica Status Solidi**, 59, n. PP. 11-26, 1980.

118. FUKAI, Y. **The Metal-Hydrogen System**. [S.l.]: Springer, 2005.

119. STROE, M. **Hydrogen Embrittlement of Ferrous Materials**. [S.l.]: Université Libre de Bruxelles, 2006.

120. RAMASUBRAMANIAN, M. . P. B. . W. R. Characterization of Hydrogen Permeation through Zinc-Nickel Alloys under Corroding Conditions. **Journal of the Electrochemical Society**, v. 145, p. P. 1907-1913, 1998.

121. JAMBO, H. . F. S. **Corrosão – Fundamentos, Monitoração e Controle**. [S.l.]: Ciência Moderna, 2008.

122. ANDREW, P. . H. A. Models for hydrogen permeation in metals. **Journal of Applied Physics**, 72, n. PP. 2749-2757, 2000.

123. KIRCHHEIM, R. . S. B. . S. P. Chemomechanical effects on the separation of interfaces occurring during fracture with emphasis on the hydrogen-iron and hydrogen-nickel system. **Acta Materialia**, 99, n. PP. 87-98, 2015.

124. SOAVE, G. Equilibrium constants from a modified Redlich-Kwong equation of state. **Chemical Engineering Science**, 27, n. PP. 1197-1203, 1972.

125. IACOVIELLO, F. . M. . C. M. Hydrogen embrittlement in the duplex stainless steel Z2CND2205 hydrogen-charged at 200°C. **Materials Science and Engineering A**, V. 224, n. PP. 116-124, 1997.

126. SALVIO, F. **Efeitos do Hidrogênio sobre as Propriedades Mecânicas e Microestrutura do Aço Inoxidável Hiper Duplex 3207**. [S.l.]: Universidade Federal do Rio de Janeiro, 2015.

127. TURNBULL, A. . H. G. Hydrogen Diffusion in Corrosion Resistant Alloys., PP. 1-12, 2004.

128. HSU, J. . T. S. . S. H. Hydrogen Embrittlement of SAF 2205 Duplex Stainless Steel. **Corrosion**, 58, n. PP. 858-862, 2002.

129. PEDERSEN, A. **Hydrogen Exchange and Diffusion on Stainless Steels under Cathodic Protection**. [S.l.]: NTNU, 2006.

130. FAST, J. **Gases in Metals**. [S.l.]: MacMillan Press, 1976.

131. OLANDER, R. Description of the Metal-Hydrogen Interaction by a Morse Potential Function. **Journal of Physics and Chemistry of Solids**, 32, n. PP. 2499-2516, 1971.

132. GAROFALO, F. . M. P. . S. G. The Influence of Temperature on the Elastic Constants of Some Commercial Steels. In: _____ **STP129 - Symposium on Elastic Constants**. [S.l.]: ASTM, 1952.

133. LOUTHAN, M. . C. G. . D. J. . R. D. Hydrogen Embrittlement of Metals. **Materials Science and Engineering**, 10, n. PP. 357-368, 1972.

134. KURKELA, M. . L. R. The Effect of Plastic Deformation on the Transport of Hydrogen in Nickel. **Scripta Metallurgica**, 13, n. PP. 927-932, 1979.

135. HIRTH, J. . J. H. On the Transport of Hydrogen by Dislocations. In: LATANISION, R. (.). **Atomistics of Fracture**. [S.l.]: Plenum Press, 1983.

136. DADFARNIA, M. . M. M. . N. A. . P. Modelling hydrogren transport by dislocations. **Journal of Mechanics and Physics of Solids**, 78, n. PP. 511-525, 2015.

137. ARSENAULT, R. S. N. Dislocation Generation Due to Differences between the Coefficients of Thermal. **Materials Science and Engineering**, 81, n. PP. 175-187, 1986.

138. QUINTERO, J. . T. E. . F. J. . C. P. . P. M. . R. A. T. A. In Situ Synchrotron Radiation Measurements During Axial Strain In Hydrogen Cathodically Charged Duplex Stainless Steel SAF 2205, v. DOI: 10.1590/1980-5373-MR-2017-0686, 2017.

139. VAN HOVE, L. Correlations in Space and Time and Born Approximation Scattering in Systems of Interacting Particles. **Physical Review**, 95, n. PP. 249-262, 1954.

140. ROSS, D. Neutron scattering studies of metal hydrogen systems. In: WIPF, H. (.). **Hydrogen in Metals III. Topics in Applied Physics**. [S.l.]: Springer, 1997.

141. RODRIGUEZ-CARVAJAL, J. **Introduction to the Program FULLPROF: Refinement of Crystal and Magnetic Structures from Powder and Single Crystal Data**. [S.l.]. 2018.

142. RODRÍGUEZ-CARVAJAL, J. **An Introduction to the Program FullProf 2000**. [S.l.]: Laboratoire Léon Brillouin (CEA-CNRS), 2001. ISBN https://www.psi.ch/lns-diffraction/LinuxEN/fullprof-manual.pdf.

ANNEX A – Neutron Scattering Fundamentals

The scattering of neutrons by nuclei is a quantum mechanics process. Formally, the process is described in terms of the wavefunctions of the neutron and the nucleus. The neutron wavevector $\vec{k}$ is a vector of magnitude 2π/λ that points along the neutron's trajectory. The magnitude of the wavevector is related to the neutron velocity v by the expression:

$$\left|\vec{k}\right| = \frac{2\pi m v}{h} \qquad \textbf{(Equation A1)}$$

where

- h: Planck's constant.
- m: mass of the neutron.

When neutrons are scattered by matter, the process can alter both the momentum and energy of the neutrons and the matter. The scattering is not necessarily elastic; the atoms can therefore recoil for example because of interaction with phonons (collective atomic displacement) or atoms diffusing in an incoherent way. The total energy and momentum are in general conserved: the energy E lost by the neutron in a collision is gained by the scattering sample. From **Equation A1**, the amount of momentum given up by the neutron during the interaction, the momentum transfer, is $(h\vec{Q})/2\pi = h(\vec{k} - \vec{k'})/2\pi$, where $\vec{k}$ is the wavevector of the incident neutrons and $\vec{k'}$ is that of the scattered neutrons. The quantity $\vec{Q} = \vec{k} - \vec{k'}$ is known as the scattering vector.

In all neutron scattering experiments, the dependence of the flux of neutrons scattered is measured as a function of Q and E. The scattered intensity $I(\vec{Q},E)$ is often referred as the neutron scattering law for the sample material. In 1954, Van Hove showed that the scattering law can be written in terms of time-dependent correlations between the positions of pairs of atoms in the sample [139]. This result implies that $I(\vec{Q},E)$ is proportional to the Fourier transform of a function that gives the probability of finding two atoms a certain distance apart. Supposing that all of the nuclei of the sample have the same scattering length "b", Van Hove showed that the scattering law $I(\vec{Q},E)$ could be written as [140]:

$$I(\vec{Q},E) = \frac{Nb^2}{h}\frac{k}{k'}\int_{-\infty}^{\infty} dt \int_{sample} G(\vec{r},t)\, e^{-i\vec{Q}.\vec{r}} e^{i(E/h)t} d\vec{r} \qquad \textbf{(Equation A2)}$$

where "N" is the number of nuclei in the sample. The function $G(\vec{r},t)$ is called "time-dependent pair correlation function", being defined as:

$$G(\vec{r},t) = \frac{1}{N}\sum_{i,j} \delta(\vec{r} - [\vec{r_i}(0) - \vec{r_j}(t)]) \qquad \textbf{(Equation A3)}$$

The position vectors $\vec{r}_i(0)$ and $\vec{r}_j(t)$ are quantum mechanics position operators. This function describes how the correlation between the positions of nuclei evolves with time. It is zero unless the separation between nucleus "i" at time zero and nucleus "j" at time t is equal to the vector $\vec{r}$. Thus, the function tells the probability that, within the sample, there will be a nucleus at the origin of the coordinate system at time zero as well as a nucleus at position $\vec{r}$ at time t.

The simplest type of coherent scattering is diffraction. As the incident neutron waves arrives at each atom, the atomic site becomes the center of a scattered spherical wave that has a definite phase relative to all other scattered waves. As the waves spread out from a regular array of sites in a crystal, the individual disturbances will reinforce each other only in particular directions. These directions are closely related to the symmetry and spacing of the scattering sites. Consequently, one may use the directions in which constructive interference occurs to deduce both the symmetry and the lattice constant of a crystal. The condition for diffraction is given by Bragg's law: for constructive interference to occur between waves scattered from adjacent planes, the path length difference must be a multiple of the wavelength λ.

$$n\lambda = 2d_{hkl}.\sin\theta \qquad \textbf{(Equation A4)}$$

where "d_{hkl}" is the distance between parallel neighboring (hkl) planes of atoms.

This effect exists only for wavelengths smaller than $\lambda_c = 2d_{max}$, where d_{max} is the maximum lattice constant of the crystal. For neutrons with $\lambda > \lambda_c$ the cross section decreases drastically.

Diffraction (or Bragg scattering) may occur for any set of planes, provided the neutron wavelength λ and the angle θ satisfy **Equation A4**. Diffraction occurs when the scattering vector $\vec{Q}$ is perpendicular to (hkl) planes. The strong neutron beam scattered at the angle 2θ from the incident beam, and 2θ from $\vec{Q}$ gives rise to a "Bragg peak" on the diffractogram.

In diffraction experiments with single crystals, the sample must be correctly oriented to obtain Bragg scattering. On the other hand, polycrystalline powders, which consist of many randomly oriented single-crystal grains, will diffract without needing a rotation of the sample as there will always be grains in the powder that are correctly oriented to diffract. This observation is the basis of the technique of "powder diffraction".

Most of the neutron powder diffractometers use the Debye-Scherrer geometry. In a powder diffractometer at a reactor neutron source, a parallel monochromatic neutron beam hits the sample contained in a cylindrical holder. The neutrons diffracted from a powder sample are collected by detectors and the signal is recorded as a function of the angles through which they were scattered by the sample. The monochromator is usually

an assembly of single crystals, oriented such as they diffract a mono-energetic beam of neutrons towards the sample.

Each Bragg peak in a typical diffraction pattern corresponds to diffraction from atomic planes with different interplanar spacings "d_{hkl}". Using this pattern, the atomic structure of a polycrystalline sample may be deduced. In practice, one needs to account carefully for the shape of the Bragg peaks in carrying out this refinement.

The simultaneous refinement of the atomic positions to obtain a powder diffraction pattern that is the same as the measured pattern is often referred to as Rietveld analysis. The principle of the Rietveld method is to calculate a theoretical diffractogram from the different variables in the equations of diffraction and taking into account the instrumental characteristics. The structural parameters (lattice parameters, atomic positions, Debye-Waller factor, site occupancy), the scale factor, the background signal and the shape function are progressively refined by a least square method to produce a calculated pattern that should be as close as possible to the experimental diffractogram. This is done by minimizing the quadratic discrepancies between calculated and experimental patterns at any point; the fit quality is evaluated by profile agreement indices such as χ^2 [102].

The calculated intensity at point "i" $I_{i,calc}$ is defined as the sum of the background contribution and all the Bragg peaks from the different phases contributing at this point [141]:

$$I_{i,calc} = I_{bi} + \sum_{\Phi} S_{\Phi} \sum_{k} j_{\Phi k}.Lp_{\Phi k}.|S_{\Phi k}|^2.\Omega_{i\Phi k} \qquad \textbf{(Equation A5)}$$

where:

- I_{bi}: background contribution.
- S_{Φ}: scale factor of the phase Φ.
- $j_{\Phi k}$: multiplicity of the reflection k.
- $Lp_{\Phi k}$: Lorentz-polarization factor, which is a function of the angle θ.
- $S_{\Phi k}$: structure factor.
- $\Omega_{i\Phi k}$: profile shape function.

Other terms can be included, such as the preferred orientation function and special corrections (special absorption corrections, extinction etc.).

The first summation concerns all the crystalline phases Φ present in the sample and the second one relates to all the reflections k=(hkl) contributing at pattern point "i". The structure factor $S_{\Phi k}$ relates the intensity of Bragg peak (hkl) to the atomic arrangement in the sample. The shape function $\Omega_{i\Phi k}$ is used to define the peak profile.

The structure factor is the Fourier transform of the scattering density, ρ(x,y,z), i.e. nuclear density taken over the whole unit cell. The scattering density ρ can be obtained from the diffraction data by Fourier reconstruction. The scattering density is usually calculated as a regular grid in *x*, y, and z. It may then be displayed as either a 2- or 3-dimensional Fourier map with contours and colors to indicate different density levels. Two-dimensional maps are typically drawn, while three-dimensional maps employ a chicken-wire style mesh representing a single level. The density distribution reflects the form of the wave functions of hydrogen in the potential field of the surrounding metal atoms and, in some cases, even suggests the possible jump paths of hydrogen atoms [142].

ANNEX B – Procedure of Neutron Scattering Profiles Refinement using Fullprof

1) Open the PCR Editor by clicking its icon on the FullProf menu. The PCR Editor has different parameters for adjustment, separated in the following groups: General, Patterns, Phases, Refinement, Constraints, Box/Restrains and Output (**Figure B1**).

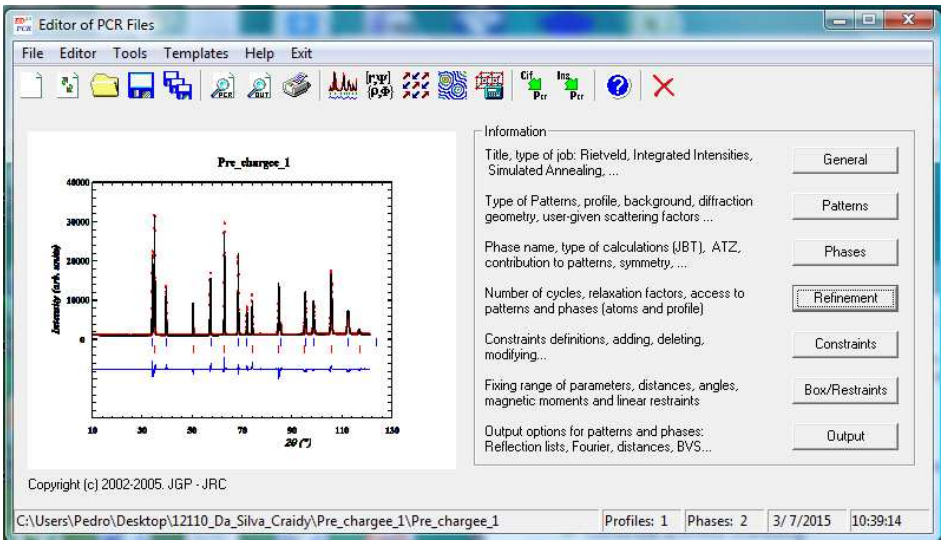

Figure B1. PCR Editor home page.

2) Open an existing PCR file. This template file will be modified to obtain an optimized refinement.

3) Press “General”, define a proper name for the project and set the option “Optimize calculations according to the particular options used in this job”.

4) Press “Patterns” and choose the option “Data File/Peak shape”-“Data File/Format”. The format should be X,Y,SIGMA (XYDATA). In the option “Refinement/Simulation”, set “Neutron – CW (Nuclear and Magnetic)”. The wavelength should be defined according to the value used in the measurements.

5) In the option “Patterns”-“Data file/Peak shape”-“Pattern Calculation/Peak Shape”, different parameters should be defined:

- Peak shape. It is important to know beforehand the best peak shape function adapted to the particular measured diffraction pattern. Different options are available: Gaussian, Lorentzian, modified Lorentzian, pseudo-Voigt, Pearson-VII, Thompson-Cox-Hastings (TCH) pseudo-Voigt, numerical, split pseudo-Voigt, tripled pseudo-Voigt etc. The TCH pseudo-Voigt profile function is recommended. In general, for constant wavelength and energy dispersive data, the pseudo-Voigt function is well adapted for X-ray and neutron

diffraction, with predominant Lorentzian character for the former and Gaussian for the latter.

- Range of calculation. Higher values of this parameter will result in longer calculation times, while too low values lead to poor fits. As a first try, one should choose between 6 and 8*FWHM.

6) In the option “Patterns”-“Background Type”, choose the option “linear interpolation”, which tends to be more stable.

7) In the option “Patterns”-“Excluded Regions”, exclude between 4º and 6° or 10º, since in the measured diffractograms, there is no important information in this range.

8) In the option “Phases” at the Editor main menu it is possible to define the “coefficient to calculate the weight percentage of the phase”, necessary for quantitative analyses. The coefficients are calculated by the following expression:

$$ATZ = Z.M_W.f^2 \qquad \textbf{(Equation B1)}$$

being:

- Z: Number of molecules of Fe per unit cell (2 for ferrite, 4 for austenite).
- M_w: Atomic mass of an atom of iron (55,85 g/mol).
- f = Occ.M/m: The occupancy “Occ” can be calculated by the following expression: Occ = O.m/M, being “O” the crystallographic site occupancy (which should be 1 when a site is fully occupied), “m” the site multiplicity (4 for austenite, 2 for ferrite) and “M” the general site multiplicity (192 for austenite, 96 for ferrite). The value of Occ is equal to 0,0208333 for both austenite and ferrite. From these results, f = 1 for both phases.

From the mentioned values, it comes that:
For austenite, f = 1, M_w = 55,85, Z = 4, so ATZ = 223,316. For ferrite: f = 1, M_w = 55,85, m = 2, Z = 2, so ATZ = 111,658.

9) Press the option “Refinement” of the main window. Several parameters should be set, but it is important to avoid selecting too many parameters to refine in each step, as it may lead to divergence.

- Choose at least 50 refinement cycles and as convergence precision shifts < 0,1 e.s.d.

- For both austenite and ferrite, start the refinement by changing the lattice parameters (a, b, c), profile parameter W and scale factor in the Profile window. The other FWHM

parameters, U and V, can also be chosen. The angular dependence of the halfwidths of the diffraction peaks can be expressed as:

$$H_K^2 = U.tg^2\theta_k + V.\ tg^2\theta_k + W \qquad \textbf{(Equation B2)}$$

where U, V, and W are the halfwidth parameters.

- In the option “Instrumental”, correction of “Zero” may be performed initially or after other refinements.

10) Save the PCR file at the appropriate directory.

11) In the FullProf main menu, click on the “Run WinPLOTR” icon. On WinPLOTR, select the icon “FP”. Select the input (PCR) and data files (_xy.DAT). The refinement will start and inform about the residuals and χ^2. The refinement should be repeated and improved, changing the parameters until the residuals and χ^2 and sufficiently low.

The quality of the agreement between observed and calculated profiles is measured by different factors. “χ^2” is defined as:

$$\chi^2 = \sum_{i=1}^{n} w_i\left(y_i - y_{c,i}\right)^2 \qquad \textbf{(Equation B3)}$$

The profile factor R_p is defined as:

$$R_p = 100\frac{\sum_{i=1,n}|y_i - y_{c,i}|}{\sum_{i=1,n} y_i} \qquad \textbf{(Equation B4)}$$

The weighted profile factor R_{wp} is defined as:

$$R_{wp} = 100\left[\frac{\sum_{i=1,n}\frac{w_i|y_i - y_{c,i}|^2}{2}}{\sum_{i=1,n} w_i {y_i}^2}\right]^{1/2} \qquad \textbf{(Equation B5)}$$

being:

- n: total number of points used in the refinement.
- y_i: observed pattern.
- $y_{c,i}$: calculated pattern.
- $w_i = 1/\sigma_i^2$, σ_i^2 is the variance of the observation y_i.

12) To create a background file, select on the WinPLOTR menu the option “Points selection”-“Automatic Background”. In order to increase the number of background points, one should enhance the “Background threshold” (for instance to 0.2) and reduce the “iteration number for smoothing” (to 1 or zero). To save the created background file, click on “Points selection”-“Save background points”.

13) The background correction is an important aspect for a proper refinement. This correction is performed on the PCR Editor; option “Refinement”. Automatic background

has frequently not an adequate accuracy. It is usually more efficient to import the background created on the previous step.

To correct the error indicated in **Figure B2**, at least two strategies are possible: (i) add points manually to the background file or (ii) set refinement of specific points. The strategy (ii) seems to be more efficient. The refinement of all points is not usually feasible.

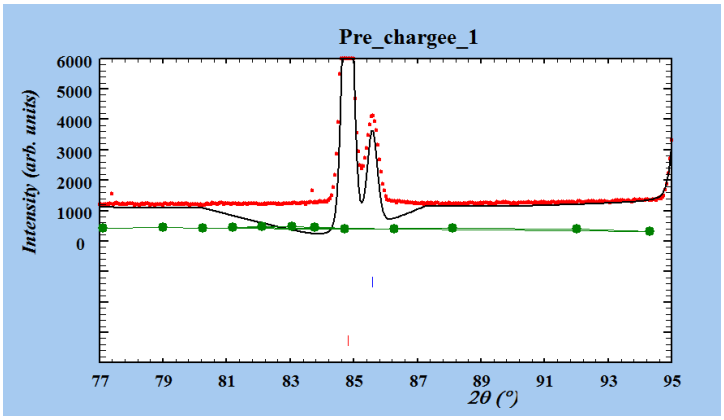

Figure B2. Example of background correction error.

14) To do Fourier map calculations, select “Output” on the main window of the PCR Editor, and the options “Pattern Output Information” - “Structure Factors File (FOU)” and tick GFOURIER.

ANNEX C – Measured X-Ray Diffraction Profiles

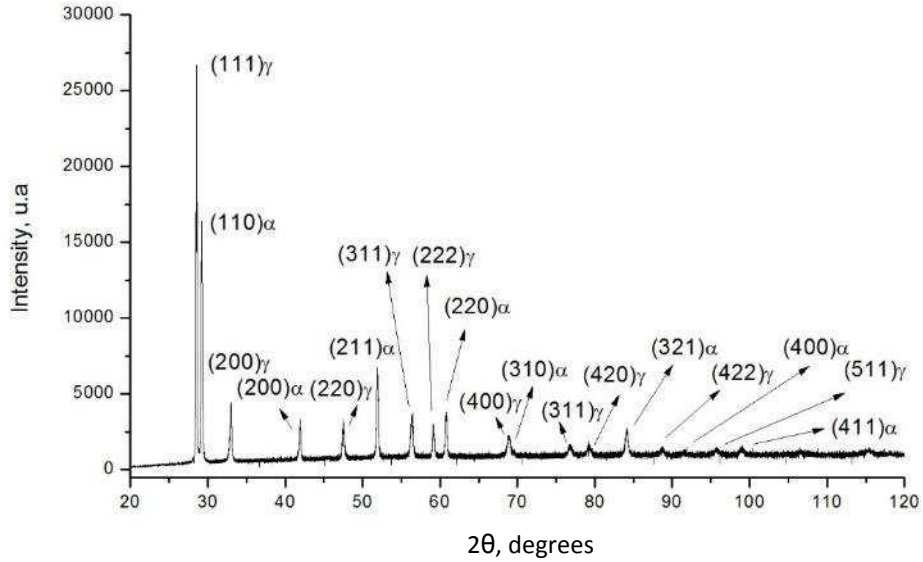

Figure C1. X-ray diffraction pattern – Non hydrogen-charged specimen 1.

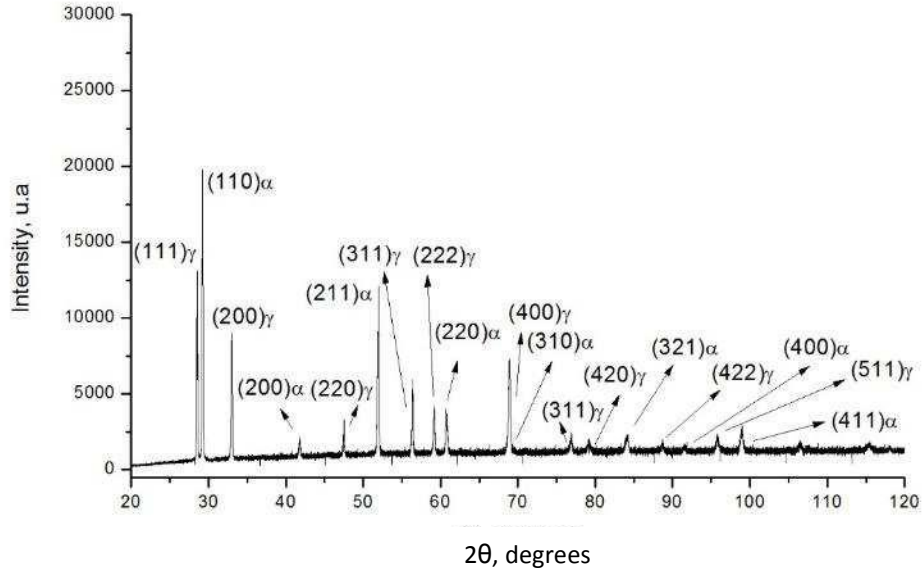

Figure C2. X-ray diffraction pattern – Non hydrogen-charged specimen 2.

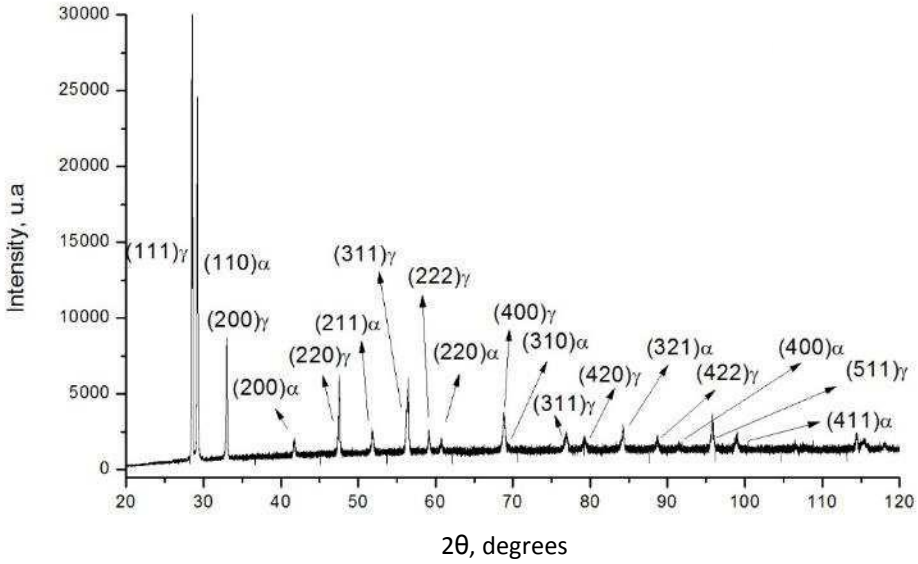

Figure C3. X-ray diffraction pattern – Non hydrogen-charged specimen 3.

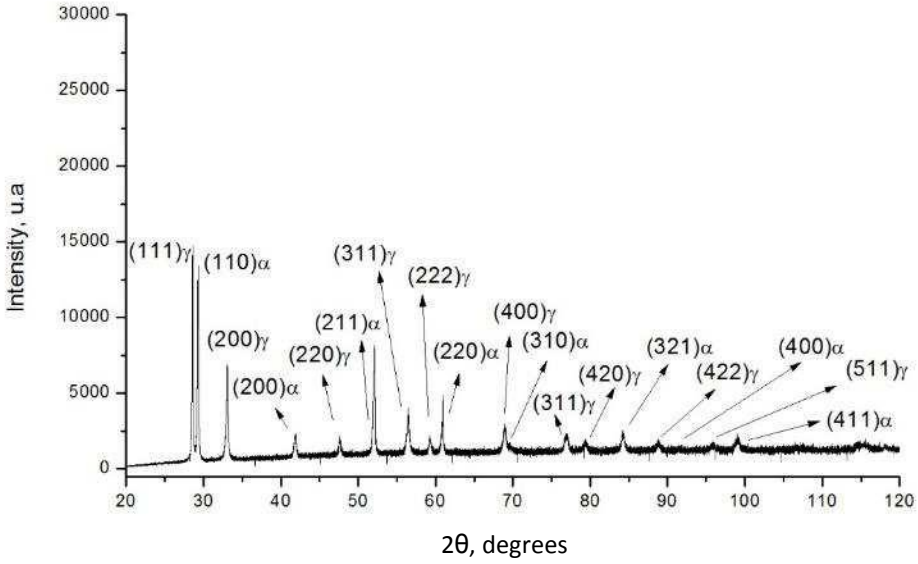

Figure C4. X-ray diffraction pattern – Non hydrogen-charged specimen 4.

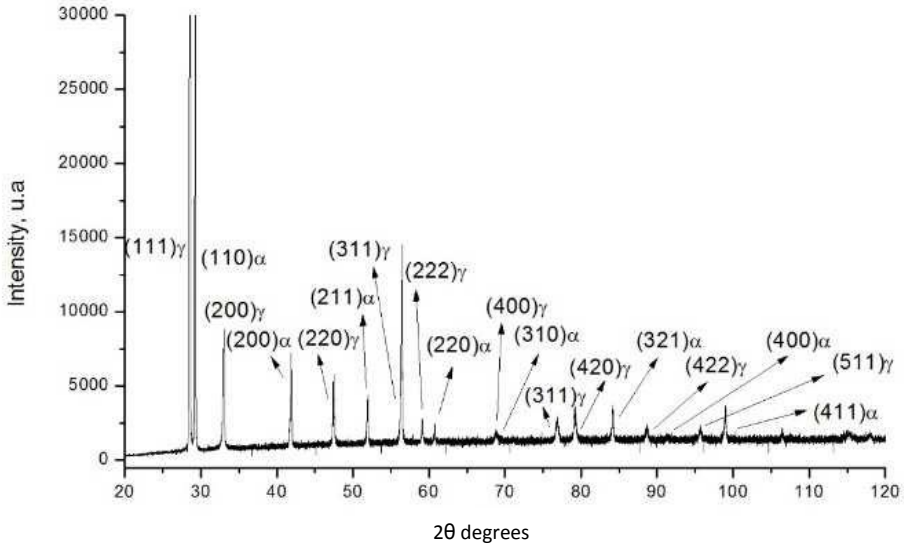

Figure C5. X-ray diffraction pattern – Hydrogen-charged specimen.

ANNEX D – Gas Permeation Tests

1) Table D1. Test Conditions.

Test	Flange position	Position of Pd layer	Temperature (ºC)	Average thickness (mm)	Test pressure (gauge, bar)	Observation
1	Body	Gas side	280	0,496	3,1-3,2	Helium detector
2	Body	Gas side	280	0,496	3,4-3,5	Helium detector, sequential to test 1
3	Body	Gas side	280	0,496	3,2-3,3	Helium detector, sequential to test 2
4	Body	Gas side	280	0,496	3,3-3,4	Old mass spectrometer
5	Body	Gas side	200	0,496	3,4-3,5	Old mass spectrometer, sequential do test 4
6	Body	Gas side	150	0,496	3,1-3,2	Old mass spectrometer, sequential to test 5
7	Body	Gas side	150	0,497	3,0 (2,99-3,01)	New mass spectrometer
8	Body	Gas side	150	0,497	3,1-3,2	New mass spectrometer, sequential to test 7
9	Body	Gas outlet	200	0,470	3,1-3,2	New mass spectrometer
10	Body	Gas outlet	150	0,470	3,3-3,4	New mass spectrometer, sequential to test 9
11	Body	Gas outlet	150	0,471	3,2-3,3	New mass spectrometer
12	Neck	Gas side	280	0,529	3,0-3,1	New mass spectrometer

13	Neck	Gas side	200	0,529	3,2-3,3	New mass spectrometer, sequential to test 12
14	Neck	Gas outlet	200	0,536	3,0-3,2	Old mass spectrometer, sequential to test 15
15	Neck	Gas outlet	150	0,536	3,6-3,7	Old mass spectrometer
16	Neck	Gas side	150	0,533	3,0-3,1	New mass spectrometer
17	Neck	Gas side	150	0,529	2,9-3,0	New mass spectrometer, sequential to test 13
18	Body	Gas inlet	80	0,209	5,2-5,3	Old mass spectrometer
19	Neck	Gas inlet	80	0,251	5,1-5,2	New mass spectrometer

2) Selected Permeation Curves

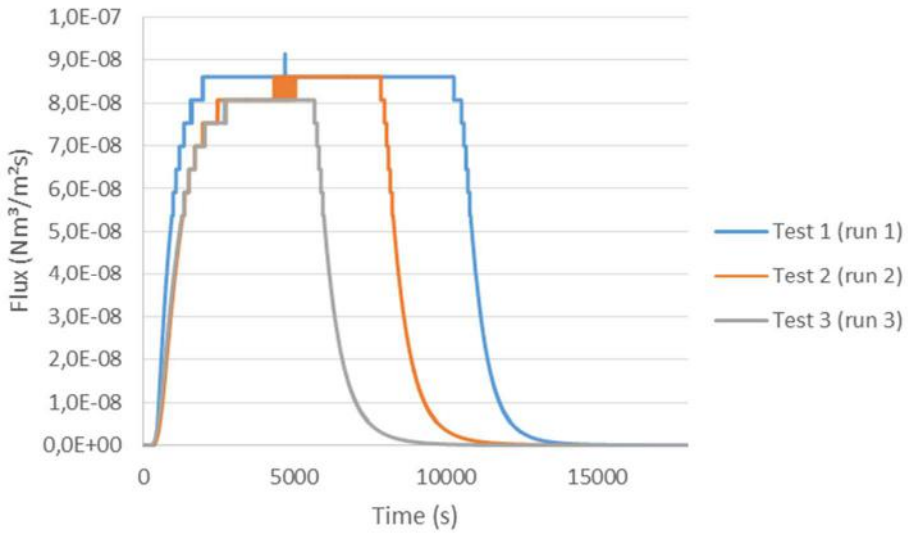

Figure D1. Permeation curves for the tests in a flange body specimen at 280ºC (Pd on entry side) – Helium detector.

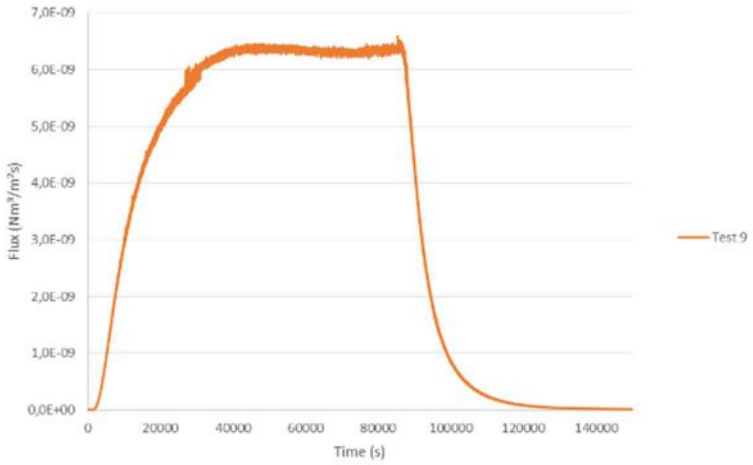

Figure D2. Permeation curves for the test in a flange body specimen at 200ºC (Pd on detection side).

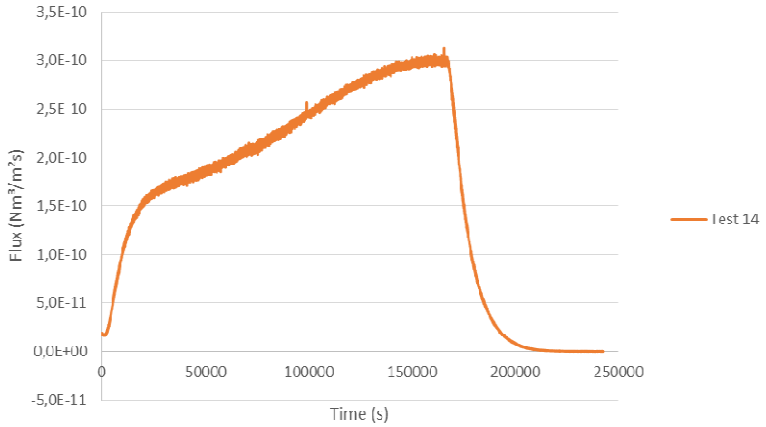

Figure D3. Permeation curves for the test in flange neck specimen at 200ºC (Pd on detection side, after test 15).

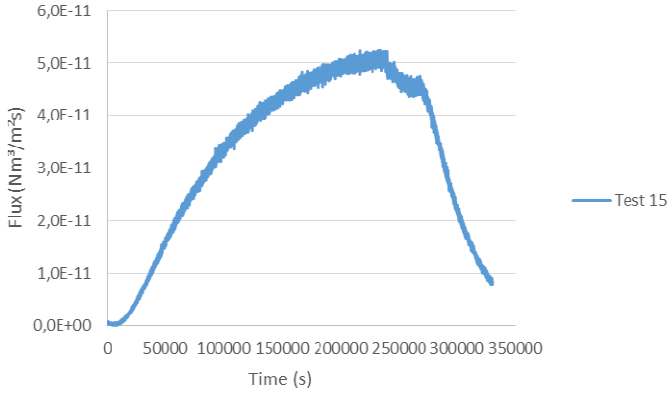

Figure D4. Permeation curves for the test in flange neck specimen at 150ºC (Pd on detection side) – Old spectrometer.

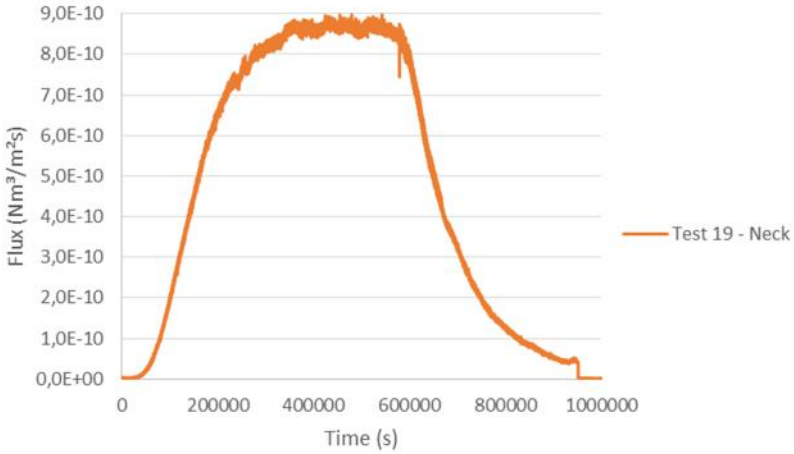

Figure D5. Permeation curves for the flange neck at 80ºC (Pd on entry side) – New spectrometer.

ANNEX E – Slow-Strain Rate Tensile Tests

1) Table E1. Test Conditions

Test	Venue	Material	Pre-charging	Environment	Initial strain rate (s^{-1})	D_o (mm)	L_o (mm)
(a) Tests in air without previous hydrogen charging							
F1B3	CEA	Body	No	Air	10^{-5}	3,79	17,88
F1B4	CEA	Body	No	Air	10^{-5}	3,79	17,15
F1N2	CEA	Neck	No	Air	10^{-5}	3,82	17,21
F1N4	CEA	Neck	No	Air	10^{-5}	3,79	17,69
F1B15	UFRJ	Body	No	Air	10^{-3}	3,82	17,87
F1B16b	UFRJ	Body	No	Air	10^{-5}	3,86	18,01
F2B32	UFRJ	Body	No	Air	10^{-6}	3,80	17,66
F1N7	UFRJ	Neck	No	Air	10^{-3}	3,82	17,66
F1N8	UFRJ	Neck	No	Air	10^{-3}	3,70	17,84
(b) Tests with in-situ gaseous H_2 charging, without previous hydrogen charging							
F1B7	CEA	Body	No	H_2, 01 bar	10^{-5}	3,80	17,56
F1B8	CEA	Body	No	H_2, 10 bar	10^{-5}	3,81	17,54
F1B5	CEA	Body	No	H_2, 50 bar	10^{-5}	3,82	17,16
F1B6	CEA	Body	No	H_2, 50 bar	10^{-5}	3,83	17,26
F1B1	CEA	Body	No	H_2, 300 bar	10^{-5}	3,79	17,15
F1B2	CEA	Body	No	H_2, 300 bar	10^{-5}	3,81	18,23
F1N5	CEA	Neck	No	H_2, 10 bar	10^{-5}	3,80	17,92
F1N6	CEA	Neck	No	H_2, 50 bar	10^{-5}	3,82	16,80
F1N1	CEA	Neck	No	H_2, 300 bar	10^{-5}	3,80	17,29
F1N3	CEA	Neck	No	H_2, 300 bar	10^{-5}	3,82	18,03
(c) Tests with in-situ electrochemical charging, without previous hydrogen charging							
F1B26	UFRJ	Body	No	3,5%NaCl, 0,5mA	10^{-5}	3,80	17,55
F1B28	UFRJ	Body	No	3,5%NaCl, 1mA	10^{-6}	3,76	17,56
F2B30	UFRJ	Body	No	3,5%NaCl, 3mA	10^{-6}	3,78	17,73
F1B25	UFRJ	Body	No	3,5%NaCl, 3mA	10^{-5}	3,84	17,13
F1B24	UFRJ	Body	No	3,5%NaCl, 30mA	10^{-5}	3,77	17,50

F1B27	UFRJ	Body	No	3,5%NaCl, 60mA	10^{-5}	3,84	17,10
F1B17	UFRJ	Body	No	3,5%NaCl, 120 mA	10^{-5}	3,79	17,84
F1B18	UFRJ	Body	No	3,5%NaCl, 490 mA	10^{-5}	3,82	18,01
F1B19	UFRJ	Body	No	3,5%NaCl, 1100 mA	10^{-5}	3,82	16,74
F1B20	UFRJ	Body	No	3,5%NaCl, 1100 mA	10^{-5}	3,79	17,50
F1B21	UFRJ	Body	No	3,5%NaCl, 3000mA	10^{-5}	3,73	17,21
F1B22	UFRJ	Body	No	3,5%NaCl, 3000mA	10^{-5}	3,84	17,53
F2N14	UFRJ	Neck	No	3,5%NaCl, 0,5mA	10^{-5}	3,83	17,56
F2N15	UFRJ	Neck	No	3,5%NaCl, 3mA	10^{-5}	3,85	17,73
F2N11	UFRJ	Neck	No	3,5%NaCl, 60mA	10^{-5}	3,87	17,96
F2N12	UFRJ	Neck	No	3,5%NaCl, 120mA	10^{-5}	3,84	17,82
F2N13	UFRJ	Neck	No	3,5%NaCl, 490mA	10^{-5}	3,86	17,94
F1N10	UFRJ	Neck	No	3,5%NaCl, 1100mA	10^{-5}	3,84	18,13
(d) Tests in air with specimens previously hydrogen charged							
F1B12	CEA	Body	Yes	Air	10^{-3}	3,82	17,55
F1B10	CEA	Body	Yes	Air	10^{-5}	3,84	17,61
F1B11	CEA	Body	Yes	Air	10^{-5}	3,81	17,4
F1B13	CEA	Body	Yes	Air	10^{-6}	3,77	16,67
F1B14	CEA	Body	Yes	Air	10^{-6}	3,83	16,98

2) Tensile properties measured in tests with in-situ gaseous H charging

Table E2. Flange body.

Property	F1B1	F1B2	F1B5	F1B6	F1B7	F1B8
Hydrogen pressure (bar)	300	300	50	50	1	10
Yield strength (MPa)	541,0	518,5	538,1	535,0	514,5	532,5
Ultimate strength (MPa)	628,3	610,4	688,4	676,3	739,4	736,3
Reduction of area (%) - ROA	14,0	11,7	15,1	14,3	59,3	46,8
Final elongation (%)	6,5	5,4	10,4	12,7	30,5	29,2
Fracture strain (%) - ε_f	3,3	2,5	8,3	7,4	29,6	24,4
Plastic fracture strain (%) - ε_{fp}	3,0	2,2	8,0	7,1	29,3	24,2
Plastic strain at maximum load (%) - $\varepsilon_{p\text{-}max}$	2,8	2,1	7,6	7,0	18,3	17,3
Relative ROA	22,2	18,5	23,9	22,7	93,9	74,1
Plastic strain at maximum load ratio	11,7	8,7	31,5	29,3	76,3	72,0
Plastic fracture strain ratio	8,6	6,2	22,9	20,3	83,6	68,9

Table E3. Flange neck.

Property	F1N1	F1N3	F1N5	F1N6
Hydrogen pressure (bar)	300	300	10	50
Reduction of area (%) - ROA	11,7	10,8	67,1	8,7
Final elongation (%)	7,3	9,4	35,7	12,0
Fracture strain (%) - ε_f	1,8	2,7	35,1	7,3
Plastic fracture strain (%) - ε_{fp}	1,4	2,4	34,8	7,0
Plastic strain at maximum load (%) - $\varepsilon_{p\text{-}max}$	1,3	2,2	23,3	6,7
Yield strength (MPa)	622,5	566,0	558,0	557,5
Ultimate strength (MPa)	660,9	646,0	755,5	688,1
Relative ROA (%)	15,1	13,8	86,2	11,2
Plastic strain at maximum load ratio (%)	5,5	9,7	101,0	29,0
Plastic fracture strain ratio (%)	4,0	6,7	96,7	19,4

3) Tensile properties obtained in tests with in-situ cathodic H charging

Table E4. Flange body.

Property	F1B17	F1B18	F1B19	F1B20	F1B24	F1B25	F1B26	F1B27	F1B28	F1B30
Current (mA)	120	490	1100	1100	30	3	0,5	60	1	3
Yield strength (MPa)	478,5	481,5	475,8	481,1	478,2	506,5	502,6	479,9	452,6	480,6
Ultimate strength (MPa)	606,0	671,1	627,8	637,2	624,9	708,7	738,2	644,1	657,8	647,8
Reduction of area (%) - ROA	18,0	18,3	6,6	17,2	13,7	29,4	78,7	19,9	74,3	17,9
Final elongation (%)	14,1	1,4	0,0	4,4	0,3	27,1	36,6	10,8	32,4	5,3
Fracture strain (%) - ε_f	5,7	7,4	8,5	6,6	8,4	22,2	32,7	10,1	30,0	10,5
Plastic fracture strain (%) - ε_{fp}	5,5	7,2	8,3	6,3	8,1	22,0	32,4	9,8	29,8	10,2
Plastic strain at maximum load (%) - $\varepsilon_{p\text{-}max}$	3,9	6,5	6,8	5,6	6,7	16,2	22,9	8,2	20,9	8,6
Relative ROA (%)	28,6	29,0	10,4	27,2	21,6	46,6	124,6	31,5	117,6	28,4
Plastic strain at maximum load ratio (%)	16,4	26,9	28,5	23,3	28,1	67,3	95,3	34,3	87,1	35,8
Plastic fracture strain ratio (%)	15,6	20,4	23,7	18,1	23,2	62,7	92,5	28,0	85,0	29,2

Table E5. Flange neck.

Property	F1N10	F1N11	F1N12	F1N13	F1N14	F1N15
Current (mA)	1100	60	120	490	0,5	3
Yield strength (MPa)	595,9	564,0	567,6	558,7	553,2	530,5
Ultimate strength (MPa)	643,9	638,0	665,0	629,5	784,0	680,0
Reduction of area (%) - ROA	10,6	10,7	14,4	19,6	79,2	32,9
Final elongation (%)	8,5	10,3	13,8	-	34,4	8,5
Fracture strain (%) - ε_f	3,7	6,7	7,8	5,5	42,7	11,7
Plastic fracture strain (%) - ε_{fp}	3,4	6,4	7,5	5,2	42,4	11,4
Plastic strain at maximum load (%) - $\varepsilon_{p\text{-}max}$	2,7	4,2	5,8	3,5	28,3	7,8
Relative ROA (%)	13,6	13,7	18,4	25,1	101,8	42,3
Plastic strain at maximum load ratio (%)	11,8	18,1	25,1	15,3	123,0	33,7
Plastic fracture strain ratio (%)	9,4	17,7	20,9	14,5	117,8	31,7

ANNEX F – Thermal Desorption Test Data

Table F1. TDS test conditions.

Test	Flange region	Pre-charging procedure	Weight (g)	Actual heating rate (ºC/s)	Actual heating rate (ºC/min)	Initial temperature (ºC)	Max temperature (ºC)
1	Body	Electrochemical	0,130	0,073	4,4	25	840,3
2	Body	Electrochemical	0,150	0,031	1,8	26	822,9
3	Body	No pre-charging	0,110	0,102	6,1	27	839,3
4	Body	Electrochemical	0,170	0,101	6,1	26	838,4
5	Body	Gaseous	0,255	0,021	1,2	26	800,0
6	Body	Gaseous	0,290	0,041	2,4	26	816,5
7	Body	Gaseous	0,299	0,061	3,7	26	813,5
8	Body	Gaseous	0,594	0,199	11,9	25	801,2
9	Neck	Electrochemical	0,199	0,033	2,0	26	800,1
10	Neck	Electrochemical	0,204	0,067	4,0	24	791,6
11	Neck	Electrochemical	0,185	0,100	6,0	25	787,5
12	Neck	Electrochemical	0,210	0,330	19,8	24	763,6

ANNEX G - Transient Regime Method

For a given time t_x so that $J_{tx}/J_\infty=x$, the general expression for the apparent diffusion coefficient is:

$$D_{t_x} = \frac{L^2}{\alpha.t_x} \qquad \textbf{(Equation G1)}$$

The values of α for the galvanostatic mode are listed in **Table G1**.

Table G1. Values of α in **Equation G1**.

J_{tx}/J_∞= x	α
0,036 (breakthrough)	19,70
0,1	15,15
0,2	11,90
0,3	9,90
0,4	8,40
0,5	7,19
0,6	6,17
0,629 (time-lag)	6,00
0,7	5,20
0,8	4,29
0,9	3,30

In the potentiostatic double mode, at $J/J_\infty=0,50$, the diffusivity is calculated by:

$$D = \frac{L^2}{4,76t_{1/2}} \qquad \textbf{(Equation G2)}$$